**UNIVERSITÀ DEGLI STUDI DI TRIESTE**

**Facoltà di Scienze Matematiche, Fisiche e Naturali**

**Dottorato di Ricerca in Fisica - XX Ciclo**

# Using hydrodynamical simulations to combine Sunyaev–Zeldovich and X–ray studies of galaxy clusters

DOTTORANDA
Silvia Ameglio

COORDINATORE DEL COLLEGIO DEI DOCENTI
Chiar.mo Prof. Gaetano Senatore, Università di Trieste

TUTORE
Chiar.mo Prof. Stefano Borgani, Università di Trieste

RELATORE
Chiar.mo Prof. Stefano Borgani, Università di Trieste

a.a. 2006/2007

# Contents

# Chapter 1

# Introduction

Cosmology has recently reached an important milestone. A wide variety of cosmological observations now support a single model for the overall architecture of the observable universe and the development of galaxies and other structures within it. According to this so–called *concordance model*, the geometry of the observable universe is indistinguishable from a flat geometry, implying that its total energy density is very close to the critical density needed to close the universe. The two dominant components of the universe appear to be a nonbaryonic form of dark matter, whose gravity is responsible for structure formation, and a mysterious form of dark energy, whose pressure is currently causing the expansion of the universe to accelerate. The mean density of baryonic matter is about 15% of the total amount of matter, and we can observe the baryonic matter only because the gravitational attraction of nonbaryonic dark matter has drawn the baryonic gas into deep potential wells, where a small fraction of it condenses into stars and galaxies.

This model explains many different features of the observable Universe, but it is not entirely satisfying because the nature of the dark matter and the origin of the dark energy remain unknown. In addition, many aspects of galaxy formation remain poorly understood. Dark matter models successfully account for the spatial distribution of mass in the universe, as traced by the galaxies, but they do not explain all the properties of the galaxies themselves. Dark matter initiates the process of galaxy formation, but, once stars begin to form, supernova explosions and disturbances wrought by supermassive black holes can inhibit further star formation by pumping thermal energy into the baryonic gas.

In this framework, clusters of galaxies are unique tracers of cosmic evolution, since they sit atop of the hierarchicy of cosmic structures, as the largest objects that have had time to collapse. Galaxy clusters are then the biggest structures whose masses can be reliably measured. Mass measurements of nearby clusters can be used to determine the amount of structure in the universe on scales of $10^{14-15}\,h^{-1}M_{\odot}$: the measurement of the present–day cluster mass distribution and its evolution with redshift can be used to measure the rate of structure formation, placing important constraints on cosmological models. In addition, galaxy clusters can be used as standard candles which directly trace the geometry of the Universe out to high redshift ($z \sim 1$). Second, clusters are essentially *closed boxes* that retain all their gaseous matter, despite the enormous energy input associated with supernovae (SN) and active galactic nuclei (AGNs), owing to their very deep gravitational wells. The baryonic component of clusters therefore contains a wealth of information about the processes associated with galaxy formation, including the efficiency with which baryons are converted into stars and the effects of the resulting feedback processes on galaxy formation.

The X–ray emission from the hot gas trapped in the potential wells of galaxy clusters was first observed in the direction of Coma, Virgo, Perseus, and other rich clusters. At that time, the astronomers postulated that the X-ray emission could be caused by two possible phenomena, *i)* bremsstrahlung emission from a non-relativistic thermal population of electrons or *ii)* inverse Compton scattering of the CMB photons by highly relativistic nonthermal electrons. It was correctly attributed to thermal bremsstrahlung several years earlier by Felten et al. (1966), who were inspired by a spurious X–ray detection of the Coma cluster (see also Cavaliere et al., 1971). Statistical samples of clusters observed in the X–rays were first obtained in the early 1970s, while the early 1990s new instruments provided an important improvement in both imaging and spectroscopy. Finally in the last decade there has been an enormous increase in the capabilities of X–ray instrumentation. In fact, the present satellites allow the detection of clusters out to $z > 1.2$ and the detailed study of gas properties (density, temperature and metal abundance) out to $z \sim 1$ in fairly large samples. These observations provided the most of present knowledge on the thermodynamic structure of galaxy clusters. At the same time, these new data showed that the thermodynamical processes acting in galaxy clusters are much more complex than previously thought. Still, a deeper understanding of the physics of baryons is required in order to calibrate them as precision tools for cosmology.

X–ray emission is not the only means to study the thermal structure of the hot IntraCluster Medium (ICM). Indeed, Sunyaev & Zeldovich (1972) suggested that the optical depth to Compton scattering of the hot gas in galaxy clusters should be large enough to boost very slightly the energy of the CMB photons. Since photon number must be conserved, this energy boost would cause a distortion of the radiation spectrum which is now called the Sunyaev–Zeldovich effect (SZ hereafter). However, early predictions of the expected SZ magnitude were somewhat optimistic, and the effort among observers to detect the SZ in galaxy clusters proceeded more slowly than expected. Over a decade passed before the first reliable detections of the SZ were made by Birkinshaw et al. (1984). Much progress has been done since that time and SZ measurements are now routinely performed by several telescopes. However, the low resolution of such instruments (compared to the X–ray ones) has represented so far the main limitation to fully exploiting the potential of SZ measurements.

The next decade promises to be very exciting for the study of galaxy clusters and cosmology, using both SZ and X–ray observations. A new generation of SZ telescopes is coming, which will be characterized by a better resolution and higher sensitivity than present instruments. Hence, deep surveys looking for the SZ effect will be finding thousands of clusters to distances well beyond a redshift of $z = 1$. Also, dedicated X–ray satellite missions to survey a large fraction of the sky for distant clusters are currently being planned or already in the phase of realization (e.g. eRosita, Predehl et al., 2006).

X–ray and SZ observations have different dependence on gas properties (density and temperature), thus their combination potentially represents a powerful instrument in cluster studies. However, the low resolution of SZ telescope now available does not allow a detailed study of cluster structure. The major application of X–ray/SZ observations has been the measure of the Hubble constant (Bonamente et al., 2006, and references therein), since the method does not require a resolved SZ profile. The situation will be much improved by the upcoming generation of SZ telescopes, which will provide high–resolution SZ images, opening the way for new applications. In particular, one interesting direction to explore will be the measure of temperature profiles (and then total mass profiles) by relying only on X–ray surface brigthness and SZ data, thus avoiding the use

of X–ray spectroscopy. The technique will also represent an improvement in the analysis of the cluster outskirts.

However, in order to fully exploit the potential of future observations, both the physics of the ICM and the possible instrumental systematics need to be fully understood. In this context cosmological hydrodynamical simulations provide an ideal test–bed to work out predictions on the capabilities of future X–ray and SZ observations to shed light on the dark sector of cosmological models. In this perspective, in this Thesis we present a study of two different techniques which make use of the combination of X–ray and SZ observations. The first method aims at measuring the angular diameter distance of galaxy clusters, thus using them as standard candles to probe the Universe geometry. The second is a deprojection technique which recovers gas density and temperature and total mass profiles, thus allowing on one hand to study in detail the thermodynamic structure of the ICM and on the other hand to have accurate mass estimates.

This Thesis is structured as follows.

Chapter 2 provides an introduction to cluster studies. It first describes the properties of the ICM in the X–ray band and through observations of Sunyaev–Zeldovich (SZ) effect. Then current X–ray observations are reviewed, together with their most important outcomings, which represent most of the present knowledge on the thermodynamics of the ICM. Then the current status of SZ observations and upcoming experiments are reviewed. Finally, the use of galaxy clusters is discussed, with particular attention to those aspects which are more relevant for the work presented in this Thesis.

Chapter 3 presents the set of simulated cluster which are used through the Thesis work. First it provides a description of the most important features of the TREESPH code GADGET2 code, with which the simulations have been performed, and the physical processes implemented to achieve a realistic description of the ICM (namely radiative cooling, star formation and galactic winds). Then, the set of galaxy clusters identified in the simulation box is presented. Finally, the procedure used to carry out projected maps of X–ray surface brightness, thermal SZ (tSZ hereafter) and temperature are described.

Chapter 4 presents a study on the systematic effects in recovering the angular diameter distance by using a combination of X–ray and tSZ data. After a description of the method, we present our results, which are obtained using both an isothermal and a polytropic model for the gas thermal structure. Finally the implications of these results for the estimate of cosmological parameters are discussed, through the fitting of the angular–diameter/redshift relation.

Chapter 5 presents a deprojection technique which has been developed to recover the gas density and temperature from the X–ray surface brightness and the tSZ signal, thus avoiding the use of X–ray spectroscopy. The method is described in detail and then tested against both an analytical cluster model and a set of simulated galaxy clusters. Furthermore, we discuss the effects of cluster elongation on our results.

Chapter 6 presents a development of the deprojection technique of Chapter 5, which includes the solution of the hydrostatic equilibrium equation. The method provides the gas density and temperature and the total mass profiles symultaneously. Two different approaches to mass modelling are discussed. The first one is model–independent, while the second one assumes an analytical model for the total mass profile. The two methods are described and tested against the set of simulated clusters.

Chapter 7 draws the main conclusions of the work presented in the Thesis and highlights the future perspectives for its development in the next years.

Finally, the Appendix provides an introduction to cosmology. In particular, we briefly review the cosmological model and the process of formation of the large scale structure, so as to describe the basic concepts of cosmology, which are used through the Thesis.

# Chapter 2

# Clusters of galaxies: an overview

Galaxy clusters have typical masses of $10^{14 \div 15}\, h^{-1} M_{\odot}$, dominated by the dark matter component ($\sim$ 80%), while baryons only constitute $\sim$ 15% of the total mass budget. Most of these baryons ($\sim$ 12% of the total mass) are in the form of a hot and diffuse gas, the IntraCluster Medium (ICM). During the process of cluster formation, this gas is shocked by merging and heated by adiabatic compression, thus reaching the virial temperature (from $\sim$ 1 keV to $\sim$ 10 keV) and correspondingly a very low density, of the order of one particle per $10^{-3}$ cm$^3$. Only a very small fraction of baryon gas ($\sim$ 3% of the total mass) cools to form stars and galaxies, which are the only component visible at optical wavelengths.

Galaxy clusters represent powerful probes for cosmology, for many reasons. First of all, their mass distribution and how it evolves with redshift are solid predictions of the standard cosmological model. Their observation thus provides a measure of fundamental cosmological parameters. Second, the matter content in galaxy clusters is considered as a fair sample of that of the Universe and then they can be used to measure the fraction of mass in baryons. Finally, galaxy clusters can be used as standard rods to directly probe the geometry of the Universe. However, to fully exploit the potential of galaxy clusters as cosmological probes it is necessary to achieve an accurate knowledge of their structure and properties.

In a simple picture of structure formation, baryonic and dark matter collapse under the only action of the gravitational attraction. During this process, the gas is shocked in accretion and/or merging events and heated by adiabatic compression. Since gravity does not have any preferred scale, this scenario predicts the formation of self–similar systems which basically appear as scaled versions of each other. By assuming that the gas lies in hydrostatic equilibrium within the dark matter potential wells, this scenario predicts self–similar scaling relations also between gas properties and total mass (see Rosati et al., 2002; Voit, 2005, for reviews).

However, the observed scaling relations deviate from those predicted by self–similar scaling. This is a clear indication that non–gravitational processes, like radiative cooling and heating from AGNs or SNe, are acting in the core of galaxy clusters. The correct interpretation of these processes makes galaxy clusters interesting astrophysical laboratories, where to study, among other things, the complex interplay between the ICM and the galaxies. At the same time, it indicates that an accurate study of the thermodynamical structure of the ICM is required in order to use galaxy clusters as precision tools for cosmology.

In this Chapter we provide an introduction to cluster studies with particular enphasis

on X–ray and SZ observations. It is structured as follows. The physics behind the X–ray and Sunyaev-Zeldovich properties of galaxy clusters is described in Sections 2.1 and 2.2, respectively. Section 2.3 reviews the status of present and upcoming X–ray and SZ observations and describes the properties of the hot gas in galaxy clusters. Section 2.4 is devoted to a short overview of the applications of galaxy clusters as tools for cosmological studies.

## 2.1 X–ray emission

Given its high temperature and very low density, the ICM gas is optically thin and fully ionized. Electrons and heavy ions are in a state of collisional equilibrium. Radiation is emitted essentially through the process of *thermal bremsstrahlung*. For a gas at temperature $T$, the emissivity per unit frequency $\nu$ is given by (e.g. Rybicki & Lightman, 1986):

$$j_\nu = 5.44 \cdot 10^{-52} \overline{Z^2} n_e n_i T^{-1/2} \overline{g}\, e^{-h\nu/kT} \ \mathrm{W/m^3/Hz} \tag{2.1}$$

where $\overline{Z^2}$ is the mean–squared atomic charge on the ions. The Gaunt factor, $\overline{g} \sim 1.2$ is a dimensionless quantity which depends on the range of distances between electrons and ions at which the scatter process occurs, with a weak dependence on $\nu$. The emissivity is proportional to the square of gas density, since the rate of collisions is proportional to the product of the electron density $n_e$ and the ion density $n_i$. Examples of X-ray spectra for typical cluster temperatures are shown in figure 2.1. Note that, due to the exponential cut–off of the bremsstrahlung emission, the continuum is very sensitive to temperature for energies greater than $T$ and rather insensitive to it at lower energies.

The emissivity in a particular band is usually rewritten as

$$\epsilon_\nu = n_e n_H \Lambda(\nu, T) \tag{2.2}$$

where $n_e$ and $n_H$ are the electron and proton number density and $\Lambda(T)$ is the *cooling function*, which depends on the frequency of the observations and the temperature of the gas. When integrated over a wide range of frequencies, it scales as $\epsilon \propto T^{1/2}$.

The observed surface brightness is given by the integral of the emissivity along the line of sight:

$$S_X = \frac{1}{4\pi(1+z)^4} \int_{los} n_e n_H \Lambda(T) dl \tag{2.3}$$

Note that it decreases with redshift as $(1+z)^{-4}$, owing to the expansion of the Universe which causes a loss of photon energy. This represents a limit for X–ray astronomy in the detection of clusters at very high redshift.

X-ray surface brightness and spectrum are powerful sources of information about the ICM in galaxy clusters.

- **Gas density.** The emissivity is not very sensitive to $T$ at low energy. Therefore X-ray images or surface brightness profiles extracted in a soft energy band (e.g. $0.5-2$ keV) are used to determine the gas density distribution. X–ray observations are characterized by an excellent resolution, so the X-ray images are ideally suited for a detailed description of the ICM morphology. The gas density is computed from the *emission measure* $EM = \int n_e^2\, dl$, which represents the normalization of

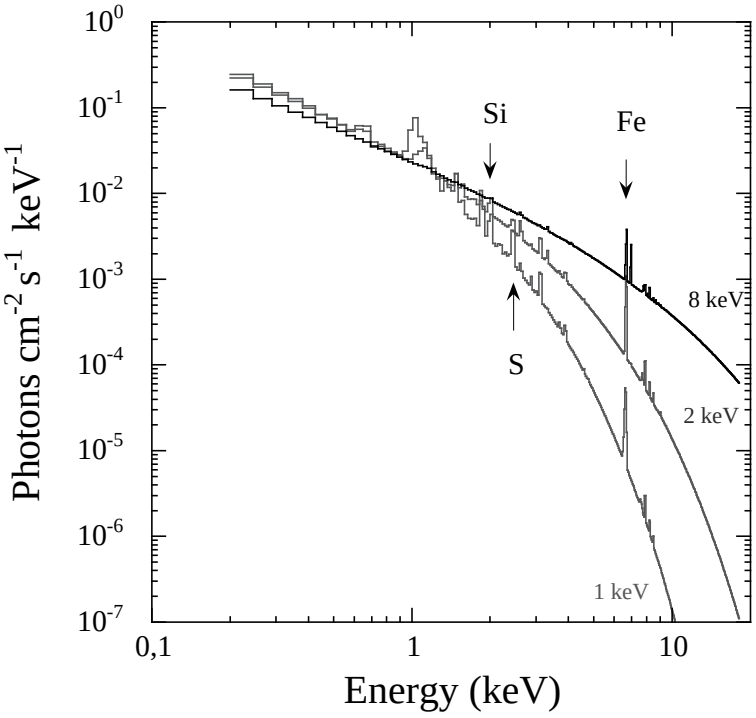


**Figure 2.1.** The X-ray emission from a thin plasma with 0.35 solar abundance at different temperatures, $T = 1, 2$ and 8 keV (plot from Arnaud, 2005).

the X–ray spectrum (see eq. 2.1). It can be deduced from the surface brightness, $S_X$, according to

$$EM = \frac{4\ \pi\ (1+z)^4\ S_X}{\Lambda(T,z)}. \tag{2.4}$$

Since $\Lambda(T, z)$ depends only weakly on the temperature in the soft band, in this equation one can generally use the average cluster temperature.

- **Gas temperature.** Its measurement requires spectroscopic data. The temperature is derived by fitting the observed spectrum with a thermal emission model convolved with the instrument response (i.e. taking into account how the effective area and spectral resolution vary over the energy range). The temperature is constrained by the position of the exponential cut-off in the spectrum. In order to have a proper determination of the temperature, one needs spectroscopic instruments which are sensitive up to energies greater than $T$, i.e., typically 10 keV. The ICM is not strictly isothermal. This means that a temperature inferred from an isothermal fit to the data is actually a *mean* value along the line of sight and within the cluster extraction region (Mazzotta et al., 2004). How this mean is computed in detail is a crucial point when comparing simulations to observations. In Section 3.4 we will discuss three definitions of mean temperature which are commonly used in the analysis of cluster simulations. Each of these definitions has different properties, which could in principle lead to biases in the comparison between observations and simulations. In Chapter 4 we present a study on the accuracy in recovering the angular diameter distance from combined X–ray and tSZ observations. Since this type of measure requires a fit of the temperature profile, we perform our analysis by adopting each

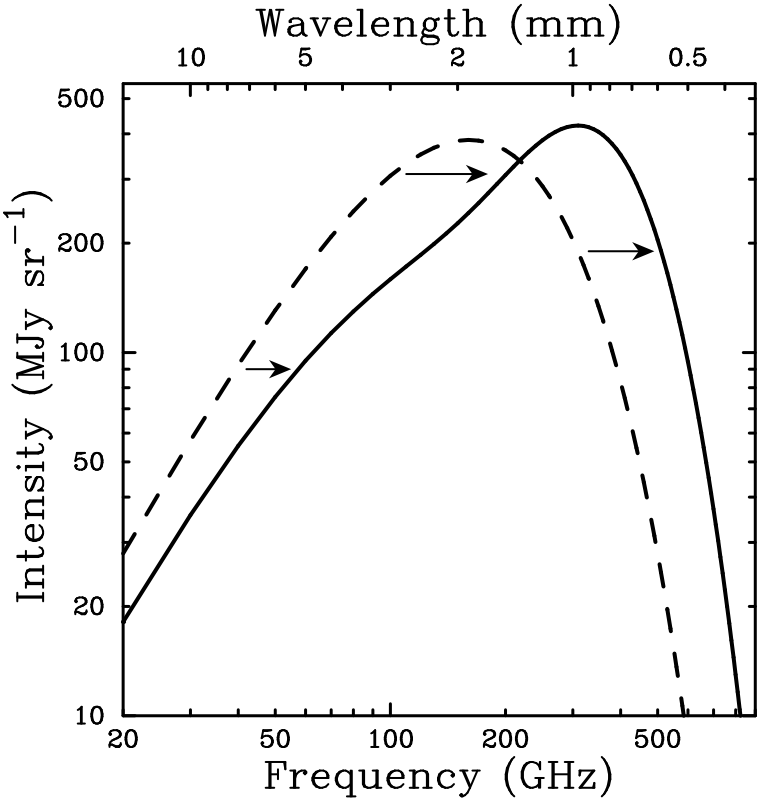


**Figure 2.2.** The CMB spectrum, undistorted (dashed line) and distorted by the tSZ (solid line). The tSZ distortion shown is for a model cluster 1000 times more massive than a typical massive galaxy cluster (plot from Carlstrom et al., 2002).

of these mean temperature definitions, in order to understand which is their impact on our final results.

- **Heavy elements.** In addition to the continuum generated by the bremsstrahlung emission, the X–ray spectrum of galaxy clusters presents a number of emission lines, which are due to the presence of heavy elements. The only line that clearly stands out at all temperatures is the Iron K line complex around 6.7 keV (see figure 2.1). We can also observe the K lines of other elements (O, Si, S, with H and He–like ionization states), as well as the L-shell complex of lower ionization states of Iron ($T \sim 1-2$ keV. However the intensity of these lines rapidly decreases with increasing temperature. Except for cool clusters ($T \lesssim 4$keV) or in the cooling core present in some clusters, it is difficult to measure the abundance of elements other than Iron because they are completely ionized. For a review on the measure of metallicity in the ICM, see e.g. Mushotzky (2004).

## 2.2 The Sunyaev–Zeldovich effect (SZ)

### 2.2.1 The thermal Sunyaev–Zeldovich effect (tSZ)

The thermal Sunyaev–Zeldovich (tSZ) effect (Sunyaev & Zeldovich, 1972) is the distortion of the Cosmic Microwave Background (CMB) spectrum due to the scattering of the CMB

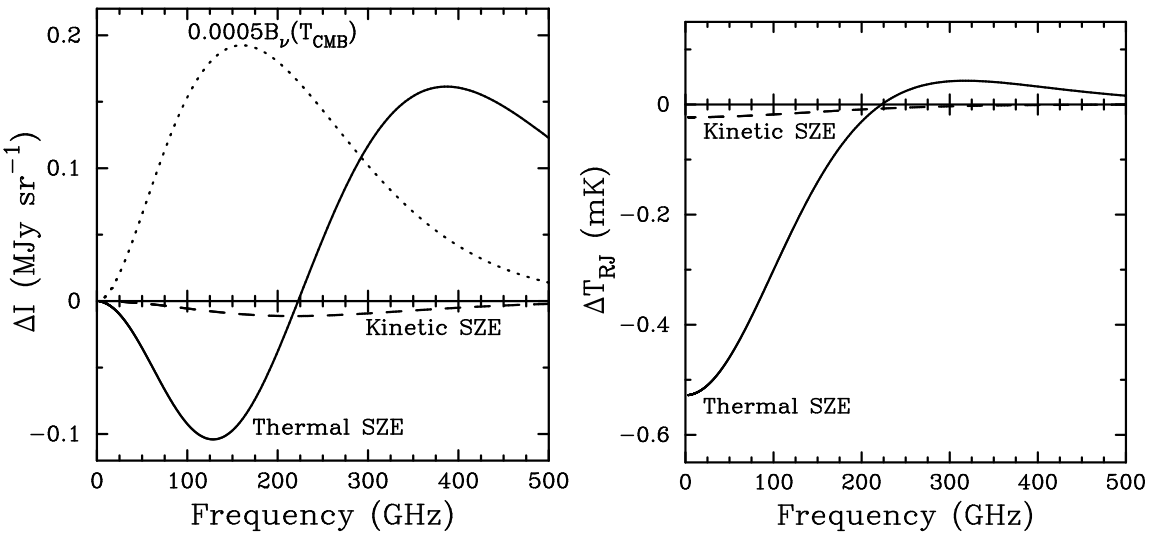


**Figure 2.3.** Spectral distortion of the CMB radiation due to the SZ effect. The left panel shows the intensity and the right panel shows the Rayleigh Jeans brightness temperature. The thick solid line is the thermal SZ and the dashed line is the kinetic SZ. For reference the 2.7 K thermal spectrum for the CMB intensity scaled by 0.0005 is shown by the dotted line in the left panel. The cluster properties used to calculate the spectra are an electron temperature of 10 keV and density of $10^{-3}$cm$^{-3}$, a Comptonization parameter $y = 10^{-4}$, and a peculiar velocity of 500 km/s (plots from Carlstrom et al., 2002).

photons off a population of thermal electrons. The distortion is represented in figure 2.2 as computed for a model cluster being 1000 times more massive than a typical massive cluster, to make it clearly visible. This effect has now been detected for a fairly large number of clusters of galaxies (e.g. Rephaeli, 1995; Birkinshaw, 1999; Carlstrom et al., 2002, for reviews).

The spectral distortion is described as a variation of the CMB temperature at different frequencies (which are expressed by the dimensionless frequency $x = h\nu/k_B T_{CMB}$):

$$\frac{\Delta T_{tSZ}}{T_{CMB}} = f(x)y \tag{2.5}$$

where the function $f(x)$ describe the frequency dependence, while the *Comptonization parameter* $y$ measures the entity of the effect. The typical size of this distortion for a thermal distribution of electrons with temperature of about 10 keV is at the level of $y \sim 10^{-4}$.

The Comptonization parameter $y$ is directly proportional to the pressure integrated along the line of sight:

$$y = \int n_e \frac{k_B T_e}{m_e c^2} \sigma_T d\ell \tag{2.6}$$

where $k_B$ is the Boltzmann constant, $\sigma_T$ is the Thomson cross section, $m_e$ is the mass of the electron, $c$ is the speed of light. By definition, it provides a redshift–independent measure of the total thermal content of the cluster.

The frequency dependence is given by

$$f(x, T_e) = \left( x \frac{e^x + 1}{e^x - 1 - 4} \right) [1 + \delta(x, T_e)] \tag{2.7}$$

where $\delta(x, T_e)$ is a correction due to relativistic effects. In the non–relativistic limit the shape of the distortion is independent of the temperature.

Expressed in units of specific intensity, as is usually done for SZ observations in the millimetric band, the tSZ distortion becomes:

$$\Delta I_{tSZ} = g(x) I_0 y \tag{2.8}$$

where $I_0 = 2(k_B T_{CMB})^3/(hc)^2$ and the frequency dependence is given by

$$g(x) = \frac{x^4 e^x}{(e^x - 1)^2} f(x)(1 + \delta_{tSZ}(x, T_e)) \tag{2.9}$$

The function $g(x)$ is plotted in figure 2.3 with the solid line, for a typical cluster having a Comptonization parameter $y = 10^{-4}$ ($T = 10$ keV and $n_e = 10^{-3}\mathrm{cm}^{-3}$). The tSZ has a unique spectral signature with a decrease of the CMB intensity at frequencies $\lesssim 218$ GHz and an increase at higher frequencies. In the Rayleigh–Jeans part of the spectrum and in the non–relativistic approximation, the function becomes $f(x) \to -2$ for $x \to 0$. The tSZ spectrum is peculiar and may be easily disentangled from primary CMB temperature fluctuations, if a multiwavelength observation is available.

Note that the tSZ effect is independent of redshift. In fact, the CMB is more intense at high $z$ by a factor of $(1+z)^4$, thus the amount of the tSZ effect $\Delta I_{tSZ}$ for a given cluster at redshift $z$ will be enhanced by the same factor (see eq. 2.8). The intensity variation will dim with redshift, as $(1 + z)^{-4}$, thus giving the same signal as a low $z$ object having the same intrinsic properties.

Relativistic correction (e.g. Itoh et al., 1998) are important if the cluster temperature is $T_e \gtrsim 5$ keV. In the extreme case of ultrarelativistic electrons, the tSZ spectrum turns out to be the same as the CMB one, but inverted, since all the scattered photons become so energetic that they exit from the wavelength range of the CMB.

Particularly relevant for finding clusters with a tSZ survey is the signal integrated over the solid angle of the cluster. Because the tSZ signal is the integrated pressure, integrating over the solid angle of the cluster provides a sum of all the electrons in the cluster weighted by temperature. This provides a relatively clean measure of the total thermal energy of the cluster. Integrating the tSZ over the solid angle of the cluster, $d\Omega = dA/D_A^2$, gives:

$$Y_{tSZ} \propto \int \Delta T_{tSZ} d\Omega \propto \frac{N_e \langle T_e \rangle}{D_A^2} \propto \frac{M \langle T_e \rangle}{D_A^2} \tag{2.10}$$

where $N_e$ is the total number of free electrons in the clusters, $\langle T_e \rangle$ is the mean electron temperature, $D_A$ is the angular diameter distance, and $M$ is the mass of the cluster (assuming that the fraction of free electrons is constant, $M$ can be considered as either gas or total mass). The integrated tSZ flux turns out to be directly proportional to the temperature weighted mass of the cluster divided by $D_A^2$. The angular diameter distance $D_A(z)$ is fairly flat at high redshift. Also, a cluster of a given mass will be denser and therefore hotter at high redshift because the universal matter density increases as $(1+z)^3$. Therefore, one expects an SZ survey to detect all clusters above some mass threshold with little dependence on redshift.

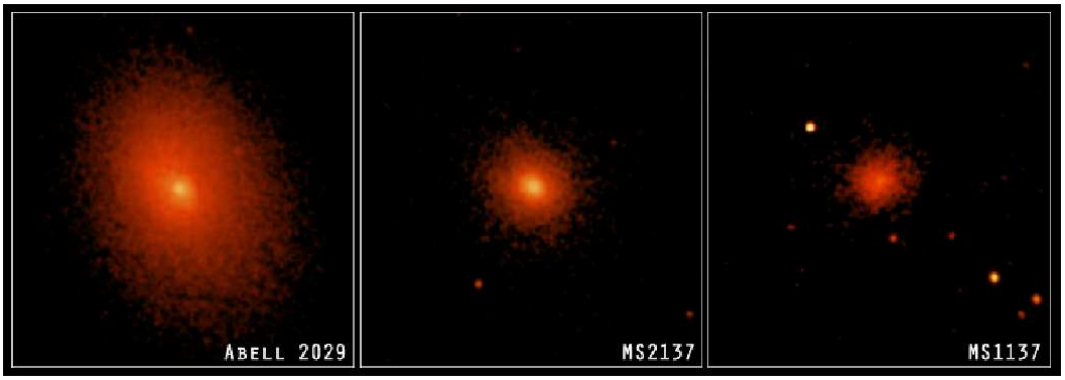


**Figure 2.4.** Chandra images of three relaxed galaxy clusters Abell 2029, MS 2137 and MS 1137, having redshift $z = 0.08$, $z = 0.3$ and $z = 0.8$ respectively, from the Chandra Photo Album.

### 2.2.2 The kinetic Sunyaev–Zeldovich effect

If the cluster is moving with respect to the CMB rest frame there will be an additional spectral distortion due to the Doppler effect of the cluster bulk velocity on the scattered CMB photons, which is called the *kinetic* SZ effect (kSZ). The dashed line in figure 2.3 reports the kSZ distortion, as a function of frequency, for a cluster having a typical peculiar velocity $v_{pec} = 500$ km/s. One may notice that it presents a spectrum which is still described completely by a Planck spectrum, but at a slightly different temperature, lower (higher) for positive (negative) peculiar velocities (Sunyaev & Zeldovich, 1972; Birkinshaw, 1999). If relativistic effects are not taken into account the effect is undistinguishable from an intrinsic fluctuation of the CMB temperature.

In the non-relativistic limit, the amplitude of the effect is given by:

$$\frac{\Delta T_{kSZ}}{T_{CMB}} = \tau_e \left(\frac{v_{pec}}{c}\right) \tag{2.11}$$

where $v_{pec}$ is the peculiar velocity of the cluster along the line of sight and $\tau_e$ is the optical depth along the line of sight. Relativistic perturbations to kSZ are due to the Lorentz boost to the electrons provided by the bulk velocity (Nozawa et al., 1998; Sazonov & Sunyaev, 1998). For a hot cluster ($T = 8$ keV) with a large peculiar velocity ($v_{pec} = 1000$ km/s) the effect is about a 9% correction to the non-relativistic term.

## 2.3 Status of observations

### 2.3.1 X–rays

X-rays are absorbed by the Earth's atmosphere. Therefore, X-ray observatories need to be placed on board satellites. Three X–ray dedicated satellites are now in operation, XMM–Newton[1], Chandra[2] and Suzaku[3].

The XMM–Newton and Chandra operate both from 1999 and most of the present knowledge on the ICM in galaxy clusters is based on observations performed with these telescopes. The two observatories are complementary under many aspects. Chandra has

[1] `http://www.esa.int/science/xmmnewton`
[2] `http://chandra.harvard.edu`
[3] `http://www.astro.isas.jaxa.jp/suzaku/`

an extremely good spatial resolution of $\Delta\theta = 0.5$", compared to 8" for XMM–Newton. The strength of XMM–Newton is its exceptional collecting area and thus sensitivity: three high–throughput telescopes are operating in parallel. The field of view is $30'$ in diameter, well adapted to cluster studies. Chandra has only one telescope, with a smaller field of view of $17' \times 17'$ (for the ACIS-I instrument) and an effective area typically 3(5) times lower than XMM–Newton at 1.5(8) keV. Figure 2.4 shows the X–ray images of three relaxed galaxy clusters obtained with the Chandra satellite. The images highlight the decrease of the signal with increasing redshift of the cluster.

The scientific payload of Suzaku initially consisted of three distinct co-aligned scientific instruments (Mitsuda et al., 2007). There are four X-ray sensitive imaging CCD cameras (X-ray Imaging Spectrometers, or XISs), having a good spatial resolution ($\Delta\theta = 2'$) but with moderate energy resolution, over a $17.8' \times 17.8'$ field of view. Each XIS is located in the focal plane of a dedicated X-ray telescope. The second instrument is the non-imaging, collimated Hard X-ray Detector (HXD), which extends the bandpass of the observatory to much higher energies with its 10-600 keV pointed bandpass. A third instrument, the X-Ray Spectrometer (XRS) was planned to provide higher spectral resolution, but unfortunately is no longer operational, due to a loss in the liquid helium cryogen.

In addition to these telescopes, cluster X–ray studies are also performed by using the X–ray Telescope[4] (XRT, Gehrels et al., 2004) on board the SWIFT satellite. The telescope is dedicated to the detection of the X–ray afterglow of gamma ray bursts, but it is also used for X–ray cluster studies.

As compared to the previous generation of satellites, present instruments represent a giantic step forward in term of sensitivity and spatial resolution. The ROSAT[5] satellite (Truemper, 1982) had good imaging capability ($\Delta\theta = 15$" for the PSPC instrument) but much lower effective area and very poor spectroscopic capability. The high energy cut-off of the telescope was $E \sim 2$ keV, so that accurate temperature measurements were limited to cool clusters. ASCA was the first X–ray observatory (Tanaka et al., 1994) with telescopes working up to 10 keV and a CCD camera at the focal plane at one of the telescopes (the other telescopes were equipped with proportional counters). As compared to spectroscopy made before with collimated spectrometers, the gain in sensitivity was very important. It was also the first time one could do spatially resolved spectroscopy of clusters. However, this was limited by the relatively large and energy dependent Point Spread Function. The spatial resolution of Beppo–SAX[6] was better, but above all it had the capability of observing sources over more than three decades of energy, from 0.1 to 200 keV (Boella et al., 1997).

With present instruments, gas density and temperature structure (and thus mass profiles) can be measured in nearby clusters over a wide radial range, from very deep inside the core, at the sub–kpc scale with Chandra (e.g Fabian et al., 2001), up to very close to the virial radius with XMM-Newton, even in low mass systems (e.g. Solovyeva et al., 2007). Last but not least, we have now precise temperature maps for unrelaxed objects and we can resolve very sharp density features. With XMM–Newton it is possible to perform spatially resolved spectroscopy in cluster cores which allowed to shed light on the complex thermal processes ongoing in this regions, which we discuss below (Peterson et al., 2001; Böhringer et al., 2002; Markevitch & Vikhlinin, 2007). We can also measure basic cluster properties up to high $z$ ($z \sim 1.3$) and down to the ROSAT detection limit

[4] http://www.swift.psu.edu/xrt

[5] http://heasarc.gsfc.nasa.gov/docs/rosat/rosat.html

[6] http://bepposax.gsfc.nasa.gov

(with XMM-Newton). This includes morphology from images, gas density radial profile, global temperature and gas mass (e.g. Arnaud et al., 2002; Rosati et al., 2004), from which total mass and entropy can be derived by assuming isothermality. For the brighter distant clusters, it is also possible to obtain crude temperature profiles (Arnaud et al., 2002) or maps (Maughan et al., 2003). Finally, X-ray selection is currently the optimal technique for constructing large, well-defined samples of distant clusters (see Rosati et al., 2002; Borgani, 2006, for reviews). Clusters at all redshifts appear as extended sources in XMM-Newton and Chandra images. However, only Chandra has the capability to perfectly remove point source contamination. The large collecting area of XMM–Newton allows one to reach high sensitivity. For instance, with this instrument Mullis et al. (2005) discovered the cluster XMMU J2235.3-2557 at $z = 1.4$. This object has an X–ray flux of $f_x = (3.6 \pm 0.3) \cdot 10^{14}$ erg/cm$^2$, which corresponds to a rest-frame X-ray luminosity of $L_X = (3.0 \pm 0.2) \cdot 10^{44} h^{-2}$ erg/s in the $0.5 - 2$ keV band, and a temperature of $T = 6.0 \pm 2.5$ keV.

The near future will see the launch of the extended ROentgen Survey with an Imaging Telescope Array[7] (eROSITA, Predehl et al., 2006). The mission will conduct an all–sky survey in the soft X–ray band and thereafter it is foreseen to conduct follow-up pointed observations of selected sources. The proposed orbit provides an order of magnitude lower particle background than those of Chandra and XMM–Newton, which will allow the detailed study of low–surface–brightness diffuse objects. The telescope is composed by $7 \times 35$cm mirrors modules each having its own CCD-detector in the focus. The spatial resolution will be of $\theta \sim 20''$ mean over the field–of–view ($\theta \sim 15''$ on–axis), the spectral resolution will be of 130 eV at 6 keV. The original plan of eROSITA observations comprised three surveys: *i)* An all-sky survey which is expected to detect about 30,000 galaxy clusters, down to a flux of $f = 1.6 \cdot 10^{-13}$ erg/s/cm$^2$ *ii)* a deeper, high galactic latitude survey to discover about 70,000 galaxy clusters down to a flux of $f = 3 \cdot 10^{-14}$ erg/s/cm$^2$, covering 20,000 deg$^2$; *iii)* a 200-300 deg$^2$ deep survey close to the south Galactic pole, which will reach very high sensitivity, having a flux limit of $f = 8 \cdot 10^{-15}$ erg/s/cm$^2$. However, for efficiency reasons a continuous scan of the sky is planned now. The pattern will be similar to ROSAT, but with poles roughly between ecliptic and galactic poles (more interesting regions of the sky). Also the poles will be smeered out to about 200 deg$^2$ areas. This produces effectively a shallower all–sky survey and two regions about a factor of 10 deeper.

In the following, we present the main observational properties of the ICM, inferred from the analysis of X–ray observations.

### The gas density profiles

The gas content and density distribution can be studied through the emission measure along the line of sight $EM(r) = \int_r^{R_{vir}} n_e^2 \, dl$, which is easily derived from the X-ray surface brightness profile (see Section 2.1). The scaled $EM$ profiles of *hot* clusters measured with ROSAT were found to be similar in shape outside typically $(0.1 - 0.2)R_{vir}$ (Neumann & Arnaud, 1999; Vikhlinin et al., 1999; Neumann & Arnaud, 2001). There is a large dispersion in the central regions, generally linked with the presence of a cooling core (see below). Outside that region the universal profile is well fitted by the $\beta$–model (Cavaliere

[7] `http://www.mpe.mpg.de/projects.html#erosita`

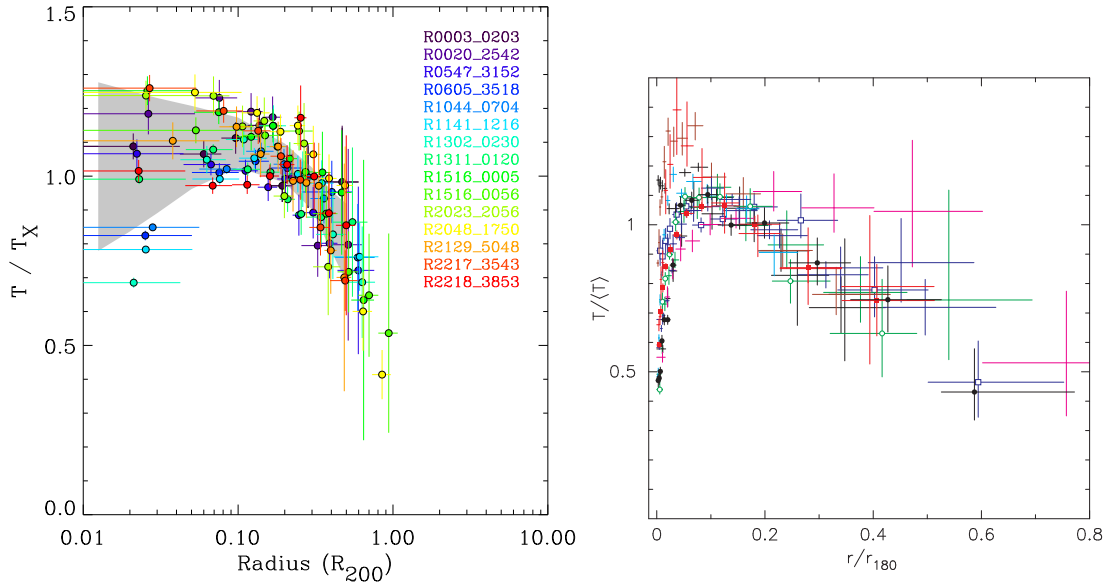


**Figure 2.5.** Gas temperature profiles for two sets of relaxed clusters, observed with the XMM–Newton satellite (left panel, from Pratt et al., 2007) and with the Chandra satellite (right panel, from Vikhlinin et al., 2005).

& Fusco-Femiano, 1976):

$$n_e(r) = n_{e0}\left[1 + \left(\frac{r}{r_c}\right)^2\right]^{-3\beta/2}, \tag{2.12}$$

where $n_{e0}$ is the electron number density in the cluster centre, $r$ is the distance from the cluster centre, $r_c$ is the core radius and $\beta$ is the power–law index. Typical values are $\beta = 2/3$ and $r_c \sim 0.12R_{vir}$. In addition, a probable steepening of the profiles has been observed at large radius, which should be taken into account when using these profiles for high precision mass measurements (Neumann, 2005; Vikhlinin et al., 2006).

The reconstructed gas density profiles are generally very accurate. However it has been pointed out that the presence of unresolved gas clumps has the effect of boosting the X–ray signal and, then, to lead to an overestimate of gas density, since it is basically inferred from the total X–ray flux. In Chapter 5 the amount of this bias is checked by applying a deprojection algorithm to X–ray and tSZ images.

### The temperature profiles

There is also a similarity in the temperature profiles of hot clusters beyond the cooling core region (e.g. De Grandi & Molendi, 2002), as one can clearly see in figure 2.5, showing the temperature profiles of two sets of nearby clusters ($z < 0.2$), analyzed by Vikhlinin et al. (2005) and by Pratt et al. (2007). In relaxed clusters, there is usually a drop of temperature towards the centre ($r \lesssim 0.1R_{vir}$). This corresponds to the cool core region (see below). There is also a tendency for clusters with cool cores to have flatter temperature profiles at large scale than non–cool core clusters, suggesting that the profile shape depends on the cluster dynamical state (e.g. De Grandi & Molendi, 2002). The self-similarity of the shape of the temperature profiles seems to be confirmed by several

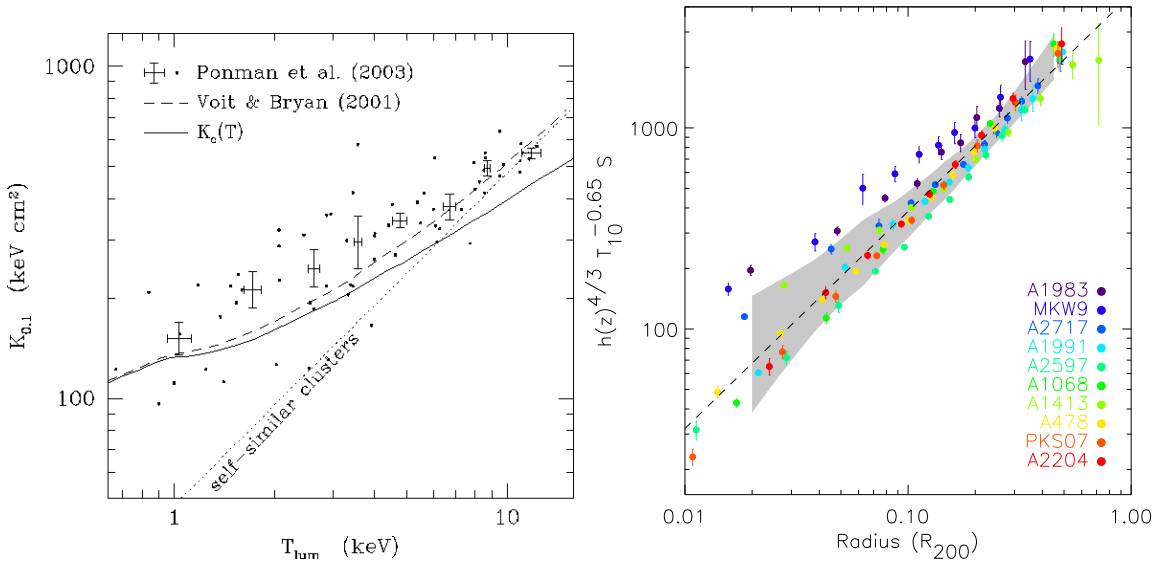


**Figure 2.6.** Left panel: comparison of entropy measured at $0.1R_{200}$ and the self–similar prediction in a large sample of clusters (Voit & Ponman, 2003). The small points represent entropy measured at $0.1R_{200}$ in a sample of 64 clusters. The points with errorbars represent the mean entropy measurement in temperature bins of eight clusters each. The dotted line represents the self–similar relation, as predicted by simulations of clusters without radiative cooling and feedback. The solid line represent the cooling threshold $K_c(T)$, defined to be the entropy at which the cooling time equals 14 Gyr (Voit & Ponman, 2003). The short–dashed line shows the predicted entropy at $0.1r_{200}$ in the model of Voit & Bryan (2001). Right panel: entropy profiles of a set of nearby clusters scaled using the empirical entropy scaling $S \propto h(z)^{4/3}T^{0.65}$ (Pratt et al., 2006). The shaded grey area corresponds to the region enclosed by the mean plus/minus the $1\sigma$ standard deviation. The dashed line denotes $S \propto R^{1.08}$.

independent studies (e.g. Allen et al., 2001; Vikhlinin et al., 2005; Piffaretti et al., 2005; Pratt et al., 2007; Zhang et al., 2006) for relaxed clusters. However, no consensus has been reached yet on the exact shape of the profiles.

In X–ray studies the temperature is usually obtained by fitting a single temperature model to the projected spectrum. In Chapter 5 we propose a geometrical deprojection technique, applied to combined X–ray and tSZ images, which avoids the use of X–ray spectroscopy. This would offer two important advantages: *i)* it should allow to probe more easily the regimes of low X–ray surface brightness (i.e. external cluster regions and high–redshift galaxy clusters), which are hardly accessible to spatially resolved X–ray spectroscopy; *ii)* it yields a temperature which is basically mass–weighted, while the spectroscopic one may be biased low by the presence of relatively cold clumps embedded in the hot ICM atmosphere (see Section 3.4).

### The gas entropy

In cluster studies the *entropy* is traditionally defined as $S = T/n_e^{2/3}$, which is related to the true thermodynamic entropy via a logarithm and an additive constant. It is a fundamental characteristic of the ICM, because it is a probe of the thermodynamic history of the gas (e.g. Voit et al., 2002). In the standard self-similar picture, which only takes into account the effects of gravity, the entropy should scale simply as $S \propto h(z)^{4/3}T$, where $h(z)$ is the

Hubble constant (see Section A.5).

Since the pioneering work of Ponman et al. (1999), it is known that the entropy measured at $0.1R_{vir}$ exceeds the value attainable through gravitational heating alone, an effect that is especially noticeable in low mass systems. In fact, the observed $S - T$ relation follows a power law but with a shallower slope than what expected from self–similar scaling. As shown in the left panel of figure 2.6, the entropy measured at $0.1R_{vir}$ scales instead as $S \propto T^{0.65}$ (Ponman et al., 2003), suggesting that in addition to the gravitational effect, the gas history depends on the interplay between cooling and galaxy feedback mechanisms (see e.g. Voit, 2005).

The right panel of figure 2.6 shows the radial entropy profiles of a set of galaxy clusters. Except in the very centre, they are self-similar in shape with close to power law behavior in the $0.05\ R_{vir} < r < 0.5\ R_{vir}$ range (e.g. Piffaretti et al., 2005; Pratt et al., 2006). The observed slope that is slightly shallower than predicted by shock heating models, i.e. $S(r) \propto r^{1.1}$ (Tozzi & Norman, 2001). Note also that the entropy amplitude scales as $S \propto T^{0.65}$ at any cluster radius.

Various non-gravitational processes have been proposed to explain the observed entropy properties, namely the gas heating before or after collapse (from SNs or AGNs) and the effect of radiative cooling. Voit et al. (2003) predicted that a smoothing of the gas density due to preheating in the infalling sub-halos would boost the gas entropy generated by accretion shocks, with a larger efficiency in smaller systems. Kay et al. (2004) proposed a simple feedback scheme for gas heating, which better reproduce the properties of gas entropy. However, a self–consistent numerical implementation of a well motivated feedback model which successfully satisfy a large body of observational constraints is still missing. Borgani et al. (2005) explored the effects of gas cooling and SNe feedback by using a set of simulated galaxy clusters. They found that pre–heating the infalling gas is efficient in amplifying the entropy, but the radiative cooling reduces the effect by a significant amount. The heating from galactic winds powered by SNe is efficient in providing an increase of the entropy in the core regions, but even the strongest ones are not able to produce an appreciable entropy amplification effect. This suggests that is still missing an efficient mechanism to distribute the SN energy in the diffuse medium. Alternatively, other source of astronomical heating could be in action, the most obvious candidates being the AGNs.

In Chapter 5, we propose a geometrical deprojection technique aiming at recovering gas density and temperature from X–ray and tSZ images. By avoiding the use of X–ray spectroscopy, this technique would allow in principle to extend entropy studies to larger radii and at larger redshifts, where the X–ray spectroscopic information may be poor.

### The complex physics in cluster core

As mentioned above, there is a very large dispersion in the core properties of the ICM, within typically $0.1R_{vir}$. This is linked to the complex physics at play in the cluster centre. In the centre of clusters the gas density is high. The cooling time, which scales as $t_{\rm cool} \propto T^{1/2}/n_e$ can be shorter than the *age* of the cluster. One would expect the temperature to decrease due to radiative cooling and the density to increase so that the gas stays in quasi hydrostatic equilibrium. A central temperature decrement is generally observed in relaxed clusters. At the same time, however, these observations contradict this simple picture.

The major surprise is probably the lack of very cool gas, which is inconsistent with

the standard isobaric cooling flow models. The clusters exhibit strong emission from cool plasma at just below the ambient temperature, $T$, down to $T/2$, but not at lower temperatures, as is predicted by the cooling flow model (Molendi & Pizzolato, 2001; Böhringer et al., 2002; Peterson et al., 2003; Kaastra et al., 2004). In parallel, high–resolution images have revealed complex interaction between AGN activity in the cluster centre and the intra-cluster medium (e.g. Blanton, 2004). One observes X-ray cavities or 'bubbles', presumably created by the central AGN radio lobes as they displace the X-ray gas. They are usually surrounded by cool rims while shock fronts are quite rare.

Whether and how both phenomena, the absence of very cool gas and AGN/ICM interaction, are connected is still unclear (for reviews see Voit, 2005; Bregman, 2004; Fabian, 2003). For instance, AGN heating may limit cooling but conduction could also play a role in heating the central region. A better understanding of cooling and AGN heating in the central part of clusters has further implications because both phenomena play a role at larger scales in clusters and during galaxy formation.

### 2.3.2 The Sunyaev–Zeldovich effect

After the first papers by Sunyaev and Zeldovich (Sunyaev & Zeldovich, 1970, 1972), over a decade of SZ experiments was necessary before the first reliable detection was realized by Birkinshaw et al. (1984) for three nearby objects (Cl 0016, Abell 665 and Abell 2218). The telescopes available at that time were enough sensitive to detect the tSZ signal towards a massive cluster, but many attempts failed due to uncontrolled systematics. Subsequently, thanks to both improvements in the observing techniques and advances in detector technology, the SZ signal has been detected in several clusters and measurements are now routine. We briefly illustrate the present status of SZ observation, for more detailed reviews see Carlstrom et al. (2002) or Birkinshaw & Lancaster (2005).

The figure 2.7 shows the images of six galaxy clusters, observed with the BIMA array (see below). Note that the strength of the tSZ signal is similar for all the clusters, although they span a wide range of redshifts ($0.17 \leq z \leq 0.89$). This represents an advantage with respect to X–ray observations. Instead, the resolution is much worse, as one may understand by looking at the synthesized beam, in the lower left corner of each image.

#### Single dish telescopes

Due to the high sensitivity of bolometric detectors at millimeter wavelengths, single dish experiments are ideally suited for the measurement of the SZ spectrum. By observing at several millimeter frequencies these instruments should be able to separate the thermal and kinetic SZ from atmospheric fluctuations and sources of astrophysical confusion. The tSZ has been routinely observed by single dish radio telescopes such as the Owens Valley Radio Observatory (OVRO) 40- and 5-meter telescopes (e.g. Mason et al., 2001) and the Nobeyama 45-meter telescope (e.g. Tsuboi et al., 1998).

In the Sunyaev-Zel'dovich Infrared Experiment[8] (SuZIE; Benson et al., 2004), pixels in a six element 140 GHz bolometer array are electronically differenced by reading them out in a differential bridge circuit (Holzapfel et al., 1997). Differencing in this way makes the experiment insensitive to temperature and amplifier gain fluctuations that produce 1/f noise. This increased low frequency stability allows SuZIE to observe in a drift scanning

[8] http://www.stanford.edu/∼schurch/suzie_science.html

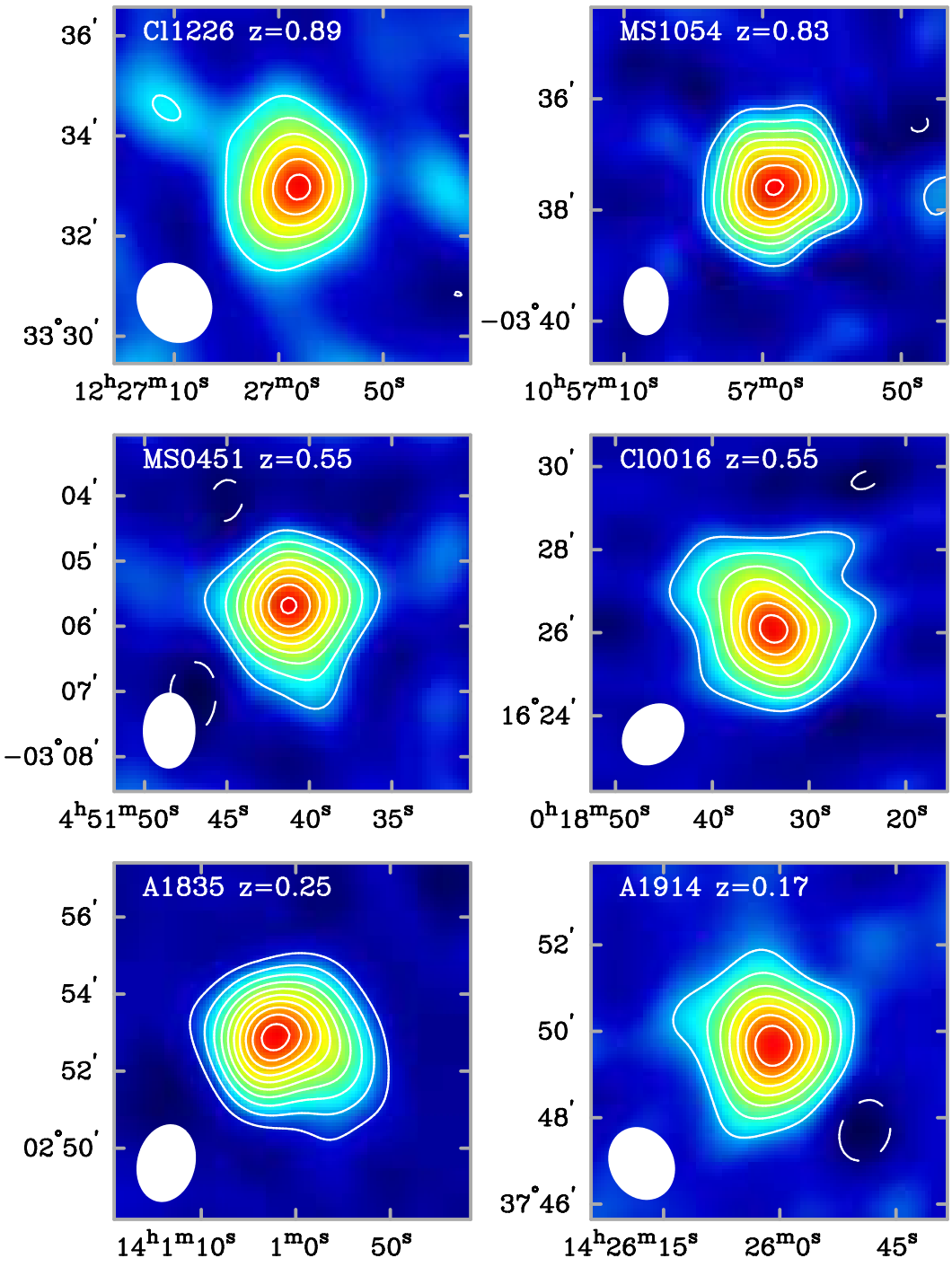


**Figure 2.7.** BIMA images of six galaxy clustes, with redshifts $0.17 \leq z \leq 0.89$, from Carlstrom et al. (2002). In the lower left corner of each image is reported the primary beam.

mode where the telescope is fixed and the rotation of the earth moves the beams across the sky. Using this drift scanning technique, the SuZIE experiment has produced high signal to noise strip maps of the SZ emission in several clusters (Holzapfel et al., 1997).

Single dish observations of the SZ are just beginning to reach their potential and the future is very promising. The development of large format millimetre wavelength bolometer arrays will increase the mapping speed of current SZ experiments by orders of magnitude. Operating from high astronomical sites with stable atmospheres and exceptionally low precipitable water vapour, future large format bolometer arrays have the potential to produce high signal to noise SZ images and search for distant SZ clusters with unprecedented speed.

The first of this new generation of instruments is the BOLOCAM[9] 151 element bolometer array (Glenn et al., 1998), operating at the Caltech Submillimeter Observatory, a 10.4 m diameter telescope on Mauna Kea in Hawai'i. The telescope works in drift scanning mode, achieving a high mapping speed at $1'$ resolution.

The Arcminute Cosmology Bolometer Array Receiver[10] (ACBAR, Runyan et al., 2003) is a sensitive multi-frequency receiver operating on the 2 m Viper telescope at South Pole Station. The South Pole, having a pressure elevation of $\sim 11,000'$, is arguably the best site on the planet for millimeter wave astrophysics. Winter observations with the ACBAR instrument will be detector noise dominated.

Another telescope located in the South Pole is just starting the operations, the South Pole Telescope[11] (SPT, Ruhl et al., 2004). It consists of a 10 m telescope designed for conducting large-area millimeter and sub-millimeter wave surveys of faint, low contrast emission.

The Atacama Pathfinder EXperiment[12] (APEX, Güsten et al., 2006) is already working. It is a modified prototype of the 12 m antennas which will constitute ALMA (see below). The telescope is located in the Atacama Desert of the Chilean Andes, which is one of the driest places on Earth, minimizing the amount of atmospheric water emission at microwave frequencies.

Not far from APEX and ALMA, other two telescopes are under construction, the 6 m Atacama Cosmology Telescope[13] (ACT, Fowler & ACT Collaboration, 2006) and the 25 m Cornell Caltech Atacama Telescope[14] (CCAT, Radford et al., 2007). The ACT telescope has no moving components in its optical path; to change pointing direction, the entire telescope moves. It is designed to scan the sky at constant elevation, to minimize the variations of the atmospheric microwave signal. Given its very large diameter, CCAT will achieve an excellent resolution in SZ images ($0.44'$ at 150 GHz) with a large field–of–view of about $10' \times 10'$, with the goal of covering a four times larger area, so as to cover one entire rich cluster down to a relatively low redshift. In chapters 5 and 6 we will model our synthetic SZ images on this instrument, which is well suited to the type of SZ observations required by our method.

The Large Millimeter Telescope[15] (LMT, Pérez-Grovas et al., 2006) is a millimeter–wavelength telescope with a primary aperture of 50-m diameter, located in Volcn Sierra Negra (Mexico) at an altitude of 4,600 m. The optical design provides a field-of-view

[9] http://www.astro.caltech.edu/~lgg/bolocam_front.htm
[10] http://cosmology.berkeley.edu/group/swlh/acbar
[11] http://spt.uchicago.edu/spt/
[12] http://www.apex-telescope.org
[13] http://www.physics.princeton.edu/act
[14] http://www.submm.org/overview.html
[15] http://www.lmtgtm.org/intro.html

of up to 8 arcminutes (diameter) with minimal aberration. The combination of the large collecting-area and available field–of–view will provide the LMT with extremely fast mapping-speeds. The first light will be in 2008.

**Interferometric Observations**

The stability and spatial filtering inherent to interferometry has been exploited to make high quality images of the SZ. Their stability is due to their ability to perform simultaneous differential sky measurements over well defined spatial frequencies. Interferometers offer an ideal way to achieve high brightness sensitivity for extended low-surface brightness emission, at least at radio wavelengths.

There are several other features which allow an interferometer to achieve extremely low systematics. For example, only signals which correlate between array elements will lead to detected signal. For most interferometers, this means that the bulk of the sky noise for each element will not lead to signal. Amplifier gain instabilities for an interferometer will not lead to large offsets or false detections, although if severe they may lead to somewhat noisy signal amplitude. The spatial filtering of an interferometer also allows the emission from radio point sources (see below) to be separated from the SZ emission. This is possible because at high angular resolution ($\lesssim 10''$) the SZ contributes very little flux. This allows one to use long baselines, which give high angular resolution, to detect and monitor the flux of radio point sources while using short baselines to measure the SZ. Nearly simultaneous monitoring of the point sources is important as they are often time variable. The signal from the point sources is then easily removed, to the limit of the dynamic range of the instrument, from the short baseline data which are sensitive also to the SZ.

The first interferometric detection of the SZ was obtained with the Ryle Telescope[16] (RT, Jones et al., 1993). The RT was built from the 5 Kilometer Array, consisting of eight 13 m telescopes located in Cambridge, England operating at 15 GHz with East-West configurations. Five of the telescopes can be used in a compact E-W configuration for imaging of the SZ.

The Owens Valley Radio Observatory[17] (OVRO) consisted of six 10.4 m antennas configured on a 500-m T-shaped track, located in the Owens Valley. The Berkeley–Illinois–Maryland Association array[18] (BIMA) consisted of ten 6.1 m antennas configured with baselines as large as two kilometres, and as small as eight meters, located at Hat Creek, California. These two observatories provided images of several tens of galaxy clusters (e.g Carlstrom et al., 1996; Patel et al., 2000; Joy et al., 2001; Reese et al., 2002; LaRoque et al., 2006; Bonamente et al., 2007)

The Ryle Telescope, OVRO, and BIMA SZ observations are insensitive to the angular scales required to image low redshift clusters, at $z < 0.1$. The Cosmic Background Imager (CBI) (Padin et al., 2001) has been used to image the SZ in a few nearby clusters (Udomprasert et al., 2004). The CBI is composed of thirteen 0.9 m telescopes mounted on a common platform with baselines spanning 1 m to 6 m.

Interferometric observations of the SZ, as for single dish observations, are just beginning to demonstrate their potential. Upcoming instruments will be over an order of magnitude more sensitive. The OVRO/BIMA SZ imaging team built the Sunyaev-

[16] `http://www.mrao.cam.ac.uk/telescopes/ryle`
[17] `http://www.ovro.caltech.edu`
[18] `http://bima.astro.umd.edu`

Zel'dovich Array (SZA)[19], consisting of eight 3.5 m telescopes. which has just produced images of clusters out to $z = 1.03$ (Muchovej et al., 2007). The array will be combined with the existing OVRO and BIMA arrays to form one large array called Combined Array for Research in Millimeter-wave Astronomy[20] (CARMA), located in Cedar Flat in the Inyo Mountains of California, which will operate from 2008.

The RT SZ team also built the Arcminute Microkelvin Imager[21] (AMI, Kaneko, 2006), which has recently begun observations. It consists of ten 3.7m telescopes operating at 15 GHz near the RT in Cambridge. It is not planned to operate AMI as a heterogeneous array with the Ryle telescope, but the RT would be used for concurrent point source monitoring.

Additionally, plans have been discussed to reconfigure the CBI to 90 GHz (now it observes at 30 GHz). It would be particularly well suited to perform SZ surveys. A similar fixed platform interferometer, the Array for Microwave Background Anisotropy[22] (AMiBA), is also being built with nineteen 1.2 m telescopes and operating at 90 GHz. AMiBA, like the reconfigured CBI, would also be ideally suited for performing SZ surveys at moderate resolution.

The Atacama Large Millimeter/submillimeter Array[23] array (ALMA) will be composed of up to $50 \times 12$m antennas, located at Atacama. Array will have reconfigurable baselines ranging from 150 m to 18 km. SZ images will achieve a resolutions as fine as $0.042''$ at 100 GHz.

**The Planck satellite.**

The main objective of the Planck mission[24] is to measure the fluctuations of the CMB with an accuracy set by fundamental astrophysical limits. To do this, Planck will image the whole sky with an unprecedented combination of sensitivity ($\Delta T/T \sim 2 \cdot 10^{-6}$), angular resolution (to $5'$), and frequency coverage ($30 - 857$ GHz). This level of performance will enable Planck to measure the angular power spectrum of the CMB fluctuations to high accuracy. It is equipped with the Low Frequency Instrument (LFI, an array of receivers based on HEMT amplifiers) covering the frequency range $30 - 100$ GHz and the High Frequency Instrument (HFI, an array of receivers based on bolometers) covering the frequency range $100 - 857$ GHz. The characteristic spectral signature of the tSZ effect will allow to identify the tSZ signal from clusters and to distinguish them from other unresolved sources. Planck will produce a large all–sky sample of clusters with easily computable selection criteria, which is expected to include about 30,000 objects. The satellite will be launched in 2008 aboard an Ariane 5 rocket together with the Herschel Space Observatory satellite.

**Contaminations**

When considering SZ observations, one has to carefully take into account several source of contamination and confusion, which could substantially affect the signal. They are briefly summarized below:

[19] http://astro.uchicago.edu/sza
[20] http://www.mmarray.org
[21] http://www.mrao.cam.ac.uk/telescopes/ami
[22] http://amiba.asiaa.sinica.edu.tw
[23] http://www.alma.nrao.edu
[24] http://www.rssd.esa.int/PLANCK

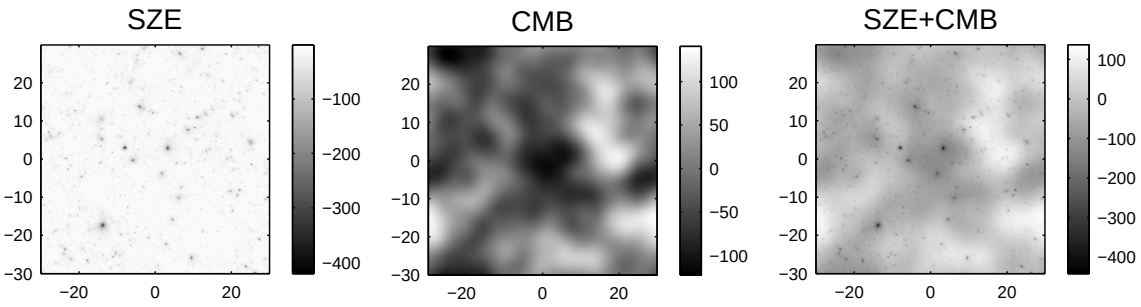


**Figure 2.8.** Illustration of the characteristic angular scales of primary CMB anisotropy and of the SZ (Carlstrom et al., 2002). The images each cover one square degree and the grey scales are in $\mu$K. The left panel shows a image of the SZ from many clusters at 150 GHz (2 mm) obtained from a hydrodynamic simulation. The clusters appear point-like at this angular scale. The centre panel is a realization of CMB anisotropy for a $\Lambda$CDM cosmology. The right panel illustrates that the SZ can be distinguished readily from primary CMB anisotropy provided the observations have sufficient angular resolution.

- **CMB anisotropy.** One such source is anisotropy of the CMB itself (see figure 2.8). For distant clusters with angular extents of a few arcminutes or less it is not a serious problem as the CMB anisotropy is expected (Hu & White, 1997) and indeed found to be damped considerably on these scales (Church et al., 1997; Subrahmanyan et al., 2000; Dawson et al., 2001, see also Holzapfel et al., 1997 and LaRoque et al., 2003 for CMB limits to SZ contamination). For nearby clusters, or for searches for distant clusters using beams larger than a few arcminutes, the intrinsic CMB anisotropy must be considered. The unique spectral behaviour of the thermal SZ can be used to separate it from the intrinsic CMB in these cases. Note, however, that for such cases it will not be possible to separate the kinetic SZ effects from the intrinsic CMB anisotropy without relying on the very small spectral distortions of the kinetic SZ due to relativistic effects.

- **Radio point sources.** Historically, the major source of contamination in the measurement of the SZ has been radio point sources. It is obvious that emission from point sources located along the line of sight to the cluster could fill in the SZ decrement, leading to an underestimate of the signal from the cluster. The radio point sources are variable and therefore must be monitored. Radio emission from the cluster member galaxies, from the central cD galaxy in particular, is often the largest source of radio point source contamination, at least at high radio frequencies (Cooray et al., 1998; LaRoque et al., 2003). The typical spectral index of the radio point sources is $\alpha \sim 0.7$ for $S_\nu \propto \nu^{-\alpha}$, where $S_\nu$ is the point source flux. In the RJ limit, the SZ flux is proportional to $\nu^2$ and therefore point sources are much less of an issue at higher radio frequencies.

  Although it is most likely that insufficient attention to radio point sources would lead to the underestimate of the SZ effect, it could also lead to an overestimate. The most obvious example is if unaccounted point sources are in the reference fields surrounding the cluster. An effect due to gravitational lensing has also been pointed out for low frequency observations where the flux from many point sources must be taken into account before a reliable measure of the SZ can be made. Essentially,

gravitational lensing increases the efficiency of detecting point sources toward the centre of the cluster which could lead to an overestimate of the SZ decrement (Loeb & Refregier, 1997). This effect should be negligible at frequencies greater than roughly 30 GHz.

- **Dust.** At frequencies near the null of the thermal SZ and higher, dust emission from extragalactic sources as well as dust emission from our own galaxy must be considered. Dust emission from our Galaxy rises steeply as $\nu^{2+\beta}$ with the observed dust opacity index $\beta$ found to be $0 < \beta < 2$ over the frequencies of interest.

  At the angular scales and frequencies of interest for most SZ observations, contamination from diffuse Galactic dust emission will not usually be significant and is easily compensated. Consider instead the dusty extragalactic sources such as those that have been found toward massive galaxy clusters with the SCUBA bolometer array (Smail et al., 1997). Spectral indices for these sources are estimated to be $\sim 1.5-2.5$ (Blain, 1998; Fischer & Lange, 1993). Sources with 350 GHz (850 $\mu m$) fluxes greater than 8 mJy are common and all clusters surveyed had multiple sources with fluxes greater than 5 mJy. A 10 mJy source at 350 GHz corresponds to $\Delta T_{CMB} = 345$ $\mu$K for $1'$ beam, or a Compton $y$-parameter of $6 \cdot 10^{-5}$. The same source scaled to 270 GHz, assuming a $\nu^2$ spectrum, corresponds to $\Delta T_{CMB} = 140$ $\mu$K at 270 GHz for $1'$ beam and a $y$-parameter of $6 \cdot 10^{-5}$. Scaling to the SZ thermal null at 218 GHz gives 3.9 mJy which corresponds to a $\Delta T_{CMB} = 85$ $\mu$K for a $1'$ beam. This in turn translates directly to an uncertainty in a measurement of the cluster peculiar velocity (eq. 2.11); for a massive cluster with an optical depth of 0.01 and an electron temperature of 10 keV, 85 $\mu$K corresponds to a peculiar velocity of 930 km/s. The contamination is more severe for less massive clusters with the dependence scaling as $\Delta v_{pec} \propto \tau_e^{-1} \propto R^2/M \propto M^{-1/3} \propto T_e^{-1/2}$. The contamination scales inversely with the beam area.

As with SZ observations at radio frequencies, the analyses of high frequency observations also need to consider the effects of point sources and require either high dynamic angular range, large spectral coverage, or both, to separate the point source emission from the SZ.

## 2.4 Cosmology with galaxy clusters

Galaxy cluster can be used as powerful cosmological probes, by applying several different methods. In this section, we review important cosmological tests to which present and future SZ experiments will provide very important contributions.

### The angular diameter distance

The combination of SZ and X–ray data provides a method to measure the angular diameter distance of galaxy clusters, taking advantage of the different dependence on gas density. This method is independent of any other distance ladder and provides distances to high–redshift galaxy clusters (out to $z \simeq 1$). The distance–redshift relation $D_A(z)$ directly probes the geometry of the Universe and then provides a measure of the cosmological parameters (see Section A.5). Data currently available only allow one to measure the normalization, that is the Hubble constant $H_0$. In principle, having data extended

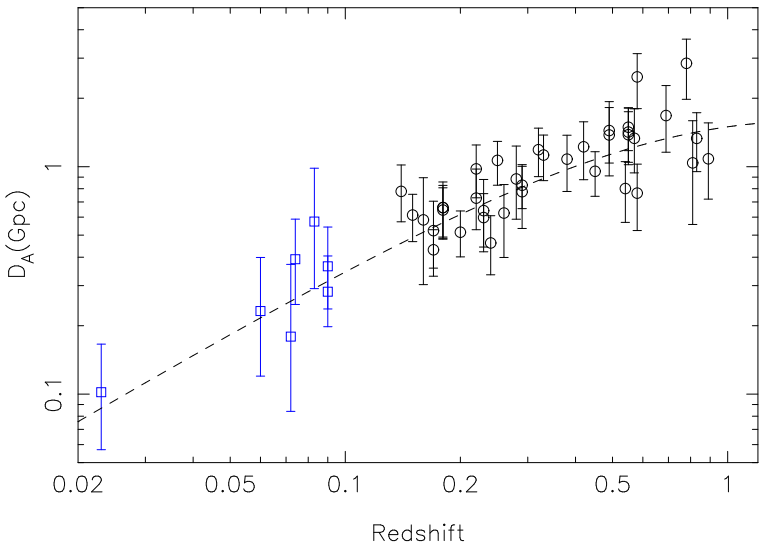


**Figure 2.9.** Angular diameter distances for a set of 38 clusters (circles). The dashed line is the best–fit angular diameter curve using the best-fit Hubble constant $H_0 = 76.9$km/s/Mpc and $\Omega_M = 0.3$, $\Omega_\Lambda = 0.7$. The squares are from another low–redshift sample (Mason et al., 2001), and they are not included in the fit (plot from Bonamente et al., 2006).

to larger redshifts would allow one to determine also the matter density parameter or to discriminate between different cosmological models. Bonamente et al. (2006) determined the distance for a large sample of 38 clusters (figure 2.9), thus obtaining an estimate of the Hubble constant of $H_0 = 76.9^{+3.9\ +10.0}_{-3.4\ -8.0}$ km/s/Mpc for an $\Omega_M = 0.3$, $\Omega_\Lambda = 0.7$ cosmology (68% confidence interval, statistical followed by systematic uncertainty). This measure is in good agreement with the CMB power spectrum estimate of $H_0 = 73.2^{+3.1}_{-3.2}$ (WMAP 3–year data, Spergel et al., 2007), from supernovae Ia $H_0 = 73 \pm 4 \pm 5$ km/s/Mpc (statistical and systematic errors, Riess et al., 2005) and the measure performed using Cefeids in the local Universe by the *HST key project*[25] of $H_0 = 72 \pm 8$ km/s/Mpc (Freedman et al., 2001).

In the method based on tSZ/X–ray observations, the main sources of systematics are the ellipticity of the clusters and the small–scale clumping of the ICM. The first is less serious because simply generate a scatter in the reconstructed distance, while the second is responsible for a boosting of the X–ray signal and thus could generate a systematic bias. This method is discussed in detail in Chapter 4. Using hydrodynamical simulations of galaxy clusters, we discuss its accuracy in the estimate of the Hubble constant and $\Omega_M$ and we asses the effect of these systematics on our results.

### The baryon fraction

The baryon fraction in galaxy clusters is generally considered as very close to the universal one, since it is believed that mass segregation do not occour at the typical scales of the formation of galaxy clusters. The baryon fraction is given by $f_b = \Omega_b/\Omega_M$, where $\Omega_b$ and $\Omega_M$ are the mean baryon density and the total matter density of the Universe. $f_b$ is the sum of the gas and galaxy mass fractions: $f_b = f_{gas} + f_{gal}$. Combined with the

[25]The HST key project determined the Hubble constant by the systematic observations of Cepheid variable stars using the Hubble Space Telescope.

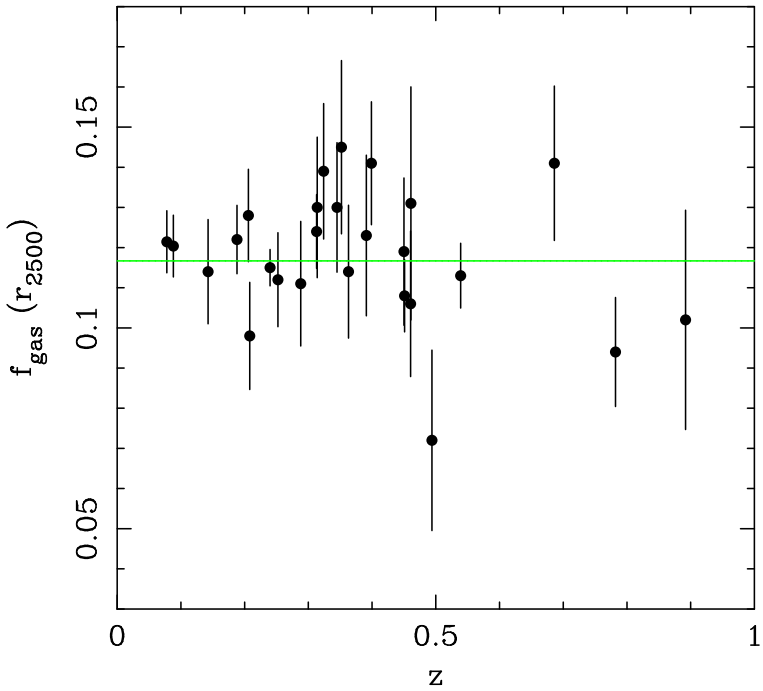


**Figure 2.10.** The X-ray gas mass fraction (with rms $1\sigma$a errors) as a function of redshift for the best–fitting cosmology (Allen et al., 2004). The green curve shows the best–fitting constant value.

$\Omega_b$ value estimated from Big Bang nucleosynthesis or CMB measurements, $f_b$ in clusters can be used to measure $\Omega_M$ (White et al., 1993). The method requires an independent knowledge of the Hubble constant $h$, which enters in the determination of $\Omega_b$ ($\Omega_b \propto h^{-2}$), of $f_{gas}$ ($f_{gas} \propto h^{-3/2}$) and of $f_{gal}$ ($f_{gal} \propto h^{-1}$). Cluster sample studies that rely on measurements of both $f_{gas}$ and $f_{gal}$ are rare. $\Omega_M$ is most often constrained from $f_{gas}$ only (which represents the dominant contribution, being one order of magnitude larger than the one given by the galaxies), assuming a constant $f_{gal}/f_{gas}$ ratio, taken from other cluster studies (e.g. Ettori et al., 2003; Allen et al., 2004). A further difficulty is that $f_{gas}$ increases with the integration radius and numerical simulations indicate that $f_{gas}$ within the virial radius is slightly smaller than the Universe's value (Eke et al., 1996). This turns out in a correction of about 20% for $f_b$ values estimated within 1/3 of the virial radius (Allen et al., 2004). One also observes a significant increase of $f_b$ with system mass, mainly resulting from the increase of $f_{gas}$ (Mohr et al., 1999; Lin et al., 2003). This is likely due to non–gravitational processes, less important in high mass systems. Therefore, most studies are restricted to massive clusters to minimize systematic errors. However, to firmly establish which cluster populations are fair samples of the Universe, the variation of $f_{gas}$ with system mass must be fully understood, which remains to be done.

The available $f_b$ data provide a tight constraint on $\Omega_M$. All recent studies favor a low $\Omega_M$ Universe and are in excellent agreement, e.g. $\Omega_M = 0.37 \pm 0.08$ from BeppoSAX data (Ettori et al., 2003), $\Omega_M = 0.28 \pm 0.03$ from ROSAT/ASCA data (Lin et al., 2003) and $\Omega_M = 0.30 \pm 0.04$ from Chandra data (Allen et al., 2004).

Assuming that the value of $f_{gas}$ does not change with redshift and thus constant it can be used as a distance indicator (Sasaki, 1996). It is pure geometrical test, which provides constraints on dark energy content $\Omega_\Lambda$ and equation of state $w$. However, the method is not free from possible systematics. In fact, $f_{gas}$ varies with radius and cluster

mass in the local Universe. So, one would need to measure $f_{gas}$ in clusters having the same mass (preferentially high) and over the same fraction of the virial radius, at different redshifts. Figure 2.10 shows the results of Allen et al. (2004), who recently applied this method to a set of Chandra observations (see also Abroe et al., 2002; Ettori et al., 2003; LaRoque et al., 2006). For a ΛCDM cosmology, they obtained: $\Omega_M = 0.245 \pm 0.04$ and $\Omega_\Lambda = 0.96 \pm 0.2$ (68% confidence level), with $\Omega_b h^2 = 0.0214 \pm 0.02$ and $h = 0.72 \pm 0.08$ as only priors. The future generation of X–ray and SZ telescopes is promising in providing images with high sensitivity, which would allow to extend this method to a larger set of galaxy clusters, at higher redshift. Such measurement will enable more accurate estimates of $\Omega_M$ and $\Omega_\Lambda$ and in principle also of the dark energy equation of state $w$ (see Section A.5), see Rapetti & Allen (2007).

An accurate estimate of the baryon fraction requires both a measurement of the gas mass and of the total mass of the cluster. The gas density profile (and then the gas mass) can be easily measured with good accuracy with X–ray data, since it does not require deep observations. The main source of systematics is probably the presence of small unresolved gas clumps, which boost the X–ray signal (recall that $S_X \propto \rho^2$), causing an overestimate of the gas mass by a few percent, as we show in Chapter 5. Instead, a much larger uncertainty is related to the measure of the total mass, which can be underestimated by $10-20\%$ due to violation of the condition of hydrostatic equilibrium (see discussion below and our analysis in Chapter 6). Unfortunately, the two masses are affected by systematic biases going in opposite directions, both causing an overestimate of $f_b$ in the cluster and thus an underestimate of $\Omega_M$.

**Evolution of the cluster mass function**

Measurements of the clusters masses and number density as a function of redshift represent sensitive probes of cosmology and can be used to constrain the matter density, $\Omega_M$, the normalization of the perturbation power spectrum $\sigma_8$ and, for sufficiently large samples, the equation of state of the dark energy $w$. Figure 2.11 shows the growth of cosmic structures in two hydrodynamical cosmological simulations, which have been carried out with a different choice of $\Omega_M$. The two simulations produce the similar pattern at the present time, but their past histories are very different. The most relevant feature is the fast decay in the abundance of hot, massive clusters as a function of redshift in the $\Omega_M = 1$ model, in contrast to the mild changes visible in the low-density model. This remarkable evolutionary difference represents one of the major motivations for conducting very deep cluster surveys.

In Section A.6.4 we discuss the mass function, showing also its evolution with redshift, both computed from analytical models and directly measured from simulations. Figure 2.12 shows instead how the redshift evolution of the mass function varies when changing the cosmological parameters, in order to understand how strong is its dependence on them (and then its potential in constraining them). As expected, it has a very strong dependence on $\Omega_M$ and only a mild dependence on $\Omega_\Lambda$. In particular, the evolution is the case $\Omega_M = 1$ is very rapid. The distance between the curves rapidly increases with redshift, indicating that the deeper the cluster detections, the better will be the constraints on the cosmological parameters.

X–ray surveys have already been used to constrain $\sigma_8$ and $\Omega_M$ (e.g. Eke et al., 1996; Borgani et al., 2001; Schuecker et al., 2002; Böhringer et al., 2004; Haiman et al., 2005; Henry et al., 2006; Böhringer et al., 2007; Finoguenov et al., 2007; Burenin et al., 2007).

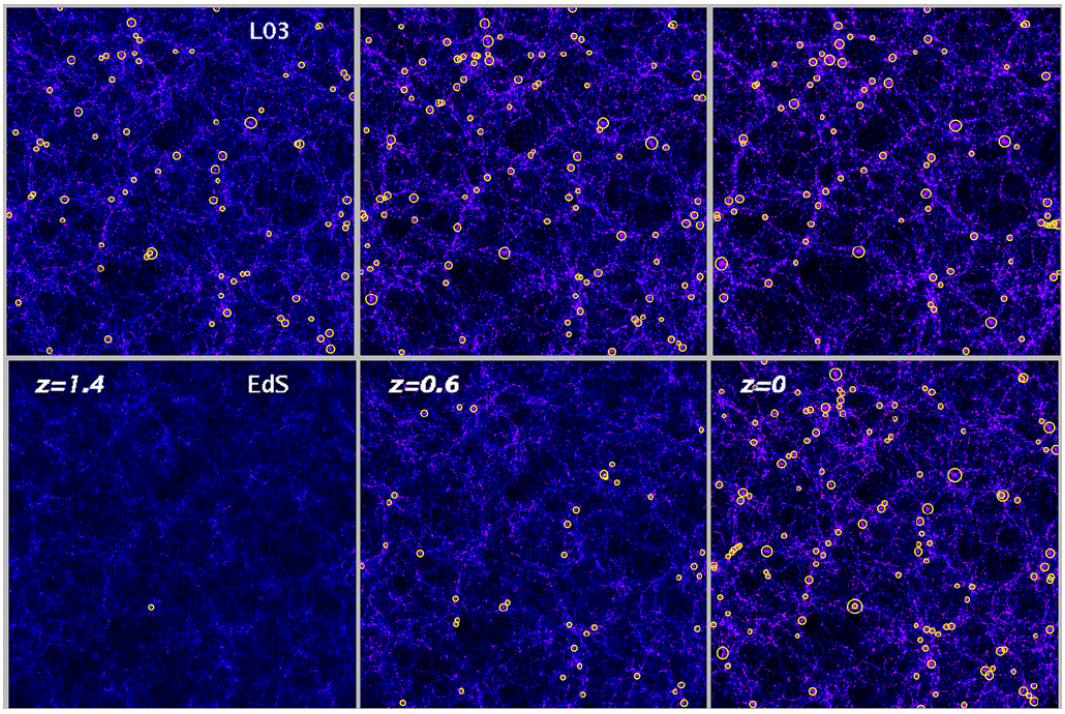


**Figure 2.11.** The evolution of the cluster population from N–body simulations in two different cosmologies (Borgani & Guzzo, 2001). Upper panels describe a flat, low–density model with $\Omega_M = 0.3$ and $\Omega_\Lambda = 0.7$ (L03); lower panels are for an Einstein–de–Sitter model (EdS) with $\Omega_M = 1$. Superimposed on the dark matter distribution, the yellow circles mark the positions of galaxy clusters with virial temperature $T > 3$ keV, the size of the circles is proportional to temperature. Model parameters have been chosen to yield a comparable space density of clusters at the present time. Each snapshot is $250h^{-1}$ Mpc across and $75h^{-1}$ Mpc thick (comoving with the cosmic expansion).

Their results are generally consistent with $\Omega_M = 0.3$ and indicate for $\sigma_8$ the interval $\sigma_8 = 0.7 - 0.8$. This value was discrepant with the first determination from the CMB power spectrum ($\sigma_8 \sim 0.9$) obtained by Spergel et al. (2003), however the more recent results from the analysis of 3 years of WMAP data gives $\sigma_8 = 0.76 \pm 0.05$ (Spergel et al., 2007). The main limitation of X–ray surveys is probably the reduced sensitivity to high redshift clusters. SZ surveys offer the attractive feature of probing the cluster abundance at high redshift as easily as in the local universe; as discussed in section 2.2, the sensitivity of a SZ survey is essentially a mass limit (Bartlett & Silk, 1994; Barbosa et al., 1996; Holder et al., 2000; Bartlett, 2000; Kneissl et al., 2001). The left panel of figure 2.13 shows the expected mass limit for a X–ray and a SZ cluster survey. The SZ effect begins to increase in flux density beyond $z \sim 0.6$, because of the redshift–independence of its surface brightness and the behaviour of $D_A(z)$, while it is already difficult to detect high–mass clusters in the X–rays beyond $z = 1$. In addition to that, an SZ survey has the remarkable quality to have a mass threshold almost independent of redshift.

The right panel of figure 2.13 represents the redshift distribution of cluster counts expected by the 400 deg$^2$ survey of the South Pole Telescope (Ruhl et al., 2004). The resulting source counts redshift distribution provides a powerful measure of the cosmological parameters. In particular, the data at higher redshift are fundamental to distinguish

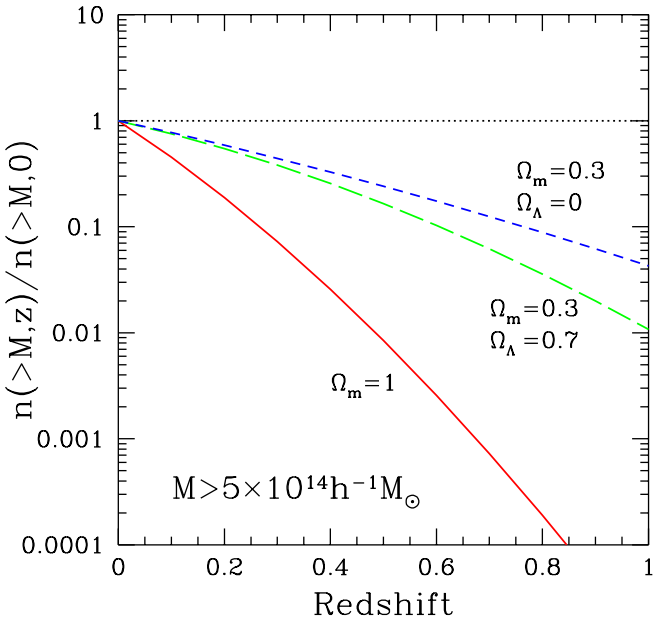


**Figure 2.12.** Evolution of the cumulative mass function for different choices of cosmological parameters (Rosati et al., 2002).

between different cosmological models.

When performing a survey (X–ray or SZ), one generally cannot directly measure the mass content of the cluster. Instead, the mass is inferred through a well–calibrated correlation (scaling relation) with a global cluster property (X–ray luminosity or temperature, SZ total flux), which may be easily measured. Understanding the scatter and the evolution with redshift (if any) of these relations is of key importance to fully exploit the potential of future experiments. The most difficult part of the job is definitely to have an accurate estimate of the cluster total mass, for which many sources of errors and biases, both intrinsic and instrumental have been identified. The mass is usually estimated by applying the hydrostatic equilibrium equation. However deviations from this equilibrium, which are commonly found in simulations, are probably responsible for an underestimate of the mass by about $10-20\%$ (Rasia et al., 2004; Nagai et al., 2007; Jeltema et al., 2007) Another key ingredient is the temperature profile: X–ray spectroscopic analysis is often limited to the inner regions of the cluster and/or to low redshift objects, while in many cases the cluster is simply assumed to be isothermal. An additional source of systematics is the eventual adoption of an analytical cluster model for gas density and temperature and/or total mass. Both these problems are discussed by Rasia et al. (2006a), by applying different methods of mass reconstruction to a set of synthetic X–ray maps of simulated clusters. In this perspective, we present in Chapter 5 and 6a geometrical deprojection technique which allows one to recover three–dimensional profiles of gas density and temperature and of total mass, by combining X–ray images and SZ observations (with no use of X–ray spectroscopic data).

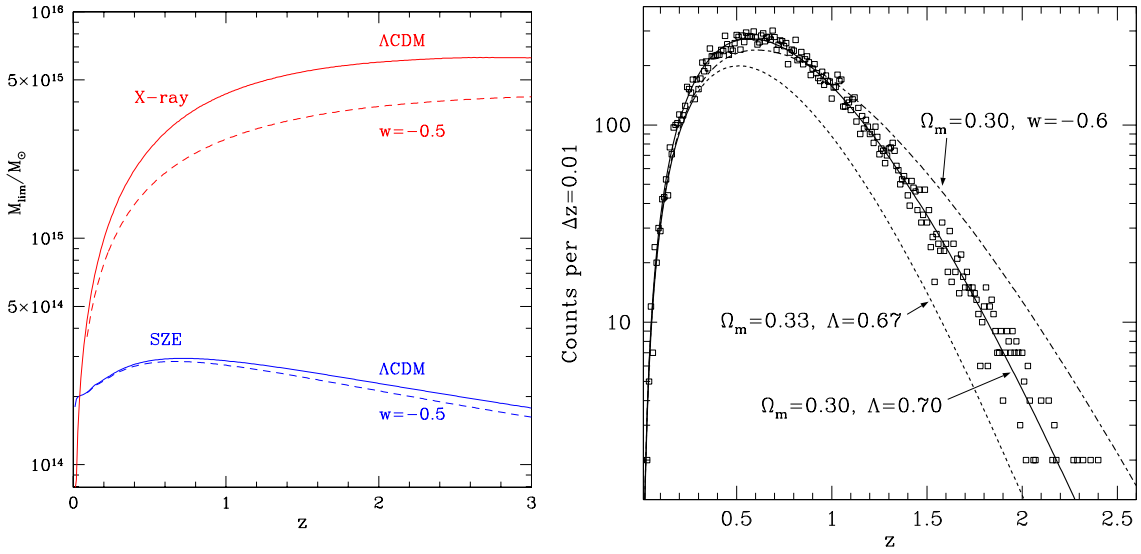


**Figure 2.13.** Left panel: limiting cluster virial masses ($M_{180}$) for detection in the X–ray survey (upper pair of curves) and in the SZ survey (lower pair of curves), from Haiman et al. (2001). The solid curves show the mass limit in a flat ΛCDM model, with $w = -1$,$\Omega_M = 0.3$ and $h = 0.65$, and the dotted curves show the masses in the same model except with $w = -0.5$. Right panel: expected number of SZ detected galaxy clusters as a function of redshift. The data points are for a 4000 deg$^2$ SPT survey with idealized sensitivity. The data points and the line passing through them were generated assuming a $\Omega_M = 0.3$, $\Omega_M = 0.7$, $\sigma_8 = 1$ cosmology. The other two lines show the effect in the expected cluster counts due to slight changes in the cosmology.

## 2.5 Conclusions

In this Chapter, we have presented an overview of X–ray and tSZ properties of galaxy clusters, which are complementary under many aspects. The first provides a complete and detailed description of gas properties; in fact, the gas density is given by the flux, while the spectroscopic analysis of the spectrum gives the gas temperature and the metallicity. However, the X–ray signal rapidly decreases with the gas density and the cluster redshift, thus making the spectroscopic analysis really challenging. On the other hand, the tSZ signal smoothly decreases in the outskirts and has no dependence on redshift. It is then ideally suited for distant cluster detection. However, the information it provides is somewhat limited, since it depends on the product of gas density and temperature and does not allow a measure of the cluster redshift. In addition, it is potentially more affected by a number of contaminations.

Given their particular position, at the top of the hierarchy of cosmic structures, galaxy clusters are natural probes for cosmology. In this Chapter we have also shortly reviewed important cosmological tests based on observations of galaxy clusters. An aspect of particular relevance is the measure of the total mass of galaxy clusters, which is affected by systematic biases (both intrinsic and instrumental), despite its important role in cosmological studies. However, in order to fully exploit their potentiality, these tests require an accurate calibration together with a careful study of possible systematics. In this context, hydrodynamical simulations have provided and will provide an important contribution. In fact, although some physical processes (in particular those related to feedback processes)

still require a more accurate numerical description, present numerical simulations have achieved an high level of accuracy in describing ICM physics and then provide a reliable representation of galaxy clusters. For this reason, simulated clusters are ideal test–beds for cosmological studies, since they could provide interesting insights on the presence of possible systematics related to the thermodynamical structure of the clusters. The most important example is probably represented by the underestimate of the total mass due to the deviations from hydrostatic equilibrium (e.g. Rasia et al., 2004; Kay et al., 2004). Following a different perspective, the creation of synthetic *observations* of galaxy clusters (namely in X–ray, tSZ or temperature) could allow to study systematics and limitations related to instrumental effects (e.g. Rasia et al., 2006a).

In the following Chapters of this Thesis we will analyze the combination of X–ray and tSZ observations in different applications, by using a set of hydrodynamical simulations. In Chapter 4 we will study the capabilities in the measurement of the angular diameter distance and, then, the cosmological parameters. In Chapter 5, we will present a technique for performing a geometrical deprojection of X–ray and tSZ images, which avoids the use of X–ray spectroscopy. This technique will allow to extend the analysis of the thermodynamic structure of the ICM to larger radii and at higher redshift than possible with X–ray only measurements. Finally, in Chapter 6 we will develop this technique by implementing the solution of the hydrostatic equilibrium equation, thus allowing us to measure also the total gravitating mass of the cluster. We will study the systematics of this procedure and how its uncertainty affects the calibration of mass scaling relation with X–ray and tSZ properties.

# Chapter 3

# Hydrodynamical simulations of galaxy clusters

N–body simulations were used for the first time in the sixties for the study of cosmic structure formation, but they become a fundamental part of the study of cosmology only in the eighties, thanks to the development of fast computers and efficient computing algorithms. Now, a large part of our knowledge on the formation and evolution of cosmic structures is based on the results from numerical simulations. Hydrodynamic codes are able to represents all the different matter components of cosmic structures (dark matter, gas, stars) and to follow their evolution in detail. The physics of gas and star formation is described in detail with recipes for cooling, heating and star formation and also a treatment of the metal production is implemented.

In this chapter, the main characteristics of numerical simulations are discussed, with particular attention to the N–body TREESPH technique, which is adopted in the GADGET2[1] code (Springel et al., 2001; Springel, 2005a), with which the set of simulated galaxy clusters analyzed in this work has been realized. Section 3.1 and 3.2 provide an introduction to the N–body TREE and SPH techniques respectively. Section 3.3 describes our set of simulated clusters and the procedure used to generate synthetic maps of the X–ray surface brightness, of the Sunyaev–Zeldovich effect and of the temperature. Finally, Section 3.4 describe the different definitions of mean temperature that we will use in the following.

## 3.1 The gravitational dynamics: the N–body TREE code

N–body simulations describe a portion of the Universe through a number (N) of particles, whose dynamics is determined only by gravitational interaction (for reviews, see e.g. Bagla, 2005). The simulations are heavily limited by the total number of particles, since the computational cost increases rapidly with it. Each simulation essentially represents a compromise between its mass resolution and its dimension, given the available computing resources.

One essentially needs to compute, for each particle, the resulting force due to the gravitation attraction of all the other particles. We first consider the simplest case of two

[1] `http://www.mpa-garching.mpg.de/gadget`

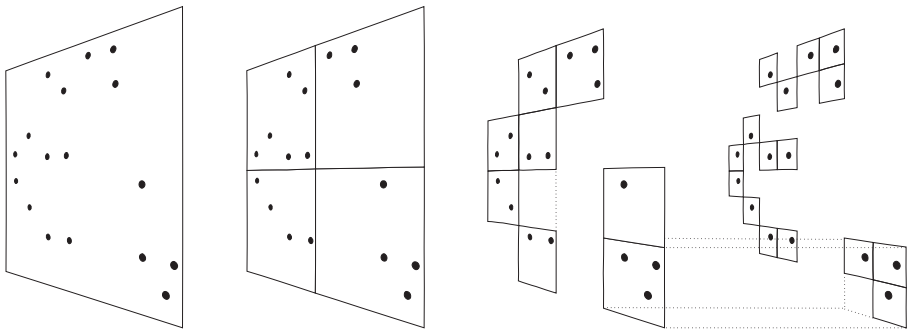

**Figure 3.1.** Schematic illustration of the TREE code scheme in two dimensions (Springel et al., 2001). The particles on the left are enclosed in a first level cell (main node) that is iteratively split into 4 squares (8 cubes for the three–dimensional case) until one particle remains (the "leaf" of the tree).

particles $i$ and $j$. The two particles attract each other with force:

$$\vec{F}_{ij} = \frac{G m_i m_j (\vec{x}_j - \vec{x}_i)}{(\epsilon^2 + |\vec{x}_i - \vec{x}_j|^2)^{3/2}} \tag{3.1}$$

where $G$ is the gravitational constant, $m_i$ and $m_j$ are the masses of the particles $\vec{x}_i$ and $\vec{x}_j$ are the coordinates of the particles and $\epsilon$ is the *softening parameter*. Since nothing prevents two particles to be very close, the gravitational force could in principle diverge, thus requiring in principle an infinite accuracy in the integration of the orbits. To prevent this, the $\epsilon$ term is added to the denominator. This term essentially represents the spatial resolution of the particle dynamics.

At each timestep it is necessary to compute the global gravitational force acting on each particle, due to the distribution of all the other particles. The simplest way to do so is to compute $\vec{F}_{ij}$ for all pairs of particles. This method was adoped by early simulations. It provides a very accurate estimate of the gravitational force, but its computational cost rapidly increases with the number of particles, since the number of operations required at each timestep is $N(N-1)/2$. In order to treat more complex systems, it is necessary to reduce the number of operations, at the cost of reducing the force resolution. The solution adopted by a large part of N–body codes is to compute the large–scale gravitational field over a grid. In this case, the computational cost is sensitively reduced, but the resolution is limited by the grid spacing. To solve this problem, modern versions of these codes supplement the force computation on scales below the mesh size with a direct summation and/or they place mesh refinements on highly clustered regions.

The TREE algorithm follows a completely different approach; the idea is to treat distant particles as one single particle by adopting a hierarchical partitioning system, which has been developed by Barnes & Hut (1986). The structure may be tought as an ideal tree. The smallest elements are cells containing one single particle, which can be tought as the *leaves* of the tree. These particle–bearing cells are grouped into larger cells, the *nodes*, which are in turn grouped into larger nodes down to the *root*, i.e. the whole simulation box. Each small and large cell will be characterized by a the total mass and center–of–mass of the particle(s) it contains. The construction of the tree follows a partitioning procedure, which is sketched in figure 3.1 for the case of a two–dimension simulation. The process starts by considering the largest cell, which contains the whole

simulation box. It is divided into $2^3$ subcells, each having side equal to one half of the side of the parent cell. If a cell contains two or more particles, it is in turn divided into subcells and the division process continues until each cell contains no more than one particle. When the partitioning process is finished, the space is divided into a number of cells of different size, which either contain exactly one particle or are progenitors to further cells, in which case each cell carries the monopole and quadrupole moments of all the particles that lie inside its volume.

The force computation proceeds by an iterative process, which *walks up* the tree, summing the appropriate contribution from each node, which is determined by the accuracy parameter $\theta$ (typically $\theta \sim 1°$) in the following way. Let $l$ be the length of a cell and $D$ the distance from the cell's centre–of–mass and the particle. Then if $l/D < \theta$ the contribution of the cell content to the total force acting on the particle $P$ is computed by treating it a single particle, otherwise its subcells are considered. This process is repeated iteratively until the resolution criterion is satisfied or a one–particle cell is reached.

## 3.2 The gas physics: Smoothed Particle Hydrodynamics (SPH)

The gas component is described by solving the equations of fluid dynamics. This can be done by following either a Lagrangian or an Eulerian approach. In the first case, the thermodynamic quantities (density, temperature, pressure, entropy) are carried by the single particles, which interact with each other. In the second more classical approach, the system is described by a grid (which may be adaptive) over which the equations are solved.

The Smoothed Particle Hydrodynamics (SPH) has been introduced by Lucy (1977) and Gingold & Monaghan (1977) to solve the fluid equation in the context of astrophysical numerical simulations (for recent reviews, see Springel et al., 2005; Monaghan, 2005). It is a Lagrangian technique in which fluid elements constituting the system are represented by particles. SPH avoids the main limitation due to the use of a grid on the dynamic range in spatial resolution or on the global geometry. Its main limitations are the treatment of the shocks, which is done by introducing an artificial viscosity, and the fact that it is not possible to represent an arbitrarily large density gradient with a finite number of particles.

The SPH is particularly well suited to be used in association with a TREE N–body code, since their underlying principles are similar. Both techniques are fully Lagrangian and neither use a grid. The resulting code naturally allows to follow the evolution of a large number of particles within a Lagrangian framework (Hernquist & Katz, 1989).

In the SPH, the fluid is modelled as composed by a number of elements which are represented by particles. Thus, if the system is evolved according to the laws of hydrodynamics, $\rho$ can be estimated form the local density of particles. Since the computational model consists of a finite number of fluid elements, local averages must be performed over volumes of nonzero extent. This is conveniently accomplished by introducing a systematic procedure for smoothing out local statistical fluctuations in the particle number. The mean value of a physical field, $f(\vec{r})$, within a given interval can be determined through kernel estimation according to

$$\langle f(\vec{r})\rangle = \int W(\vec{r}-\vec{r}';h) f(\vec{r}')d\vec{r}' \tag{3.2}$$

where $W(\vec{r})$ is known as the *smoothing kernel*, $h$ is the smoothing length, which specifies the extent of the averaging volume, and the integration is over all space. The smoothing kernel is normalized to 1. It is also required that $\langle f(\vec{r})\rangle \rightarrow f(\vec{r})$ for $h \rightarrow 0$. Within reasonable assumptions on the kernel function $W(\vec{r})$, Hernquist & Katz (1989) show that the error made in approximating $f(\vec{r})$ by its smoothed estimate $\langle f(\vec{r})\rangle$ is $O(h^2)$.

If the values of $f(\vec{r})$ are known only at a finite number of discrete points, distributed with number density $n(\vec{r}) = \sum_{j=1}^{N} \delta(\vec{r} - \vec{r}')$, then the smoothed equivalent can be written as (Hernquist & Katz, 1989):

$$\langle f(\vec{r})\rangle = \sum_{j=1}^{N} \frac{f(\vec{r}_j)}{\langle n(\vec{r})\rangle} W(\vec{r} - \vec{r}_j; h). \tag{3.3}$$

In particular, if a mass $m_j$ is associated with each fluid element then

$$\langle \rho(\vec{r})\rangle = \sum_{j=1}^{N} m_j W(\vec{r} - \vec{r}_j; h). \tag{3.4}$$

In every timestep the SPH code must solve the fluid equations: the mass conservation is assured by the fact that the kernel function is normalized to 1 ($\int W(\vec{r}) d^3r = 1$), while in the adiabatic regime the Euler and the energy conservation equations become:

$$\left(\frac{d\vec{v}}{dt}\right)_n = -\sum_{j=1}^{N} m_j \left[\frac{p}{\rho^2} + \frac{p_j}{\rho_j^2}\right] \vec{\nabla} W(|\vec{r} - \vec{r}_j|, h) \tag{3.5}$$

and

$$\left(\frac{d\epsilon}{dt}\right)_n = \frac{p}{\rho^2} \sum_{j=1}^{N} m_j (|\vec{v} - \vec{v}_j|) \cdot \vec{\nabla} W(|\vec{r} - \vec{r}_j|, h) \tag{3.6}$$

respectively.

The description of a non–conservative physical system can be implemented by modifying eq. 3.6, for example a radiative gas is obtained by adding a cooling term. On the contrary the description of phenomena like shock–heating requires the addition of artificial viscosity terms in eq. 3.5.

An important advantage of the SPH formalism is that it provides a natural means for estimating gradients of the local fluid properties. Gradients of the physical variables are replaced by derivatives of the smoothing kernel, thereby constraining $W(\vec{r})$ to be differentiable or at least the same order as that of the terms present in the dynamical equations. In addition, the kernel should be sharply peaked and approach a delta function as $h \rightarrow 0$, in order that the smoothing estimates retain a local character. A kernel with compact support is generally preferred for reasons of computational cost, so as to perform the integration over a finite portion of volume.

In our simulations, we adopt the following kernel:

$$W(x) = \frac{8}{\pi h^3} \begin{cases} 1 - 6x^2 + 6x^3 & 0 \leq x \leq \frac{1}{2} \\ 2(1-x)^3 & \frac{1}{2} \leq x \leq 1 \\ 0 & x \geq 1 \end{cases} \tag{3.7}$$

where $x = r/h$ and $r$ is the distance from the particle position. Note that both the first and the second derivatives of the above kernel are continuous.

The local spatial resolution is determined by the smoothing length $h$. A more traditional approach adopts the same $h$ for all particles. However, a constant $h$ would yield relatively more accurate estimates in regions with a high density of particles than in lower density regions. Furthermore, all the structures smaller than $h$ would not be resolved, thus not taking full advantage of the adaptive Lagrangian nature of the SPH method. An adaptive $h$ instead allows at the same time to achieve the necessary resolution in denser regions and to maintain the same level of accuracy at all points on the fluid, thus improving consistency and efficiency of the code. The value of $h$ is then determined from the local particle density, by keeping the number of neighborhoods[2] either exactly, or at least roughly, constant.

## 3.3 The set of simulated clusters

The sample of simulated galaxy clusters used in this Thesis has been extracted from two sets of cosmological hydrodynamical simulations, both realized with the treeSPH GADGET-2 code. These simulations adopted a "concordance" ΛCDM model with $\Omega_m = 0.3$ for the matter density parameter at present time, $\Omega_\Lambda = 0.7$ for the cosmological constant term, $\Omega_\mathrm{b} = 0.019\,h^{-2}$ for the baryon density parameter, $h = 0.7$ for the Hubble constant in units of 100 km s$^{-1}$Mpc$^{-1}$. The first simulation has $\sigma_8 = 0.8$, while the second has a larger value $\sigma_8 = 0.9$. Besides gravity and hydrodynamics, the simulations include the treatment of radiative cooling, the effect of a uniform time–dependent UV background, a sub–resolution model for star formation from a multiphase interstellar medium, as well as galactic winds powered by SN explosions (see below).

The larger part of the galaxy clusters analyzed in this Thesis comes from the first simulation. The run follows the evolution of $480^3$ dark matter particles and an equal number of gas particles in a large cosmological box of size $192h^{-1}$ Mpc. The mass of the gas particles is $m_\mathrm{gas} = 6.9 \cdot 10^8\,h^{-1}M_\odot$, while the Plummer-equivalent force softening is $7.5h^{-1}$ kpc at $z = 0$. We refer to Borgani et al. (2004) for a detailed presentation of this simulation. Figure 3.2 shows a map of the gas density over the whole box of the simulation at $z = 0$, through a slice having thickness of $12h^{-1}$Mpc. In the image, the bright spots clearly identify the galaxy clusters. This region contains the more massive one of the simulation, which has a virial mass $M_{vir} = 1.3 \cdot 10^{15}\,h^{-1}M_\odot$ (see Section A.6.3), located in the upper right corner of the map. It also shows the large–scale matter distribution. The clusters are separated by regions characterized by a very low density (voids) and connected by filamentary structures.

In order to extend our analysis to more massive and hotter systems, which are mostly relevant for current SZ observations, we include four more galaxy clusters having $M_\mathrm{vir} > 10^{15}\,h^{-1}M_\odot$ and belonging to a different set of hydrodynamical simulations (Borgani et al., 2006), which are shown in Figure 3.3. These clusters have been extracted from a dark-matter only simulation with a box-size of 479 $h^{-1}$Mpc (Yoshida et al., 2001) and resimulated at higher mass and force resolution. The new initial conditions for this system have been generated by applying the Zoomed Initial Condition (ZIC) technique (Tormen et al., 1997). This method allows one to increase the mass resolution in a suitably chosen high–resolution Lagrangian region surrounding the structure to be resimulated, and at the same time to correctly describe the large–scale tidal field of the cosmological environment

[2]The number of neighborhood is defined as the number of particles lying inside the smoothing radius of a particle.

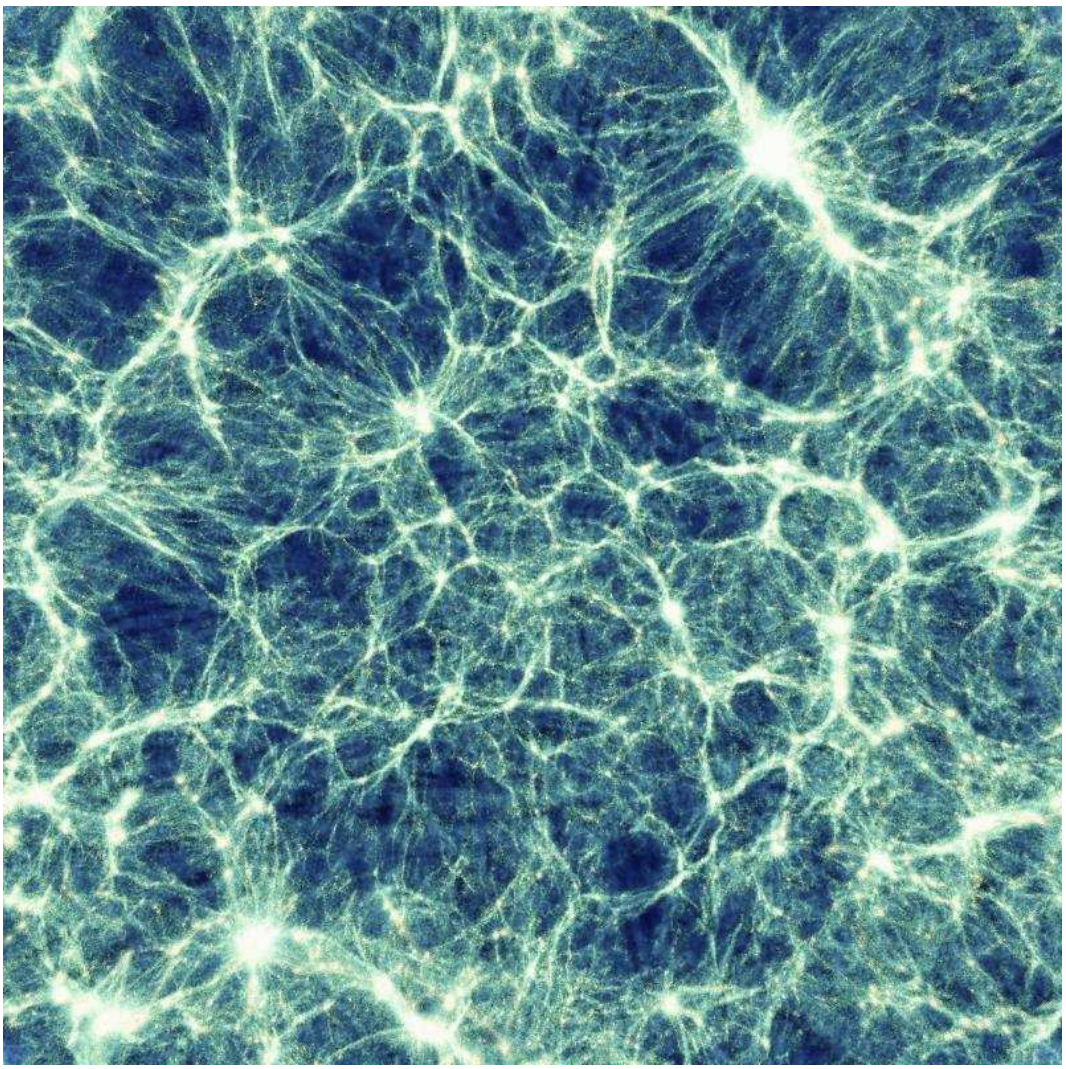

**Figure 3.2.** Map of the gas density over the whole box of the first simulation at $z = 0$ (Borgani et al., 2004), projected using a ray–tracing technique through a slice having thickness of $12h^{-1}$Mpc, and containing the most massive cluster found in this simulation (upper right–hand side of the figure).

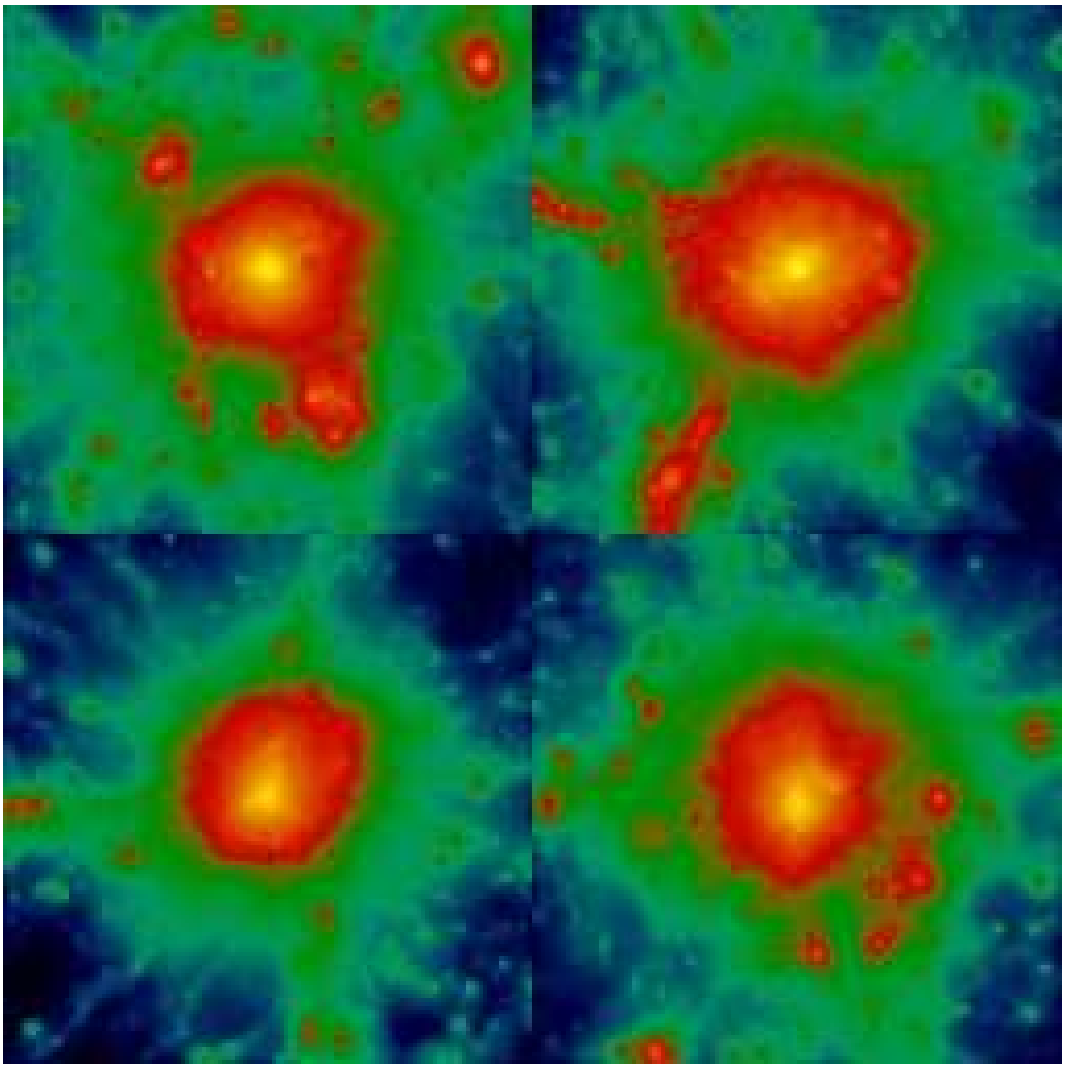

**Figure 3.3.** Map of the gas distribution of the four massive cluster from the second simulation set, having mass $M_{vir} \gtrsim 10^{15}\, h^{-1} M_{\odot}$. The maps enclose a region of $2R_{vir}$ from the center of the cluster.

by using low–resolution particles. These objects have a better mass resolution, with $m_{\rm gas} = 1.69 \cdot 10^8\, h^{-1} M_\odot$. The gravitational softening length was kept fixed at $\epsilon = 30.0 h^{-1}$kpc comoving (Plummer-equivalent) and was switched to a physical softening length of $\epsilon = 5.0 h^{-1}$ kpc below $z = 5$.

### 3.3.1 Thermal processes in the IntraCluster Medium (ICM)

The simple hydrodynamics does not completely describe the complex thermal evolution of the ICM. For this reason, the simulations include some important physical processes which play a key role in the thermodynamic evolution of the ICM. They are summarized below:

- **Radiative cooling** is computed assuming an optically thin gas of primordial composition (mass–fractions of $X = 0.76$ for hydrogen and $1 - X = 0.24$ for helium) in collisional ionization equilibrium, following Katz et al. (1996). The simulation also includes a photoionizing, time–dependent, uniform ultraviolet (UV) background expected from a population of quasars (e.g. Haardt & Madau, 1996), which reionizes the Universe at $z \simeq 6$. The effect of a photoionizing background is that of inhibiting gas collapse and subsequent star formation within the haloes of sub-$L_*$ galaxies (e.g. Benson et al., 2002), thus having a secondary impact at the resolution of our simulation. Although the code includes a method to follow metal production, the effects of metals are not included on the cooling function, owing both to code limitations and to the approximate treatment of metal generation and diffusion. See Tornatore et al. (2007) for a detailed description of metal enrichment in cluster simulations with GADGET2.

- **Star formation** is treated using the hybrid multiphase model for the interstellar medium introduced by Springel & Hernquist (2003). We refer to this paper for a detailed description of the method, providing here only a short summary of the model. The ISM is pictured as a two–phase fluid consisting of cold clouds that are embedded at pressure equilibrium in an ambient hot medium. The clouds form from the cooling of high–density gas, and represent the reservoir of baryons available for star formation. When stars form, according to a Salpeter IMF (Salpeter, 1955), the energy released by supernovae heats the ambient hot phase of the ISM, and in addition, clouds in supernova remnants are evaporated. These effects establish a tightly self–regulated regime for star formation in the ISM. The numerical implementation of this multiphase model describes each gas particle as composed by a hot component, having its own mass and density, and a cold neutral component. The relative amount of these two phases is determined by the local value of gas density and temperature.

- **Galactic winds.** If not counteracted by some sort of feedback process, cooling is well known to overproduce the amount of stars both in the average environment and in the group/cluster overdense environment (e.g. Balogh et al., 2001; Borgani et al., 2004, and references therein). As discussed by Springel & Hernquist (2003), their multiphase ISM model alone does, however, not fully resolve this problem, despite its ability to regulate the consumption of cold gas into stars within the ISM. This is because the cooling rates within haloes remain essentially unaffected in the model, i.e. the supply of gas to the dense star-forming ISM is largely unchanged,

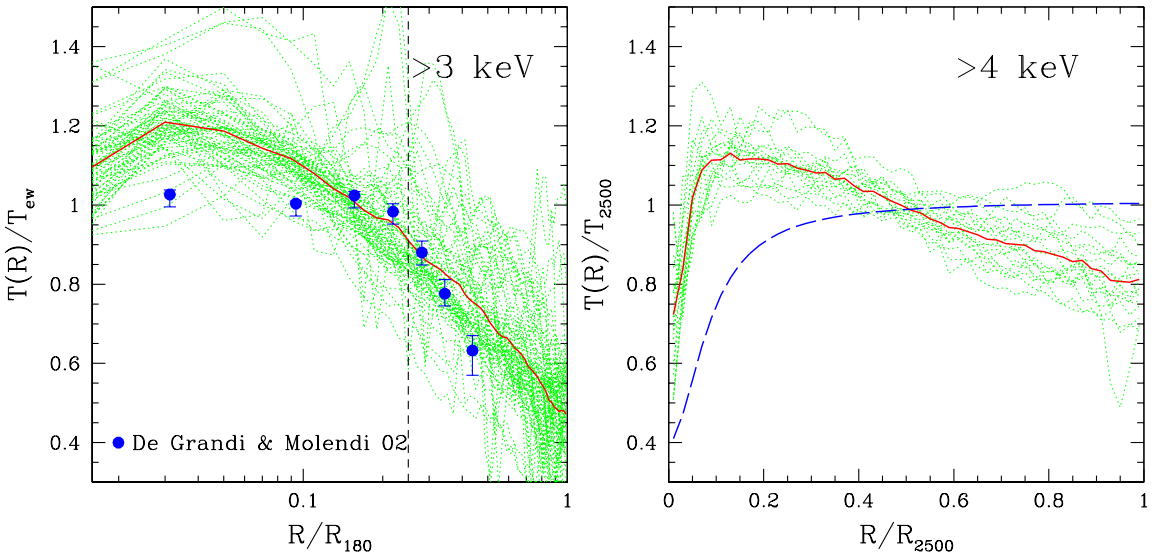


**Figure 3.4.** Comparison between simulated and observed projected temperature profiles. Left–hand panel: comparison between simulated clusters with $T_{\rm ew} > 3$ keV and the observational data points from the analysis of BeppoSAX data for 17 clusters by De Grandi & Molendi (2002). Right-hand panel: comparison between simulated clusters with $T_{\rm ew} > 4$ keV and the best–fitting universal temperature profiles measured by Allen et al. (2001) from their analysis of Chandra data for a set of six relaxed clusters (dashed curve). In both panels, dotted lines are the profiles for each single simulated cluster, while the heavy solid line is for the average profile. For reference, the vertical dashed line in the left-hand panel indicates the average value of $R_{2500}$.

while by construction the phases of the ISM remain coupled to each other, preventing baryons to leave the ISM (except for dynamical effects such as gas stripping in mergers). However, galactic outflows are observed and expected to play a key role in transporting energy and metals produced by the stellar population into the IGM/ICM. To account for them, Springel & Hernquist (2003) suggested a phenomenological description of galactic winds as an extension of their model, which has been included in the simulation. According to the choice of parameters for the feedback and wind scheme, star-forming gas particles contribute to the wind with a mass outflow rate two times larger than their star formation rate, with a wind velocity of approximately 360 km/s.

Physical processes included in the simulation are able to account for the basic properties of clusters, such as the scaling relations between mass, temperature and luminosity (Borgani et al., 2004). At the same time, there are still some discrepancies between simulated and observed properties, in particular for the temperature and entropy profiles. This may suggest that a more efficient way of providing non–gravitational heating from feedback energy and/or additional physical processes are required to better reproduce observed properties of the ICM, particularly in the inner regions.

The most interesting aspect is probably the temperature profile. Figure 3.4 presents a direct comparison between the projected temperature profiles of the clusters in the first simulation and two different sets of observations, namely the datapoints from the analysis of 17 clusters observed with BeppoSAX by De Grandi & Molendi (2002) and the best–fitting universal temperature profiles measured by Allen et al. (2001) from a set of

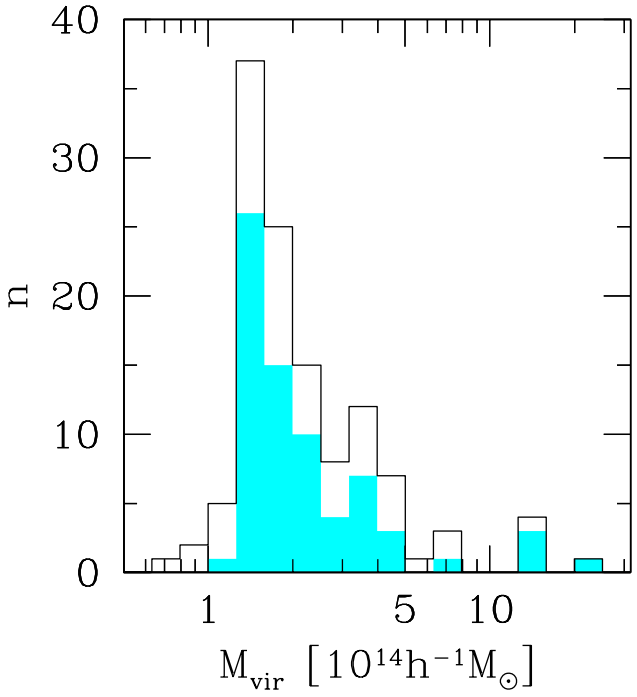


**Figure 3.5.** The distribution of virial masses for the set of simulated clusters. The solid line is for the whole sample, the shaded area is for the subset of clusters classified as regular (see text).

six relaxed clusters observed with Chandra, in the left and right panel respectively. For a proper comparison with the observational results only simulated clusters with $T > 3$ keV have been selected in the first case, and $T_{\rm ew} > 4$ in the second case. The simulated clusters show neither evidence for an isothermal core, nor a central smooth decline down to approximately 1/2 of the virial temperature, as is found in the observations. Instead, they steadily increase toward the cluster centre down to $R \simeq 0.04 R_{180}$, while a temperature decrease is observed only in the innermost regions. It is worth noting that the slope of the simulated profiles in the outer regions is similar to, although slightly shallower than, the observed one. The comparison with observations suggests that there is an excess of cooling (or more probably a lack of heating) in the simulation. In fact, the radiative cooling causes a lack of pressure support in the cluster centre, so that the gas flows in from outer regions, being heated by adiabatic compression (e.g. Tornatore et al., 2003). As a result, the temperature actually increases in cooling regions, causing steeply increasing temperature profiles.

### 3.3.2 The sample of simulated clusters

Clusters in the simulation box are selected by applying a friends–of–friends halo finder to the distribution of DM particles, with a linking length equal to 0.15 times their mean separation. For each group of linked particles with more than 500 members, we identify the particle having the minimum value of the gravitational potential. This particle is then used as a starting point to run a spherical overdensity algorithm, which determines the radius around the target particle that encompasses an average density

equal to the virial density for the adopted cosmological model, $\rho_{vir}(z)\Delta_c(z)\rho_c(z)$, where $\rho_c(z) = [H(z)/H_0]^2\rho_{c,0}$ is the critical density at redshift $z$ and the overdensity $\Delta_c(z)$ is computed as described in Eke et al. (1996).

In the box of the first simulation we identify 117 clusters with virial mass $M_{vir} > 10^{14}\,h^{-1}M_\odot$, to which we add the four more massive clusters coming from the second simulation. Therefore, our total sample comprises 121 objects, spanning the range of virial masses $M_{vir} \simeq 8 \cdot 10^{13} - 3 \cdot 10^{15}\,h^{-1}M_\odot$. Their mass distribution is reported in Figure 3.5. The dynamical state of the clusters is a key ingredient in tSZ and X–ray studies, since almost all ICM models rely on the hypothesis of spherical (or at least axial) symmetry of the gas distribution. For this reason, we select the clusters in our sample which show a relaxed morphology in their X–ray image. Figure 3.6 shows a typical relaxed cluster, characterized by a smooth profile, while figure 3.7 shows an unrelaxed cluster, which instead exhibits a number of substructures. We select 71 relaxed clusters in our sample, whose mass distribution is shown as well in figure 3.5, with the shaded area.

### 3.3.3 Generation of tSZ, X–ray and temperature maps

The work presented in this Thesis is based on the analysis of synthetic SZ, X–ray and temperature maps of simulated clusters. This section describes the procedure used to compute ideal maps, which are used for the analysis presented in Chapter 4. In Chapter 5 and 6 instead these ideal SZ and X–ray maps are convolved with a noise scheme modelled on the CCAT and on the Chandra telescope respectively, in order to introduce instrumental effects (see Section 5.2.1).

The X–ray maps presented here have also been used to study the role of merger processes in defining scatter into the mass–temperature relation (Ventimiglia et al., 2006), by using three different statistics designed to measure X–ray surface brightness substructures (namely the centroid variation $w$, the axial ratio $\eta$ and the power rations $P_{20}$ and $P_{30}$, see the paper for details). The deviation of each cluster from the mass–temperature relation is found to be correlated with each of the adopted substructure estimators. In particular, clusters with more substructures tend to be cooler for a fixed halo mass. These results suggest that a three–parameter fit of the mass–temperature relation which includes substructure information should be preferred with respect to the simple two–parameter fit.

Around each cluster we extract a spherical region extending out to 6 $R_{vir}$. Following Diaferio et al. (2005), we create maps of the relevant quantities along three orthogonal directions, extending out to about 2 $R_{vir}$ from the cluster centre. Each map is a regular $512 \times 512$ grid.

We distribute the quantity of each particle on the grid points within a circle of radius equal to the smoothing length $h$ (see Section 3.2) centred on the particle, according to the SPH smoothing kernel $W(x)$ eq. (3.7). Specifically, we compute a generic quantity $q_{jk}$ on the $(j,k)$ grid point as

$$q_{jk}d_p^2 = \int q(r)dld_p^2 = \sum_i q_i(m_i/\rho_i)w_i \tag{3.8}$$

where $d_p^2$ is the pixel area, the sum runs over all the particles, and $w_i \propto \int W(x)dl$ is the weight proportional to the fraction of the particle proper volume $m_i/\rho_i$ which contributes to the $(j,k)$ grid point. For each particle, the weights $w_k$ are normalized to satisfy the relation $\sum_k w_k = 1$ where the sum is now over the grid points within the particle circle.

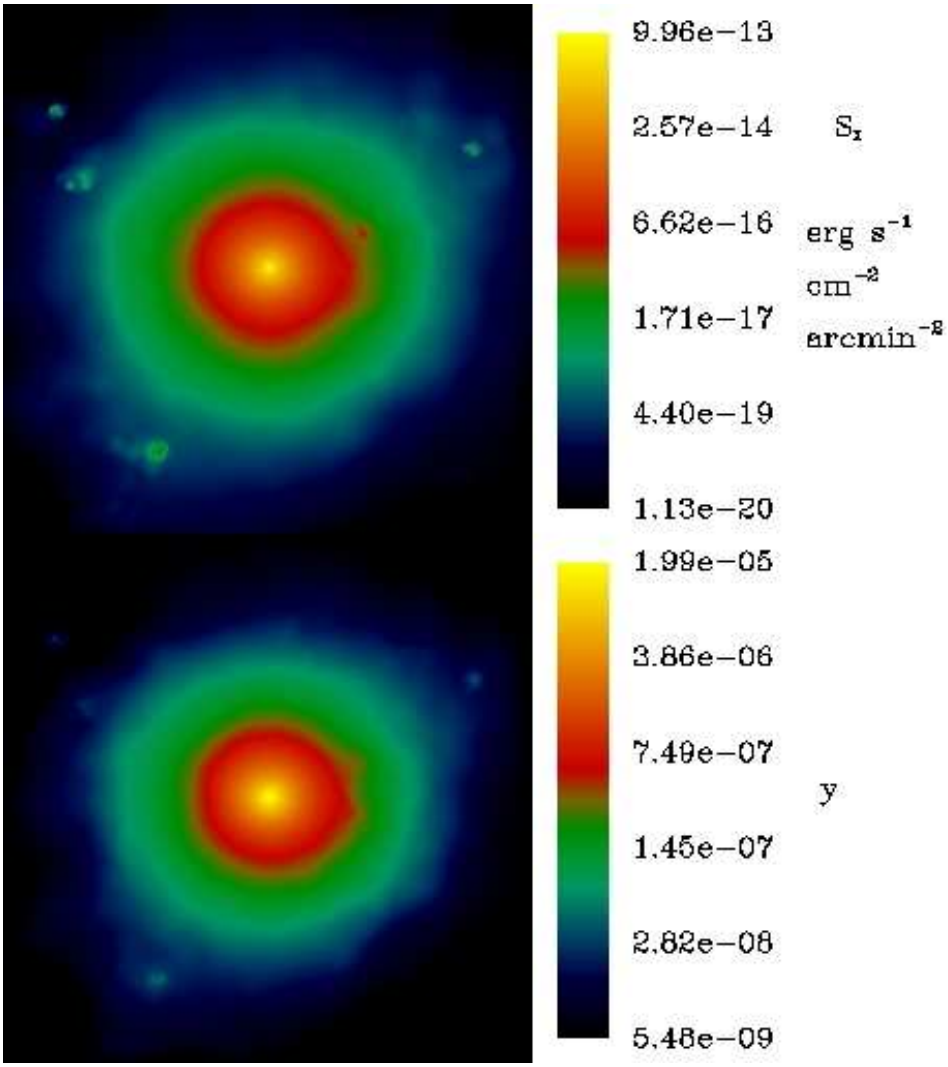


**Figure 3.6.** Maps of the X-ray brightness and SZ $y$ parameter for a regular simulated cluster having virial mass $M_{vir} \simeq 1.4 \cdot 10^{14}\, h^{-1} M_{\odot}$, $R_{500} = 0.53 h^{-1} Mps$ and $T_{\rm sl} = 2.2$ keV. The map extends out to 2 $R_{\rm vir}$, so that it covers a physical scale of 6.05 $h^{-1}$Mpc for this cluster. Each map is done with a $512 \times 512$ pixelization.

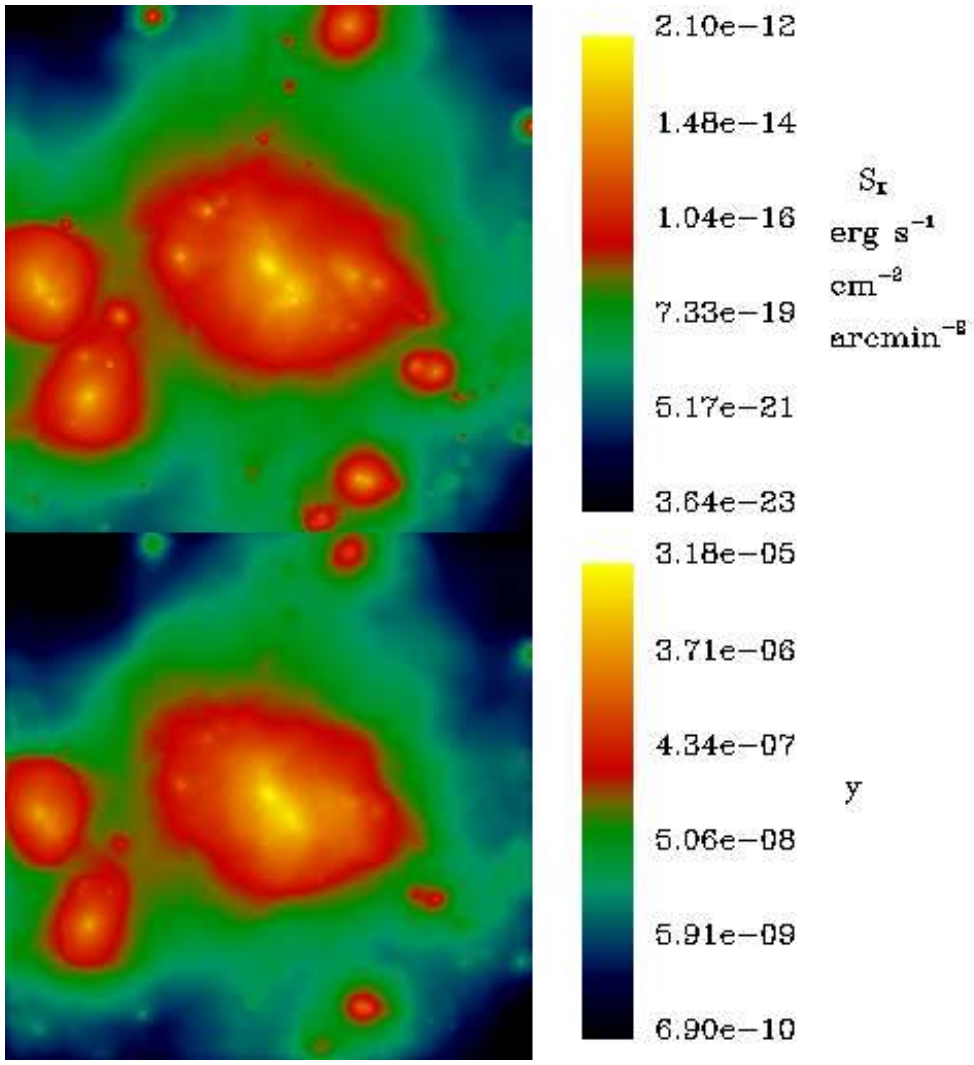


**Figure 3.7.** The same as figure 3.6, but for an unrelaxed simulated cluster having virial mass $M_{vir} \simeq 4.1 \cdot 10^{14}\, h^{-1} M_{\odot}$.

When $h_i$ is so small that the circle contains no grid point, the particle quantity is fully assigned to the closest grid point.

### Maps of the X–ray surface brightness

The X–ray surface brightness is given by the integral of gas emissivity $\epsilon$, i.e. by taking:

$$q \equiv \frac{1}{4\pi(1+z)^4}\,\epsilon = \frac{1}{4\pi(1+z)^4} n_e n_H \Lambda(T) \tag{3.9}$$

The number density of electrons $n_e$ and of protons $n_H$ and the cooling function $\Lambda(T)$ are computed by assuming a completely ionized gas with primordial chemical composition (with mass fractions $X_H = 0.76$ and $X_{He} = 0.24$ for hydrogen and helium respectively). Note also that the cooling function has to be redshifted, so it is actually $\Lambda(T, z)$. However, we compute (and then analyze) the maps in the rest–frame of the cluster, regardless of its redshift. Since our aim is to study the integrated flux in order to derive the gas density profile, the soft band [0.5–2] keV is assumed, which has a weak dependence on temperature and do not present strong emission lines.

The upper part of Figure 3.6 shows an example of the X-ray surface brightness map of a cluster in our simulation (with $M_{vir} \simeq 1.4 \cdot 10^{14}\, h^{-1} M_\odot$). In the image visible a number of substructure and clumps are clearly visible, which are emphasized by the dependence of the X–ray signal on the squared gas density. In X–ray observations most of these clumps remains undetected, owing to the instrument resolution. They have the effect of artificially boosting the X–ray signal, thus generally leading to an overestimate of gas density.

### Maps of the thermal Sunyaev–Zeldovich effect (tSZ)

We generate the maps of the $y$ parameter, since this quantity is independent of the assumed observing frequency, so in this case:

$$q \equiv n_e \frac{k_B T_e}{m_e c^2} \sigma_T. \tag{3.10}$$

As in the X–ray maps, the electron number density $n_e$ is computed by assuming a completely ionized gas of primordial composition.

The lower part of Figure 3.6 shows an example of the tSZ map of a cluster in our simulation (with $M_{vir} \simeq 1.4 \cdot 10^{14}\, h^{-1} M_\odot$). Owing to its dependence on $n_e T$, the tSZ signal is much less affected than the X–ray surface brightness by the presence of gas clumping. For the same reason, the tSZ signal decreases more slowly with radius (note the difference in the scale of the X–ray and tSZ maps: the first encompasses 8 orders of magnitude, the second only 4). This means that on one hand the tSZ can be detected out to fairly large cluster radii, but on the other hand it is more sensitive to the presence of fore/background contaminations, which may give a substantial contribution to the total signal.

### Maps of temperature

The projected temperature represents the mean of the temperature of the gas along the line of sight. In a general form the mean temperature can be defined as

$$\langle T \rangle = \frac{\sum_i w_i T_i}{\sum_i w_i} \tag{3.11}$$

where $w_i$ is the weighting function, which depends on the assumed temperature definition. The projected temperature map will be given by the ratio of two maps, of which the first (nominator, N) is the integral of the temperature weighted by the function $w$, while the second (denominatior, D) represents the normalization. The two maps are computed by assuming:

$$q_N \equiv w_i T_i \tag{3.12}$$

and

$$q_D \equiv w_i \tag{3.13}$$

for the contribution carried by eache pixel to the numerator and denominator of eq. (3.11). In the following section, we will describe three temperature definitions, which have been introduced with the purpose of comparing simulation results with observations.

## 3.4 Definitions of temperature

The comparison between the properties of simulated and real galaxy clusters is complicated by different problems, produced both by projection effects and by instrumental artefacts, like instrument response, sky background and instrumental noise. A further complication can arise from a possible mismatch between the spectroscopic temperature estimated from X–ray observations and the temperature definition used for numerical results. In most X–ray studies, the temperature is obtained by fitting the projected spectrum with a single–temperature model. One generally expects the resulting temperature to represent a mean of the temperature of the emitting gas along the line of sight. However, the way in which this mean should be computed is not obvious, despite the fact that it represents a critical point when aiming at comparing thermal properties of simulated galaxy clusters with those found in X–ray observations.

The *electron temperature* is naturally defined by:

$$T_e = \frac{\sum_i n_{e,i} T_i}{\sum_i n_{e,i}}, \tag{3.14}$$

where $n_{e,i}$ and $T_i$ are defined as the electron number density and the temperature carried by the $i$–th simulation gas particle. It coincides with the mass–weighted temperature in the limit of a fully ionized plasma of uniform metallicity. This temperature definition has a relevant physical meaning, since it represents a measure of the thermal energy of the gas, which is simply $E \propto mT_e$. Unfortunately, this temperature definition would give temperature estimates which differ significantly from what would be derived from X–ray observations.

In order to have a more realistic comparison with the spectroscopic fits, a different definition was then introduced, the *emission–weighted temperature* (e.g. Evrard et al., 1996):

$$T_{\rm ew} = \frac{\sum_i \epsilon_i T_i}{\sum_i \epsilon_i}, \tag{3.15}$$

where $\epsilon_i \propto n_{e,i}^2 \Lambda(T_i)$ is the emissivity associated to the $i$-th gas particle. The cooling function $\Lambda(T)$ can be computed over an energy band, comparable to that where the X–ray spectrum is fitted in observational data analyses. In the following, we compute the emission–weighted temperature in the [0.5–7] keV band, since this is the band tipically used for spectral fittings in X–ray observations. Since the X–ray emissivity is proportional

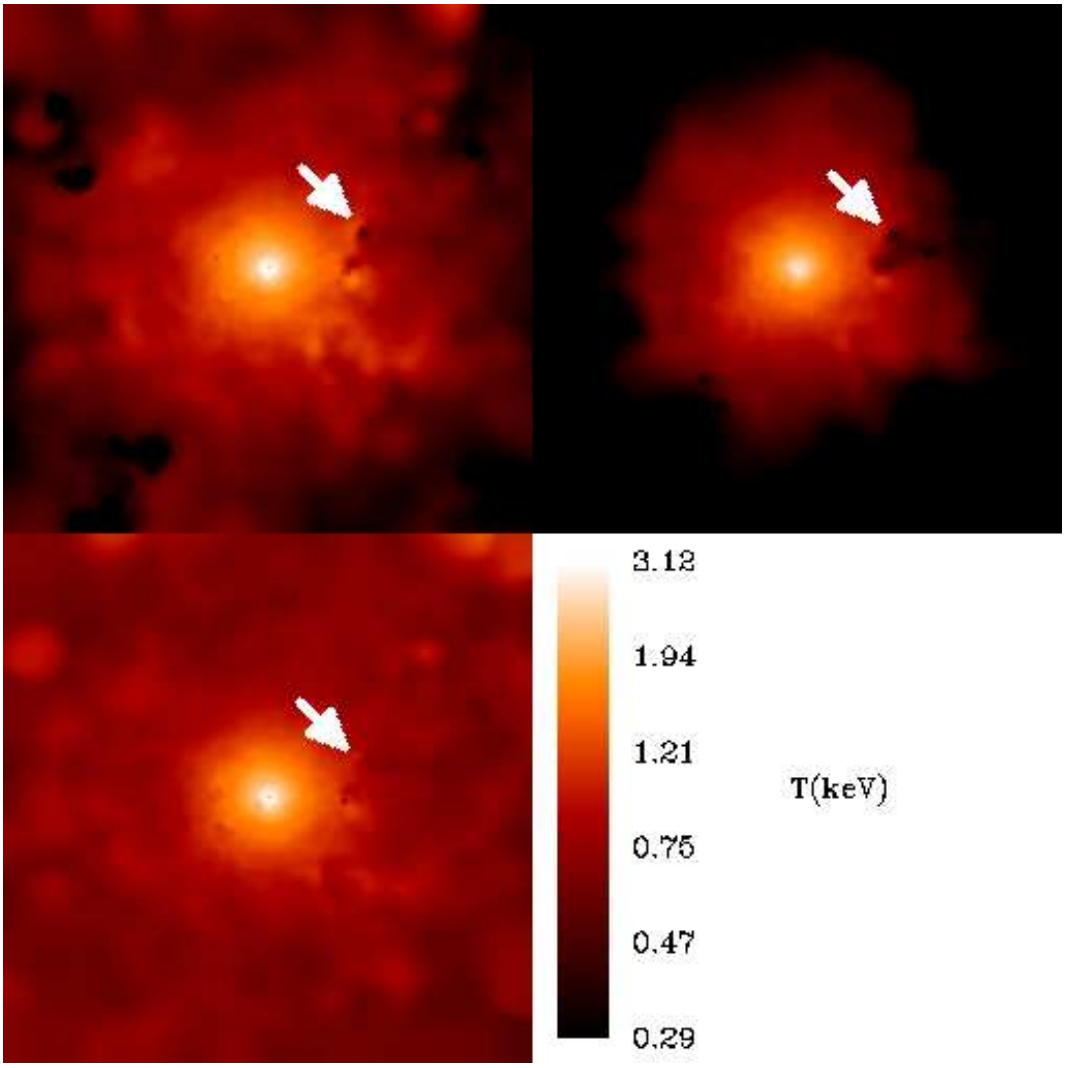


**Figure 3.8.** Maps of the emission-weighted (top left), mass-weighted (top right) and spectroscopic-like (bottom left) temperature for the same cluster of Figure 3.6.

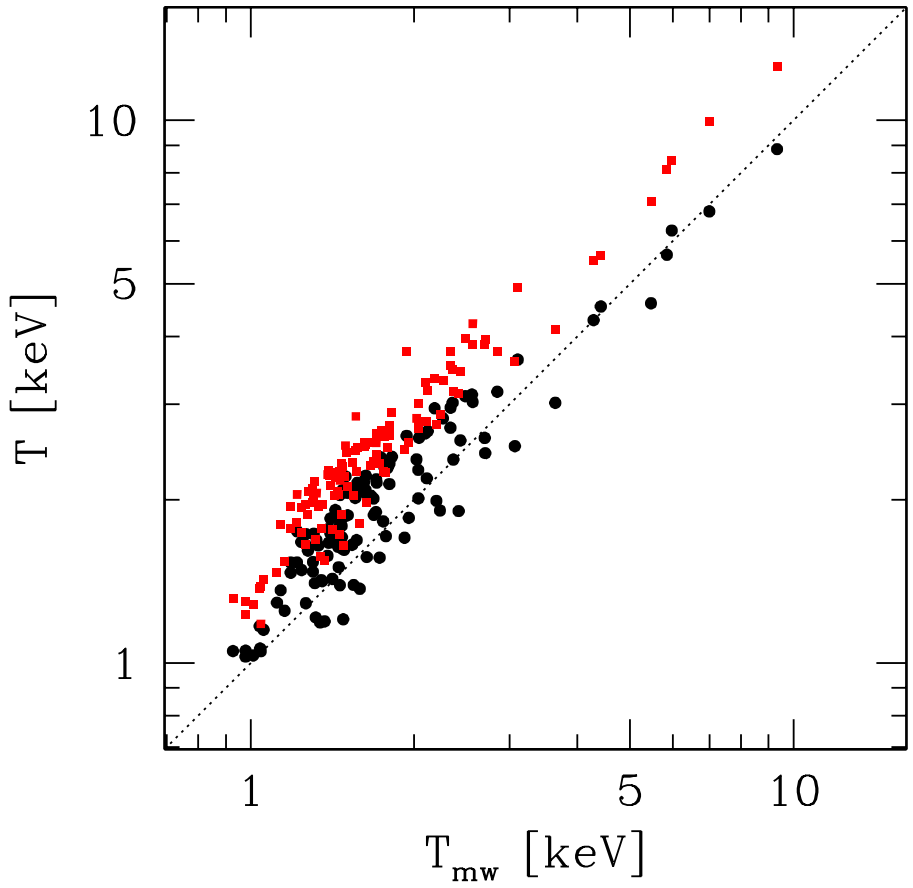


**Figure 3.9.** Comparison between different temperature definitions for the same cluster, i.e. $T_{\rm sl}$ and $T_{\rm ew}$ vs $T_{\rm mw}$. Red squares and black circles represent $T_{\rm ew}$, $T_{\rm sl}$ and $T_{\rm mw}$ respectively. The dotted line represents the one–to–one relation. All quantities are computed within the virial radius.

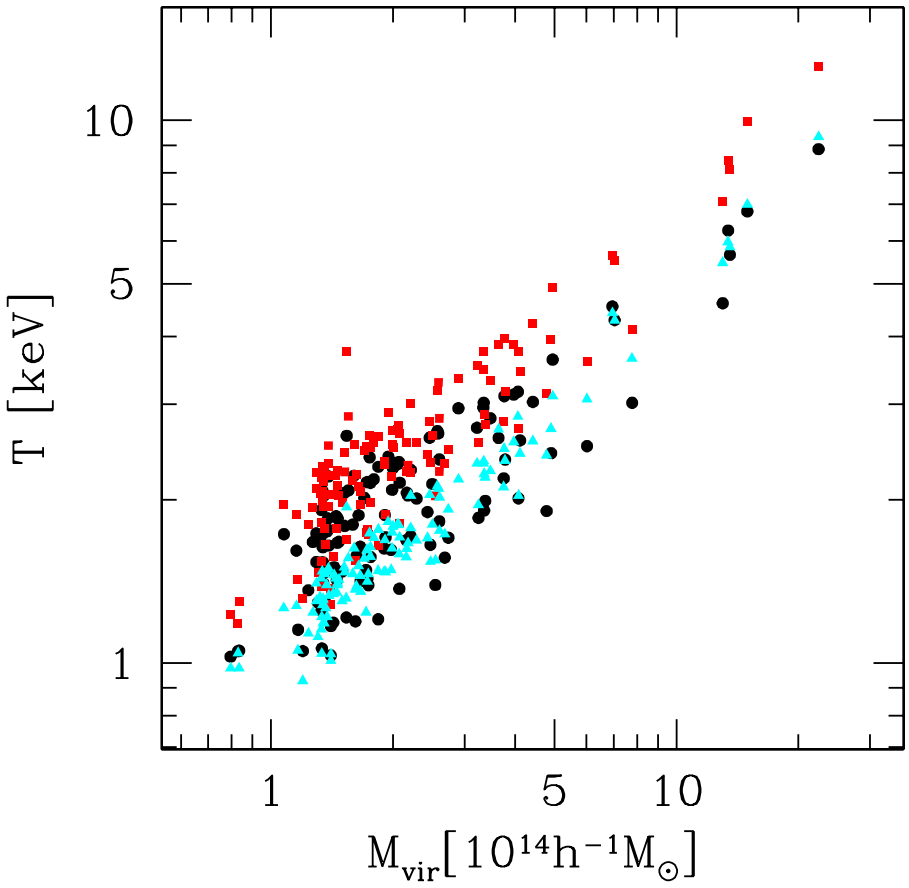


**Figure 3.10.** Relation between the virial mass of the cluster and its mean temperature, computed following the three definitions. Red squares, black circles and cyan triangles represent $T_{\rm ew}$, $T_{\rm sl}$ and $T_{\rm mw}$ respectively. All quantities are computed within the virial radius.

to the square of the gas density, then it is expected that the spectroscopic temperature, based on the numer of emitted photons, is determined more by regions at higher density than by those at lower density.

However, Mathiesen & Evrard (2001) were the first to show that the emission–weighted temperature does not necessarily represent an accurate approximation to the spectroscopic temperature. Mazzotta et al. (2004) have further motivated and quantified this difference, connecting it to a thermally complex structure of the ICM. These authors suggested an approximate expression for the spectroscopic temperature, the *spectroscopic–like temperature*:

$$T_{\rm sl} = \frac{\sum_i n_{e,i}^2 T_i^{a-1/2}}{\sum_i n_{e,i}^2 T_i^{a-3/2}} \,, \tag{3.16}$$

where $a$ is a fitting parameter. Mazzotta et al. (2004) have shown that eq.(3.16) with $a = 0.75$ closely reproduces the spectroscopic temperature of clusters at least as hot as $2 - 3$ keV, with a few per cent accuracy, after excluding all the gas particles colder than 0.5 keV from the sums in eq.(3.16). More recently, Vikhlinin (2006) has generalized the above expression for $T_{\rm sl}$ to include the cases of lower temperatures and arbitrary ICM metallicity.

In Figure 3.8 are the maps of the emission-weighted, mass-weighted and spectroscopic-like temperature for the same cluster of Figure 3.6, which highlights the effects of using different definitions when computing the projected temperature. Generally $T_{\rm ew}$ overestimates the gas temperature, since it mostly weights the central regions of the cluster, which are characterized by a higher temperature, as highlighted by the steep negative temperature profiles in the core regions. Instead, $T_{\rm sl}$ is generally biased toward the colder thermal components, which dominate the spectrum. Another important difference among them is capability of detecting steep temperature gradients, as those related to shock fronts. In the maps one can see two small merging structures (see the arrow in the figure). The temperature jump is clearly visible in the $T_{\rm ew}$ map, still present in the $T_{\rm mw}$ map, but it almost disappears in the $T_{\rm sl}$ map. This may explain why shock fronts are common features in simulations of galaxy clusters, while they have been clearly observed only in very few cases of extremely strong merging events.

In the figures 3.9 and 3.10 we show the relations between these temperature definitions and the mass-weighted temperature and the virial mass, respectively. Both the $T_{\rm ew}$ and the $T_{\rm sl}$ are generally larger than the $T_{\rm mw}$. As for the relation with the mass, the $T_{\rm ew}$ shows a larger normalization than $T_{\rm sl}$, by about $20 - 30\%$. This difference has important implications when this relation is used for cosmology studies; in fact Rasia et al. (2005) showed that this turns out into a 15% difference in the inferred $\sigma_8$. Also the scatter is quite different when using these three temperature definitions. As expected, $T_{\rm mw}$ has a very tight relation with mass, since it is directly proportional to the total thermal content of the cluster. Also $T_{\rm ew}$ has a low scatter, however one may notice some deviations mainly due to large substructures. Finally, $T_{\rm sl}$ is highly sensitive to the presence of cold clumps, hence it shows a larger scatter compared to the other two.

# Chapter 4

# The angular diameter distance measurement

For almost three decades it has been recognized that the combination of X–ray and tSZ observations of galaxy clusters provides a direct measurement of the cosmic distance scale, under the assumption of spherical symmetry for the intra–cluster gas distribution (e.g. Gunn, 1978; Silk & White, 1978; Cavaliere et al., 1979; Birkinshaw, 1979). The method is based on the different dependence on the electron number density, $n_e$, of the X–ray emissivity ($\propto n_e^2 T_e^{1/2}$ for thermal bremsstrahlung; here $T_e$ is the electron temperature) and of the tSZ signal ($\propto n_e T_e$).

Due to the crucial role played by the assumption of spherical symmetry, a great deal of efforts have been spent either to select individual clusters having very relaxed and regular morphology (e.g. Holzapfel et al., 1997; Hughes & Birkinshaw, 1998; Grainge et al., 2002; Bonamente et al., 2004), or to build suitable cluster samples over which averaging out the uncertainties due to intrinsic cluster ellipticity (e.g. Mason et al., 2001; Reese et al., 2002; Udomprasert et al., 2004; Jones et al., 2005). These analyses have provided estimates of the Hubble constant, $H_0$, which are generally consistent with those obtained from the Cepheid distance scale (e.g. Freedman et al., 2001) or inferred from the spectrum of the CMB anisotropies (e.g. Spergel et al., 2003), although with fairly large uncertainties. Although the dominant source of uncertainty is probably represented by the contamination of the tSZ signal by the CMB and point–sources (e.g. Udomprasert et al., 2004), significant errors are also associated to cluster asphericity, clumpy gas distribution and incorrect modeling of the thermal structure of the intra–cluster medium (ICM).

So far, the limited number of high–redshift clusters with both tSZ and X–ray observations, with their relatively large uncertainties, made the calibration of the cosmic distance scale mostly sensitive to the value of $H_0$, while no significant constraints have been placed on the values of the matter density parameter $\Omega_m$ and the cosmological constant. In the coming years, ongoing X–ray (e.g., Mullis et al., 2005), optical (e.g., Gladders & Yee, 2005), and planned or just started tSZ surveys (see Section 2.3.2). promise to largely increase the number of observed clusters out to $z \sim 1.5$. This may well open the possibility to use tSZ/X–ray cluster observations to place constraints on the dark matter and dark energy content of the Universe through the redshift dependence of the angular diameter distance (Molnar et al., 2002). This highlights the paramount importance of having observational uncertainties and potential biases under control.

In this respect, numerical hydrodynamical simulations of galaxy clusters may offer an

important test–bed where to quantify observational biases and keep the corresponding uncertainties under control. For instance, eliminating $n_e$ from the tSZ and X–ray signal leaves a sensitive dependence of the angular–diameter distance, $D_A$, on the electron temperature (see §2). On the other hand, temperature measurements of the ICM have been so far entirely based on fitting the X–ray spectrum to a suitable plasma model. How close is the resulting spectral temperature to the electron temperature depends on the complexity of the thermal structure of the ICM (e.g., Mazzotta et al., 2004). Hydrodynamical simulations of clusters offer a natural way to quantify the bias introduced by replacing the electron temperature with the X–ray temperature.

Furthermore, the standard assumption in the tSZ/X–ray calibration of the cosmic distance scale is that of the isothermal ICM, while X–ray observations of clusters clearly show the presence of significant temperature gradients (e.g. Markevitch et al., 1998; De Grandi & Molendi, 2002; Vikhlinin et al., 2005). To overcome this problem, several authors estimate the bias introduced by the isothermal approximation, finding that the distance can be biased by $\lesssim 20$ per cent (e.g. Birkinshaw & Hughes, 1994; Udomprasert et al., 2004; Holzapfel et al., 1997). Simulations of galaxy clusters naturally produce temperature gradients that, at least at large radii, are close to the observed ones (e.g., Loken et al., 2002; Borgani et al., 2004; Kay et al., 2007; Nagai et al., 2007). Therefore, simulations can be used to quantify the bias introduced by the assumption of isothermal gas.

Finally, using a representative set of galaxy clusters in a cosmological framework allows one to trace the distribution of ellipticity and, therefore, to calibrate the corresponding scatter in the measurement of the distance scale. Nowadays, cosmological hydrodynamical codes have reached a high enough efficiency, in terms of both achievable resolution and description of the gas physics, to provide a realistic description of the processes of formation and evolution of galaxy clusters (e.g. Borgani et al., 2004; Kravtsov et al., 2005). For instance, Kazantzidis et al. (2004) found that halos in hydrodynamical simulations including cooling are significantly more spherical than in non–radiative simulations. Since the assumption of sphericity is at the basis of the X–ray/tSZ method to estimate $D_A$, this highlights the relevance of properly modeling the physics of the ICM for a precise calibration of the cosmic distance scale.

The purpose of the analysis presented in this Chapter is to understand the impact of the above discussed systematics on the calibrations of the cosmic distance scale from the combination of tSZ and X–ray observations, by analyzing an extended set of hydrodynamical simulations of galaxy clusters. These simulations have been performed using the TREE+SPH GADGET–2 code (Springel et al., 2001; Springel, 2005b), for a concordance $\Lambda$CDM model, and include the processes of radiative cooling, star formation and supernova feedback. The set of simulated clusters contains more than 100 objects having virial masses in the range $(2-20)\times 10^{14}h^{-1}M_{\odot}$.

The plan of the Chapter is as follows. In Section 4.1 we present the polytropic $\beta$–model which we adopt. In Section 4.2 we review the method to estimate the angular–diameter distance from X–ray and tSZ cluster observations. We present our results in Section 4.3, where we show the results on the accuracy of the measurement of $D_A$. We discuss and summarize our main results in Section 4.4.

## 4.1 The polytropic $\beta$–model

A common procedure adopted to extract $D_A$ from the combination of eqs. (2.6) and (2.3) is based on modeling the electron density profile with the $\beta$-model (see Section 2.3.1):

$$n_e(r) = n_{e0}\left[1+\left(\frac{r}{r_c}\right)^2\right]^{-3\beta/2}, \tag{4.1}$$

As for the temperature structure of the ICM, a number of analyses of X–ray data independently show that galaxy clusters are far from being isothermal. Significant negative gradients characterize the temperature profiles of galaxy clusters, at least on scales $R \gtrsim 0.2R_{200}$ (e.g. Markevitch et al., 1998; De Grandi & Molendi, 2002; Pratt & Arnaud, 2002; Piffaretti et al., 2005; Vikhlinin et al., 2005; Pratt et al., 2007), with positive gradients associated only to the innermost cooling regions (e.g. Allen et al., 2001; Snowden et al., 2007). The dynamic range covered by the tSZ signal extends on scales which are relatively larger than those sampled by the X–ray emission. For this reason, one may expect that a systematic effect is introduced by assuming the ICM to be isothermal when combining X–ray and tSZ observations. Since the tSZ signal has a stronger dependence on the ICM temperature than the X–ray one, the effect of assuming an isothermal ICM, in a regime where the temperature is decreasing, may lead to predict $y(\theta)$–profiles which are shallower than the intrinsic ones (see figure 4.1).

In order to account for the presence of temperature gradients, we introduce a polytropic equation of state, $p \propto \rho^\gamma$, which relates the gas pressure $p$ to the density $\rho$, where $\gamma$ is the polytropic index ($\gamma = 1$ for isothermal gas). The three-dimensional temperature profile is thus

$$T_e(r) = T_{e0}\left(\frac{n_e}{n_{e0}}\right)^{\gamma-1} = T_{e0}\left[1+\left(\frac{r}{r_c}\right)^2\right]^{-3\beta(\gamma-1)/2}, \tag{4.2}$$

where $T_{e0}$ is the temperature at the cluster center.

## 4.2 $D_A$ from combined X-ray and tSZ observations

Using the above expression for the temperature profile in the definition of the Comptonization parameter of eq. (2.6) gives

$$y(\theta) = y_0\left[1+\left(\frac{\theta}{\theta_c}\right)^2\right]^{(1-3\beta\gamma)/2}, \tag{4.3}$$

where the Comptonization parameter at the cluster center is

$$y_0 = D_A n_{e0}\theta_c\sigma_T\frac{k_B T_{e0}}{m_e c^2}\sqrt{\pi}\frac{\Gamma(3\beta\gamma/2-1/2)}{\Gamma(3\beta\gamma/2)}, \tag{4.4}$$

where $k_B$ is the Boltzmann constant, $\sigma_T$ is the Thomson cross section, $m_e$ is the mass of the electron, $c$ is the speed of light.

Similarly, we obtain the X–ray surface brightness profile

$$S_X(\theta) = S_{X0}\left[1+\left(\frac{\theta}{\theta_c}\right)^2\right]^{\{1-6\beta[(\gamma+3)/4]\}/2}, \tag{4.5}$$

where the central surface brightness is

$$S_{X0} = D_A n_{e0}^2 \theta_c \frac{\mu_e/\mu_H \Lambda_{eH}(T_{e0})}{4\sqrt{\pi}(1+z)^4} \frac{\Gamma(3\beta[(\gamma+3)/4]-1/2)}{\Gamma(3\beta[(\gamma+3)/4]}, \tag{4.6}$$

where $\mu_e$ and $\mu_H$ are the mean molecular weights of electrons and protons, respectively, and $\Lambda_{eH}$ is the X–ray cooling function normalized to $n_e n_H$.

In deriving the above equation, the dependence of the cooling function on $T_e$ is assumed to be a power law, $T^\alpha$, with index $\alpha = 0.5$. This is valid in the case of pure bremsstrahlung emission and represents a good approximation in the case of bolometric emissivity. However, our emissivity maps are build in the soft band ([0.5-2] keV). In this energy range the cooling function is significantly flatter (e.g. Ettori, 2000), owing to different reasons in different temperature regimes. For relatively cool systems ($T \lesssim 2$ keV) the flattening is due to the contribution of metal emission lines. At higher temperatures instead the restricted energy window (compared to the bolometric one) does not encompasses the cut–off energy of the radiation spectrum. So, an increase in the temperature of the emitting gas, which shifts the cut–off to higher energies, will substantially increase the emissivity in the bolometric band, but will have a very little effect in the soft one. In order to test the effect of approximating the cooling function with a bremsstrahlung shape, we repeated our analysis also in the bolometric band and found variations in the final distance estimates by $\lesssim 10\%$.

Finally, by eliminating $n_{e0}$ from eqs.(4.4) and (4.6), we obtain the angular–diameter distance

$$\begin{aligned} D_A &= \frac{y_0^2}{S_{X0}} \left[\frac{m_e c^2}{k_B T_{e0}}\right]^2 \frac{\Lambda_{eH}(T_{e0})\mu_e/\mu_H}{4\pi^{3/2}\sigma_T^2(1+z)^4} \frac{1}{\theta_c} \\ &\times \left[\frac{\Gamma(3\beta\gamma/2)}{\Gamma(3\beta/2-1/2)}\right]^2 \frac{\Gamma(3\beta[(\gamma+3)/4]-1/2)}{\Gamma(3\beta[(\gamma+3)/4])}\,. \end{aligned} \tag{4.7}$$

For $\gamma = 1$, the above expression reduces to that usually adopted in observational analyses based on combining X–ray and tSZ cluster observations (e.g. Reese et al., 2002; Udomprasert et al., 2004; Bonamente et al., 2004), which relies on the assumption of isothermal gas.

It is worth reminding here that, while simulations are rather successful in reproducing the negative temperature gradient in the outer cluster regions (e.g. Evrard et al., 1996; Eke et al., 1998; Loken et al., 2002; Rasia et al., 2004), they generally produce too steep profiles in the central cluster regions, especially when radiative cooling is included (e.g. Katz & White, 1993; Tornatore et al., 2003; Valdarnini, 2003; Borgani et al., 2004). Since observed clusters are characterized by a core region which is closer to isothermality than the simulated ones, we expect that the effect of using a polytropic temperature profile when analyzing simulated clusters is larger than the actual effect taking place in real clusters.

In the following, besides using the electron temperature, we also perform our analysis by relying on the temperature proxies of eqs.(3.15) and (3.16). Therefore, comparing the results based on the electron temperature and on the spectroscopic–like temperature provides a check of the bias introduced by using the X–ray temperature in the estimate of $D_A$, a bias possibly present also in the analysis of real data. Furthermore, the comparison between emission–weighted and spectroscopic–like temperature provides a hint on the bias introduced in the simulation analysis when using an inaccurate proxy to the X–ray

temperature. It is worth reminding here that, due to the finite time for electron–ion thermalization, the corresponding electron and ion temperature may differ, for instance as a consequence of continuous shocks (e.g., Yoshida et al., 2005). A sizable difference among these two temperatures may induce a bias in the estimate of the distance scale.

Except for using different definitions of temperature, we do not investigate the effect of a realistic observational setup for the detection of both the tSZ and X–ray signals. Besides the statistical errors associated to time–limited exposures, we also neglect the effects of systematics (e.g., instrumental noise, foreground and background contribution from contaminants, etc.). A detailed analysis of the contaminations in the tSZ signal has been provided by Knox et al. (2004) and by Aghanim et al. (2004). A comprehensive description of the instrumental effects on the recovery of X–ray observables, calibrated on hydrodynamical simulations, has been provided by Gardini et al. (2004) (see also Rasia et al., 2006b). In this sense, our analysis will be based on ideal maps, which are free of any noise. We defer to a future analysis the inclusion of the errors associated to realistic X–ray and tSZ observational setups.

## 4.3 Results

In this section we present our results on the reliability of the usual procedure to recover the angular–diameter distance from the combination of the tSZ and X–ray emission of clusters, by using both the isothermal and a more general polytropic equation of state for the ICM. The set of simulated clusters which we analyze is described in Section 3.3.

### 4.3.1 Results from the isothermal model

Unlike X–ray observations, current observations of the tSZ effect in clusters do not allow to perform any spatially resolved analysis. For this reason, the commonly adopted procedure is to determine the parameters $\theta_c$ and $\beta$, which determine the $\beta$–model density profile, from the X-ray imaging alone, along with the normalization $S_{X0}$. The tSZ profile is then used to obtain the central value of the Comptonization parameter, $y_0$, by using the $\beta$-model parameters as determined from the X-ray profile. By following this procedure, we fitted all the profiles out to $R_{500}$, which is defined as the radius encompassing an average density of 500 times the critical cosmic density. We point out that $R_{500}$ corresponds to the typical outermost radius where X-ray observations provide surface brightness and temperature profiles. We exclude from the analysis the central regions of the clusters, within $1/20 R_{\rm vir}$, which are strongly affected by gas cooling and are close to the numerical resolution of the simulations.

In Figure 4.1 we show the profiles of the X–ray surface brightness and Compton–$y$ for the example cluster of figure 3.6, along with the best–fitting $\beta$–model for the isothermal case. For this relaxed cluster, the $\beta$–model provides a rather good fit to the X-ray profile. Only the central point, which is anyway excluded from the fit, is higher than the $\beta$–model extrapolation, as a consequence of the high–density gas residing in the cluster cooling region. The resulting values of the fitting parameters for this cluster are $\beta = 0.835$ and $r_c/R_{500} = 0.196$. Fitting the $y(R)$ profile with eq. (4.3), after setting $\beta = 0.835$ and $\gamma = 1$, leads to an underestimate of $y_0$. In fact, the resulting Compton–$y$ profile is significantly shallower than measured (Figure 4.1). This result follows from neglecting the presence of negative temperature gradients. Consequently we tend to underestimate $D_A$, because $D_A \propto y_0^2$ (seeeq. 4.7). In this particular case we underestimate $D_A$ by 56 per cent.

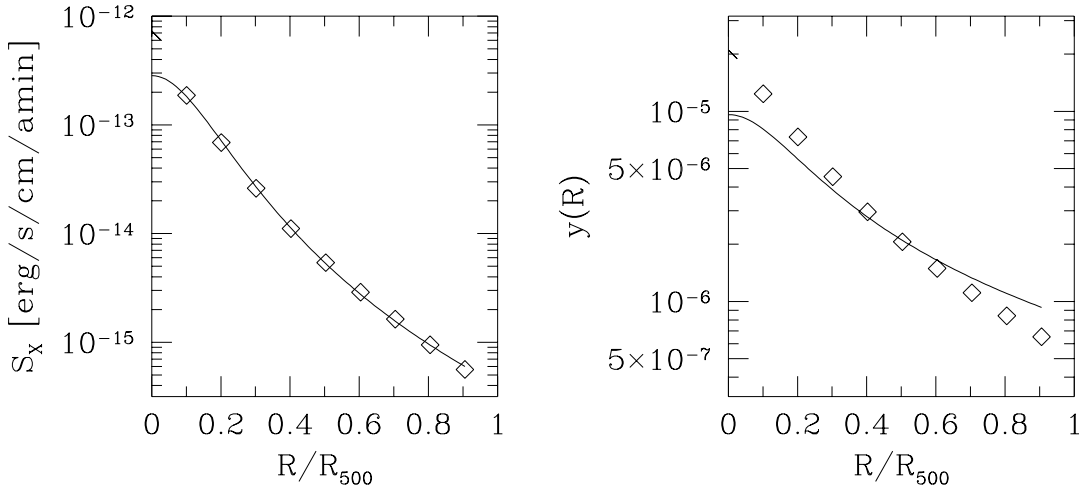


**Figure 4.1.** The projected radial profiles of $X$–ray surface brightness (left panel) and of Compton–$y$ parameter (right panel) for the cluster shown in figure 3.6. Symbols are for the results of the simulation analysis while the solid curves are the predictions of the isothermal $\beta$–model.

This result for one particular cluster is confirmed by the distribution shown in the left panel of Figure 4.2 (see also Table 4.1). In this figure we report the distribution of the ratios $D_A^{\rm rec}/D_A^{\rm true}$ between the recovered and the true values of the angular–size distance. Such results clearly demonstrate that the angular–size distance is biased low, on average, by more than a factor two, as a consequence of the underestimate of $y_0$ induced by the assumption of an isothermal ICM. In order to verify a possible temperature dependence of the $D_A$ distribution, in the left panel of figure 4.2 we also show the results for the clusters with $T_{sl}$ in the range 2.5–5 keV and for those hotter than 5 keV. While the latter are too few to allow any meaningful conclusion, the clusters at intermediate temperature have a distribution which is statistically consistent with that of the whole sample. This indicates the absence of any obvious trend of our results with the cluster size. The results reported in this figure have been obtained by using the electron–weighted temperature estimate for the simulated clusters. If we had used the emission–weighted temperature, we would have obtained an even stronger bias (eq. 4.7), because this temperature generally overestimates the electron temperature.

Including dynamically disturbed clusters does not significantly affect the average value of the recovered $D_A$. However, the resulting distribution is clearly asymmetric and presents a large tail towards low $D_A$ values. In fact, eqs. (2.6) and (2.3) show that that $D_A \propto \langle n_e\rangle^2/\langle n_e^2\rangle$. Therefore, the presence of clumps in the gas distribution produces an underestimate of $D_A$ by this factor with respect to a completely smooth gas distribution. By looking at the distributions of the $\beta$ and $r_c$ (central and left panels of figure 4.2), unrelaxed structures tend to have rather flat gas density profiles. Fitting them with a $\beta$–model forces the slope to be very small, with a preference for the core radius to be consistent with zero. For instance, the cluster shown in figure 3.7 requires $\beta = 0.52$ and $r_c/R_{500} = 0.03$, while its estimate of the angular–size distance gives $D_A^{\rm rec}/D_A^{\rm true} = 0.17$.

As a word of caution in interpreting such results, we emphasize that this bias in the $D_A$ estimate, due to the isothermal gas assumption, is likely to represent an overestimate of the actual effect in real cluster observations for at least two reasons. First, radiative

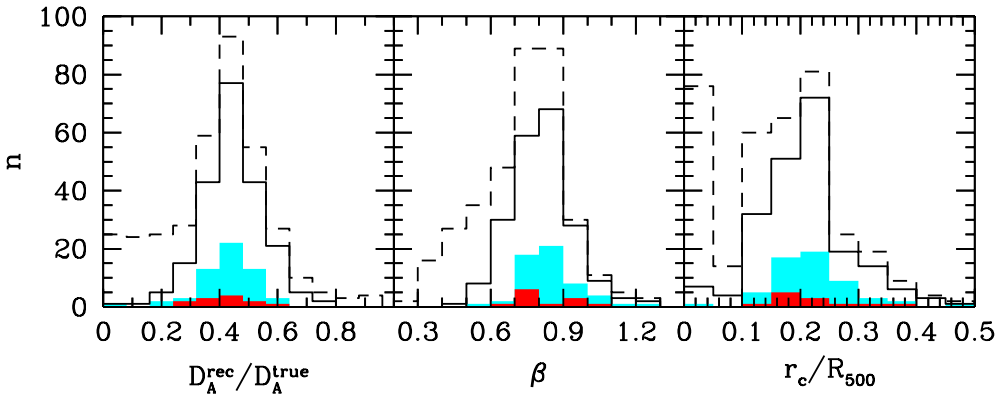


**Figure 4.2.** The distribution of the values of $D_A^{rec}/D_A^{true}$ (left panel), of $\beta$ (central panel) and of $r_c$ (in units of $R_{500}$; right panel). The dashed and the solid lines are for the whole sample and for the subset of clusters classified as regular, respectively. Also shown with the light and dark gray areas are the corresponding distributions for the subset of the clusters with $2.5 < T_{sl}(keV) < 5$ and $T_{sl}(keV) > 5$, respectively. The distribution of $D_A^{rec}/D_A^{true}$ is obtained by using the electron–weighted temperatures of the simulated clusters in eq. (4.7).

simulations of clusters are known to produce temperature gradients that, in the central regions, are steeper than observed (see Section 3.3.1). As a consequence, simulated clusters exaggerate the departure from isothermality. Second, the $\beta$–model fitting to the Compton–$y$ profile has been performed by assigning equal weight to all radial bins, with the more external regions bringing down the overall normalization of the model profile. In a realistic observational setup, the signal from central cluster regions should have a relatively larger weight, thus reducing the bias in the recovered $y_0$. Addressing appropriately this issue would require implementing detailed mock tSZ observations of our simulated clusters, a task that we defer to a future analyses. Even keeping in mind these warnings, it is clear that deviations from isothermality must be taken into account for a precise calibration of the cosmic distance scale from the combination of X–ray and tSZ observations of galaxy clusters (e.g., Udomprasert et al., 2004).

### 4.3.2 Results from the polytropic fit

In the case of a more general polytropic equation of state, the parameters $\beta$ and $\gamma$ are calculated by requiring the model to reproduce at the same time both the X-ray surface brightness and the temperature profiles. After obtaining the core radius $r_c$ and the normalization $S_{X0}$ from the X-ray profile, and $T_0$ from the temperature profile, we combine the two exponents in eqs. (4.5) and (4.2) to derive both $\beta$ and $\gamma$, with $y_0$ finally obtained from the tSZ profile.

In Figure 4.3 we show the temperature and Compton–$y$ profiles for our example cluster, along with the best–fitting predictions of the polytropic $\beta$–model, for the three different definitions of temperature. The polytropic equation of state provides a reasonable approximation to all temperature profiles and, unlike the isothermal case, allows us to correctly predict also the Compton–$y$ profile. The corresponding distributions of $\beta$ and $\gamma$ are shown in Figure 4.4 (we do not report the distribution of $r_c$, since it is, by definition,

| | All clusters | Regular clusters |
|---|---|---|
| Isothermal | $0.41 \pm 0.27$ | $0.44 \pm 0.11$ |
| | $0.42^{+0.14}_{-0.22}$ | $0.45^{+0.10}_{-0.10}$ |
| Polytropic | | |
| $T_{ew}$ | $0.76 \pm 0.74$ | $0.80 \pm 0.15$ |
| | $0.78^{+0.19}_{-0.37}$ | $0.81^{+0.14}_{-0.17}$ |
| $T_e$ | $0.95 \pm 0.49$ | $1.04 \pm 0.22$ |
| | $0.98^{+0.31}_{-0.47}$ | $1.05^{+0.21}_{-0.26}$ |
| $T_{sl}$ | $0.99 \pm 0.26$ | $0.97 \pm 0.18$ |
| | $0.92^{+0.25}_{-0.46}$ | $0.98^{+0.18}_{-0.20}$ |

**Table 4.1.** The values of the accuracy in recovering the angular–diameter distance, $D_A^{\rm rec}/D_A^{\rm true}$, using both the isothermal and the polytropic model, and using the emission–weighted, the electron and the spectroscopic–like definitions of temperature. For each of them, the first line reports the mean and standard deviation, the second the median and the limiting values encompassing 68% of the data.

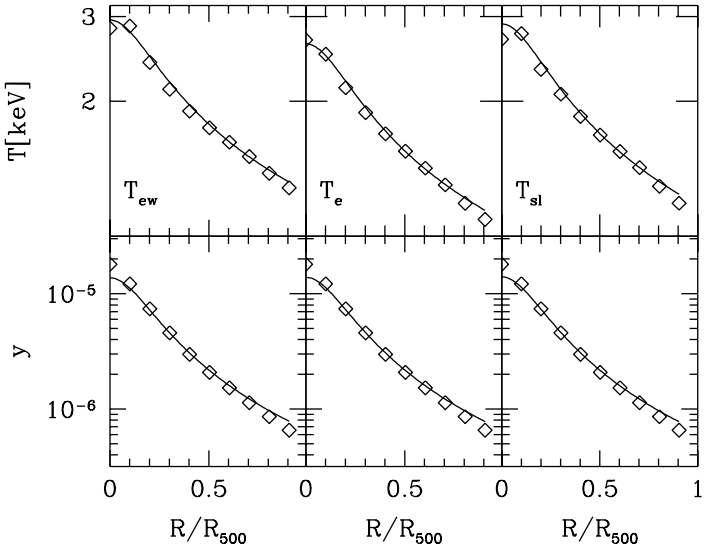


**Figure 4.3.** Profiles of temperature (upper panels) and of Compton–$y$ parameter (lower panels) for the cluster of figure 3.6. Left, central and right panels corresponds to using emission–weighted, electron and spectroscopic–like temperature, respectively. Open symbols are for the profiles from the simulation analysis, while the curves are the best–fitting polytropic $\beta$–model.

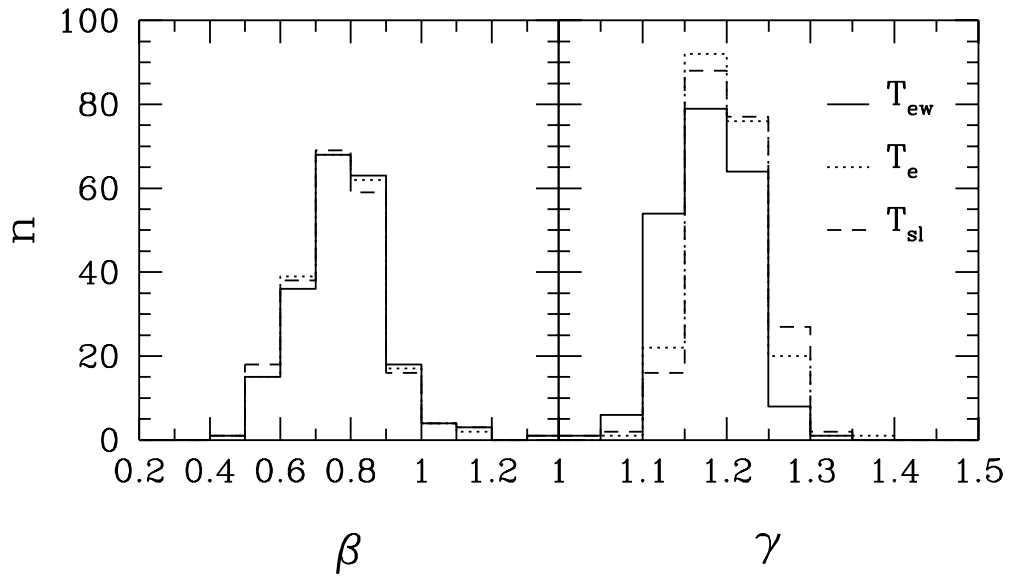


**Figure 4.4.** Distributions of the values of $\beta$ (left panel) and $\gamma$ (right panel), using emission–weighted (solid line), electron (dotted line) and spectroscopic–like (dashed lines) temperatures, respectively, as obtained for the whole sample of 121 clusters.

identical to that of the isothermal model). For both quantities, the effect of using different definitions of temperature is rather small. As expected, using a polytropic temperature profile implies only a modest decrease of the $\beta$ values, because of the weak temperature dependence of the cooling function. All the three distributions of $\gamma$ have an average value $\simeq 1.2$, similar to observational estimates (e.g. De Grandi & Molendi, 2002). Moreover, the scatter in this distribution is so small to make the isothermal ICM an extremely unlikely event.

The results obtained for $D_A$ are shown in Figure 4.5, and also reported in Table 4.1, using emission–weighted, electron and spectroscopic–like temperatures. Quite interestingly, the improved quality of the fit to the profile of the Compton–$y$ parameter now makes the distribution peak at a value much closer to the correct $D_A$, independently of whether we use the whole sample or the subsample of relaxed clusters.

The angular–diameter distance is correctly recovered when using either the electron or the spectroscopic–like temperature with deviations which are always $\lesssim 5$ per cent, on average. This is a rather encouraging result, since it indicates that any bias, induced by using the temperature as measured from X–ray observations, is in fact rather small. Using instead the emission–weighted temperature turns into a systematic underestimate of $D_A$ by about 20 per cent, as a consequence of the fact that it is systematically higher than the electron temperature. For all the definitions of temperature we find a significant intrinsic scatter, of about 20 per cent on average, in spite of our selection of regular objects.

The fact that the scatter is stable against the definition of temperature implies that it is almost insensitive to the thermal structure of the ICM and, therefore, to the details of the ICM physics. This scatter instead quantifies the effect of departure from spherical symmetry of the ICM spatial distribution. In fact, the above scatter increases to about

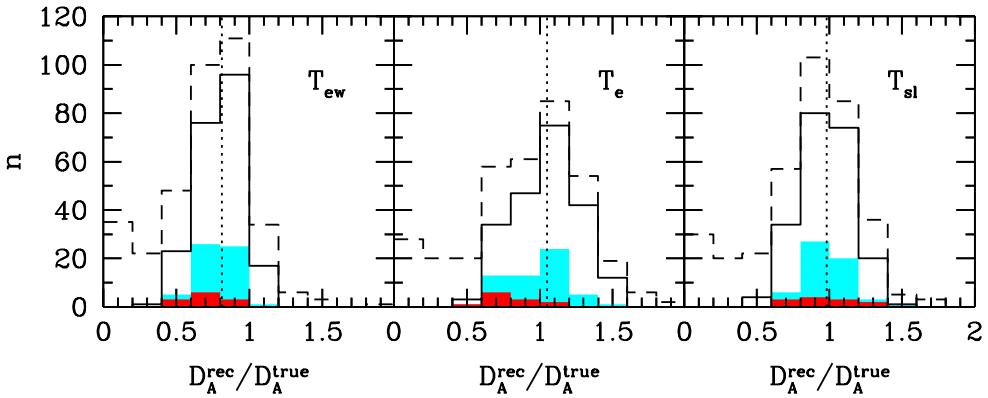


**Figure 4.5.** Distributions of the accuracy in recovering the correct value of the angular–diameter distance, $D_A^{\rm rec}/D_A^{\rm true}$, using the polytropic $\beta$–model for the whole sample (dashed line) and for the subset of regular clusters (solid), using emission–weighted (left panel), electron (central panel) and spectroscopic–like (right panel) temperature. Also shown with the light and dark gray areas are the corresponding distributions for the subset of the clusters with $2.5 < T_{sl}(keV) < 5$ and $T_{sl}(keV) > 5$, respectively. The vertical dotted line in each histogram represents the mean value of the distribution for the sample of regular clusters.

50 per cent, if no preselection of regular clusters is implemented (Table 4.1). Quite remarkably, the intrinsic scatter calibrated with our simulations is rather close to the 17 per cent value, reported by Hughes & Birkinshaw (1998), for the uncertainty induced by the intrinsic cluster ellipticity.

Similarly to the case of the isothermal fit, we note from figure 4.5 that the low–$D_A$ tails of the distributions are contaminated by irregular clusters, for which $D_A$ is very badly recovered. For instance, for the irregular cluster shown in figure 3.7 we find $D_A^{\rm rec}/D_A^{\rm true} = 0.30$ when using the electron temperature. Similarly to the case of the isothermal fit, also in this case the distribution of the hot clusters is consistent with that of the regular cluster subset.

### 4.3.3 Implications for cosmological parameters

The precision in the recovery of the angular–size distance when using the polytropic model indicates that this method is potentially accurate to estimate cosmological parameters. In order to test this we create a simple mock catalog of clusters, which is obtained by distributing 2/3 of our regular clusters uniformly in redshift in the range $0.1 < z < 0.5$, while the remaining 1/3 is distributed uniformly in the range $0.5 < z < 1.5$. Recall that each simulated cluster is observed along three orthogonal lines of sight and the redshift of each projection is chosen randomly. Figure 4.6 shows the resulting distribution of clusters in the $D_A$–$z$ plane. We remind here that our simulated clusters have been identified at $z = 0$. Therefore, our procedure to distribute them at $z > 0$ neglects the effect of their possible morphological evolution. We have been forced to this choice by the small volume of our simulation box, which implies the rapid disappearance of reasonably massive clusters inside the high–redshift simulation box.

For the estimate of the Hubble constant, $H_0$, we limit the analysis to the 66 clusters

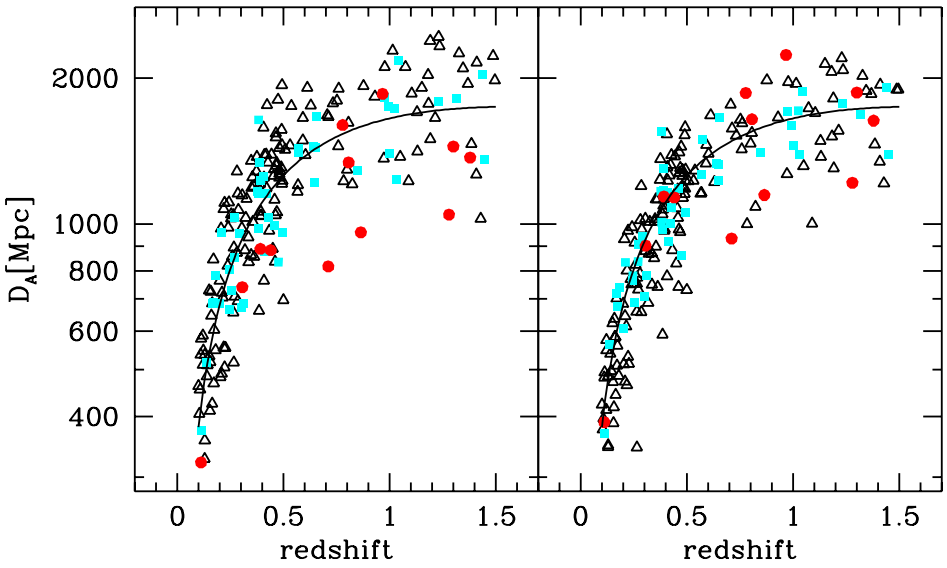


**Figure 4.6.** Estimated $D_A$ vs. $z$ for the regular cluster sample: 2/3 of this sample was uniformly distributed in the redshift range $0.1 < z < 0.5$ and 1/3 in the range $0.5 < z < 1.5$. On the left (right) panel is shown the angular–size distance obtained using the electron (spectroscopic-like) temperature and the polytropic gas model. The symbols indicate clusters spectroscopic temperature: $T_{sl}(keV) < 2.5$ (triangles), $2.5 < T_{sl}(keV) < 5$ (squares) and $T_{sl}(keV) > 5$ (circles). The solid line shows the $D_A$–$z$ relation for the $\Lambda$CDM cosmology assumed in the simulations.

at $z < 0.3$. Including high redshift objects would make the recovery of $H_0$ progressively more dependent on the knowledge of the underlying cosmology. When using the electron temperature, the distribution of the $H_0$ values has mean $H_0 = 70 \pm 2\,\mathrm{km\,s^{-1}Mpc^{-1}}$; when using the spectroscopic temperature this mean is $H_0 = 75 \pm 2\,\mathrm{km\,s^{-1}Mpc^{-1}}$. In both cases the uncertainties are the $1-\sigma$ standard deviations. These values are obtained by assuming the correct values of $\Omega_M$ and $\Omega_\Lambda$. When assuming the Einstein–de-Sitter model, we find $H_0$ biased low by 8 per cent.

As for the estimate of the matter density parameter $\Omega_m$, we fix the value of $H_0$ to its true value and assume flat geometry. In this case, we use the 73 clusters lying at $z > 0.5$. Estimating $\Omega_m$ as the average of the values yielded by each cluster would provide unreliable results; in fact, inaccurate values of $D_A$ can imply negative values of $\Omega_m$, which are clearly unphysical. Therefore, we compute the best–fitting value of $\Omega_m$ with a $\chi^2$–minimization procedure. To associate the uncertainty to the estimated $\Omega_m$, we resort to a bootstrap resampling procedure (e.g. §15.6 of Press et al. 1992). Each bootstrap sample is constructed by randomly selecting, with repetition, the objects from the original sample. Each time that a cluster is selected, its $D_A$ is perturbed with a Gaussian random shift with variance 20%, independently of redshift, to account for the "observational" uncertainties. The application of this procedure, when using the electron temperature, gives $\Omega_m = 0.29 \pm 0.05$; we obtain $\Omega_m = 0.36 \pm 0.06$, when using the spectroscopic–like temperature. The uncertainties are the $1-\sigma$ standard deviations computed with 100 bootstrap resamplings. The two temperature definitions provide two $\Omega_m$'s whose difference is consistent with the difference in the median values of $D_A$. Moreover, and

reassuringly, in both cases the central values are consistent with the true value of $\Omega_m$.

The small size of the errobars of the estimated $\Omega_m$'s should be clearly taken with caution for at least two reasons. First of all, we have assumed errors in $D_A$ to be 20 per cent, independently of redshift. High–quality tSZ and X–ray observations will eventually allow to bring statistical errors down to this level in the near future. Of course, systematic errors in tSZ observations, associated for instance to point–source contamination and CMB signal removal, are different in nature and more difficult to eliminate.

## 4.4 Conclusions

In this Chapter we have applied the method to calibrate the cosmic distance scale from the combination of X–ray and Sunyaev–Zeldovich (tSZ) observations to an extended set of hydrodynamical simulations of galaxy clusters. The simulations have been performed with the GADGET2 code, for a flat ΛCDM model with $\Omega_m = 0.3$, $h = 0.7$ and $\sigma_8 = 0.8$, and include the effect of cooling, star formation and supernova feedback. The aim of our analysis was to understand the possible biases introduced by the assumptions of isothermal gas and the X–ray temperature as a close proxy to the electron temperature, as usually done in the analysis of real clusters. Furthermore, the application of this method to a large set of simulated clusters allows us to quantify the intrinsic scatter associated with a cluster-by-cluster variation of their shapes.

Our main results can be summarized as follows.

- Neglecting the temperature gradients in the application of the $\beta$–model produces a significant underestimate of the central value of the Comptonization parameter, $y_0$. In turn, this introduces a severe bias in the estimate of the angular–size distance, $D_A$.

- Accounting for the presence of the temperature gradients with a polytropic $\beta$–model substantially reduces this bias to a few per cent level. While this result holds when using either the electron or the spectroscopic–like temperature, using the emission–weighted temperature gives a $\sim 20$ per cent underestimate of $D_A$.

- Cluster-by-cluster variations of the asphericity and of the degree of gas clumpiness cause an intrinsic dispersion of about $\sim 20$ per cent in the estimates of $D_A$. This dispersion significantly increases in case unrelaxed clusters are included in the analysis.

- The set of simulated clusters is used to generate a mock sample of clusters out to redshift $z = 1.5$. By assuming a 20 per cent precision in the estimate of $D_A$ for each cluster, we find that the correct value of $H_0$ is recovered with a statistical error of $2\,\mathrm{km\,s^{-1}}$ at $1\sigma$. Furthermore, assuming a prior for the Hubble constant and flat geometry, we find that also the matter density parameter can be estimated in an unbiased way with a statistical error of $\Delta\Omega_m = 0.05$.

It is worth reminding here that our results are based on the analysis of simulated X–ray and tSZ maps, which are ideal in a number of ways. First of all, they have been generated by projecting the signal contributed by the gas out to about six virial radii. A more rigorous approach would require projecting over the cosmological light cone, to properly account for the fore/background contamination. While projection effects ought to be

marginal for the X–ray maps, they may substantially affect the tSZ signal (e.g., White et al., 2002; Dolag et al., 2005). Furthermore, our noiseless maps need to be properly convolved with the "response function" of both X–ray and tSZ telescopes under realistic observing conditions. Neglecting the observational noise clearly leads to an underestimate of the uncertainties in the determination of the parameters defining gas density and temperature profiles. Accounting for such effects would definitely require passing our ideal maps through suitable tools to simulate X–ray (e.g., Gardini et al., 2004) and tSZ observations (e.g., Kneissl et al., 2001; Pierpaoli et al., 2005). Finally, the effect of neglecting the departure from isothermality depends on the physical description of the ICM provided by the simulations. Since simulated clusters have central temperature gradients, which are steeper than the observed ones, the above effect is probably overestimated. This demonstrates that a proper use of hydrodynamical simulations to calibrate galaxy clusters as standard rods also requires a correct description of the physical properties of the intra–cluster gas.

The results presented in this Chapter have been published in Ameglio et al. (2006).

# Chapter 5

# Joint deprojection of Sunyaev–Zeldovich and X–ray images

A precise observational characterization of the thermal structure of the intra–cluster medium (ICM) is of crucial relevance for at least two reasons. On one hand, the ICM thermodynamics is determined not only by the gravitational accretion of gas into the dark matter potential wells forming clusters, but also by energy feedback processes (i.e., from supernova explosions and active galactic nuclei), which took place during the cosmic history of the cluster assembly. On the other hand, a precise characterization of the temperature structure of clusters is highly relevant to infer the cluster masses, under the assumption of hydrostatic equilibrium, and, therefore, to calibrate clusters as precision tools for cosmological applications (e.g., Rosati et al., 2002; Voit, 2005; Borgani, 2006, for reviews).

The study of the ICM properties has been tackled so far through X–ray observations. Data from the Chandra and XMM–Newton satellites are providing precise measures of the temperature and surface brightness profiles for a fairly large number of nearby ($z \lesssim 0.3$) clusters, reaching $z \simeq 0.5$ for the brightest objects (e.g., Piffaretti et al., 2005; Pratt & Arnaud, 2005; Vikhlinin et al., 2005; Kotov & Vikhlinin, 2006).

These observations have indeed allowed to trace in detail the mass distribution in galaxy clusters for the first time. However in the X-rays the accessible dynamic range is limited by the $\rho^2_{gas}$ dependence of the emissivity which causes measurements of the temperature profiles to be generally limited to 2–3 core radii, extending out to $r_{500}$ only in the most favorable cases. This is not the case for clusters' studies performed with the thermal Sunyaev–Zeldovich effect (Sunyaev & Zeldovich 1972, tSZ; see Birkinshaw 1999; Carlstrom et al. 2002 for reviews). Since the tSZ signal has a weaker dependence on the local gas density, it is in principle better suited to sample the outer cluster's regions, which can be accessed by X–ray telescopes only with long exposures and a careful characterization of the background noise. Clusters are currently observed through their tSZ signal and tSZ surveys of fairly large area of the sky promise to discover in the next future a large number of distant clusters out to $z \gtrsim 1$.

Thanks to the different dependence of the tSZ and X–ray emission on the electron number density $n_e$, and temperature $T_e$, the combination of these two observations offers in principle an alternative route to X–ray spectroscopy for the study of the structural

properties of the ICM. Indeed, while the X–ray emissivity scales as $n_e^2\Lambda(T)$ (where $\Lambda(T)$ is the cooling function), the tSZ signal is proportional to the gas pressure, $n_eT_e$, integrated along the line-of-sight. Recovering the temperature structure of galaxy clusters through the combination of X–ray and tSZ data has several advantages with respect to the more traditional X–ray spectroscopy. First of all, X–ray surface brightness profiles can be recovered with a limited number ($\sim 10^3$) of photons, while temperature profiles require at least ten times more counts. Therefore, the combination of X–ray surface brightness and tSZ data should allow to probe more easily the regimes of low X–ray surface brightness (i.e. external cluster regions and high–redshift galaxy clusters), which are hardly accessible to spatially resolved X–ray spectroscopy. Furthermore, fitting X–ray spectra with a single temperature model is known to provide a temperature estimate which is generally biased low by the presence of relatively cold clumps embedded in the hot ICM atmosphere (Mazzotta et al., 2004; Vikhlinin, 2006). On the other hand, combining X–ray and tSZ does not require any spectral fitting procedure and, therefore, yields a temperature which is basically mass–weighted.

The combination of X–ray and tSZ observations is currently used to estimate the angular diameter distance of clusters (see Chapter 4) and to recover the gas mass fraction (e.g., LaRoque et al., 2006). Clearly, performing a spatially–resolved reconstruction of the thermal structure of the ICM requires the availability of high–resolution tSZ observations with a sub-arcmin beam size, with a sensitivity of few $\mu$K on the beam. Although observations of this type can not be easily carried out with millimetric and sub–millimetric telescopes of the present generation, they are certainly within the reach of forthcoming and planned instruments of the next generation, based both on interferometric arrays and on single dishes with large bolometer arrays (see Chapter 2).

Combining X–ray and tSZ data to reconstruct the three dimensional gas density and temperature structure of galaxy clusters is not a new idea and different authors have proposed different approaches. Zaroubi et al. (1998) used a deprojection method, based on Fourier transforming tSZ, X–ray and lensing images, under the assumption of axial symmetry of the cluster. After applying this method to simple analytical cluster models, they concluded that the combination of the three maps allows one to measure independently the Hubble constant $H_0$ and the inclination angle. This same method was then applied by Zaroubi et al. (2001) to cosmological hydrodynamical simulations of galaxy clusters. They found that this method provides a reliable determination of the cluster baryon fraction, independently of the inclination angle. Reblinsky (2000) applied a method based on the Richardson–Lucy deconvolution to combined tSZ, X–ray and weak lensing data to a set of simulated clusters. Doré et al. (2001) used a perturbative approach to describe the three dimensional structure of the clusters, to combine tSZ and lensing images. In this way, they were able to predict the resulting X–ray surface brightness. After testing their method against numerical simulations of clusters, they concluded that the dark matter and gas distributions can both be recovered quite precisely. Lee & Suto (2004) proposed a method, based on assuming a polytropic equation of state for gas in hydrostatic equilibrium, which allowed them to recover the three dimensional profiles of clusters using the tSZ and the X–ray signals. Puchwein & Bartelmann (2006) applied the same method of Reblinsky (2000) to deproject X–ray and tSZ maps, so as to recover the gas density and the temperature structure of clusters, under the assumption of axial symmetry. Cavaliere & Lapi (2006) applied the combination of tSZ and X–ray observations to recover the ICM entropy profiles.

As for applications to real clusters, Zhang & Wu (2000) combined X-ray surface bright-

ness and tSZ data, for a compilation of clusters, to estimate the central temperature, and found it to be in reasonable agreement with the X–ray spectroscopic determination. Pointecouteau et al. (2002) used ROSAT–HRI imaging data of a relatively distant cluster ($z \simeq 0.42$) with tSZ observations to infer the global temperature of the system.

De Filippis et al. (2005) combined X–ray and tSZ data to constrain the intrinsic shapes of a set of 25 clusters. By applying a deprojection method based on assuming the $\beta$–model (Cavaliere & Fusco-Femiano, 1976), they confirmed a marginal preference for the clusters to be aligned along the line-of-sight, thus concluding that X–ray selection may be affected by an orientation bias. Sereno (2007) analyzed the potentiality of combining tSZ, X–ray and lensing data to constrain the 3D structure of the clusters. He found that these data are enough to determine the elongation along the line of sight (together with the distance), without however fully constraining shape and orientation.

Some of the detailed methods applied to numerical cluster models account for the presence of a realistic noise in the tSZ and X–ray maps. However, they generally do not present any detailed assessment of how this noise determines the uncertainties in the deprojected profiles, which ultimately characterize the ICM thermodynamics. Having a good control on the errors is especially crucial in any deprojection technique, since errors at a given projected separation affect the deprojected signal in the inner regions, thereby introducing a non–negligible covariance in the reconstruction of the three-dimensional profiles.

In this Chapter we discuss a method to recover the three–dimensional temperature and gas density profiles from the joint deprojection of X–ray surface brightness and spatially resolved tSZ data, testing its performance against idealized spherical clusters and full cosmological hydrodynamical simulations. This method is based on the assumption of spherical symmetry, but do not assume any specific model for the gas density and temperature profiles. We will describe two different implementations. The first one is analogous to that already applied to deproject spectroscopic X–ray data (e.g., Kriss et al., 1983) and is based on assuming a onion–like structure of the cluster, in which projected data of X–ray and tSZ "fluxes" are used to recover gas density and temperature in the external layers and then propagated to the internal layers in an iterative way. The second implementation is based instead on a multi–parametric fitting procedure, in which the fitting parameters are the values of gas density and temperature within different three–dimensional radial bins. The values of these parameters are then obtained through a Monte Carlo Markov Chain maximum likelihood fitting by comparing the resulting projected X–ray and tSZ profiles to those measured from the maps. As we shall discuss in detail, this second method naturally provides the error correlation matrix, which fully accounts for the covariance between error estimates at different radii and among different (i.e. gas density and temperature) profiles. The quality of the X–ray data required by our methods are basically already available with the current generation of X–ray telescopes. As for the tSZ data, exploiting the full potentiality of the deprojection requires spatially resolved data. For illustrative purposes, we will assume the forecast observing conditions and sensitivity of the CCAT (Sebring et al., 2006, see also http://www.submm.caltech.edu/∼sradford/ccat/doc/2006-01-ccat-feasibility.pdf), although our computations can be easily repeated for other telescopes.

The plan of this Chapter is as follows. In Section 5.1 we describe the two implementations of the deprojection method, while we describe in Section 5.2 their application on a spherical polytropic $\beta$–model. Section 5.3 presents the results of the analysis on the hydrodynamical simulations of clusters. The main conclusions of our analysis are

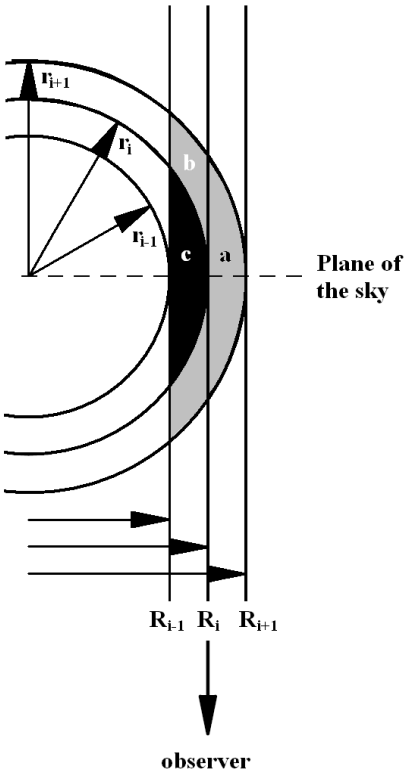


**Figure 5.1.** Illustration of the onion–skin model adopted for the geometrical deprojection (see text in Sect. 2.1; adapted from McLaughlin 1999).

summarized in Section 5.4.

## 5.1 The methods of deprojection

### 5.1.1 The geometrical deprojection technique

The first method that we apply to recover the three–dimensional profiles of temperature and gas density is based on a geometrical technique originally introduced by Kriss et al. (1983), and subsequently adopted (e.g., Buote, 2000; Ettori et al., 2002; Morandi et al., 2007) to deproject X–ray images and spectra of galaxy clusters. This method of geometrical deprojection is fully non–parametric and allows to reconstruct the 3-dimensional profile of a given quantity from its 2-dimensional observed projection, under the assumption of spherical symmetry.

Following Kriss et al. (1983), the cluster is assumed to have a onion–like structure (see figure 5.1), with $N$ concentric spherical shells, each characterized by uniform gas density and temperature within it. Therefore, the cluster image in projection is divided into rings, which are generally assumed to have the same radii of the 3D spherical shells. Let us define $\epsilon_i$ as the signal to be recovered from the deprojection method within the $i$-th shell. In our analysis $\epsilon_i$ will be proportional to either $n_e T_e$ for the tSZ signal, or to $n_e^2 \Lambda(T)$ for the X–ray emissivity. In this way, the contribution of the $i$-th shell to the

surface brightness[1] in the ring $j$ of the image will be given by $s_{i,j} = \epsilon_i \cdot V_{i,j}/A_j$, where the matrix $V_{i,j}$ has as entries the values of the volume of the shell $i$ which is projected on the ring $j$, whose area is $A_j$. By definition, $s_{i,j} = 0$ for $j > i$. Accordingly, the surface brightness $S'_j$ in the ring $j$ can be obtained by summing up the contributions from all the shells,

$$S'_j = \frac{1}{A_j} \sum_{i=j}^{N} s_{i,j} = \sum_{i=j}^{N} \epsilon_i \cdot V_{i,j} \,, \tag{5.1}$$

where the sums extend over the $N$ radial bins. The deprojection amounts to invert the above equation, i.e. to recover the values of $\epsilon_i$ from the observed projected signal $S'_j$. We refer to figure 5.1 to illustrate how this deprojection is performed in practice. Let the shell $i$, limited by $r_i$ and $r_{i+1}$, be the outermost one. Then, from the surface brightness $S'_i$ in the ring $i$ (limited by $R_i$ and $R_{i+1}$), one can directly compute the emissivity of the shell $i$ simply by knowing the volume of the region (a) and the area of the ring. In this case, the sum in eq. (5.1) has only the term $j = i = N$. The adjacent inner ring, having index $i-1$ and limited by $R_{i-1}$ and $R_i$, takes instead a contribution from both the $i-1$ and $i$ shells. The former is computed by multiplying the emissivity of that shell by the volume of the region (b). After subtracting it, the only remaining contribution is that of the sell $i-1$ from which the emissivity $\epsilon_{i-1}$ is computed. This procedure is then repeated from ring to ring down to the centre of the cluster.

For this simple scheme to be applied, one requires to have images extended out to the true external edge of the cluster, i.e. out to the radius where the surface brightness goes virtually to zero. Clearly, this situation is never attained in practical applications for at least two reasons. First, clusters are always embedded in a large–scale cosmic web, which makes it difficult to define a sharp outer boundary. Second, and more important, both instrumental and cosmic backgrounds often dominate the genuine signal from the cluster well before its virial boundary is reached.

To overcome this problem, it is then necessary to take into account the emission from the gas, which extends outside the $N$-th shell. This emission does not have a corresponding ring in the image but can give a non–negligible contribution to the surface brightness in all rings. To account for this contribution, we follow the approach of McLaughlin (1999), who modeled the volume emission from the gas beyond the last observable annulus as a power law, $\epsilon(r) \propto r^{-\alpha}$ (we refer to their Appendix A for a more detailed description). The idea behind this method is that the exact contribution to each ring from the external part can be calculated by integrating the volume emission $\epsilon(r)$. Then, the normalization of the power law shape of $\epsilon(r)$ is fixed by the requirement of matching the total surface brightness of the last ring. This correction can be expressed as an additional term to eq. (5.1), which is proportional to the surface brightness of the last ring:

$$S_j = S'_j + f_j \cdot S_N \,, \tag{5.2}$$

Here, $f_j$ is a geometrical factor which is uniquely specified by the values of the limiting radii of the $j$-th ring and by the exponent $\alpha$. Eq. (5.2) must be actually interpreted as a set of $2N$ equations, which corresponds to the separate deprojection of the tSZ and of the X–ray signal, each performed for $N$ radial bins. The geometrical deprojection is then performed by inverting each set of $N$ equations, starting from the outermost

[1]For the sake of clarity, we indicate here with surface brightness the projected quantity, which can be both a genuine X–ray surface brightness and the tSZ signal.

bin and proceeding inward. This procedure provides the radial profiles of $n_e T_e$ and of $n_e^2 \Lambda(T)$, whose combination finally gives the 3D profiles of electron number density and of temperature. We emphasize that the temperature so obtained is the actual electron temperature and not the deprojected spectroscopic temperature, usually obtained from the fitting of X–ray spectra.

Given the iterative nature of this procedure, the uncertainty associated to each ring propagates not only to the corresponding 3D shell, but also to all the inner shells. For this reason, it is very difficult with this method to have a rigorous derivation of the statistical uncertainties associated to the deprojected profiles. This is particularly true for the X–ray profiles, that also involve a derivative of the cooling function with respect to the temperature. The commonly adopted solution is based on performing MonteCarlo simulations, over which to compute the errors (e.g. Ettori et al., 2002).

Furthermore, errors associated to different radial bins are not independent. This is due to the fact that the projected signal in a given ring is contributed by several shells. The resulting covariance in the signals recovered in different shells is not provided by this deprojection method. This is a rather important point on which we will come back in Section 5.3.

### 5.1.2 The maximum likelihood deprojection

This technique is based on performing the deprojection by maximizing a likelihood function, which is computed by comparing the observed tSZ and X–ray profiles with the ones obtained by projecting the onion–skin model in the plane of the sky. This approach offers more than one advantage with respect to the geometrical deprojection, described in the previous section. First, the deprojection of both X–ray and tSZ profiles is performed simultaneously, directly obtaining the whole density and temperature profiles and their errors. Second, besides the variance, it is also possible to compute the correlation matrix for all parameters, without any extra computational cost. Finally, it is possible to introduce in the likelihood extra terms in order to improve the accuracy and robustness of the technique. As we shall describe in the following, we adopt a regularization technique, which is based on imposing a suitable constraint to the likelihood function, to smooth out spurious oscillations in the recovered profiles induced by the covariance in the parameter estimate.

The definition of the likelihood is the most important part of the whole procedure. We define a joint likelihood for the tSZ profile, $\mathcal{L}_{tSZ}$, and for the X–ray surface brightness profile, $\mathcal{L}_{Xray}$, also including a term associated to the regularization constraint, $\mathcal{L}^{\lambda}_{reg}$. Since these three terms are independent, the total likelihood is given by the product of the individual ones:

$$\mathcal{L} \equiv \mathcal{L}_{tSZ} \cdot \mathcal{L}_{Xray} \cdot \mathcal{L}^{\lambda}_{reg}. \tag{5.3}$$

For both the tSZ and the X–ray profiles, the take the Gaussian form for the likelihood,

$$ln(\mathcal{L}_{tSZ,X-ray}) = -\frac{1}{2}\chi^2 = -\frac{1}{2}\sum_i \left(\frac{O_i - M_i}{\sigma_i}\right)^2, \tag{5.4}$$

where $O_i$ are the values of the profiles in the $i$-th bin, measured from the maps, while $M_i(x)$ are the model–predicted profile values, as obtained for the set $x$ of parameters. Finally, $\sigma_i$ is the uncertainty on the measured values $O_i$.

While the Gaussian expression is adequate for the tSZ signal, its application to the X–ray signal requires the number of photons sampling the surface brightness map in each

radial shell to be large enough to neglect the Poisson noise. As we shall discuss in the following, even in the outermost rings, we always have at least 20 photons in the "noisy" X–ray maps.

For the regularization constraint, we adopt the Philips-Towmey regularization method (Bouchet, 1995, and references therein). This method has been already used also by Croston et al. (2006) to deproject X–ray imaging and spectral data. The method consists of minimizing the sum of the squares of the $k^{th}$-order derivatives around each data-point, so as to smooth out oscillations in the profiles. Here we choose to minimize the second–order derivative, since we aim to eliminate fluctuations in the profiles, but not the overall gradient. As we shall discuss in the following, such oscillations are due either to genuine substructures or to noise which propagates from adjacent bins in the deprojection. The local derivative of the function $x_i$ at the $i$-th radial interval is computed by fitting its value and the values at the adjacent points, $x_{i-1}$ and $x_{i+1}$, with a second order polynomial. Let $r_i$ be the value of the equally–spaced cluster–centric distances, at which the profiles are sampled, and $\Delta_r$ the spacing. Then, the regularization likelihood can be cast in the form

$$ln(\mathcal{L}^{\lambda}_{reg}) = -\frac{1}{2}\lambda' \sum_{i=3}^{N-1} \left( \frac{2f_i - f_{i-1} - f_{i+1}}{\Delta_r^2} \right)^2 \equiv$$
$$\equiv -\lambda \sum_{i=3}^{N-1} (2f_i - f_{i-1} - f_{i+1})^2 \qquad (5.5)$$

The quantity between parenthesis in the first line of the above equation is the exact value of the local second–order derivative around $r_i$. All the constant factors are included in the coefficient $\lambda$, which is called the *regularity parameter*. The choice of its value is determined by the compromise one wants to achieve between the fidelity to the data (low $\lambda$) and the regularity of the solution (high $\lambda$). A small $\lambda$ value will give an inefficient regularization, while a too high $\lambda$ will force the profile to a straight line, especially if the signal-to-noise ratio, S/N, is low. We apply the regularization constraint only to the temperature profile, which is that generally showing large oscillations, while the density profile has always a rather smooth shape. The sum in eq. (5.5) starts from $i = 3$ since we prefer to exclude the innermost point from the regularization procedure.

With this approach, the values of the 3D gas density and temperature profiles are computed at $N = 15$ radii each. Therefore, the total number of parameters to be determined with the maximum likelihood approach is 30. In order to optimize the sampling of such a large parameter space, we adopt a Markov Chain Monte Carlo (MCMC) fitting technique (Neal, 1993; Gilks et al., 1996; MacKay, 1996).

What the MCMC computes is the (marginalized) distribution of each parameter of a set, $x_i$ (i.e. the values of density and temperature into each bin), for which the global (posterior) probability $P(x)$, which is proportional to the likelihood function, is known at any point in the parameter space. In the case of an high number of parameters or of a particularly complex $P(x)$, this is quite difficult to be done analytically, or simply computationally very expensive. Instead, the MCMC performs the exploration of the parameter space with a limited computational cost, thanks to an iterative Monte Carlo approach, by sampling the $P(x)$ distribution. At each iteration, new values of the parameters are drawn from a symmetric proposal distribution, that in our case is a Gaussian,

$$q(x_i, \hat{x}_i) \propto e^{-(x_i - \hat{x}_i)^2/2\alpha_i^2} . \qquad (5.6)$$

Here $x_i$ and $\hat{x}_i$ are the entries of two vectors, having 30 components each, which represent the updated and the old values of the fitting parameters, respectively. The parameter $\alpha_i$ determines the possible range for $x_i$ given $\hat{x}$ .

After the likelihood function is computed for a new set of parameters $x$, these new values are accepted or rejected with a probability (A) given by the so–called Metropolis criterion (Metropolis et al., 1953):

$$A(x, \hat{x}) = min \left\{ 1, \frac{P(x)}{P(\hat{x})} \right\}, \tag{5.7}$$

where $P(x)$ is the distribution sampled by the MCMC [2].

The width of the proposal distribution appearing in eq. (5.6), $\alpha_i$, determines the behavior of the chain: a small value of $\alpha_i$ increases the acceptance rate since the new proposed value is close to the old one, while a high value provides a faster exploration of the parameter space. Our criterion to choose the values of $\alpha_i$ is that the resulting acceptance rate, given by eq. (5.7), is around 10 per cent.

Each parameter is allowed to vary within a finite interval, in order to avoid that the MCMC finds secondary maxima in unphysical regions of the parameter space. As for gas density, we allow it to vary within a large range, $0.1 < n_e < 10^{-6}$ cm$^{-3}$. Since density is mostly constrained by the X–ray signal, which is proportional to $n_e^2$, it is always fairly well constrained and the above large interval of variation does not create convergence problems in any of our objects. The upper and lower limits allowed for the temperature are 25 keV (never reached along the chain) and 0.5 keV. Even though none of our clusters reach such low temperatures within the virial radius, the exploration of the parameter space during the Markov Chain run could reach such a low temperature regime. When this happens, the rapid drop of the cooling function $\Lambda(T)$ below 0.5 keV generates a maximum in the likelihood probability distribution, with unphysically low temperature and very high density.

The iterative procedure described above is repeated until a suitable number of new sets of parameters are accepted in the chain (typically $\gtrsim 5 \times 10^4$). In this condition, the frequency of the occurrence in the chain of the $i$-th parameter $x_i$ approaches its true probability distribution, $P(x_i)$. Note that each parameter distribution is already marginalized over the distributions of all the other parameters.

We perform the statistical analysis of the chain by using the code *getdist* of the COSMOMC package (Lewis & Bridle, 2002). In addition to a complete statistical analysis of the chain, the code performs a series of convergence tests: the Gelman & Rubin R statistics (Gelman & Rubin, 1992), the Raftery & Lewis test (Raftery, 2003) and a split–test (which essentially consists in splitting the chain into 2, 3 or 4 parts and comparing the difference in the parameter quantiles). We check the convergence of our result against all these three tests.

[2]Hastings (1970) has generalized this treatment to non–symmetric proposal distributions, by adding a factor in eq. (5.7) which takes into account the proposal distribution $q(x, \hat{x})$:

$$A(x, \hat{x}) = min \left\{ 1, \frac{P(x)}{P(\hat{x})} \frac{q(x, \hat{x})}{q(\hat{x}, x)} \right\}, \tag{5.8}$$

This is called the Metropolis–Hastings criterion.

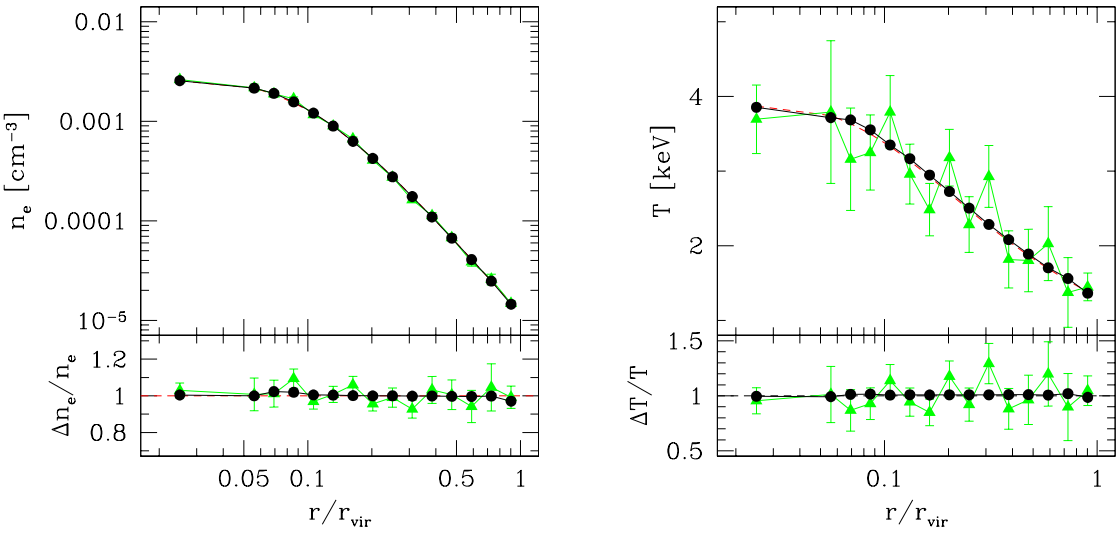


**Figure 5.2.** Results of the geometrical deprojection of the analytical model: density profile (left panel), temperature profile (right panel). The dashed line represents the true profile. The circles (triangles) connected by a solid line represent the reconstructed profiles without (with) the inclusion of the noise. Errorbars represent $1\sigma$ deviations over 1000 Monte Carlo resamplings over the data (see text for details, Section 5.2.1)

## 5.2 Application to an idealized cluster model

In order to investigate the presence of possible systematics in the geometrical deprojection technique, we carry out a test on an ideal cluster model. We construct this model cluster by assuming the $\beta$–model for the gas density profile, with an effective polytropic equation of state to define the temperature profile:

$$\begin{aligned} n_e &= n_{e0}\left(1+\frac{r^2}{r_c^2}\right)^{-3\beta/2} \\ T &= T_0\left(\frac{n_e}{n_{e0}}\right)^{\gamma-1} = T_0\left(1+\frac{r^2}{r_c^2}\right)^{-3\beta(\gamma-1)/2} \end{aligned} \tag{5.9}$$

The values of the model parameters are fixed as follows: $\beta = 0.8$, $\gamma = 1.2$ for the effective polytropic index, $n_{e0} = 3 \cdot 10^{-3}$ cm$^{-3}$ for central electron number density, $T_0 = 4$ keV for the central temperature, $r_c = 200$ kpc for the core radius. The "virial" radius, which represents here the largest cluster-centric distance out to which the profiles are followed, is fixed at $r_{vir} = 2$ Mpc. We assume the cluster to be placed at redshift $z = 0.1$.

We create tSZ and X–ray images of this model in X–ray and tSZ. The maps are composed by a grid with 512x512 pixels. The physical dimension of the pixel is $\sim 16$ kpc, which corresponds to an angular scale of $\sim 4$ arcsec at the above redshift. In realizing the map of X–ray surface brightness, we adopt for the cooling function the pure bremsstrahlung expression $\Lambda(T) = \Lambda_0(T/T_0)^{0.5}$ where $\Lambda_0 = 5 \cdot 10^{-23}$ erg/s cm$^3$. We prefer this simple formula since at this stage our main interest is to investigate the systematics of the deprojection itself, rather than the uncertainties introduced by the dependence of the X–ray emissivity on the temperature (which we expect anyway to be quite small).

We adopt the same binning strategy for both the ideal cluster and for the simulated objects, that we shall describe in the next Section. The first bin is taken from $r = 0$ to $r = 0.05 r_{vir}$ which always corresponds to $\gtrsim 100$ kpc in our set of simulated clusters. Then, we compute the profile in 10 (15) bins out to $R_{500}$ ($R_{vir}$) which are equally spaced in logarithm. This choice represents a good compromise between the needs of accurately resolving the profile and of having an adequate signal-to-noise (S/N $\gtrsim 5$) in each bin. We point out that a proper binning criterion is important in order to get an unbiased reconstruction of the profiles. One should keep in mind that the spherical shells are assumed to have homogeneous gas density and temperature structures, thus neglecting any internal radial gradient. On the other hand, the portion of each shell, which is projected on the corresponding ring in the image, is located at a larger radial distance from the center than the portion of the same shell which is projected into the inner rings. Therefore, if the bin width is comparable to or larger than the scale length of the internal radial gradient of the shell, the emissivity contributed to the correspondent ring is lower than expected from a homogeneous gas density, while it is larger for all the inner rings. As a consequence, the emissivity of the shell is underestimated while that of all the inner shells is overestimated in order to correctly reproduce the cluster image.

In order to check for the presence of such systematics, we first apply the deprojection technique in the case of an ideal observation, free of any noise. The reconstructed density and temperature profiles are shown in figure 5.2. The reconstruction in this extremely idealized case is excellent, with very small or no deviations in all bins. Larger deviations are in the outermost bins and are related to the subtraction of the contribution of the fore–background contaminations. This contamination is due to the fact that the $\beta$–model used to produce our maps ideally extends out to infinity. Nevertheless, all deviations are smaller than a few percent and are negligible with respect to any observational noise. The results obtained in this test case show that taking equally log-spaced bins is in fact a good choice.

### 5.2.1 Geometrical deprojection of the noisy maps

The case of noiseless observations discussed in the previous section is highly idealized. The impact of including a realistic noise is instead very important and cannot be neglected. The recipe to add noise to the maps, that we describe here, will also be used in the study of the simulated clusters, discussed in Section 5.3.

As already mentioned, recovering detailed temperature profiles from the combination of X–ray imaging and tSZ data requires both of them to have an adequate spatial resolution. While this is certainly the case for the present generation of X–ray satellites, the combination of good sensitivity and spatial resolution for tSZ observations should await the next generation of sub-millimetric telescopes.

For the purpose of our analysis, we model the noise in the tSZ maps by using as a reference the performances expected for the planned Cornell–Caltech Atacama Telescope (CCAT), which is expected to start operating at the beginning of the next decade (Sebring et al., 2006). The telescope will be a single–dish with 25 m diameter. The required field–of–view is of about $10 \times 10$ arcmin$^2$, with the goal of covering a four times larger area, so as to cover one entire rich cluster down to a relatively low redshift. The best band for tSZ observations will be centered on 150 GHz. At this frequency CCAT is expected to have a Gaussian beam of 0.44 arcmin FWHM. The first step of noise setup is to convolve the maps with this beam. Then we add a Gaussian noise of $3\mu$K/beam. This level of noise

should be reached with about 6 hours of exposure with CCAT. In the present study, we neglect in the tSZ maps any contamination, in particular we do not consider the presence of unresolved radio point sources. A detailed analysis of the contaminations in the tSZ signal has been provided by Knox et al. (2004) and by Aghanim et al. (2004).

As for X–ray observations, the Chandra satellite is currently providing imaging of superb quality, with a sub–arcsec resolution on axis. A proper simulation of X–ray observations should require generating spectra for each pixel, to be convolved with the response function of a given instrument. However, in order to apply our reconstruction method we only need to generate X-ray surface brightness maps with a given number of events (photons), regardless of their energy. For this purpose we simulate the X–ray photon counts by using a Monte Carlo sampling of the surface brightness map. We fix to $N = 10^4$ the total number of photons within the virial radius of the cluster, which is quite typical for medium–deep observations of relatively nearby clusters. Each photon event is generated in a particular pixel $i$, with probability

$$P_i = \frac{s_i}{\sum_j s_j}, \tag{5.10}$$

where $s_i$ is the surface brightness of the pixel and the sum is extended to all the pixels of the map. The number of expected counts into each pixel will be given by a Poisson probability distribution with mean $n_i = NP_i$. The conversion between counts and surface brightness is then given by $\Sigma = \sum_i s_i/N$, so that the total flux in the map is conserved.

Clearly, this method of introducing noise in the X–ray maps only takes into account the statistical errors associated to finite exposures. However, it neglects the effects of any systematics (e.g., contribution of the instrumental and cosmic background, etc.) which should be included in a more realistic observational setup. A comprehensive description of the instrumental effects on the recovery of X–ray observables, calibrated on hydrodynamical simulations, has been provided by Gardini et al. (2004) (see also Rasia et al., 2006a). Probably the most serious limitation in our approach is that we assume the absence of any background or, equivalently, that the background can be characterized and removed with arbitrary accuracy.

In figure 5.3 we show the tSZ and X–ray images of the idealized cluster, once noise is added. In figure 5.2 we show the results of the deprojection of the noisy maps of the idealized cluster, for both the density and the temperature profiles. In order to estimate the errors in the deprojected profiles, we perform a MonteCarlo resampling of the projected X–ray and tSZ profiles: the value of the profile within each radial ring is randomly scattered according to a Gaussian distribution, whose width is given by the error associated to the noise introduced in the map. The $1\sigma$ errors in the deprojected profiles is then obtained as the scatter within a set of 1000 deprojections of the MonteCarlo–resampled tSZ and X–ray profiles.

The density is the best determined quantity, with uncertainty lower than 10 per cent. This is quite expected, owing to the sensitive dependence on gas density of both the X–ray signal ($\propto n_e^2$) and of the tSZ one ($\propto n_e$). The temperature has instead higher errors, of about 20–30 per cent. This is due to the fact that the X–ray signal has a weaker dependence on the temperature (only contained in the cooling function $\Lambda(T)$). For this reason, the determination of the temperature profile, independent of any X–ray spectroscopic analysis, is strictly related to the possibility of having high–quality tSZ data.

The introduction of noise generates fluctuations in the tSZ and X–ray profiles which

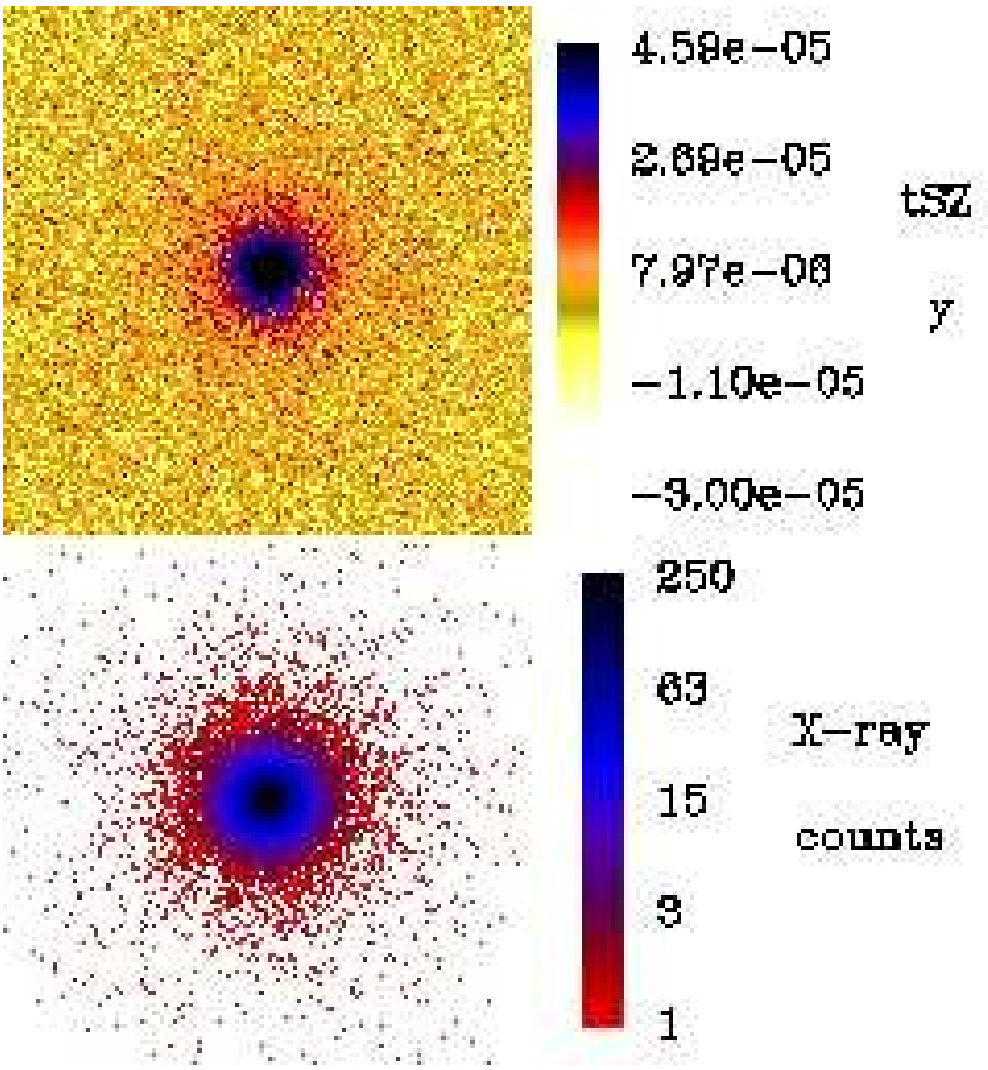


**Figure 5.3.** The tSZ (upper panel) and the X–ray (lower panel) maps of the ideal cluster. The side of the map corresponds to $2R_{vir} = 4$ Mpc. Note that the scale is linear in the tSZ map and logarithmic in the X–ray one.

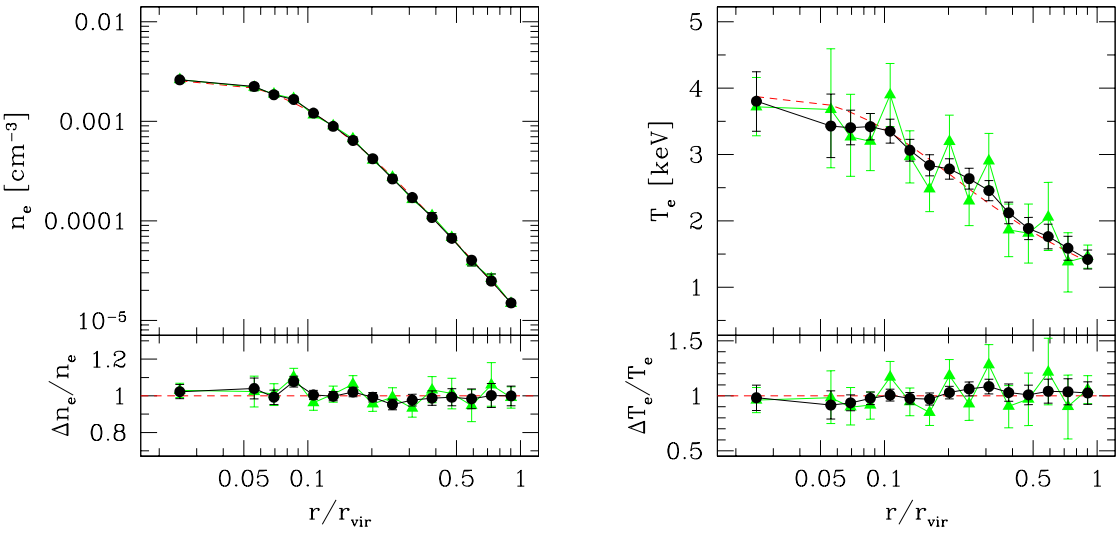


**Figure 5.4.** Results of the maximum–likelihood deprojection on the density profile (left panel) and temperature profile (right panel) for the idealized cluster. In the upper part of each panel we show the correct profile (dashed curve) and the reconstructed profile with and without the regularization constraint (circles and triangles, respectively). In the lower part we show the fractional deviation of the recovered profiles from the true one.

translate into variations of the recovered density and temperature. Looking at the bottom panels of figure 5.2, positive fluctuations in the density correspond to negative fluctuations in the temperature (and viceversa). Furthermore, any fluctuation in a given direction in one radial bin generally corresponds to a fluctuation in the opposite direction in an adjacent bin, within the same profile. This pattern in the fluctuations witnesses the presence of a significant covariance among nearby bins in the same profile and between the values of density and temperature recovered within the same radial bin. As for the covariance between neighbor bins, it is due to the onion–skin structure assumed in the deprojection: every time that a quantity is over(under)estimated in a radial bin, the deprojection forces the same quantity to be under(over)estimated in the adjacent inner bin, so as to generate the correct projected profile. As for the covariance between different profiles, it is mostly induced by the tSZ signal, which has the same dependence on both $n_e$ and $T$. Although such oscillations are present for both density and temperature, they are smaller for the former, due to its faster decrease with radius.

### 5.2.2 Maximum likelihood deprojection of the noisy maps

We verified that using the maximum–likelihood technique, as described in Section 5.1.2, generally produces very similar results to those of the geometrical deprojection, at least when the regularization term, $\mathcal{L}^{\lambda}_{reg}$ is not included in the analysis. The results of this deprojection method on the polytropic $\beta$-model are shown in figure 5.4, where we also show the effect of introducing the regularization term. The effect of the regularization constraint is evident: most of the fluctuations, which are due to the degeneracies between fitting parameters, disappear and the deprojected profiles become much more regular, and with smaller errorbars in the profiles, while the accuracy of the reconstruction remains

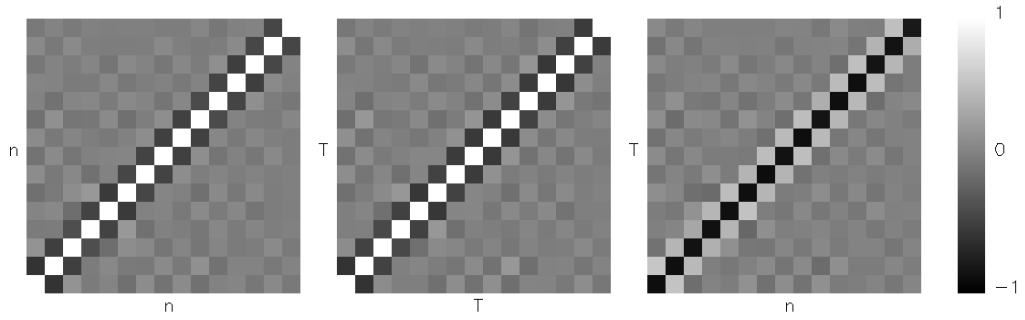


**Figure 5.5.** The correlation matrix of density and temperature without the regularization constraint: density-density (left panel), temperature-temperature (central panel) and density-temperature (right panel). White pixels correspond to the presence of strong positive correlation, while black pixels are for strong anti–correlation.

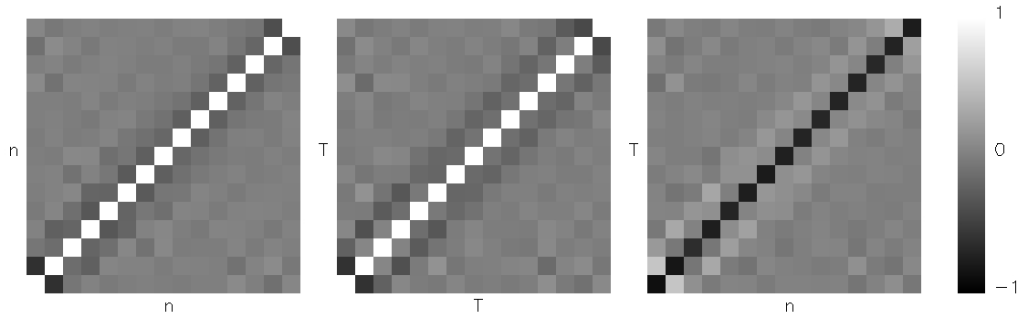


**Figure 5.6.** The correlation matrix of density and temperature while using a regularization constraint: density-density (left panel), temperature-temperature (central panel) and density temperature (right panel). The color-coding of the pixels is the same as in figure 5.5.

essentially unbiased.

In order to study in detail the presence of correlations among the fitting parameters, we compute the correlation matrix, which is defined as $C_{ij} = \sigma_{ij}/\sigma_i\sigma_j$, where $\sigma_{ij}$ is the covariance between the $x_i$ and the $x_j$ fitting parameters, while $\sigma_i^2$ is the variance for the $x_i$ parameter. The covariance matrix is computed along the Markov Chain. Therefore, $C_{ij}$ is in our case a matrix with $30 \times 30$ entries. In figures 5.5 and 5.6 we plot the entries of the correlation matrix for the density–density (DD), temperature–temperature (TT) and density–temperature (DT) "blocks", before and after introducing the regularization term in the likelihood function, respectively. By definition, the variance terms in the diagonal of the DD and TT matrices are characterized by the maximum correlation. On the contrary, the diagonal of the DT matrix has the maximum anticorrelation, thus demonstrating that any positive fluctuation in the recovered profile of one quantity corresponds to a negative fluctuation of the other quantity at the same radius. We also note that the next-to-diagonal terms in the DD and TT blocks have a degree on anticorrelation, thus explaining the fluctuating profile shown in figures 5.2 and 5.4. When the regularization is introduced, the correlations between density or temperature of adjacent bins is efficiently suppressed.

| Cluster | $T_e$ keV | $M_{vir}$ $10^{14}M_\odot$ | $R_{vir}$ Mpc |
|---|---|---|---|
| C1 | 2.5 | 4.0 | 2.1 |
| C2 | 4.3 | 10.1 | 2.6 |
| C3 | 5.5 | 26.6 | 3.1 |
| C4 | 7.0 | 30.5 | 3.3 |

**Table 5.1.** Characteristics of the simulated clusters, for which the detail of the analysis are presented. Col. 1: electron (mass–weighted) temperature; Col. 3: virial mass; Col. 4: virial radius.

## 5.3 Application to simulated clusters

The sample of clusters analyzed here is composed by a subset of 14 simulated objects extracted from the sample describes in Section 3.3, which have virial mass $M_{vir} \gtrsim 4 \times 10^{14} M_\odot$ and spectroscopic temperature $T_{\rm sl} \gtrsim 3$ keV.

The substructures are well known to represent an important source of bias in the deprojection, especially of the X–ray signal, which is highly sensitive to gas clumping. In order to remove this contaminating signal, we follow the same method that is often adopted in the analysis of observational data. We first identify the detectable clumps by visual inspection of the X–ray maps. The corresponding regions are then masked out both in the X–ray and in the tSZ maps. The masked regions are excluded from the computation of the signals to be deprojected. This leads to an increase of the statistical uncertainties in those rings which have a significant overlap with the masked regions. Clearly, due to the finite photon statistics in the X–ray maps, small clumps may fall below the detection threshold, while their presence may still affect the emissivity.

In the following, we will show detailed results for a subset of 4 clusters. The basic characteristics of these four selected clusters are reported in Table 5.1. The first three of them are extracted from the cosmological hydrodynamical simulation, while C4 is one of the massive clusters simulated at higher resolution. C2, C3 and C4 are typical examples of clusters at low, intermediate and high temperature, while C1 is an interesting case to understand the effect of fore–background contaminations. We show in figure 5.7 the X–ray surface brightness and Compton–$y$ maps for these four clusters. All the maps are generated by placing the cluster at redshift $z = 0.1$, so that the maps, which extend out to $r_{vir}$, have an angular size ranging from about 9 arcmin for C1 to 14 arcmin for C4.

### 5.3.1 tSZ and X–ray maps

Around each cluster we extract a spherical region extending out to 6 $R_{vir}$. Following Diaferio et al. (2005), we create maps of the relevant quantities along three orthogonal directions, extending out to about 2 $R_{vir}$ from the cluster center, by using a regular $512 \times 512$ grid.

A number of different analyses, based on a joint deprojections of SZ and X–ray cluster maps under the assumption of axial symmetry, indicate that the X–ray selection tends to favor objects which are elongated along the line-of-sight (e.g., De Filippis et al., 2005, and references therein). In order to control the effect of this selection bias, we decided to choose the axes of projection to be aligned with the principal axes of inertia of the cluster. This will allow us to quantify the difference in the reconstructed profiles when

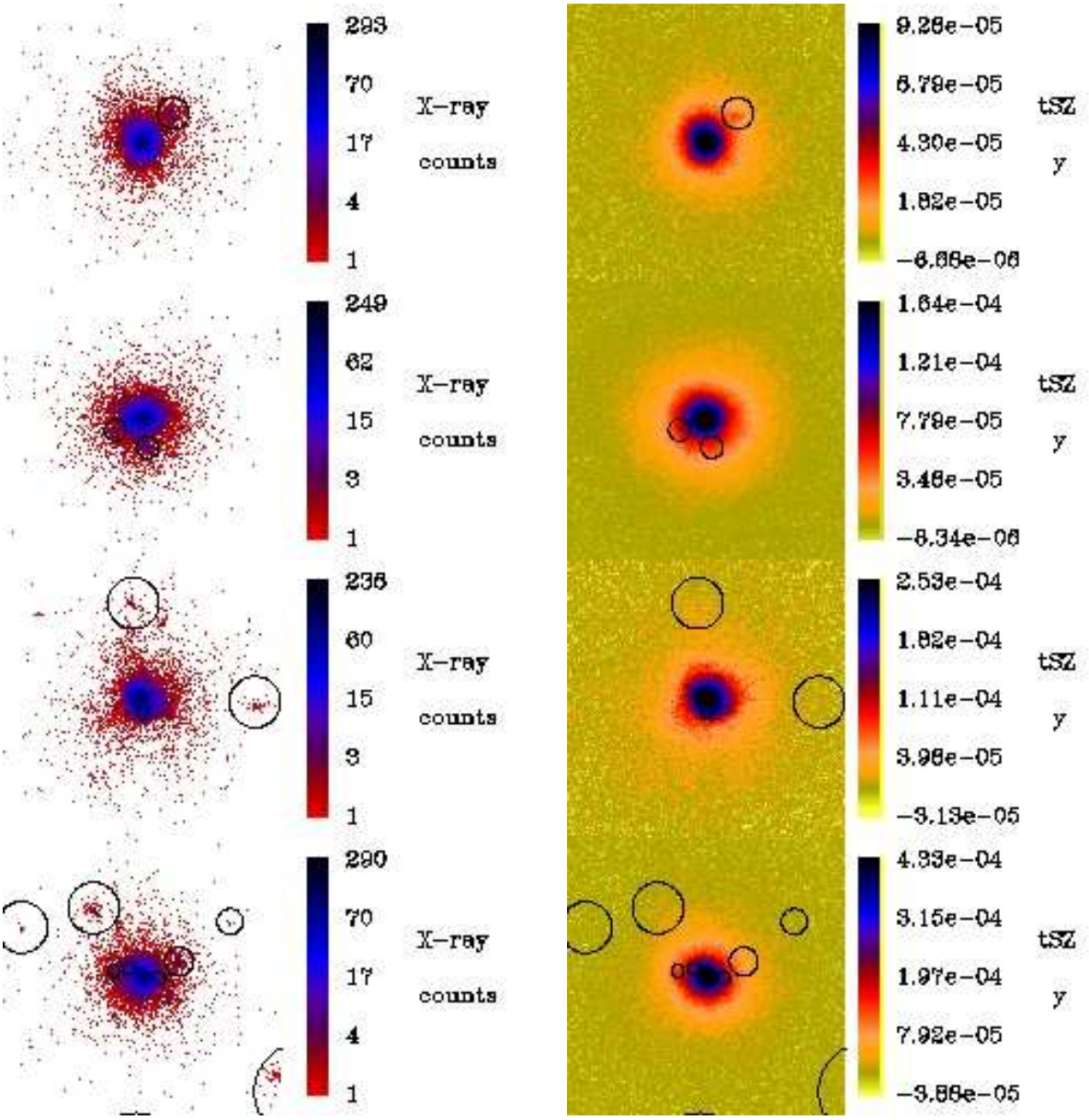


**Figure 5.7.** Maps of the X–ray surface brightness (left panel) and of the Comptonization parameter (right panel) for the C1 to C4 simulated clusters (from top to bottom). Each map extends out to $R_{vir}$. Noise is added according to the recipe described in Section 3.1. The circles mark the regions which have been masked, due to the presence of detected substructures.

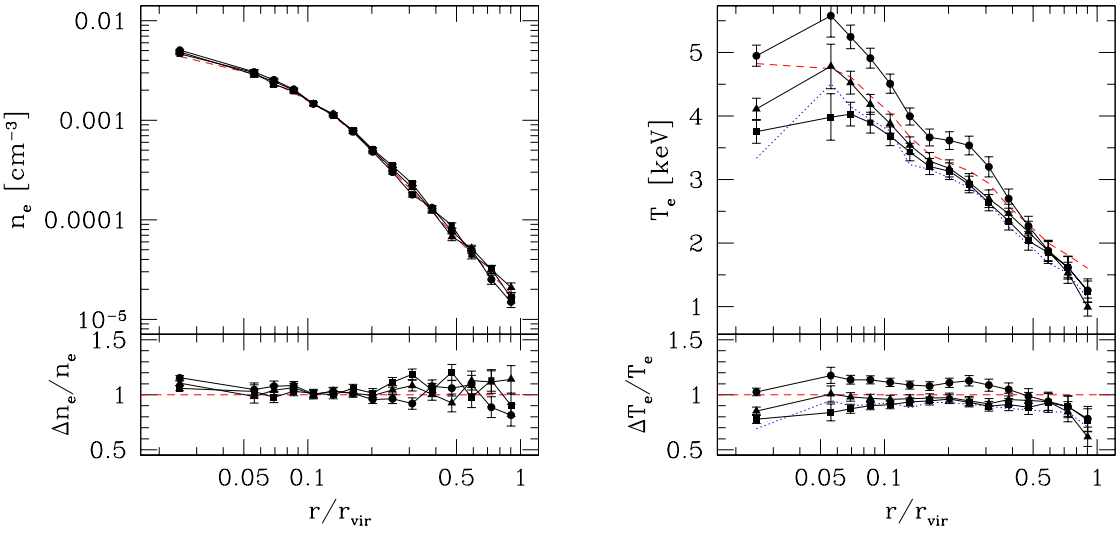


**Figure 5.8.** Application of the regularized maximum likelihood deprojection on the cluster C1, out to $R_{vir}$. The tree solid lines connecting dots with errorbars represent the reconstructed profile, for three orthogonal projection directions: along the $x$ (squares), the $y$ (triangles) and the $z$ (circles) axes. Errorbars correspond to the asymmetric 68 per cent confidence levels, computed from the distribution of values taken by the likelihood function along the Markov Chain. The dashed line represents the true 3-dimensional profile. The dotted line in the right panel shows the profile of the spectroscopic–like temperature. In the bottom panels, we plot the fractional deviation of the reconstructed profiles from the true electron temperature.

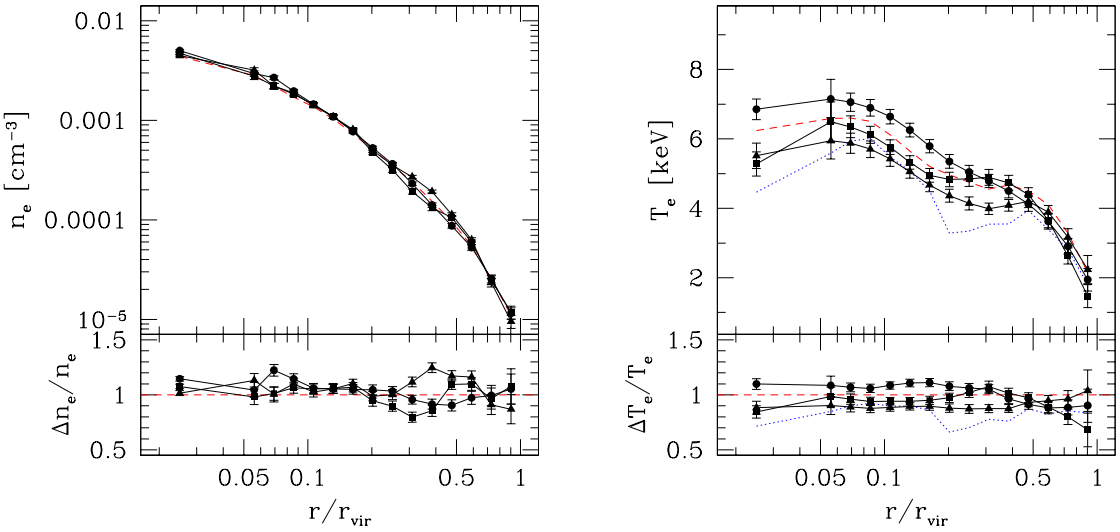


**Figure 5.9.** The same as in figure 5.8, but for the C2 cluster.

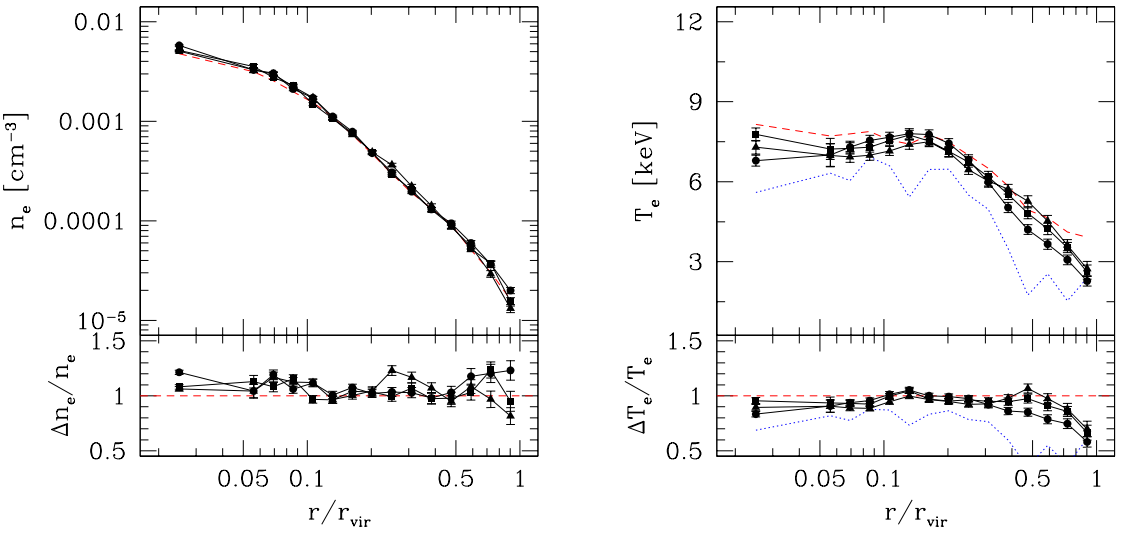


**Figure 5.10.** The same as in figure 5.8, but for the C3 cluster.

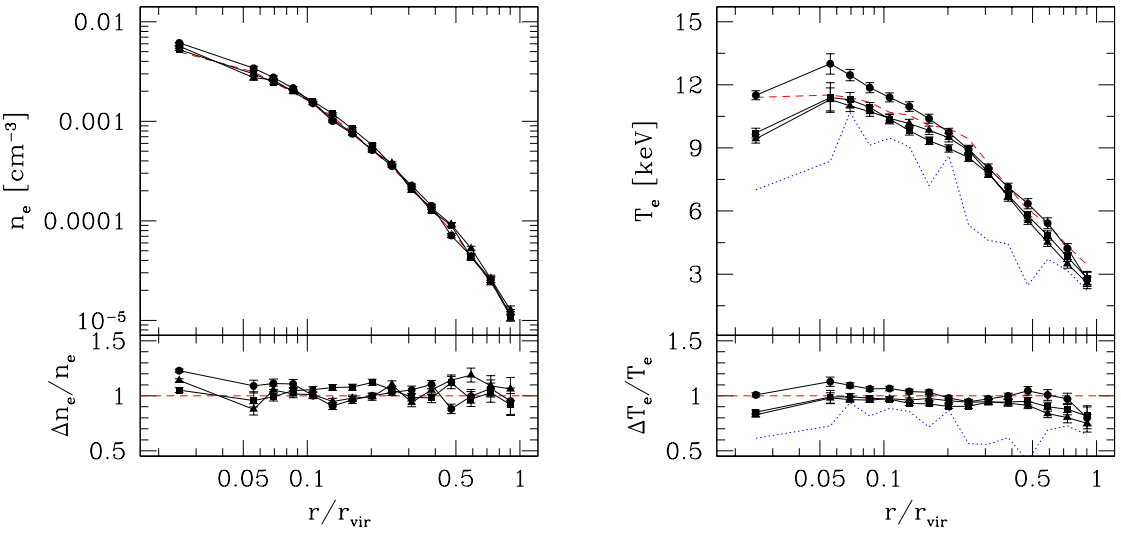


**Figure 5.11.** The same as in figure 5.8, but for the C4 cluster.

the projection direction is that of maximum cluster elongation.

To derive these axes, we diagonalize the inertia tensor, which is given by

$$I_{ij} = \sum_{p=1}^{N} (r_i r_j) \rho_p^2 \tag{5.11}$$

where $i, j = 0, 1, 2$ are the coordinate axes, $r_i$ is the $i$-th coordinate of the particle $p$ with density $\rho_p$ and the sum is extended over all the gas particles. We weight each particle by $\rho_p^2$ so as to mimic the elongation in the X–ray emissivity.

The eigenvectors of the $I$ tensor provide the principal axes of the best–fitting ellipsoid. The semi–axes $a_i$ of this ellipsoid are proportional to square root of the corresponding eigenvalues $a_i \propto \sqrt{\lambda_i}$ (e.g. Plionis et al., 1991). We choose the direction of projection $z$ to be that corresponding to the largest semi–axis (i.e. the maximum elongation), while the $y$ and $x$ directions correspond to the medium and to the smallest semi–axes, respectively.

Noise is finally added as described in Section 5.2.1. We fix the total number of photons in the virial radius to $10^4$ also for simulated clusters. For the tSZ map, we adopt a noise level of 10 $\mu$K/beam for the objects having spectroscopic temperature $T_{sl} > 4$ K and 3 $\mu$K/beam for those having 3 K $< T_{sl} <$ 4 K.

### 5.3.2 Results

Having tested the reliability of the deprojection method, with the regularization of the likelihood, we apply now this technique to the more realistic case of hydrodynamical simulations. In this case, a number of effects, such as deviations from spherical symmetry, presence of substructures and presence of fore/background tSZ contaminating structures, are expected to degrade the capability of the deprojection to recover the three-dimensional profiles.

We show in detail the results on the density and temperature deprojection the selected subset of four clusters presented in Table 5.1 while the whole set of 14 clusters will be used to assess on a statistical basis the efficiency with which the total gas mass can be recovered.

The C2 and C4 objects are rather typical examples of our set of clusters. They are fairly relaxed and with a modest amount of substructures. As for the presence of substructures, they are well known to represent an important source of bias in the deprojection, especially of the X–ray signal, which is highly sensitive to gas clumping. In order to remove this contaminating signal, we follow the same method that is often adopted in the analysis of observational data. We first identify the detectable clumps by visual inspection of the X–ray maps. The corresponding regions are then masked out both in the X–ray and in the tSZ maps. The masked regions are excluded from the computation of the signals to be deprojected. This leads to an increase of the statistical uncertainties in those rings which have a significant overlap with the masked regions. Clearly, due to the finite photon statistics in the X–ray maps, small clumps may fall below the detection threshold, while their presence may still affect the emissivity.

The recovered density and temperature profiles of C2 and C4 are shown in figures 5.9 and 5.11. Once all the detectable clumps are masked out the reconstruction of the density profile is generally good, but with a systematic overestimate of $\sim$5 per cent, that we attribute to a residual small–scale gas clumping. Although this effect is rather small, its presence highlights the need to have a sufficient photon–count statistics to identify

gas inhomogeneities and remove their contribution in the deprojection procedure. The slight density overestimate corresponds, as expected, to a small underestimate of the temperature, which is forced by the requirement of reproducing the tSZ signal, $y \propto n_e T_e$. For these two objects we also note that there are rather small differences in the 3D profiles recovered from three orthogonal projection directions, thus indicating that they are almost spherical and without significant substructures along the different projection directions. Errorbars are always of the order of a few percent, in both density and temperature. We stress that these very small errorbars, especially in temperature, are partly a consequence of the regularization constraint.

As for the C3 cluster, we note that it has larger substructures which will have a stronger impact on the recovered profiles. Even after masking all the detectable substructures, we still have a number of unresolved clumps. As expected, in this case the density profile (see figure 5.10) is overestimated by a larger factor, $\sim 10$ per cent, with a corresponding more significant underestimate of the temperature. The deviations of the deprojected profiles in the outer parts are also larger. This is due to stronger contaminations from the fore/background structures, which are both placed at the outskirts of the cluster and along the projection direction, in the cosmic web surrounding the cluster. In fact, we remind that both tSZ and X–ray maps are produced by projecting a region of 6 $R_{vir}$ in front and in the back of the cluster center.

In this respect, the C1 cluster is particularly interesting. Along the $x$-axis projection there is a merging groups along the same line of sight, at a distance of $\sim 1.2 R_{vir}$ from the centre of the main cluster. In figure 5.12 we show the projected mass surface density of the gas along the three projection directions, after removing the mass of the main cluster within $R_{vir}$. While the residual mass surface density is quite small along the $x$ and $y$ directions, a presence of a gas clump are shows up in the $z$ projection. While this structure provides a rather small contribution to the X–ray signal, its gas pressure is comparable to that of the main cluster, thereby significantly contaminating the tSZ effect signal. As a consequence, the density profile (see figure 5.8) is essentially unaffected, while the temperature is clearly boosted by $\sim 20$ per cent with respect to that obtained from the other two projections. Although this is a quite peculiar case, in which the secondary structure is relatively large and aligned with the main cluster along the line of sight, it illustrates the role of projection contamination from unidentified structures in recovering the 3D thermal structure of the ICM.

We note in figures 5.8–5.11 that the density profiles recovered from the projection of maximum elongation are overestimated at small radii, while they are underestimated in the outskirts. In order to quantify this effect, we show in the left panel of figure 5.13 the ratio between the true and the reconstructed density profiles, after averaging over the sample of simulated clusters. By averaging over all the projection directions, the density is generally overestimated by about 5 per cent at all cluster radii. This result is confirmed also by analyses performed on synthetic X–ray observations of simulated clusters (Rasia et al., 2006a; Nagai et al., 2007). On the other hand, the density profile reconstructed from the projection along the $z$ axis is confirmed to be significantly larger than along the other directions in the very inner part, with an inversion at $r \gtrsim 0.2 r_{\rm vir}$. Indeed, the elongation causes the objects to appear more compact in the X–ray maps, which drive the density reconstruction. This boosts the deprojected central density, while depletes it in the outskirts.

As shown in the right panel of figure5.13, the temperature is generally underestimated by $\lesssim 10$ per cent out to $\simeq 0.7 r_{vir}$. At larger radii this underestimate increases, reaching

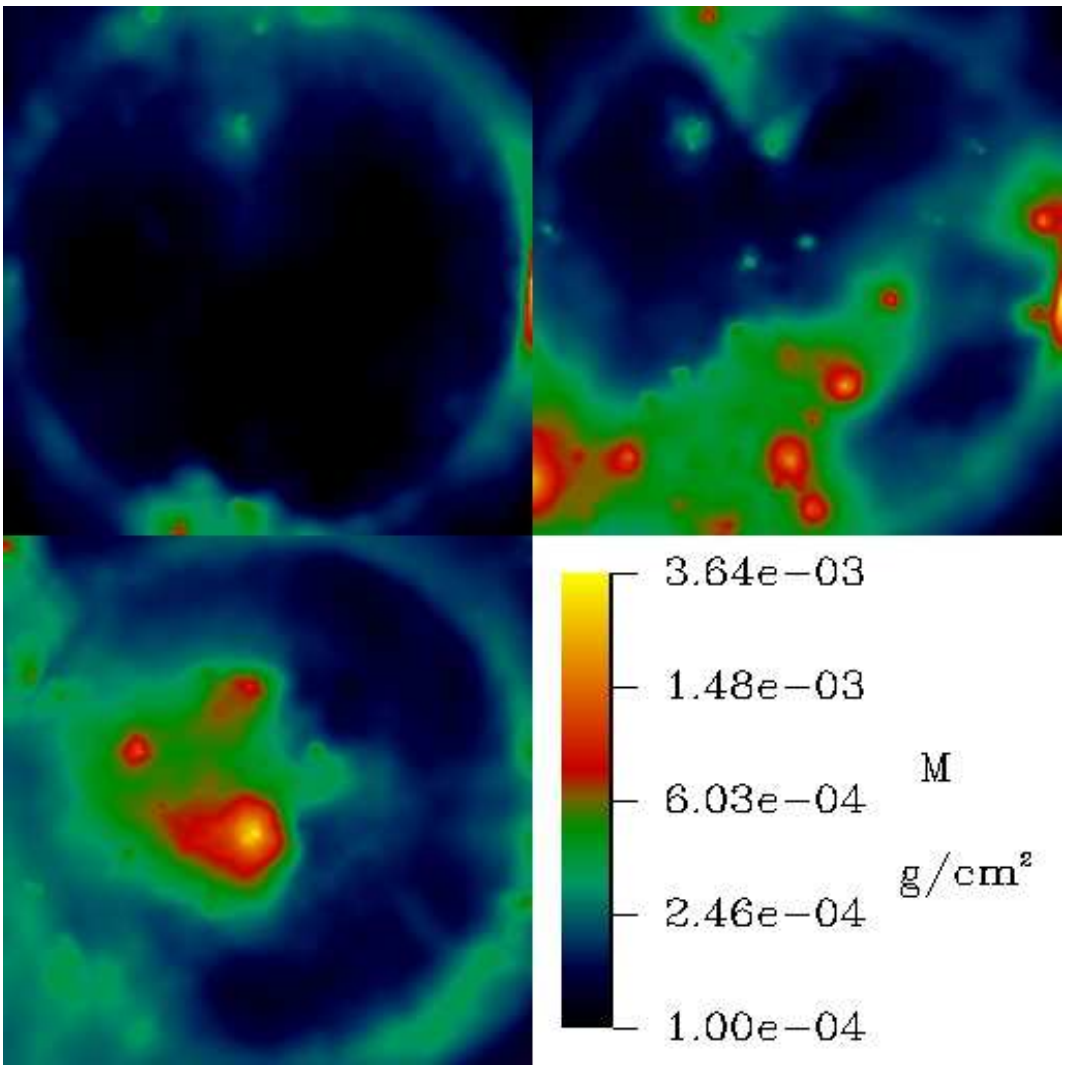


**Figure 5.12.** Projected surface gas mass density of the C1 cluster along the $z$ (top left), $y$ (top right) and $x$ (bottom left) directions, after removing the contribution from all gas particles which inside the virial region of the cluster.

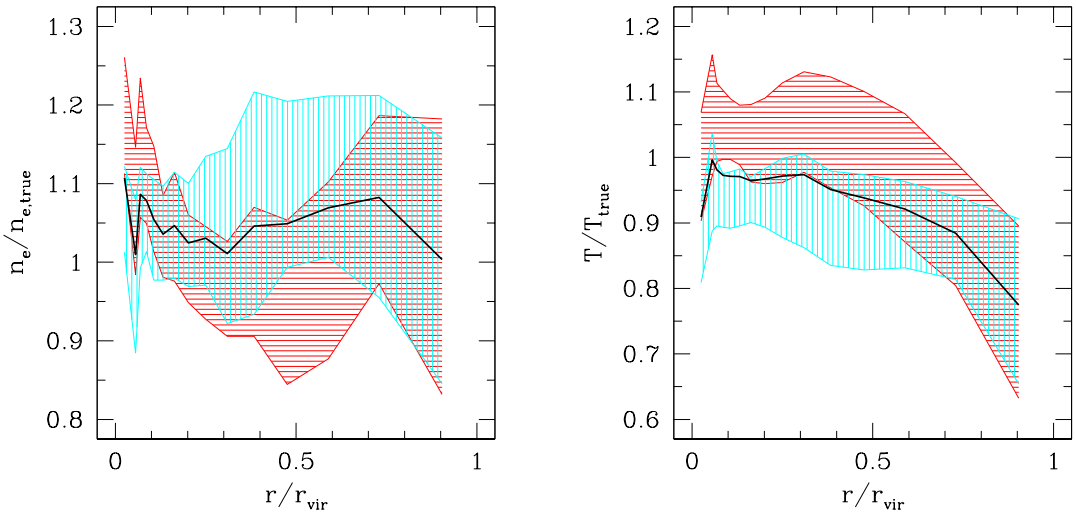


**Figure 5.13.** The ratio between the reconstructed and the true (mass–weighted) temperature and density profiles. The shaded areas encompass the $\pm 1\sigma$ regions of the recovered profiles over the ensemble of simulated clusters. The horizontally shaded area is for the projections along the $z$ axis, while the vertically shaded area is for the projections along the other two axes. The black line shows the mean over all projections of all clusters.

a mean value of about 20 per cent at $r_{vir}$, as a consequence of the relatively larger contamination by fore/background structures. The scatter is generally larger than the uncertainty introduced by the noise, so that it has to be considered as intrinsic to the measure. This scatter has different origins, such as unresolved gas clumps, asphericity of the clusters, fore–background contaminations. In general, the temperature recovered from the projection along the $z$ axis is slightly larger than the one from the other two axes. The difference is more apparent in the central regions and becomes smaller in the outskirts. The reason for this behaviour is that the temperature reconstruction is more affected by the tSZ signal. Along the direction of maximum elongation, this signal is enhanced since the ICM pressure is integrated along a larger path. The tSZ signal receives then an important contribution from cluster regions where the density is underestimated. As a result the reconstructed temperature is correspondingly increased to compensate for this effect.

In figures 5.8–5.11 we also show with a dotted line the three–dimensional profile of the spectroscopic–like temperature (see Section 3.4). This temperature gives more weight to the low–temperature phase in a thermally complex ICM. This is the reason for the drop of the $T_{sl}$ profile at the cluster centre and for the wiggles which mark the positions of merging sub-clumps which are relatively colder than the ambient ICM. In general, the profile of $T_{sl}$ are lower than those of the electron temperature, by an amount which is larger for hotter systems (see also Rasia et al., 2005). These figures highlight that the temperature profiles, as obtained from our deprojection analysis, are much closer to the mass–weighted temperature, which measures the total thermal content of the ICM, than to $T_{sl}$. An important consequence of this difference will clearly be the estimate of the total cluster mass from the application of hydrostatic equilibrium. We will discuss the application of our deprojection method to cluster mass estimates in Chapter 6.

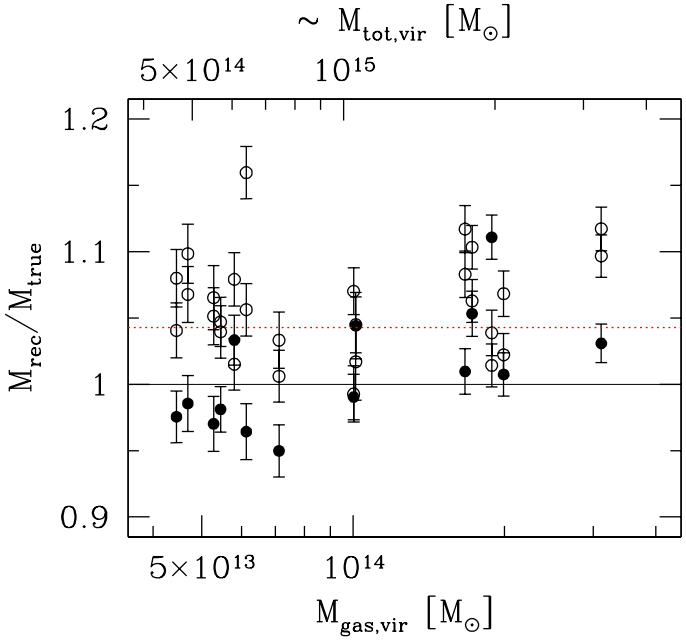


**Figure 5.14.** The ratio between the recovered and the true values of the total gas mass for simulated clusters out to $R_{vir}$. For each cluster we show the result of the deprojection along the three orthogonal directions, with the projection corresponding to the maximum elongation being marked with a filled circle. Errorbars correspond to the $1\sigma$ confidence level, by accounting for the full error correlation matrix when integrating the 3D gas density profiles. The horizontal dotted line shows the average value of the ratio.

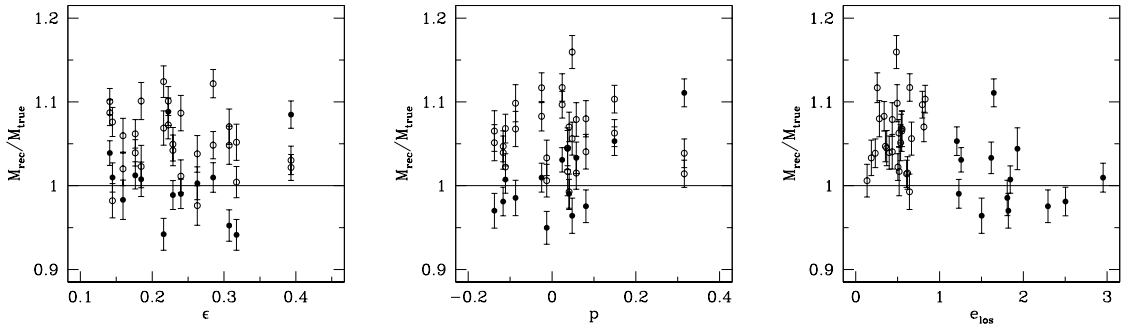


**Figure 5.15.** The same of figure 5.14, but as a function of cluster ellipticity (left panel), prolateness (central panel) and elongation along the line of sight (right panel).

### 5.3.3 Recovering the gas mass

As a first application of our deprojection procedure, we compute the gas mass of the clusters, which is calculated simply by summing up the mass contained in each radial bin. Since the bins are not independent, the errors on the total gas mass have been calculated by using both variances and covariances of the values of the density at different radii.

$$\sigma_M^2 = \frac{1}{N-1} \sum_{i=0}^{N} \sum_{j=0}^{N} \sigma_{m,ij}, \tag{5.12}$$

where $\sigma_{m,ij}$ is the covariance between the mass content of the $i$-th and of the $j$-th shells, directly obtained from the covariance between the gas density in different bins (e.g., see left panel of figure5.6). Note that since the covariance between the density in adjacent bins is generally negative, neglecting it would lead to a systematic overestimate of the error on the mass.

We give the results on the estimate of gas mass for the whole set of 14 simulated clusters. The small overestimate found for the density profiles is obviously propagated to the estimate of the total gas mass. The resulting bias turns out to be very small, and amounts to about 4 percent, with no obvious trend with the cluster mass. This demonstrates that residual gas clumping, after the removal of the substructures identified in the X–ray maps, has a small effect on the our capability of recovering the total mass of the ICM. We note that the cluster-by-cluster variance is often comparable to the "projection variance", i.e. to the difference found when projecting the same clusters along different directions. We also note that the uncertainties in the individual $M_{gas}$ estimates, typically of the order of a few per cent, are smaller than the scatter. This indicates that the intrinsic scatter in the recovered gas mass is in fact associated to the deviations of the simulated clusters from perfect spherical symmetry.

### 5.3.4 The effect of morphology

In order to better understand how morphology affects the deprojection, we plot in figure 5.15 the recovered gas mass as a function of cluster ellipticity, prolateness and elongation along the line of sight. The ellipticity of a triaxial object is defined as:

$$\epsilon = \frac{1}{2} \frac{a_{min}^{-1} - a_{max}^{-1}}{a_{min}^{-1} + a_{med}^{-1} + a_{max}^{-1}} \tag{5.13}$$

and the prolateness as:

$$p = \frac{1}{2} \frac{a_{min}^{-1} - 2a_{med}^{-1} + a_{max}^{-1}}{a_{min}^{-1} + a_{med}^{-1} + a_{max}^{-1}} \tag{5.14}$$

The elongation is defined as the ratio between the semi–axis aligned with the line of sight and the larger of the other two semi–axes.

The gas mass recovered from the projection along the principal axis is generally lower than those from the other two projections. This underestimate generally is anticorrelated with the elongation of the cluster, although with a substantial scatter. From the left and the central panels of figure 5.15, we do not find any significant correlation between the global 3D morphology of the clusters (prolateness and ellipticity) and the bias in the deprojection. Instead, as shown in the right panel, any effect in the gas mass recovery is driven by the orientation of the cluster.

## 5.4 Conclusions

In this Chapter we have presented results of our deprojection methods, aimed at recovering the three-dimensional density and temperature profiles of galaxy clusters, by combining X–ray surface brightness and thermal SZ (tSZ) maps. The main aim of our analysis is to verify to what accuracy one can recover the thermal structure of the ICM by taking advantage of the different dependence of the X–ray and tSZ signal on the gas density and temperature, thereby avoiding performing X–ray spectroscopy. The two deprojection methods considered are both based on assuming spherical symmetry of the clusters.

The first one follows a geometrical approach, in which the 3D profiles are recovered with an iterative procedure that deprojects the observed images starting from the outermost ring and proceeding inwards. The second method assumes the values of the 3D gas density and temperature profiles at different radii and computes from them the expected SZ and X–ray surface brightness which is then compared to the observations with a maximum likelihood approach. In the computation of the likelihood, we also introduced a regularization term, which allows us to suppress spurious oscillations in the recovered profiles. Using a Monte Carlo Markov Chain (MCMC) approach to optimize the sampling of the parameter space, this second method also allows us to recover the full correlation matrix of the errors in the parameter fitting.

The main results of our analysis can be summarized as follows.

- The application of both methods to an idealized spherical polytropic $\beta$–model shows that the 3D profiles are always recovered with excellent precision (of about 3–4 per cent), thus demonstrating that such methods do not suffer from any intrinsic bias.

- The application of the maximum–likelihood method to hydrodynamical simulations of galaxy clusters always provides deprojected profiles of gas density and temperature, which are in good agreement with the true ones, out to the virial radius. We find a small ($\lesssim$ 10 per cent) systematic overestimate of the gas density, which is due to the presence of some residual gas clumping, which is not removed by masking out the obvious substructures identified in the X–ray maps.

- The total gas mass is recovered with a small bias of 4 per cent, with a sizable scatter of about 5 per cent. This result shows that residual gas clumping should have a minor impact in the estimate of the total gas mass. We do not find any trend in the recovery of the gas mass with the total cluster mass.

- The gas mass reconstructed along the maximum elongation axis is generally lower (by up to 10 per cent) with respect to the mass reconstructed along the other two projection axes, the size of this effect being larger for more elongated clusters.

- The temperature is generally well recovered, with $\sim$ 10 per cent deviations from the true one out to $\simeq 0.7 R_{\rm vir}$. The rather small size of this bias confirms that the combination with tSZ data is a valid alternative to X–ray spectroscopy for temperature measurements. The temperature reconstructed from the projection along the axis with maximum elongation is slightly higher than those from the other two axes, particularly in the inner regions.

Our results confirm the great potentials of combining spatially resolved tSZ and X–ray observations to recover the thermal structure of the ICM. In the next Chapter, we

present a development of this method, which implements the solution of the hydrostatic equilibrium equation, in order to reconstruct also the total mass of the cluster.

The results presented in this Chapter have been published in Ameglio et al. (2007).

# Chapter 6

# Reconstruction of the cluster total masses

A number of important cosmological tests are based on mass measurements in galaxy clusters. In particular the mass function and its redshift evolution are highly sensitive to the underlying cosmology and provides constraints on $\Omega_M$, $\Omega_\Lambda$, $\sigma_8$ and possibly on the dark energy equation of state $w$. Precise mass measurement in galaxy cluster are then necessary to calibrate clusters as precision tools for cosmology (e.g., Haiman et al. 2001; Rosati et al. 2002; Pierpaoli et al. 2003; Voit 2005).

In X–ray studies, the total collapsed mass of a cluster is determined by applying the hydrostatic equilibrium equation to gas density and temperature profiles. Rasia et al. (2004) (see also Kay et al., 2004) analyzed a set of hydrodynamical simulations and found that the gas is not in a state of perfect hydrostatic equilibrium. Instead, they found deviations up to 20%, which have the effect of systematically biasing low the reconstruction of the total gravitating mass. To quantify this bias, several authors analyzed sets of hydrodynamical simulations by following the same procedure which is used in X-ray observations, finding that generally the reconstructed mass is underestimated by 10–20%. The amount of this underestimate depends on both the model assumed and the dynamical state of the cluster. Rasia et al. (2006a) showed that adopting an appropriate model for gas and/or mass may substantially increase the bias. In particular, the isothermal $\beta$–model seems to give the worst reconstruction. Nagai et al. (2007) differentiated their sample in relaxed and unrelaxed clusters, with the latter showing a larger scatter in mass reconstruction. Following the same direction, Jeltema et al. (2007) found a correlation between the quantitative measures of the morphology of the X–ray images and the bias in the mass reconstruction, although with a quite large scatter. Finally, Puchwein & Bartelmann (2007) probed the deviations from hydrostatic equilibrium in different stages of a merger process.

The total mass reconstruction via the hydrostatic equilibrium equation involves the derivative of both gas density and temperature. Then, an accurate mass determination requires high–quality temperature measurements. For this reason, X–ray studies are often limited to the inner regions of the clusters and to objects at moderate redshift. Instead, we propose to use a combination of X–ray imaging and tSZ data, which avoids the use of X–ray spectroscopy. Different algorithms, which use a combination of tSZ and X–ray data, have been proposed by other authors and applied to analytical cluster models and/or sets of simulated clusters. A brief review of the relevant papers is presented in the

introduction of Chapter 5. Owing to the low resolution of past tSZ telescopes, this method has been applied to a handful of observed clusters (Zhang & Wu, 2000; Pointecouteau et al., 2002), with results that are generally consistent with those obtained by analyzing the same objects through X–ray spectroscopy.

Accurate mass profiles reconstruction can also be used as probes for cosmology. In fact, mass profiles are expected to follow a unique functional form, which is valid over a wide range of masses, from white dwarfs to massive galaxy clusters. A formulation for this function has been provided by fitting the mass profiles in a set of N–body simulations by Navarro et al. (1997) (NFW hereafter). High quality X–ray data from Chandra and XMM–Newton observations seem to confirm the validity of the NFW model, out to large portions of the cluster virial radius (e.g. Pratt & Arnaud, 2002; Pointecouteau et al., 2005; Vikhlinin et al., 2006; Zappacosta et al., 2006).

In this Chapter, we extend the deprojection algorithm presented in Chapter 5, by including the solution of the hydrostatic equilibrium equation. Using this technique, we analyze a set of 14 simulated clusters having $T_{\rm sl} \gtrsim 3$ keV, reconstructing the total mass profiles from X–ray and tSZ images. Our results show that the total mass profile can be recovered, with a bias which is mostly due to deviations from perfect hydrostatic equilibrium. The analysis present here could be easily performed with the present generation of X–ray telescopes. However, future X–ray observations with much lower background (as expected from the eROSITA mission) will allow to extend further in redshift the suitable sample of galaxy clusters. As for the tSZ data, exploiting the full potential of the technique would require spatially resolved observations, which will be available from upcoming (or just started) SZ experiments.

This Chapter is structured as follows. In Section 6.1 we present the hydrostatic equilibrium equation and probe the deviations from this equilibrium in the ICM of our set of simulated clusters. This represents a preliminary test which will provide a better understanding of our final results. The deprojection technique is explained in detail in Chapter 5, while section 6.2 describes the implementation of the hydrostatic equilibrium equation in the algorithm. We use the same subset of simulated clusters having $T_{sl} \gtrsim 3$ keV, which is described in Chapter 5 and also the four clusters (C1, C2, C3 and C4) chosen as examples are the same. Section 6.3 presents our results on the analysis of simulated clusters. Finally, our main conclusions are summarized in Section 6.4.

## 6.1 The hydrostatic equilibrium

The total mass profiles from observations of the ICM in galaxy clusters is determined by assuming that the gas is in hydrostatic equilibrium in the gravitational potential. For a spherically symmetric cluster, the equation of the hydrostatic equilibrium can be cast in the form:

$$M_{tot}(< r) = -\frac{kT\, r}{G\mu m_p}\left[\frac{d\ln n_e}{d\ln r} + \frac{d\ln T}{d\ln r}\right], \tag{6.1}$$

where $G$ is the gravitational constant, $\mu$ is the mean molecular weight of the gas ($\mu \simeq 0.6$ for a gas of primordial composition), $m_p$ is the proton mass and $r$ is the distance from the center of the cluster. Note that the mass at a given radius depends only upon the local pressure derivative and is unaffected by the regions interior or exterior to the radius of interest.

Eq. (6.1) essentially states that the gas pressure balances the attraction due to the gravitational field and keeps the gas on a stable (static) equilibrium. This would be

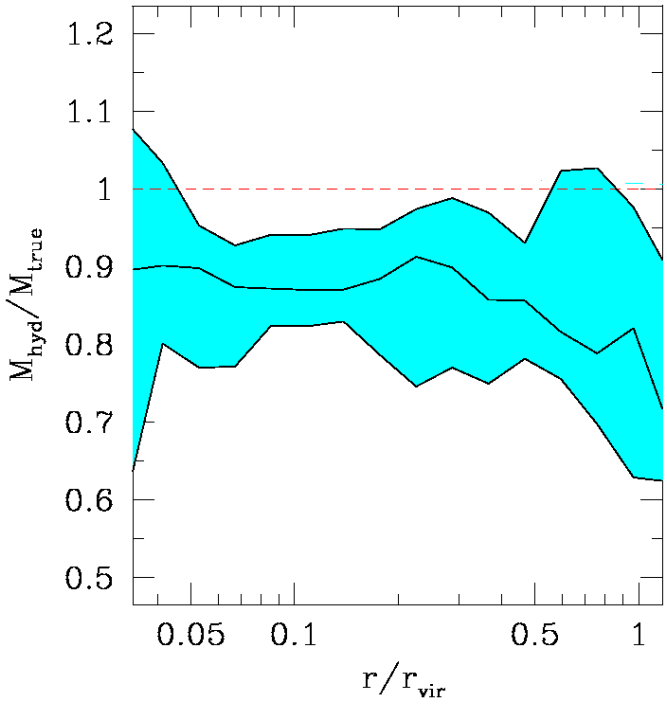


**Figure 6.1.** Ratio between the hydrostatic and the true mass profile averaged over the set of simulated clusters. The shaded area encompasses the 16 and 84 percentile over the ensemble of the clusters.

the case of a perfectly relaxed cluster. Indeed, deviation from this perfect equilibrium are instead quite common, owing to non–thermal pressure support given by turbulent motions (Rasia et al., 2004; Kay et al., 2004; Dolag et al., 2004; Nagai et al., 2007). These processes are responsible for an extra, non–thermal pressure support in eq. (6.1). thus leading to an underestimate of the total gravitating mass. As a consequence, the mass estimated through the hydrostatic equilibrium equations is found in simulations to be systematically lower than the true one. Rasia et al. (2004) show that an extra–term should be added in the equation of the hydrostatic equilibrium, which takes into account turbulent gas motions. Jeltema et al. (2007) find a correlation between the amount of substructures and the underestimate of the total mass, in a set of hydrodynamical simulations. However, the large scatter in this correlation around the mean relation suggests that substructures may not be the only sources of the bias in the mass reconstruction.

Before applying our procedure of mass reconstruction, we probe the deviations from the hydrostatic equilibrium in our simulated clusters, in order to better understand the origin of the errors in our final results. We apply the eq. (6.1) to the true, 3-D density and temperature profiles, by performing a numerical derivative in the log-log space. We will refer to the mass so computed as *hydrostatic mass* $M_{hyd}$ hereafter. In the case of a perfect hydrostatic gas, this would coincide with the total mass profile. In figure 6.1 we show the profiles of the ratio $M_{hyd}/M_{true}$ averaged over our set of simulated clusters. From the analysis of simulated cluster, we generally find an underestimate of the total mass $\sim$ 10–15% out to about $R_{500}$, which is in line with the values found by other authors (Nagai et al., 2007; Puchwein & Bartelmann, 2007; Jeltema et al., 2007). In the outskirts

the underestimate increases to about 20% at the virial radius, owing to a larger fraction of turbulent motions. This is consistent with the expectation that outer cluster regions dieviate more from the hydrostatic equilibrium condiction, due to the presence of ongoing merging and accretion processes.

## 6.2 Methods of mass profile reconstruction

The analysis presented in this Section represents a development of the maximum likelihood deprojection described in section 5.1.2. The algorithm is modified in order to solve the hydrostatic equilibrium equation while deprojecting the cluster images. In this way, the gas density and temperature and the total mass profiles are derived simultaneously and in a fully self–consistent procedure.

The fitting parameters are in this case the gas density and the total mass profiles. As described in Section 5.1.2, the cluster image is divided into N concentric annuli equally spaced in logarithm. The cluster is then modelled as composed by N concentric spherical shells, having the same radii of the annuli. However, in this case the gas density and the total mass are the fitting parameters, while the gas temperature is derived by solving the hydrostatic equilibrium equation.

As for the gas density in each spherical shell, it is treated as a free parameter, as described in Section 5.1.2. As for the total mass, the adopt two different approaches.

- **Method 1**. This method does not assume any particular functional form for the mass profile. Instead, the integrated mass enclosed by the mean radius of each shell is treated as a free parameter. The only constraint that we impose is that the mass has to increase with radius, in order to avoid unphysical solutions. The advantage of this method is that it provides a completely model–independent reconstruction of the mass profile, which relies only on the hydrostatic equilibrium assumption. However, the request of having a mass growing with radius could slightly bias high the recovered profile.

- **Method 2**. This method adopts the NFW functional form. Its major advantage is that the reconstruction becomes much more stable, at the cost of assuming a particular model for the mass profile. The NFW functional form is:

$$M(< r) = 4\pi r_s^3 \rho_{crit} \delta_c f(x) \tag{6.2}$$

  where $r_s$ is a characteristic scale length, $x$ is the distance from the center of the cluster in units of $r_s$, $f(x) = ln(1+x) - x/(1+x)$, $\rho_{crit}$ is the critical density for collapsing Universe and $\delta_c$ is a characteristic overdensity. It is common (and more convenient) to rewrite the above equation by expressing $\delta_c$ as a function of the concentration parameter $c = r_\Delta / r_s$, where $\Delta$ is a given overdensity. Here and in the following, we adopt the virial overdensity, which in our cosmology corresponds to $\Delta = 100$. The characteristic overdensity is rewritten in terms of:

$$\delta_c = \frac{\Delta}{3} \frac{c^3}{f(x=c)} \tag{6.3}$$

  The NFW profile becomes now:

$$M(< r) = \frac{4\pi}{3} (r_s c)^3 \rho_{crit} \Delta \frac{f(x)}{f(x=c)} \tag{6.4}$$

As for the temperature profile, it is computed in both cases by assuming that the gas is in hydrostatic equilibrium in the potential well of the total mass distribution (see paragraph 6.1). By inverting the equation of the hydrostatic equilibrium one first obtains the gas pressure profile and then the gas temperature, by combining it with the gas density. In this way we obtain:

$$kT(r) = \frac{1}{n_e(r)} \left\{ G\mu m_p \int_{r_{out}}^{r} \frac{n_e M_{tot}(< r)}{r^2} dr - P(r_{out}) \right\}, \tag{6.5}$$

where the integral is performed from the outermost radius from which the deprojection is performed, $r_{out}$, and the radius of interest $r$.

For both methods, at each iteration of the Markov Chain Monte Carlo procedure, new profiles for gas density and total mass are proposed and the corresponding temperature profile is computed. The gas density and temperature profiles are combined to compute the X–ray and tSZ profiles, which are compared to the ones in the maps to compute the joint likelihood. The new values are either accepted or rejected according to the criterion described in Section 5.1.2.

Since the hydrostatic equilibrium equation constraints only the pressure difference between two points, it is necessary to introduce a further parameter $P_{out}$, which represents the pressure at the outermost radius (see also Morandi et al., 2007). In particular, in the case of the free profile this parameter is completely degenerate with the mass enclosed in the outermost bin. The mass has only a lower boundary, given by the fact that it cannot be lower than the mass enclosed by the inner bin. This turns into an instability of the fit which generates an overestimate of the global mass. This problem is solved by applying to the pressure profile the regularization constraint which is described in Section 5.1.2.

## 6.3 Results

### 6.3.1 Total mass profiles: method 1

The deprojection technique reconstruct the gas properties (density and temperature) together with the total mass profiles. However, we point out that the recontructed gas properties are virtually identical to those obtained with the analysis presented in Chapter 5 (i.e. without solving the hydrostatic equilibrium equation). For this reason, here we will show only the mass reconstruction.

In figure 6.2 we show the reconstructed profiles of the 4 clusters chosen as examples. We generally find an underestimate of about 10–15% throughout the virial radius, with slightly larger deviations in the center and in the outskirts of the clusters. In many cases, in the first inner bin we do not find a lower boundary for the mass. We point out that the reconstructed profiles are generally closer to $M_{hyd}$ than to the true mass profile, thus suggesting that the main source of systematics is intrinsic, namely the deviation of the gas from perfect hydrostatic equilibrium. However, in the outskirts the reconstructed profile tends to be larger than $M_{hyd}$. We attribute this to a lower signal–to–noise (SNR $\sim 4-5$) and to a larger impact of fore/background contaminations in these regions. In fact, the recovered mass at these radii has only a lower boundary (i.e. it cannot be lower than the mass at inner radii), but not an upper one. As a consequence, any deviation will be in the direction of increasing the mass.

In the case of the C1 cluster (figure 6.2, upper left panel) one can see the effect of fore/background contaminations. The recovered mass is systematically overestimated by

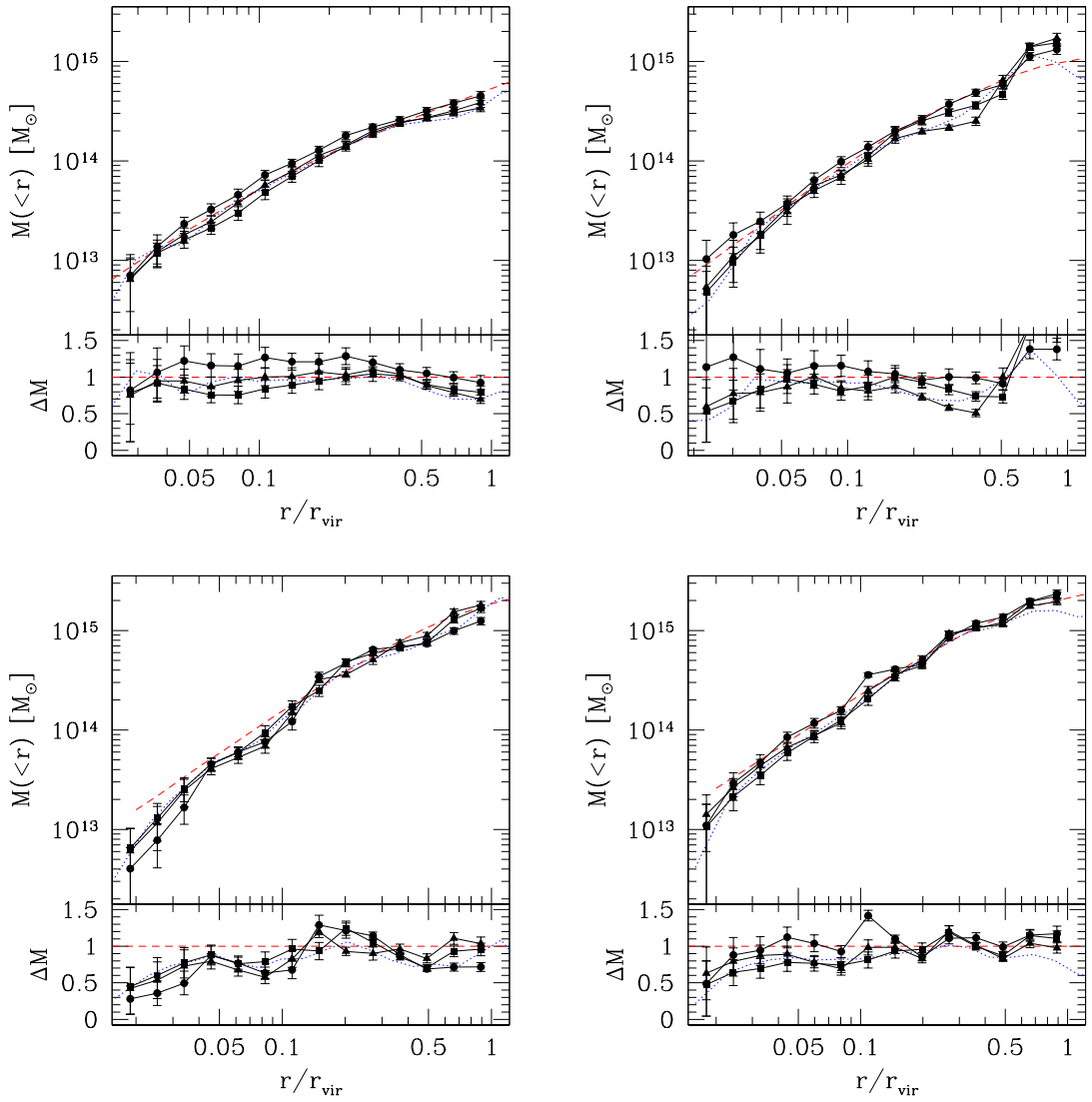


**Figure 6.2.** Mass reconstruction for the clusters C1 (upper left), C2 (upper right), C3 (lower left) and C4 (lower right), while adopting the free mass profile. The black triangles (squares, circles) and line represent the reconstruction along the $x$ ($y$, $z$) axis. The red dashed line represents the true mass profile, while the blue dotted line is hydrostatic mass obtained from the application of eq. (6.1) to the true 3–dimensional gas density and temperature profiles. The lower part of each panel shows the ratio between the same quantities and the true mass.

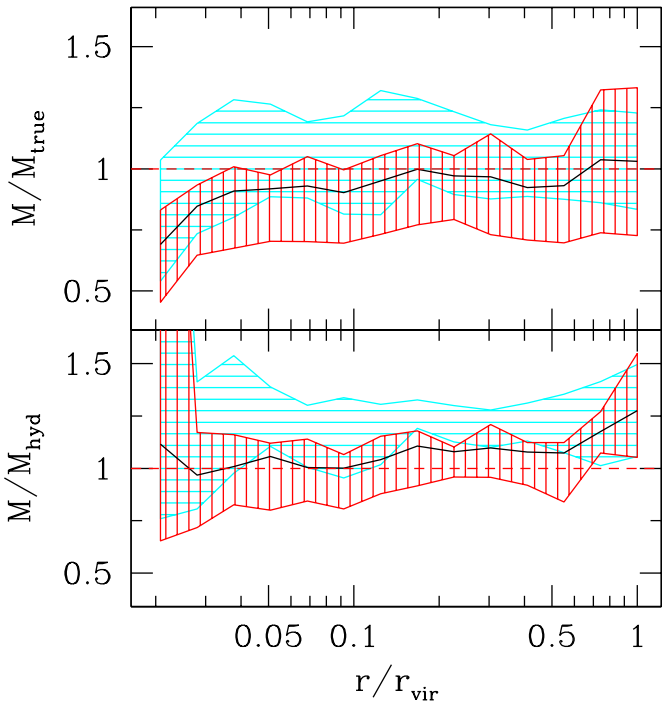


**Figure 6.3.** Reconstructed vs. true (upper panel) and hydrostatic (lower panel) mass, averaged over the set of simulated clusters. In each panel, the orizontally (vertically) shaded area represents the mean$\pm 1\sigma$ over the projections along the $z$ ($x$ and $y$) axis. The black line represents the mean over all the projections of all the clusters.

about 20%. In Section 5.3.2, by analyzing the same object, we show that the effect of such contaminations is basically to boost the temperature profile by a comparable factor. By considering eq. (6.1) it is clear that this is the origin of the mass overestimate.

In all these four clusters, the mass reconstructed from the projection along the maximum elongation axis $z$ is larger (by different amounts) than the one reconstructed from the other two projections. This behaviour is confirmed when considering the whole set of simulated clusters, as shown in figure 6.3. As also observed in the example clusters, the reconstructed profiles generally underestimate the true mass by a factor of about 10–15%, except in the outskirts, where they seem to well recover the true mass. However, we point out that this better agreement is likely a consequence of a small systematic of our technique, as discussed above. Futhermore, they are very close to the hydrostatic mass in the inner regions, while they tend to be much larger than the hydrostatic mass when moving towards the outskirts. This clearly indicates that the main source of systematic uncertainty are the deviation of the ICM form the hydrostatic equilibrium and that our method of reconstruction is basically unbiased, in that it precisely recovers the hydrostatic mass profiles.

### 6.3.2 Total mass profiles: method 2

In figure 6.4 we show the reconstructed profiles of the 4 clusters chosen as examples. The figure does not reports the errorbars because the uncertainties on the reconstructed

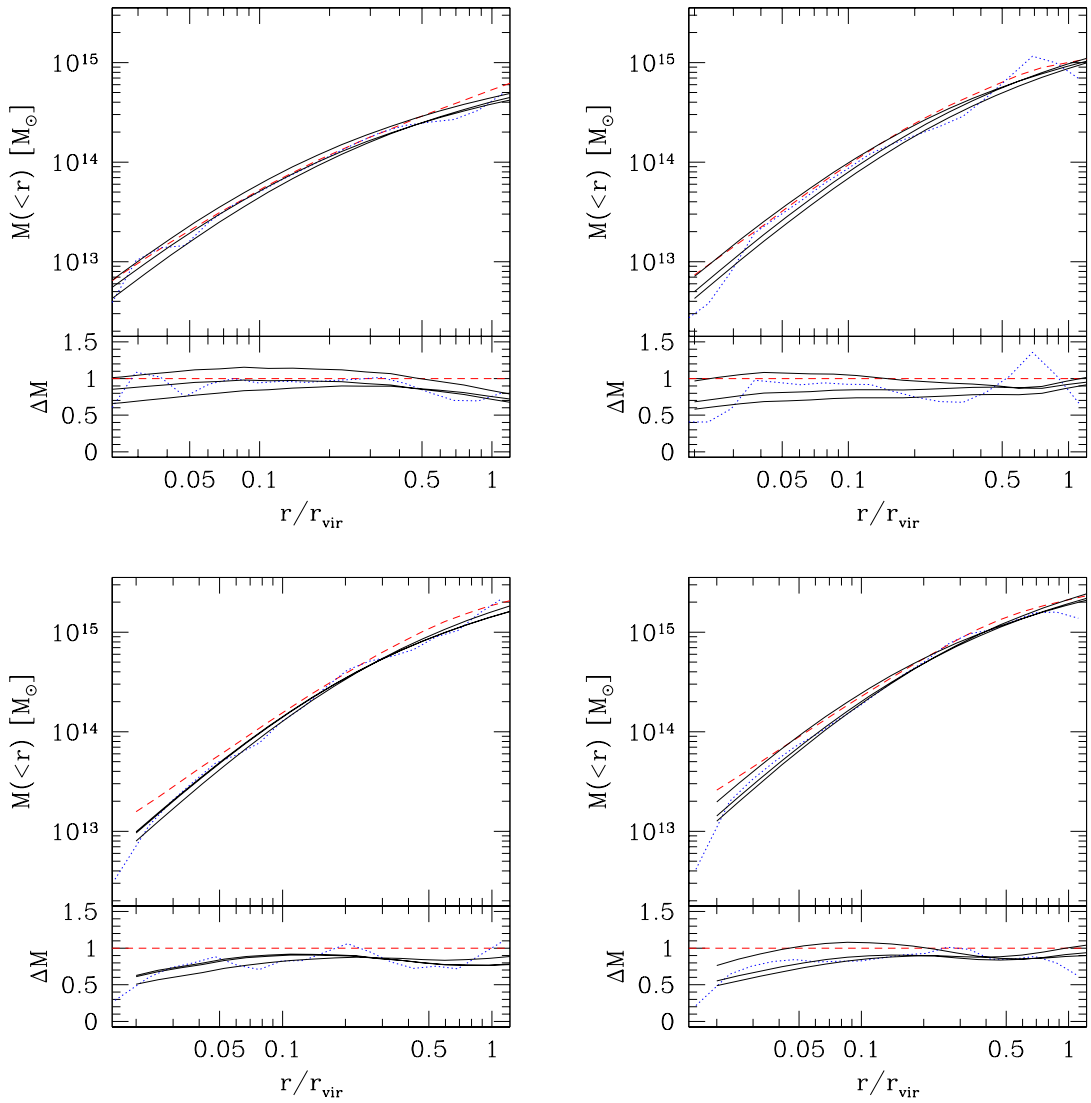


**Figure 6.4.** Mass reconstruction for the clusters C1, C2, C3 and C4, with the NFW mass profile. The black line represent the reconstruction along the three axes of projection. The red line represents the true mass profile, the blue dashed line the hydrostatic mass

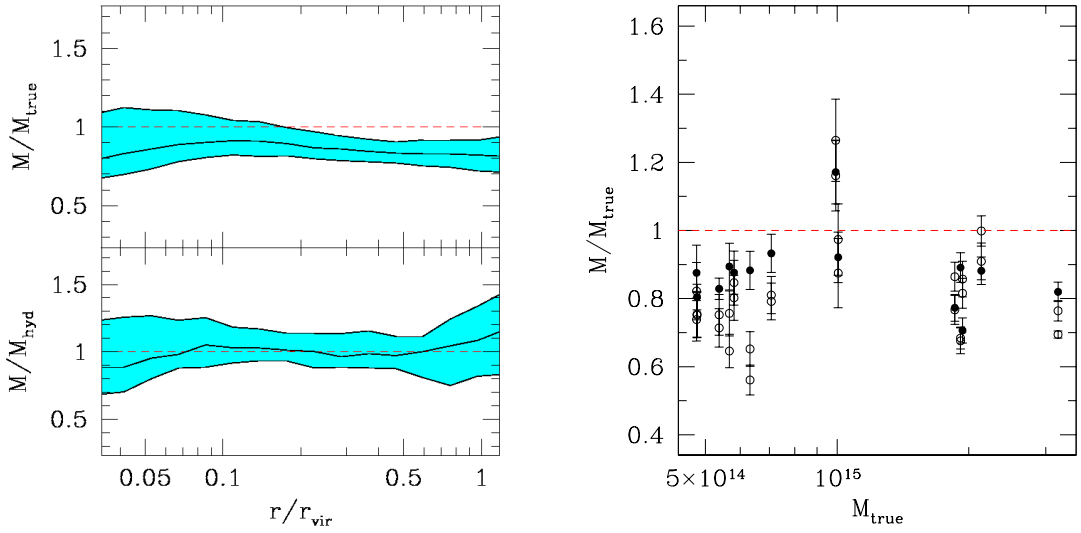


**Figure 6.5.** Left panel: reconstructed vs. true (upper panel) and hydrostatic (lower panel) mass profiles, averaged over the whole set of simulated clusters, while fitting the NFW profile over the whole virial radius (method 2). The shaded area encompasses 68% of the recovered profiles, while the solid line reports the median. Right panel: accuracy in the virial mass reconstruction. Filled (empty) circles are for the reconstruction from the projection along the $z$ ($x$, $y$) axis. Errorbars represent the $1\sigma$ confidence level.

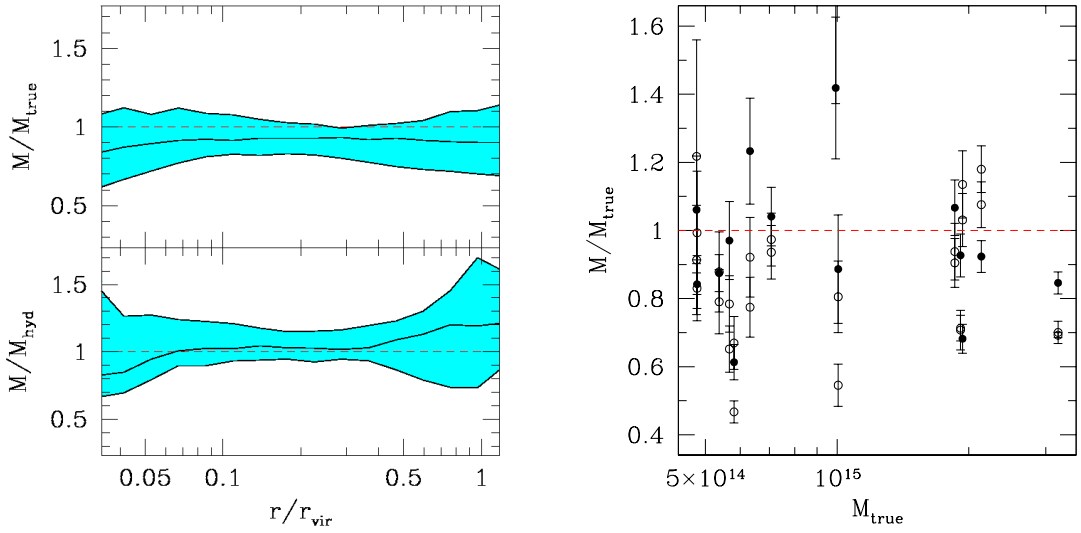


**Figure 6.6.** The same as figure 6.5, but fitting the NFW profile out to only $R_{500}$ end extrapolating the profile in the outer regions.

profiles are contained in the errors on the model parameters $r_s$ and $c$, which are generally recovered with typical errors of a few percent. However, the $c$ and $r_s$ values that we find are larger and smaller, respectively, than those generally found by the analysis of N–body simulations, at a given mass. The origin of this difference can be the way in which the fit is performed. In fact, this fit is commonly done on the differential *density* profile, while we use the integrated mass profile. Hence, our fit give more relative weight to the outskirts than to the inner regions. We point out that this difference does not substantially affect the accuracy of the mass profiles reconstruction, since the we recovered values of $r_s$ and $c$ in the direction of degeneracy of the fitting in the pararameter space. A more detailed comparison of our values with the values in literature is left to future work. Clearly, imposing an analytical form for the mass profiles has the important advantage of providing a much more stable reconstruction and a smooth profile. Similarly to the case of the method 1, the recovered mass is much closer to the hydrostatic mass than to the true one.

The lower part of the left panel of figure 6.5 shows the accuracy of the recoverd mass, averaged over the whole set of simulated clusters. We find that the mass profile is generally underestimated by a factor of 15–20%. The larger bias with respect to Method 1 is probably due to the fact that here we are adopting an analytical model. The origin of this bias may be understood by noting that in the outskirts the hydrostatic mass tends to underestimate the true one by a larger amount (see figure 6.1). Since the procedure aims at fitting the whole profile, a choice of parameters which produce a lower normalization turns out to be favoured. The right panel of the same figure reports instead the accuracy in recovering the total mass as a function of the true mass of the cluster. We find that the virial mass on average is recovered with a $\sim 20\%$ accuracy, $M_{rec}/M_{true} = 0.80 \pm 0.09$. We do not find any significant trend with cluster mass.

This result suggests that the mass is better recovered while limiting the fit to a smaller region, typically $r < R_{500}$. This radius represents the outer limit of most of the present X–ray observations. For this reason, we repeat the analysis by limiting the fit to this radius and extrapolating the NFW model out to the virial radius. The accuracy of this technique is shown in figure 6.6, left panel, after averaging over the whole set of simulated clusters. We find that the recovered profiles are close to the hydrostatic mass out to the fitting radius, as expected, with the mass underestimated by 10% out to the virial radius. This is quite interesting since the fit is limited to a much smaller radius. This suggests that: *i)* the outskirts are much more disturbed and there are more deviations from hydrostatic equilibrium *ii)* the NFW provides a well description of the mass profile; since its extrapolation out to $R_{vir}$ still provides a good description of the mass profile. The virial mass is recovered with good accuracy, $M_{rec}/M_{true} = 0.88 \pm 0.18$ (see figure 6.6, right panel). The larger scatter is due to the fact the we are now fitting a smaller region of the cluster.

### 6.3.3 Estimating the virial radius

In the results shown so far, we used the virial radius computed directly from the simulation data. For real objects, instead, the virial radius is generally not known in advance, but it is estimated directly from the recovered mass profile. However, if the mass profile is under/overestimated, also the estimate of the virial radius will be biased low/high. This turns out into a larger bias in the recovered virial mass (see also Nagai et al., 2007). The left panel of figure 6.7 shows the reconstructed virial radii $R_{vir,fit}$ versus the true ones

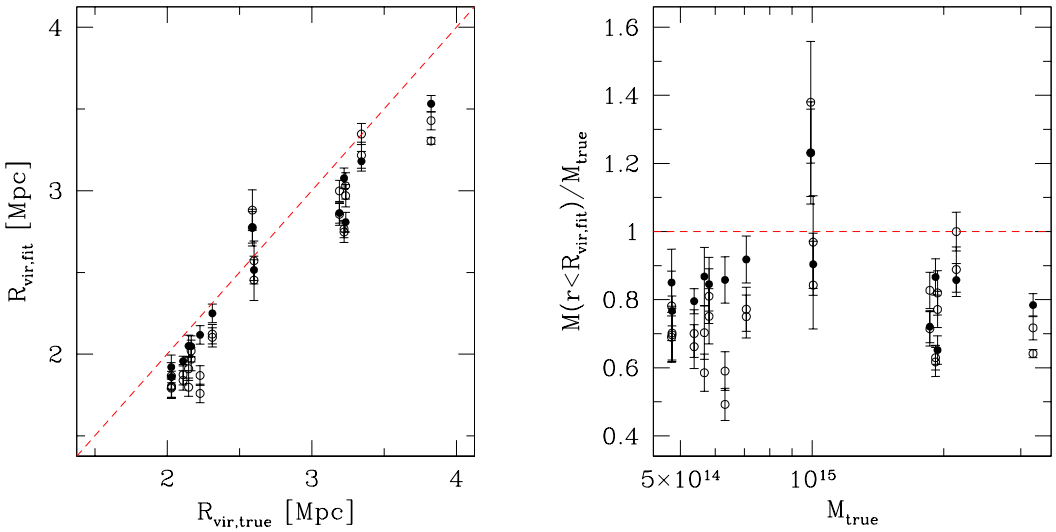


**Figure 6.7.** Left panel: estimated virial radius $R_{vir,fit}$ versus the one computed from simulation data $R_{vir,sim}$. The dashed line reports the one–to–one relation. Right panel: recovered vs. true mass, while using $R_{vir,fit}$. Note that the two masses correspond to different radii. In both panels, filled (empty) circles are for the reconstruction from the projection along the $z$ ($x$, $y$) axis. Errorbars represent $1\sigma$ confidence level.

$R_{vir,sim}$ for the set of simulated clusters. The right panel of the same figure reports the recovered virial mass while using $R_{vir,fit}$ versus the true virial mass. This plot looks very similar to the right panel of figure 6.5, which presents the same quantity, but adopting the virial radius directly on the simulation data. Indeed, for all the cluster the bias is slightly larger, owing to the fact that the two masses are now computed at different radii. In fact, the mean values is now $M_{vir,fit}/M_{vir,true} = 0.75 \pm 0.11$, which is about 4% lower.

## 6.4 Conclusions

Correctly measuring the total cluster mass is of fundamental importance for clusters to be used as tools for precision cosmology. In cluster studies based on the observations of the ICM the mass is obtained by assuming that the gas lies in hydrostatic equilibrium in the cluster gravitational potential. In this Chapter we discussed a development of the maximum–likelihood deprojection technique described in Chapter 5, in which we implemented the solution of the hydrostatic equilibrium equation, so as to derive profiles of gas density and temperature and total mass simultaneously. We first probe the condition of hydrostatic equilibrium by computing the *hydrostatic mass*, which is obtained by applying the equation to the true gas density and temperature profiles, given by the simulation data. Then, we showed the results obtained with two different methods to recover the total mass profile. Method 1 adopts a model–independent approach, with the only constraint of having a mass which increases with radius, in order to avoid unphysical solutions. Method 2 is instead based on assuming the profile proposed by Navarro et al. (1997) (NFW hereafter).

Our main conclusions may be summarized as follows.

- We find in our simulated clusters that deviations from hydrostatic equilibrium are quite common, due to the presence of non–thermal pressure support (e.g. stochastic and bulk gas motions). The deviations are of about 10% of the true mass, in line with previous results presented in the literature. This bias increases from $r \sim 1/2R_{vir}$, reaching 20% at $R_{vir}$, probably owing to stronger impact of merger events in the ourskirts, which cause stronger departures from the condition of hydrostatic equilibrium.

- When applying Method 1, we find that the mass is recovered with about 10–15% underestimate. The requirement of having increasing mass values slightly artificially boost the reconstructed mass in the outskirts. The scatter is quite large (about 15%), owing to the large number of free parameters. A mass reconstruction based on an analytical model is probably preferable, however this method has the advantage of providing a mass profile completely free of any assumption, except that of spherical symmetry.

- Cluster elongation also affects the mass reconstruction. In fact, the mass reconstructed from the projection performed along the maximum elongation axis is larger than the mass reconstructed from the other two projections. This is clearly due to the corresponding overestimate of the gas temperature.

- With the Method 2, we perform two different analyses. The first one is based on fitting the model out to $R_{vir}$. In this case, we find an underestimate of the total mass of about 20%, which is larger than that obtained from Method 1. This larger underestimate is due to the assumption of an analytical model, which should fit the inner regions as well as the outskirts. Since in the outskirts the deviations from equilibrium are larger, a lower normalization turns out to be favoured. We found a scatter in the recovered mass profiles of about 10%, thuslower than found with Method 1.

- The second analysis performed with Method 2 stops the fit at $R_{500}$ and extrapolates the model out to $R_{vir}$. In this case, the bias is appreciably reduced, clearly owing to the fact that in the internal regions the gas has smaller deviations from hydrostatic equilibrium. Unfortunately, limiting the fit to a smaller region originates a larger scatter, which increases to about 15%

- In all cases discussed above, the recovered mass is much closer to the hydrostatic mass than to the true mass profile, thus confirming that the main source of systematics is intrinsic (i.e. the non–thermal pressure support), while our procedure is basically unbiased.

Our results show that the combination of X–ray images and tSZ data is efficient in recovering the total mass profile of galaxy clusters. In fact, the main bias that we found is intrinsic, since it is due to deviations from perfect hydrostatic equilibrium.

This approach has several advantages with respect to the traditional one based on X–ray spectroscopy. First, the temperature recovered from the fit of the X–ray spectra is known to provide a biased estimate of the total thermal content of the ICM, the size of this bias increasing with the complexity of the plasma thermal structure (e.g., Mazzotta et al., 2004; Vikhlinin, 2006). Secondly, X–ray surface brightness profiles can be obtained with good precision with a relatively small number of photon counts. Also, once the

cosmic and instrumental backgrounds are under control, the surface brightness can be recovered over a large portion of the cluster virial regions, as already demonstrated with ROSAT-PSPC imaging data (e.g., Vikhlinin et al., 1999; Neumann, 2005). Since the tSZ has the potential of covering a large range in gas density, then its combination with low–background X–ray imaging data will allow one to recover the mass profiles out to the cluster outskirts.

A limitation of the analysis presented in this Chapter is that we did not include realistic backgrounds in the generation of the X–ray and tSZ maps. As we have just mentioned, there are reasonable perspectives for a good characterization of the X–ray background. However, the situation may be more complicated for the tSZ background. In this case, contaminating signals from unresolved point–like radio sources (e.g., Bartlett & Melin, 2006) and fore/background galaxy groups (e.g., Hallman et al., 2007) could affect the tSZ signal in the cluster outskirts. In this respect, the possibility of performing multi–frequency observations with good angular resolution will surely help in characterizing and removing these contaminations.

Single–dish sub-millimetric telescopes of the next generation promises to provide tSZ images of clusters with a spatial resolution of few tens of arcsec, while covering fairly large field of views, with 10–20 arcmin aside, with a good sensitivity. At the same time, future satellites for X–ray surveys (e.g. eROSITA) will have the capability of surveying large areas of the sky with a good quality imaging and control of the background. These observational facilities will open the possibility of carrying out in survey mode high–quality tSZ and X–ray imaging for a large number of clusters. The application of deprojection methods, like those presented in this Chapter will provide reliable determinations of the temperature profiles and, therefore, of the total cluster mass. This will greatly help to exploit the potentiality of galaxy clusters as tools for precision cosmology.

# Chapter 7

# Conclusions

Galaxy clusters are virialized structures which are the result of a long and complex formation process. Their study has implications on both the thermodynamical processes ongoing in the hot intra–cluster medium (ICM) and on the cosmological models of structure formation. Indeed, the ICM thermodynamics is determined not only by the gravitational accretion of gas into the dark matter potential wells forming clusters, but also by energy feedback processes (e.g. from supernova explosions and active galactic nuclei), which took place during the cosmic history of the cluster assembly. A characterization of the ICM thermodynamics out to larger radii than accessible with present X–ray observations would provide a better understanding of these important processes. Moreover, a number of important cosmological tests are based on mass measurements in galaxy clusters. In particular the mass function and its redshift evolution are highly sensitive to the underlying cosmology and in principle can constrain the equation of state of the dark energy. The redshift evolution of the gas mass fraction in galaxy clusters is also able to constrain cosmological parameters. Indeed, precise mass measurements in galaxy clusters are highly relevant to calibrate clusters as precision tools for cosmology (e.g., Haiman et al., 2001; Rosati et al., 2002; Pierpaoli et al., 2003; Voit, 2005).

The main focus of the research presented in the Thesis was the study of the potentiality and possible systematics in combining observations of the thermal Sunyaev-Zeldovich effect (tSZ) and of the X–ray emission in galaxy clusters. The advantage of the combination of these two types of observations is that they have a different dependence on the properties (density and temperature) of the Intra Cluster Medium (ICM). Also the behavior with redshift is completely different: X–rays provide very bright images for nearby clusters, but rapidly dimming with redshift, while the SZ is independent of redshift and is more suitable to observations of distant objects. At present, the X–ray data have far better sensitivity and resolution than the SZ ones. For this reason, our attention is mainly directed to the upcoming generation of SZ telescopes, which should produce high signal–to–noise images, with improved angular resolution. In this perspective, we analyzed a sample of galaxy clusters extracted from a set of cosmological hydrodynamical simulations, which have been realized with the GADGET-2 code. These simulations include the effects of radiative cooling, star formation and supernovae feedback and, as such, they provide a realistic description of the ICM.

**Angular diameter distance**

A widely adopted technique to measure the angular diameter distance of galaxy clusters is based on the combination of X–ray and tSZ observations (e.g. Bonamente et al. 2006 and references therein). The method is completely independent of any other distance ladder and provides a measure of the Hubble constant out to $z \simeq 1$. In Chapter 4 we studied the systematics of this type of measure through the analysis of simulated clusters.

First, we found that correctly modelling the temperature profile is of key importance. It is common practice in observations to assume an isothermal model. We find that this model does not provide a satisfactory description of our simulated clusters and, thus, leads to a systematic underestimate of the angular diameter distance, of about 40%. The bias is probably amplified by the fact that temperature profiles of simulated clusters are steeper than those observed in the cool core region of real objects, which generally show an isothermal core. However, our results suggest that the non–isothermal temperature profiles should be taken into account.

By adopting a polytropic model to account for the temperature profiles, we found that the angular diameter distance is correctly recovered, with an intrinsic scatter of about 20%. The origin of this scatter has to be considered as intrinsic to the measurement and is mainly related to cluster asphericities. In fact, the measure of the distance is based on the assumption that the elongation of the cluster along the line of sight (given by X–ray/tSZ analysis) is equal to its dimension in the plane of the sky (given by its image). Assuming that cluster ellipticities are distributed randomly, this only leads to a scatter, but not to a bias. This fact highlights the importance of an appropriate selection of unbiased cluster samples.

Finally, we generated a redshift distribution of our clusters in order to test the capabilities of this technique in recovering the cosmological parameters, by fitting the distance–redshift relation. We first limit the fit to redshift $z < 1$, which corresponds to the capability of present observations. In this case, only the normalization of the relation can be fitted, thus obtaining an unbiased estimate of the Hubble constant, with an uncertainty of only 2%. Then, we extend this type of measure out to $z \simeq 1.5$, in the perspective of having in the future such datasets. Assuming a prior for the Hubble constant and a flat geometry, the method would allow to correctly recover also the density parameter $\Omega_m$ with a typical error of about 0.05.

**Joint deprojection of Sunyaev–Zeldovich and X–ray images of galaxy clusters**

Given the limited resolution of the present tSZ telescopes, the principal source of information on the internal structure of galaxy clusters comes from X–ray data, for which both imaging and spectroscopy are available. In the perspective of having new high-resolution tSZ images, in Chapter 5 we proposed a technique aiming at reconstructing gas density and temperature by combining them with the X–ray images, without the need of X–ray spectroscopy which is a potential source of biases in the measure of the ICM temperature.

The method is based on a joint deprojection of tSZ and X–ray images and requires the only assumption of spherical symmetry. Gas density ($\rho$) and temperature ($T$) can be recovered by taking advantage of the different dependence of the two signals on gas properties: tSZ $\propto \int \rho T dl$ while X–ray $\propto \int \rho^2 \Lambda(T) dl$, where $\Lambda(T)$ is the cooling function at X–ray energies and the integrals are performed along the line of sight.

Our technique implements the deprojection by following a Markov Chain Monte Carlo approach, which allows us to deproject both images simultaneously, by the maximization

of a joint (tSZ + X–ray) likelihood function. From this method, we obtain at the same time an accurate estimate of the uncertainty on the recovered profiles of density and temperature, together with an analysis of all degeneracies in the fitting parameters.

A typical feature of the geometrical deprojection is to introduce spurious fluctuations in the profiles, which are due to the presence of noise. The effect increases rapidly when reducing the width of the bins adopted in the deprojection. Our statistical approach instead allows us to introduce a regularization constraint which has the effect of smoothing out these spurious fluctuations, thus offering a much more stable reconstruction of the gas properties.

We test the whole procedure against an idealized cluster, realized by assuming a polytropic $\beta$–model. First we perform a classical geometrical deprojection. Then we apply our maximum—likelihood technique, but switching off the regularization constrain. Finally we apply the complete procedure. We find that the geometrical deprojection is able to recover the density and temperature of the ICM unbiased, with errors $< 5\%$ and about 20% respectively. Our technique without regularization constraint obtain identical results, with the advantage of providing also an accurate analysis of the statistical errors and an estimate of the degeneracies (which are not trivial). Finally, we find that the introduction of the regularization constraint is very efficient in suppressing spurious fluctuations, without introducing any bias.

By applying this method to the simulated clusters we find a general overestimate of density from 5 to 10%, which we attribute to small-scale inhomogeneities and to small unresolved gas clumps which cause a boosting of the X–ray surface brightness. As a consequence the temperature is slightly underestimated. By integrating the gas density profiles one directly obtains the gas mass content of the cluster. Together with an estimate of the total mass, it allows us to measure the gas mass fraction, which is another important constrain on cosmological models. Since the density within each shell depends on the density of all the other shells, it is important to have an estimated of the full covariance matrix, which is naturally provided by the Markov Chain Monte Carlo method. We find that the gas mass is also overestimated by about 5-10%, with a statistical uncertainty of about 5%.

A common way to select samples of clusters is to fix a lower limit in their X–ray flux. This criterion may slightly favor the selection of objects which are elongated along the line of sight. This represents a potential source of bias when these samples are used for a statistical analysis of cluster properties. To address this issue, we carried out three synthetic observations of each cluster by projecting it along the three principal axes of the inertia tensor, in order to understand the impact of cluster morphology on the reconstruction of gas properties. We find that cluster elongation along the line of sight biases the deprojected gas density profile upwards at $r < 0.2 r_{vir}$ and downwards at larger radii. A comparable bias is also found in the deprojected temperature profile. Overall, this turns into a systematic underestimate of the gas mass, by up to 10%.

**Total mass estimate**

As already emphasized, correctly measuring the total cluster mass is of fundamental importance for clusters to be used as tools for precision cosmology. In cluster studies based on the observations of the ICM the mass is obtained by assuming that the gas lies in hydrostatic equilibrium in the cluster gravitational potential. In Chapter 6 we discussed a development of the maximum–likelihood deprojection technique, in which

we implemented the solution of the hydrostatic equilibrium equation, so as to derive profiles of gas density and temperature and total mass simultaneously. In practice, this involves a derivative of gas density and temperature profiles, for which the above discussed regularization constraint is quite useful. We implement two methods to recover the total mass profile. Method 1 adopts a model–independent approach, with the only constraint of having a mass which is increasing with radius, in order to avoid unphysical solutions. Method 2 is instead based on assuming the profile proposed by Navarro et al. (1997) (NFW hereafter).

The assumption that the gas is in perfect hydrostatic equilibrium is actually idealized. Instead, deviations from such equilibrium are expected in our simulations, due to any non–thermal pressure support (e.g. stochastic velocity fields and residual bulk motions). In order to better characterize the sources of systematics in mass measurements, we also computed the profile of the *hydrostatic mass* ($M_{hyd}$), which is obtained by applying the hydrostatic equilibrium equation to the true gas density and temperature profiles, given by the simulation data. It basically measures how far the gas is from a situation of perfect hydrostatic equilibrium. We found that $M_{hyd}$ generally provides an underestimate, by about 10%, of the true mass, in line with previous results presented in the literature. This underestimate increases from $r \sim 0.5R_{vir}$, reaching 20% at $R_{vir}$, probably owing to more frequent merger events in the outskirts, which cause stronger departures from the condition of hydrostatic equilibrium.

When applying Method 1, we find that the mass is recovered with about 10–15% underestimate. The recovered mass is much closer to the hydrostatic mass than to the true mass profile, thus confirming that the main source of systematics is intrinsic (i.e. the non–thermal pressure support), while our procedure is basically unbiased. Following the same approach of Chapter 5, we asses the effects of cluster elongation also on the mass reconstruction. We find that the mass reconstructed from the direction of maximum elongation is generally larger than the mass reconstructed from the other two projections. This is clearly due to the overestimate of gas temperature.

As for Method 2, we perform two different analyses. The first one is based on fitting the model out to $R_{vir}$, the second stops at $R_{500}$ and extrapolates the model out to $R_{vir}$. In the first case, we find an underestimate of the total mass of about $\lesssim 20\%$, which is larger than the one obtained from Method 1. This larger underestimate is due to the assumption of an analytical model, which should fit the inner regions as well as the outskirts. Since in the outskirts the deviations from equilibrium are large, a lower normalization turns out to be favored. The bias is appreciably reduced by limiting the fit to $R_{500}$ in the second analysis. However, limiting the fit to a smaller regions originates a larger scatter, which increases from 10% to 15%

**Future perspectives**

New X–ray and tSZ surveys have just started or will start in a few years. In order to extract the maximum cosmological information from these surveys, it is necessary to precisely calibrate the relations between X–ray and tSZ measurable quantities and the cluster mass in both normalization and scatter, in order to have systematic and statistical errors under control. In this respect, hydrodynamical simulations will keep providing an important contribution in the coming years. Present simulations have achieved an high degree of complexity in describing the thermodynamical processes ongoing in the ICM. Some discrepancies with observations are still present in the core regions, however

the global properties are generally well reproduced and we can safely assume that the simulated clusters provide a realistic description of the real ones. We plan to use already available and future simulations of clusters to calibrate scaling relations in two directions. On one hand, to test how well a given observable correlates with the true cluster mass, which would not be directly measured in real clusters. On the other hand, to check if any additional systematics or scatter is introduced when trying to calibrate these relations using real clusters, which may be affected by systematics, both intrinsic and instrumental. This can be achieved by carrying out synthetic observations of simulated cluster with dedicated software and then by analyzing them with exactly the same techniques used in observations. The first step is straightforward, the second requires a much more complex work.

The noise scheme implemented in our synthetic maps is quite simple and does not account for all possible instrumental effects. We plan to improve it, in order to achieve a more realistic characterization of possible systematics. On the X–ray side, Rasia et al. (2006) realized the X–ray MAps Simulator X–MAS, which produces realistic synthetic observations of both the XMM–Newton and the Chandra satellites. As for the tSZ, we plan to implement more sophisticated noise scheme, modelled on radio–interferometers like the Sunyaev–Zeldovich Array (SZA). The goal of this project will be to test the capabilities and possible systematics of our deprojection procedure, in the perspective of applying it to real clusters.

The new generation of tSZ instruments, which are now starting observations, will provide suitable data for our deprojection technique. We plan to combine new tSZ observations performed with the the SZA and the CARMA (Combined ARray for Millimiter Astronomy) arrays with data available from public archives of the Chandra and XMM–Newton satellites. For nearby clusters, we will compare the tSZ–derived gas temperature and total mass profiles with those obtained via X–ray analysis, to check for inconsistencies. Then we will extend the analysis both to more distant objects and reaching larger radii, were the X–ray spectral analysis can be really challenging. This will provide a better characterization of the outskirts of galaxy clusters and an extended analysis of cluster properties at high redshift, when they are in an earlier stage of their formation process. Both aspects are highly relevant for cosmology studies.

The future will see the development of new X–ray and SZ instruments, which will shed a new light on our knowledge of galaxy clusters and cosmology. As for the X–rays, thanks to a its low background, the eROSITA mission will provide images of galaxy clusters out to $z = 1$ in survey mode. Furthermore, technology of X–ray mirrors will reach maturity in a ten–year timescale to allow carrying out X–ray surveys with improved sensitivity, even with respect to eROSITA. As for the SZ, experiments like CCAT working in survey mode will provide images of large samples of galaxy clusters to be combined with X–ray data. Furthermore, new interferometers like ALMA will provide exquisite high resolution follow–ups of interesting objects, also at high redshift. There is no doubt that this new generation of X–ray and SZ instruments will then start a new promising epoch for exploiting the potentiality of galaxy clusters as cosmological probes.

# Appendix A

# Basics of cosmology

The birth of modern cosmology can be placed in the 1920's, with the formulation of the *Standard model* or *Big Bang model*. After that Hubble discovered that other galaxies exist in addition to the Milky Way and that all these galaxies move away from ours with a uniform and isotropic expansion (Hubble, 1926; Hubble & Humason, 1931). Einstein already formulated the General Relativity theory. However, he spent many efforts in trying to avoid the solution of a non–static Universe, which it instead implies. On the contrary, Friedmann developed some models of Universe, based on Einstein's theory, which found an observational validation in Hubble results. Since then, much progress has been made in different directions, from the primordial nucleosynthesis to the thermal history of the Universe, from the study of the large scale structure formation to the observations of the Cosmic Microwave Background radiation (CMB). An important advancement has been provided in 1981, when Guth & Weinberg (1981) introduced the theory of *inflation*, which solved some serious problems of the standard Big Bang model.

This Appendix provides a introduction to modern cosmology. The topics which are more relevant for the work presented in this Thesis are discussed. For a complete treatment of the Standard Model one may see Coles & Lucchin (2002), Longair (1998), Peacock & Murdin (2002) or Padmanabhan (2002).

## A.1 The cosmological principle

Modern cosmology is based on a fundamental assumption, which has been called *cosmological principle* because of its importance. It states that on large scales, the Universe is to a good approximation homogeneous and isotropic: this means that there are no favourable positions or directions. The justifications for this assumption are mostly observative and will be presented in the following.

## A.2 Properties of the Universe on large scales

### A.2.1 The Hubble law

Hubble & Humason (1931) found that galaxies move away from us with a velocity directly proportional to their distance:

$$v = H_0 d, \tag{A.1}$$

where $v$ is the velocity of the galaxy, $d$ is its distance and $H_0$ is the *Hubble constant*. This constant is usually written in terms of the dimensionless parameter $h$:

$$h = \frac{H_0}{100\text{km/s/Mpc}}. \tag{A.2}$$

Recent observational determinations of $h$, based on independent methods, agree with each other and indicate a value in the range $h = 0.7 \div 0.8$. The CMB power spectrum gives an estimate of $h_0 = 0.732^{+0.03.1}_{-0.03.2}$ (WMAP 3–year data, Spergel et al., 2007), the supernovae Ia give $h_0 = 0.73 \pm 0.04 \pm 0.05$ km/s/Mpc (statistical and systematic errors, Riess et al., 2005), finally the measure performed using Cefeids and SNIa in the local Universe by the *HST key project* gives $h_0 = 0.72 \pm 0.08$ km/s/Mpc (Freedman et al., 2001). The Hubble constant can be also inferred from combined X–ray and Sunyaev–Zeldovich observations; the most recent determination from Bonamente et al. (2006) gives $h_0 = 0.769^{+0.039\ +0.1}_{-0.034\ -0.08}$ km/s/Mpc. See also Section 2.4.

The Hubble law is valid only over a restricted interval of distances. If the galaxies are too close, the peculiar motions of the galaxies will dominate their velocity. If they are too far, the law in not valid anymore. In fact, it represents the local approximation of a more general relation, which is explained in Section A.5.

### A.2.2 The isotropy of the Cosmic Microwave Background radiation (CMB)

The isotropy of the CMB represents the most striking evidence of the isotropy of the Universe itself. In addition, the fluctuations in its pattern give direct information on the primordial density perturbations which gave rise to present large scale structures (galaxies and clusters of galaxies).

The isotropy of the CMB is related to the problem of the cosmological horizon[1]. The cosmic background formed when the photons decoupled from baryonic matter, about 380,000 year after the Big Bang when the Universe had a temperature of about 0.3 eV. The cosmological horizon at that time is now subtended by an angle of $\theta \sim 2^\circ$. However, the CMB is substantially isotropic on scales much larger than $\theta$, thus clearly indicating that the Universe at that time was homogeneous at scales larger than the cosmological horizon. This could not be explained until 1981, when Guth & Weinberg (1981) proposed the *inflationary theory*, so called since it predicts a period of very rapid (exponential) expansion of the Universe. During this period, regions which are now distant could have been in contact, thus justifying the present homogeneity.

### A.2.3 The mean density of the Universe

The total density of the Universe is given by the sum of different components. The contribution of each component is usually given in units of the *critical density*, which corresponds to the density required to have a Universe with flat geometry (see eq. A.23). The critical density is given by:

$$\rho_{crit} = 1.9 \cdot 10^{-29} h^2 \text{g/cm}^3 \tag{A.3}$$

[1]The cosmological horizon at a given time is the maximum distance from which a signal travelling at the speed of the light could arrive. This means that two points which are separated by a distance larger than the cosmological horizon cannot be related in any way. At present time it is roughly equal to $l \simeq c/H_0 \simeq 3000h^{-1}$ Mpc

The *density parameter* associated to the $i$–th component is then defined by:

$$\Omega_{0,i} = \frac{\rho_{0,i}}{\rho_{c,0}}, \tag{A.4}$$

where $\rho_{0,i}$ is the mean cosmic density of this component, $\rho_{c,0}$ is the critical density and the subscript "0" indicates the quantities are computed at the present time.

### Photons and neutrinos

Also the CMB gives a contribution to the total density of the Universe, although very small. Its density parameter is:

$$\Omega_r \simeq 2.6 \cdot 10^{-5} h^{-2}. \tag{A.5}$$

The Standard Model predicts, in addition to the background radiation, a neutrino background. However, it is too weak to be detected with present instruments, mainly because of the very small cross–section of these particles. The density of the neutrinos depend on their mass, which is still unknown:

$$\Omega_\nu \simeq 0.1 N_\nu \frac{\langle m_\nu \rangle}{10 \text{ eV}} h^{-2}, \tag{A.6}$$

where $N_\nu$ is the number of neutrino species and $\langle m_\nu \rangle$ is the mass averaged over the three species.

### Galaxies

The contribution due to the galaxies is estimated by multiplying their mean luminosity per unit volume $\mathcal{L}_g$ by the mean value of ratio between mass and luminosity in galaxies $M/L$. A typical value of the mass–luminosity ratio is $\left\langle \frac{M}{L} \right\rangle \simeq 10h \frac{M_\odot}{L_\odot}$. The measurements of this ratio showed the presence of large halos composed by dark matter around galaxies. The dark matter component is typically $3 - 10$ times larger than the luminous one. This is particularly evident in spiral galaxies, since they show a flat rotation curve also in the outskirts. However, dark matter halos are observed also around elliptical galaxies. Then, the contribution due to the galaxies turns out to be $\rho_{g,0} \simeq 6 \cdot 10^{-31} h^2$ g/cm$^3$, with density parameter:

$$\Omega_g \simeq 0.03. \tag{A.7}$$

### Galaxy clusters

The galaxy clusters have typical masses of $M_{Cl} \simeq 10^{14-15}\, h^{-1} M_\odot$. They have a much larger mass–luminosity ratio with respect to galaxies, typically $M/L \sim 300 M_\odot/L_\odot$. The dark matter is then the dominant matter component in these objects (and it determines their dynamics). By assuming that all the matter in the Universe has the same $M/L$ as in clusters, one obtains:

$$\Omega \sim 0.3 \tag{A.8}$$

**The baryons**

The theory of the primordial nucleosynthesis gives very accurate constraints on the density of baryonic matter $\Omega_b$, since it is very sensitive to this parameter. From present abundances of light elements (namely $^2$H, $^3$He, $^4$He, $^7$Li) one obtains:

$$1.1 \cdot 10^{-2} h^{-2} < \Omega_b < 2.5 \cdot 10^{-2} h^{-2}, \tag{A.9}$$

while from the CMB (Spergel et al., 2007):

$$\Omega_b = (2.23 \pm 0.07) \cdot 10^{-2} h^{-2}. \tag{A.10}$$

Most of the baryons in the Universe are in the form of diffuse gas, while the stars in galaxies give a contribution of only a few percent. However, the hot gas observed in galaxy groups and clusters in the local Universe corresponds to only about half of the total amount of baryons, thus indicating that a part of the baryons is still missing. The situation is different in the distant Universe. In fact, estimates from the *Ly*$\alpha$ forest[2] are able to account for the totality of the baryons. This fact strongly supports the fact that most of the missing baryons are actually in the form of a warm diffuse gas, which is not currently detected owing to its very low X–ray brightness. Other candidates, such as black holes or white dwarfs, are though to give a negligible contribution. A detailed estimate of the baryon budget in different states can be found in Fukugita et al. (1998).

### A.2.4 The non–baryonic dark matter

The estimates of the gravitational field in the outskirts of both spiral and elliptical galaxies and, to a much larger amount, in galaxy clusters show evidence of the presence of a dark matter component, whose nature is still unknown. In fact, the estimates of the baryonic density clearly indicate that this component cannot be of baryonic origin. Instead, it should be a new type of particle, which has never been observed and which constitutes about 90% of the total amount of matter in the Universe. Its presence is also required to explain the process of formation of cosmic structures. In fact, theoretical models show that baryonic matter should not be able to form the structures which we observe today. Instead, it is necessary the presence of different type of particles, which are of non–collisional nature and thus do not have a pressure term. Such particles should serve as catalyser for the collapse of the baryonic matter. The dark matter particles should have a very small cross–section at least for two reasons: *i)* they have never been observed; *ii)* they should decouple from radiation before the nucleosynthesis, in order to not altering its results. They interact through gravitational forces, so they must have mass, which may be also very large. For these reasons, these particles are generally called WIMPs (Weakly Interacting Massive Particles). An additional constraint on dark matter theories is to explain why we do not observe the effects of these particles in the Solar system. Some candidates have been drawn from theoretical particle physics, which can be divided into two main categories.

- **Cold Dark Matter (CDM):** The particles decoupled when they were not relativistic, so their number density distribution follows the Boltzmann distribution $n = g(mT/2\pi)^{3/2} e^{-m/T}$. Particles in this category are typically drawn from the supersymmetric theory.

[2]The observations of absorption lines in the spectra of distant quasars, which represent a direct measure of the amount of neutral hydrogen along the line of sight.

- **Hot Dark Matter (HDM):** In this case the particles decoupled when they were still relativistic. They should have a number density comparable to that of the photons. The principal candidate in this category is the massive neutrino.

The two types of particles determine well different scenarios of structure formation. In HDM, the dark matter particles cancel small–scale structures just by free–streaming across the small potential well. This leads to the *top–down* scenario, in which the largest structures form first and the smaller ones descend for fragmentation. Instead in the CDM scenario the smallest structures (namely the galaxies) are those which form first, becoming the building blocks for the largest ones (*bottom–up*). This second scenario is favoured, since it naturally provides a good description of the formation of large scale structures, while the presence of HDM would not be compatible with the observed rate of formation of structures.

## A.3 The Einstein's equations and the cosmological constant

Einstein first wrote the equations of General Relativity in 1916. They allow to relate the space–time metric $g_{\mu\nu}$ with the tensor of energy–impulse $T_{\mu\nu}$, which describes the content of the Universe:

$$R_{\mu\nu} - \frac{1}{2} g_{\mu\nu} R = -\frac{8\pi G}{c^4} T_{\mu\nu}, \tag{A.11}$$

where $R_{\mu\nu}$ and $R$ are the Ricci tensor and scalar, respectively.

The energy–impulse tensor of a perfect fluid is given by:

$$T_{\mu\nu} = -p g_{\mu\nu} + (p + \rho c^2) U_\mu U_\nu, \tag{A.12}$$

where $p$ is the pressure, $\rho c^2$ is the energy density (which includes also the contribution of the rest mass) and $U_\mu$ is the four–dimensional velocity of the fluid (normalised as $U_\mu U^\mu = 1$).

Only one year later, Einstein introduced in the equations a term of *cosmological constant* $\Lambda$, in order to obtain a static Universe. In fact, this can be done with eqs. (A.11) only by assuming $\rho = -3p/c^2$, which is unphysical for ordinary matter. He modified the equations in the following way:

$$R_{\mu\nu} - \frac{1}{2} g_{\mu\nu} R - \Lambda g_{\mu\nu} = -\frac{8\pi G}{c^4} T_{\mu\nu}. \tag{A.13}$$

From this modified version of the equations, with a suitable value for $\Lambda$, one can obtain a static Universe.

It is common to modify the expression of the energy–impulse tensor, the pressure and the density, in order to rewrite these equations in a form similar to the eqs. (A.11).

$$\tilde{T}_{\mu\nu} = T_{\mu\nu} + \frac{\Lambda c^4}{8\pi G} g_{\mu\nu} = -\tilde{p} g_{\mu\nu} + (\tilde{p} + \tilde{\rho} c^2) U_\mu U_\nu \tag{A.14}$$

$$\tilde{p} = p - \frac{\Lambda c^4}{8\pi G} \tag{A.15}$$

$$\tilde{\rho} = \rho + \frac{\Lambda c^2}{8\pi G}, \tag{A.16}$$

where $p$ and $\rho$ are the quantities relative to the perfect fluid and $\tilde{\rho}$ and $\tilde{p}$ are called *effective density* and *effective pressure* respectively. The Einstein's equations now become:

$$R_{\mu\nu} - \frac{1}{2} g_{\mu\nu} R = -\frac{8\pi G}{c^4} \tilde{T}_{\mu\nu}. \tag{A.17}$$

These new equations have the same solutions of the original ones, with the only difference that here there are $\tilde{p}$ e $\tilde{\rho}$ instead of $p$ e $\rho$.

A model of static universe (with $p = 0$), called *Einstein model*, is obtained by assuming:

$$\Lambda_E = \frac{4\pi G \rho}{c^2}. \tag{A.18}$$

When the expansion of the Universe was discovered, the cosmological constant lost its importance and was defined by Einstein as the biggest error of his life. However, after the introduction of the inflationary model, it became of fundamental importance: its contribution to the density $\rho_\Lambda$ and to the pressure $p_\Lambda$ were interpreted as the density and pressure of *vacuum*, i.e. of the state of minimum energy of the quantistic state.

According to the now standard cosmological scenario, the cosmological constant represents the dominant component of the density of the Universe. It is called Dark Energy, since its origin is unknown. Its density parameter is:

$$\Omega_\Lambda \sim 0.7 \tag{A.19}$$

## A.4 The Robertson–Walker metric

The cosmological principle proposes a spatially homogeneous and isotropic Universe. At least in regions as large as the present Hubble volume[3] these two assumptions are well verified; the most evident proof is the isotropy of the CMB. The Robertson–Walker metric represents the most general form in which is it possible to describe a space with these two properties.

The matter in the Universe can be described as a continuum fluid, giving to each of its elements three spatial coordinates $x^i (i = 1, 2, 3)$ and a time $t$, which represents the proper time, as would be measured by a clock moving in the fluid itself. The spatial coordinates are called *comoving coordinates*.

The quantity $ds^2$ determines the interval (both in time and in space) between two events having coordinates $x^i$ and $x^i + dx^i$. By assuming a generic metric tensor $g_{\mu\nu}$, $ds^2$ is given by[4]:

$$ds^2 = g_{\mu\nu}(x) dx^\mu dx^\nu \quad (\mu, \nu = 0, 1, 2, 3). \tag{A.20}$$

The metric tensor determines all the geometrical properties in the system of the coordinates $x^\mu$. If the matter distribution is uniform, the space is homogeneous and isotropic: it is then possible to choose a *proper time*, such that at any time the metric of the tri–dimensional space is identical at any point and in any direction. In this case, the space–time metric becomes:

$$ds^2 = (cdt)^2 - dl^2 = (cdt)^2 - \tilde{g}_{ij} dx^i dx^j \quad (i, j = 1, 2, 3), \tag{A.21}$$

where the tensor $\tilde{g}_{ij}$ is the metric tensor of the tri–dimensional space.

[3]The Hubble volume or sphere is defined as a region of the Universe causally connected

[4]Repeated indexes are summed up, following the Einstein's convention.

Given the properties of this metric, it is more convenient to rewrite it in polar comoving coordinates$(r, \theta, \phi)$. Its more general expression, which is called *Robertson-Walker metric*, is the following:

$$ds^2 = (cdt)^2 - a^2(t)\left[\frac{dr^2}{1-Kr^2} + r^2(d\theta^2 + \sin^2\theta d\phi^2)\right], \tag{A.22}$$

where $a(t)$ is the *scale factor* and $K$ is the *curvature parameter* of the Universe. This metric is invariant under rotation and translation: the Universe does not have any preferred position or direction. The scale factor has the dimensions of a length ($r$ is dimensionless) and for a non–flat Universe it is related to the curvature parameter by the relation $R_G = a/\sqrt{K}$. The curvature parameter determines the spatial curvature of the Universe:

- $K = 0$: flat space, Euclidean, infinite;
- $K = 1$: close space, spherical, having a finite volume but without borders;
- $K = -1$: hyperbolic space, open and infinite.

## A.5 The Friedmann equations

In the Robertson–Walker metric (eq. A.22) and with this expression for the energy–impulse tensor, the Einstein equations (eqs. A.11) give for the time–time and space–space components, respectively:

$$\ddot{a} = -\frac{4\pi}{3}G\left(\tilde{\rho} + 3\frac{\tilde{p}}{c^2}\right)a \tag{A.23}$$

and

$$a\ddot{a} + 2\dot{a}^2 + 2Kc^2 = 4\pi G\left(\tilde{\rho} - \frac{\tilde{p}}{c^2}\right)a^2, \tag{A.24}$$

where the dot indicates the derivative with respect to the proper time $t$. The space–time components give instead the identity $0 = 0$. Finally, by eliminating $\ddot{a}$ between the eqs. (A.23–A.24) one obtains the so–called *Friedmann cosmological equations*:

$$\begin{cases} \ddot{a} = -\dfrac{4\pi}{3}G\left(\tilde{\rho} + 3\dfrac{\tilde{p}}{c^2}\right)a \\ \dot{a}^2 + Kc^2 = \dfrac{8\pi}{3}G\tilde{\rho}a^2. \end{cases} . \tag{A.25}$$

The content in matter and energy is described as a perfect fluid (eq. A.12). The density and pressure of each component are simply related by an equation of state:

$$p_x = w\rho_x c^2, \tag{A.26}$$

where $p_x$ and $\rho_x c^2$ are the pressure and the energy density of the $x$ component respectively. The parameter $w$ depends on the nature of the fluid. For ordinary matter and radiation it is in the so–called *Zeldovich interval*, i.e. $0 \leq w \leq 1$. It is related to the adiabatic sound speed: $v_s = cw^{1/2}$ (this relation also explains its superior limit). If the Universe is dominated by dust, it has no pressure term, so $w = 0$. If instead radiation dominates, then $w = 1/3$. Finally, the cosmological constant is characterised by a negative pressure, with $w = -1$.

All models having $-1/3 \leq w \leq 1$ predict the *Big Bang singularity*, which corresponds to an epoch at which the scale factor vanished.

### The redshift

The redshift is an observable quantity which has an important role in cosmology, since it is related to the expansion of the Universe and is directly measurable.

The redshift is the shift towards lower (and then redder) wavelengths of the radiation emitted from a source located at a cosmological distance:

$$z = \frac{\lambda_0 - \lambda_e}{\lambda_e}, \tag{A.27}$$

where $\lambda_0$ is the observed wavelength (at present time) and $\lambda_e$ is the emitted one. The variation in wavelength is due to the expansion of the Universe and is related to the scale factor $a(t)$ by the relation:

$$1 + z = \frac{a_0}{a}. \tag{A.28}$$

### The deceleration parameter

Another important quantity for cosmology is the present–time deceleration parameter $q_0$, which is defined as:

$$q_0 = -\frac{\ddot{a}(t)a(t)}{\dot{a}^2(t)}. \tag{A.29}$$

### Definitions of distance

In a space which is described by the Robertson–Walker metric the distance between two points is not a well defined quantity. In fact, it depends on the way in which it is measured.

The *proper distance* between a point $P$, having coordinates $r, \theta, \phi$, and a point $P_0$, chosen as the origin of the coordinate system, is defined as the distance measured at the time $t$ by a chain of observers which connect $P_0$ to $P$. Assuming $dt = 0$ and using the eq. (A.22), one obtains:

$$d_{pr} = \int_0^r \frac{a dr'}{(1 - Kr'^2)^{1/2}} = a \begin{cases} r & \text{per } K = 0 \\ \arcsin(r) & \text{per } K = 1 \\ \text{arcsinh}(r) & \text{per } K = -1 \end{cases} \tag{A.30}$$

In the case of a flat Universe ($\Omega_k = 0$) the above integral gives:

$$d_{pr} = \frac{cz}{H_0(1+z)} \left[ 1 + \frac{z(1-q_0)}{(1+2q_0z)^{1/2} + 1 + q_0 z} \right] \tag{A.31}$$

The proper distance depends on the time $t$; its value at present time $t_0$ is obtained from the relation:

$$d_{pr}(t_0) = a_0 f(r) = \frac{a_0}{a} d_{pr}(t). \tag{A.32}$$

Assuming that the quantity $d_c = a_0 f(r)$ is the comoving radial coordinate of the point $P$, one obtains:

$$d_c = \frac{a_0}{a} d_{pr}. \tag{A.33}$$

However, the proper distance is not very useful in the perspective of astronomical observations, since it is clearly impossible to measure simultaneously all the elements between $P_0$ and $P$.

We first consider the case in which the distance to an astronomical object, located in at the position $r$, is computed by knowing its physical dimension $d$, which is given by:

$$d = a(t) r \Delta\theta, \tag{A.34}$$

where $\Delta\theta$ is the angle subtended by $d$. The *angular diameter distance* is define as:

$$D_A = ar = \frac{D}{1+z}, \tag{A.35}$$

where we have been introduced the quantity $D = a_0 r$. In this way, the relation between $\Delta\theta$ and $D_A$ is equal to the one defined in an Euclidean space:

$$\Delta\theta = \frac{d}{D_A}. \tag{A.36}$$

Finally, we consider the case of a source having luminosity $L(\nu_1)$ at the frequency $\nu_1$, from which we receive the flux $F(\nu_0)$. Note that the observing frequency $\nu_0$ is different from the emitting one $\nu_1$ because of the redshift. The source luminosity is

$$L(\nu_1) = \frac{N(\nu_1) h\nu_1}{\Delta\nu_1 \Delta t_1}, \tag{A.37}$$

where $N(\nu_1)$ is the number of photons (with energy $h\nu_1$) emitted in the band $\Delta\nu_1$ and in the interval of proper time $\Delta t_1$. The photons are instead observed at present time at the frequency $\nu_0 = \nu_1/(1+z)$, in the band $\Delta\nu_0 = \Delta\nu_1/(1+z)$ and in the interval of proper time $\Delta t_0 = (1+z)\Delta t_1$, while the number of photons reaching a telescope having area $dA$ is $N(\nu_0) = [dA/4\pi D^2] N(\nu_1)$. The measured flux will be:

$$F(\nu_0) = \frac{L(\nu_1)}{4\pi D^2 (1+z)^2}. \tag{A.38}$$

By introducing the *luminosity distance*:

$$D_L = (1+z) D \tag{A.39}$$

one obtains instead of eq. (A.38) a law similar to the classical one:

$$F(\nu_0) = \frac{L(\nu_1)}{4\pi D_L^2}. \tag{A.40}$$

The luminosity and angular diameter distance are clearly not independent, but they are related by:

$$D_A = \frac{D_L}{(1+z)^2}. \tag{A.41}$$

**The Hubble law**

The proper distance of a source depends on time, since it contains the scale factor $a(t)$. Then, it will have a radial velocity equal to the derivative of the proper distance with respect to the time:

$$v_r = \dot{a} f(r) = \frac{\dot{a}}{a} d_{pr}. \tag{A.42}$$

This is the Hubble law (see Section A.2) and then the Hubble constant is equal to:

$$H(t) = \frac{\dot{a}}{a}. \tag{A.43}$$

This *constant* actually depends on time, so it is often called *the Hubble parameter*.

**The critical density**

The critical density is defined as the density of a flat Universe, in the absence of a term of cosmological constant. By assuming $K = 0$ in eq. (A.25), one obtains:

$$\rho_{crit} = \frac{3H^2}{8\pi G} = 1.9 \cdot 10^{-29} h^2 \mathrm{g/cm}^3 \tag{A.44}$$

This quantity represents the unit of measure of the density in cosmology. Note that it depends on time as $H^2(t)$.

**The curvature parameter**

The curvature of the Universe is usually described in terms of the *curvature parameter*, which is defined as (using the first of the Friedmann equations):

$$\Omega_k = 1 - \tilde{\Omega} \equiv -\frac{K}{a^2 H^2}, \tag{A.45}$$

where $\tilde{\Omega}$ accounts for all density components (matter, radiation and cosmological constant).

### A.5.1 The Friedmann models

Friedmann developed three classes of models, depending on the curvature of the Universe.

**The flat Universe**

The flat Universe is the simplest one, in which $\Omega_k = 0$. If also $w = 0$, this model is called the *Einstein–de Sitter model* (EdS hereafter). In this case the eq. (A.25) can be easily integrated, obtaining:

$$a(t) = a_0 \left(\frac{t}{t_0}\right)^{\frac{2}{3(1+3w)}}, \tag{A.46}$$

or

$$t = t_0 (1+z)^{-\frac{3(1+w)}{2}}. \tag{A.47}$$

These relations show that the model predicts an infinite expansion in the future, always feeling the effect of self–gravity.

One may find also:

$$H = \frac{2}{3(1+w)t} \tag{A.48}$$

and

$$q = \frac{1+3w}{2} = constant \tag{A.49}$$

The density is equal to the critical one, by definition:

$$\tilde{\rho} \equiv \rho_{crit} = \frac{3H^2}{8\pi G} = \frac{1}{6(1+w)^2 \pi G t^2}. \tag{A.50}$$

| Parameter | CMB only | all datasets |
|---|---|---|
| $100\Omega_b h^2$ | $2.229 \pm 0.073$ | $2.186 \pm 0.068$ |
| $\Omega_m h^2$ | $0.1277^{+0.0080}_{-0.0079}$ | $0.1324^{+0.0042}_{-0.0041}$ |
| $H_0$ | $73.2^{+3.1}_{-3.2}$ | $70.4^{+1.5}_{-1.6}$ |
| $\tau$ | $0.089 \pm 0.030$ | $0.073^{+0.027}_{-0.028}$ |
| $n_s$ | $0.958 \pm 0.016$ | $0.947 \pm 0.015$ |
| $\Omega_m$ | $0.241 \pm 0.034$ | $0.268 \pm 0.018$ |
| $\sigma_8$ | $0.761^{+0.049}_{-0.048}$ | $0.776^{+0.031}_{-0.032}$ |

**Table A.1.** Power Law ΛCDM Model Parameters and 68% Confidence Intervals from Spergel et al., (2007). The first column represents the results obtained from the CMB data only, the second column includes all data sets.

#### The open Universe

If $\Omega_k < 0$ the scale factor grows without an end, as in the case of a flat Universe. An analytic expression can be found only for a Universe dominated by dust ($w = 0$), in the parametric form:

$$\begin{cases} a(\theta) = a_0 \dfrac{\Omega}{2(1-\Omega)}(\cosh\theta - 1) \\ t(\theta) = \dfrac{\Omega}{2H_0(1-\Omega)^{3/2}}(\sinh\theta - \theta). \end{cases} \tag{A.51}$$

#### The closed Universe

These models have $\Omega_k > 0$. Their behaviour depends on both the amount of matter and the value of the cosmological constant. If $\Lambda = 0$ (or if it is low enough) these model have a unique property: it exists a time $t_{max}$ at which the derivative of the scale factor vanishes, which corresponds to the maximum expansion of the Universe. After this moment, the scale factor starts decreasing and the Universe collapses at a time $t = 2t_{max}$, which is called the *Big Crunch*. Otherwise, they expand forever as the flat and open ones.

As for the case of the open Universe, an analytic solution can be found for a Universe dominated by dust ($w = 0$):

$$\begin{cases} a(\theta) = a_0 \dfrac{\Omega}{2(1-\Omega)}(1 - \cos\theta) \\ t(\theta) = \dfrac{\Omega}{2H_0(1-\Omega)^{3/2}}(\theta - \sin\theta). \end{cases} \tag{A.52}$$

### A.5.2 Constraints from observations

Figure A.1 shows the principal constraints that we currently have on the content of the Universe.

- **The CMB**: it represents the most tight constraint on cosmological parameters. Fitting the power spectrum of the CMB temperature fluctuations. The most recent measure of the CMB power spectrum has been performed by the Wilkinson Microwave Anisotropy Probe (WMAP) satellite. These observations found results

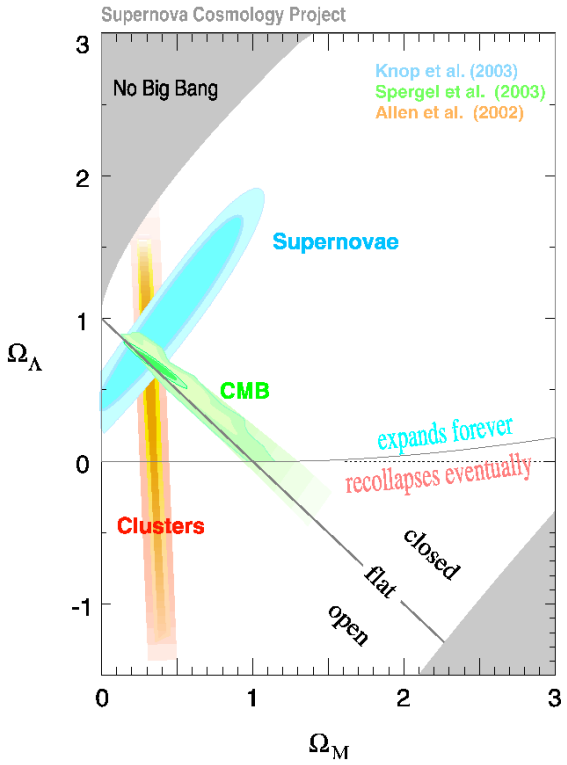


**Figure A.1.** Confidence regions for $\Omega_M$ and $\Omega_\Lambda$ from a combination of different datasets (namely the CMB, the SNIa and the galaxy clusters), from the Supernova Cosmology Project (Knop et al., 2003).

indicate that our Universe is consistent with being flat, within rather small uncertainties. The inferred curvature parameter is in fact:

$$\Omega_k = 0.01 \pm 0.02. \tag{A.53}$$

The inflationary paradigm provides a dynamical explanation of why the Universe is so close to a flat one (and why this does not mean that it *is* flat). In fact, one can demonstrate during the period of rapid accelerated expansion the density approaches very rapidly the critical one. Note however that any inflationary expansion, lasting for a finite time, is not able to change the geometry (flat, open or close) of the Universe.

- **SNIa**: the SNIa are used as standard candles to probe the geometry of the Universe, since they allow to fit the distance–redshift relation out to $z \gtrsim 3$ (Knop et al., 2003). Their intrinsic luminosity is not exactly constant, however it can be computed quite precisely if their light curve is known, by comparing it with the observed flux, one finally obtains their luminosity distance. The observation of these objects represent the major direct evidence for the cosmic acceleration and thus for a positive cosmological constant.

- **Galaxy clusters**: this topic is discussed in detail in Section 2.4. The observation of galaxy clusters principally give tight constrains on $\Omega_M$, with only a few percent uncertainty.

These three types of measurements are in remarkably good agreement in determining $\Omega_M$ and $\Omega_\Lambda$, as one may see from figure A.1. This leads to the definition of the so–called $\Lambda$CDM model, which generally assumes a flat geometry, with a cold dark matter component and a cosmological constant. Fiducial values are $\Omega_M = 0.3$ and consequently $\Omega_\Lambda = 0.7$.

The CMB power spectrum is a precious source of information and provides constraints on a large set of cosmological parameters, which are listed in the upper part of table A.1 (Spergel et al., 2007). These results are obtained by assuming a $\Lambda$CDM model and a power–law spectrum for the primordial density fluctuations (see below). In the right column of the same table instead the results from the CMB are combined with other sets of observables (namely the galaxy surveys, the SNe and the small–scale CMB measurements, see Spergel et al., 2007, for details).

## A.6 The formation of cosmic structures

The large scale structures that we observe today are the result of the gravitational collapse of tiny density fluctuations in the primordial density field. These fluctuations are now observable in the form of anisotropies of the CMB. We first present a statistical approach to the description of such fluctuations. Then, we describe the process of formation of structures; first we adopt a simple linear treatment which however is accurate only until the fluctuations are small. Then we introduce the more complex spherical collapse model which provides a reasonable description of the whole formation process. Finally, we describe the Press–Schechter mass function of collapsed dark matter halos, also discussing its extensions and the cosmological applications.

### A.6.1 The spectrum of density perturbations

The spectrum of density perturbations provides a statistical description of the distribution of matter in the Universe and its evolution.

The density field can be described through the superposition of plain waves, which have the advantage that they evolve independently while the fluctuations are still linear. This effectively means that one represents the distribution as independent components Fourier space. In this way, the density $\delta(\vec{x}) \equiv \delta$ at the point $\vec{x}$ is given by:

$$\delta(\vec{x}) = \frac{1}{(2\pi)^3} \int d^3k \hat{\delta}(\vec{k}) e^{-i\vec{k}\cdot\vec{x}}, \tag{A.54}$$

where $\hat{\delta}$ is the Fourier transform of $\delta(\vec{x})$:

$$\hat{\delta}(\vec{k}) = \int d^3x \delta(\vec{x}) e^{i\vec{k}\cdot\vec{x}}. \tag{A.55}$$

If the density field is a isotropic Gaussian random field, then its statistics is entirely described by the *power spectrum* $P(k) = \langle|\delta_k^2|\rangle$. The quantity $P(k)d^3k$ returns the contribution of the perturbations on scale $k$ to create a generic fluctuation $\delta(\vec{x})$ on the configuration field, i.e. it is a measure of the fluctuation power density.

The primordial fluctuations are thought to be produced during the inflation epoch and can be represented by a *scale–free* power spectrum:

$$P(k) \propto k^n, \tag{A.56}$$

where the exponent $n$ is called the *spectral index*, which actually need not to be constant over the entire range of wave numbers. Physical reasons limit the possible $n$ values to $n > -3$ for $k \to 0$ and to $n < -3$ for $k \to \infty$. Inflationary models predict a primordial spectrum of nearly scale–invariant form with $n \simeq 1$.

The mean value of the perturbation $\delta(\vec{x})$ is identical to zero by definition, however its mean square value, i.e. its *variance* $\sigma^2$, is not. It can be shown that:

$$\sigma^2 = \langle|\delta^2(\vec{x})|\rangle = \frac{1}{(2\pi)^3}\int P(\vec{k})d^3k. \tag{A.57}$$

It describes the amplitude of perturbations, but does not carry information about their spatial structure: in fact it does not depend on spatial position but only on time, since the perturbation amplitude $\delta$ evolves.

The variance $\sigma^2$ might be formally infinite. Hence, it is more convenient to construct a statistical description of the fluctuation field as a function for some scale $R_f$. This can be done by convolving the density contrast with a filter or *window function* $W(|\vec{x}' - \vec{x}|, R_f)$:

$$\delta(\vec{x}, R_f) = \int d^3x' W(|\vec{x}' - \vec{x}|, R_f)\delta(\vec{x}') =$$

$$= \frac{1}{(2\pi)^3}\int d^3k \hat{W}(kR_f)\hat{\delta}(\vec{k})e^{-i\vec{k}\cdot\vec{x}}, \tag{A.58}$$

where $\hat{W}(kR_f)$ is the Fourier transform of $W(x, R_f)$. If $\langle M\rangle = \langle\rho\rangle V_R$ is the mean mass inside the volume $V_R$ encompassed by the window function of size $R_f$, the variance at mass scale $M$ is then given by:

$$\sigma_M^2 = \frac{\langle(M - \langle M\rangle)^2\rangle}{\langle M\rangle} = \frac{1}{2\pi^2}\int_0^\infty P(k)k^2\hat{W}^2(kR)dk. \tag{A.59}$$

The choice of the filter is very important, since it defines the way in which model predictions and observations are compared. The simple one is a step function, which is called the *top-hat filter*. It has a constant value below a given radius $R$ and vanishes at larger radii:

$$W(r) = \begin{cases} 3/(4\pi R^3) & r < R \\ 0 & r > R \end{cases} \tag{A.60}$$

In this case the window volume is $V_R = (4\pi/3)R^3$. The $\sigma$ value found by using this filter with $R = 8h^{-1}$ Mpc (comoving) has been historically adopted to define the *power–spectrum normalisation* $\sigma_8$.

Another typical example is the so–called *Gaussian filter*:

$$W(r) = \frac{1}{(2\pi)^{3/2}R^3}\exp\left(-\frac{r^2}{2R^2}\right), \tag{A.61}$$

for which $V_R = (2\pi R^2)^{3/2}$.

### The transfer function

Besides gravitation, other causal processes, taking place inside the horizon, affect the growth of perturbations; they are accounted through a *Transfer Function* $T(k)$ which is defined through the relation $P(k) = P_0(k) \times T^2(k)$, where $P(k)$ and $P_0(k)$ are the final and original perturbation spectra respectively. The most important are:

- **Meszaros effect**: the growth of density fluctuations entering the horizon before equivalence is *frozen* until the equivalence is reached.
- **Free streaming** fluctuations are erased by free streaming of relativistic particles (in the HDM scenario).
- **Silk damping**: the diffusion of photons, which then *drag along* the baryons in the radiation-dominated era, has the same effect of the free streaming of HDM particles.
- **Jeans mass**: baryonic density fluctuations which reach this critical mass (whose meaning is explained below) start collapsing and forming structures., while fluctuations on a smaller scale are supported by pressure and behave as acoustic oscillations.

### A.6.2 The linear theory of gravitational collapse

Clusters form through gravitational collapse, which is driven by dark matter. This strongly simplifies our problem, since the dark matter, whatever it is, must behave as a collisionless fluid, and therefore it is not affected by dissipative processes, unlike the baryons, which are pressure supported. Since we are interested in the total mass, we can neglect, on a first instance, the physical processes affecting only the baryons.

The linear theory of gravitational collapse has been developed by Jeans at the beginning of the 1900's. He demonstrated that small fluctuations in density $\delta\rho$ and velocity $\delta v$ embedded in a homogeneous and isotropic fluid can evolve in time. In particular, the density fluctuations can grow as long as the repulsive effect of pressure is negligible with respect to the gravitational attraction. This process is called *Jeans gravitational instability*. Jeans formulated this theory with the aim of explaining the formation of stars and planets, but it can also describe the large scale structure formation.

To describe the evolution of a collisionless fluid under its own gravity, we can use the Eulerian equations of motion describing a perfect fluid (continuity, Euler and Poisson equations, see Kolb & Turner, 1990):

$$\frac{\partial\rho}{\partial t} + \nabla\cdot(\rho\vec{v}) = 0 : \tag{A.62}$$

$$\frac{\partial\vec{v}}{\partial t} + (\vec{v}\cdot\nabla)\vec{v} = -\frac{1}{\rho}\nabla p - \nabla\phi; \tag{A.63}$$

$$\nabla^2\phi = 4\pi G\rho, \tag{A.64}$$

where $\phi$ is the gravitational field generated by the density field itself.

One may notice that these equations do not allow a static solution. In fact, by adopting $\rho = \rho_0$ and $\vec{v} = 0$ in the eq. (A.63) one obtains $\nabla\phi = 0$, which in the eq. (A.64) gives $\rho = 0$. However, Jeans decided to neglect this initial inconsistency and to develop its theory, which leads to correct consequences. This assumption is called the *Jeans swindle*.

Following this approach, one considers the evolution of small positive density perturbations $\rho_1$ with respect to a uniform and static background with constant density $\rho_0$, so that one can easily linearise the system of equations:

$$\begin{cases} \rho = \rho_0 + \rho_1 \\ \vec{v} = \vec{v}_1 \\ p = p_0 + p_1 \\ \phi = \phi_0 + \phi_1 \end{cases} \tag{A.65}$$

One can write the equations for the perturbed system (by considering only the first order perturbations), which then give a differential equations describing the evolution of the density perturbations:

$$\begin{cases} \dfrac{\partial \rho}{\partial t} + \rho_0 \nabla \cdot \vec{v}_1 = 0 \\ \dfrac{\partial \vec{v}_1}{\partial t} + \dfrac{v_s^2}{\rho_0} \nabla \rho_1 + \nabla \phi_1 = 0 \\ \nabla^2 \phi_1 - 4\pi G \rho_1 = 0 \end{cases} \rightarrow \frac{\partial^2 \rho_1}{\partial t^2} - v_s^2 \nabla^2 \rho_1 = 4\pi G \rho_0 \rho_1. \tag{A.66}$$

where $v_s = \sqrt{\partial p / \partial \rho}$ is the sound speed in the fluid.

Finally, one describes the density perturbation in terms if its linear components: $\rho_1 \propto e^{-i(\vec{k}\cdot\vec{x} - \omega t)}$. From eq. (A.66) one obtains the equation of a harmonic oscillator with dispersion relation:

$$\omega^2 = v_s^2 \vec{k}^2 - 4\pi G \rho_0. \tag{A.67}$$

The solution depends on the value of $\omega^2$: if it is positive, the pressure is large enough to balance the gravity and then the perturbation is stable; if instead it is negative, the perturbation can collapse. The critical value is given by the *Jeans length scale*, which represents the minimum dimension for which the perturbation can collapse:

$$\lambda_J = \frac{2\pi}{k_J} = v_s \sqrt{\frac{\pi}{G\rho_0}}. \tag{A.68}$$

The mass of a perturbation having dimension $\lambda_J$ is called the *Jeans mass* and represents the minimum mass which leads to the growth of a density perturbation:

$$M_J = \frac{\pi^{5/2}}{6} \frac{v_s^3}{\sqrt{G^3 \rho_0}}. \tag{A.69}$$

The above analysis considers a static fluid. Instead, we are interested in a solution in an expanding background. The same theory applies also a fluid in homogeneous expansion, obtaining similar results. In this case, it is more convenient to write the eqs. (A.62–A.64) in Lagrangian form, so that one can follow the evolution of a particular fluid element:

$$\frac{d\rho}{dt} + \rho \nabla \cdot \vec{v} = 0 \tag{A.70}$$

$$\frac{d\vec{v}}{dt} = -\frac{1}{\rho} \nabla p - \nabla \phi \tag{A.71}$$

$$\nabla^2 \phi = 4\pi G \rho. \tag{A.72}$$

The interesting variable is now defined as the overdensity $\delta = (\rho - \rho_0)/\rho_0 \equiv \rho_1/\rho$. In addition, the physical coordinates $\vec{r}$ are transformed into the comoving ones $\vec{x}$, which is defined as $\vec{r} = a\vec{x}$, assuming $a_0 = 1$ for the sake of simplicity. In this new system of variables, eq. (A.66) becomes:

$$\ddot{\delta} + 2\frac{\dot{a}}{a}\dot{\delta} = \frac{v_s^2}{a^2} \nabla^2 \delta + 4\pi G \rho_0 \delta, \tag{A.73}$$

where the dot indicates the total derivative with respect to time and the spatial derivatives are done with respect to $\vec{x}$.

To show a specific example, let us now consider the EdS model, which has the advantage of giving simple analytic solutions. In this case, one obtains only the growing solution:

$$\delta \propto a \propto t^{2/3}. \tag{A.74}$$

Therefore, in an EdS Universe, the linear growth of a density perturbation is proportional to the expansion factor $(1+z)$. Extending this theory to more general cosmological models is also possible. In general, one finds that the fastest is the expansion, the slowest is the linear growth of perturbations. It is more convenient to describe the linear evolution of the perturbation in terms of the *linear fluctuation growth factor* $D(z)$ which contains the dependence on the assumed cosmology (e.g. Peebles, 1993). The evolution in redshift of a generic perturbation $\delta(z)$ will be given by

$$\delta(z) = \delta_i \left[\frac{D(z)}{D(z_i)}\right], \tag{A.75}$$

where $\delta_i$ is the overdensity of the fluctuation at the initial redshift $z_i$.

### A.6.3 The spherical collapse

Consider a fluctuation of the density field having a spherical shape, embedded in a flat Universe, described by the EdS model (see Section A.5.1). Following the Birkoff theorem, this overdense sphere behaves like a closed Universe, within which the expansion law is given by:

$$H^2 = \frac{8\pi G}{3} - \frac{k}{a^2}, \tag{A.76}$$

while the matter outside the sphere do not affect the dynamics inside it. One obtains then:

$$\frac{d^2R}{dt^2} = -\frac{GM}{R^2} = -\frac{4\pi G\rho_0 R(1+\delta)}{3}, \tag{A.77}$$

where $\rho_0$ is the mean density in the surrounding space, $R$ and $\delta$ are the radius and the overdensity of the sphere, respectively.

In the case of the Friedmann model for the closed Universe, described in Paragraph A.5, the sphere expands out to a maximum radius $R_{max}$ at the time $t_{max}$ and then collapses. Owing to the geometry of the problem, the time of the collapse $t_c$ is twice the time $t_{max}$, while the radius will obviously be zero. In this case, the sphere follows the same evolution, until the collapse is slowed and finally stopped by the pressure support. The system, after a few oscillations, achieve a stable configuration. This process is called *virialization*, since at the end the property of the system are those given by the virial theorem.

At the time of maximum expansion, it can be shown that the ratio between the density of the perturbation and that of the surrounding environment is:

$$\chi = \frac{\rho(t_{max})}{\rho_0(t_{max})} \simeq \frac{9}{16}\pi^2 \simeq 5.55, \tag{A.78}$$

The virialization generally occurs at a time $t_{vir}$, which is approximately equal to the time of the collapse of the Friedmann model $t_{vir} = t_c \simeq 2t_{max}$, within a sphere having radius $R_{vir} = R_{max}/2$. By recalling that $\rho \propto R^{-3}$ and $\rho_0 \propto t^{-2}$ for the perturbation and

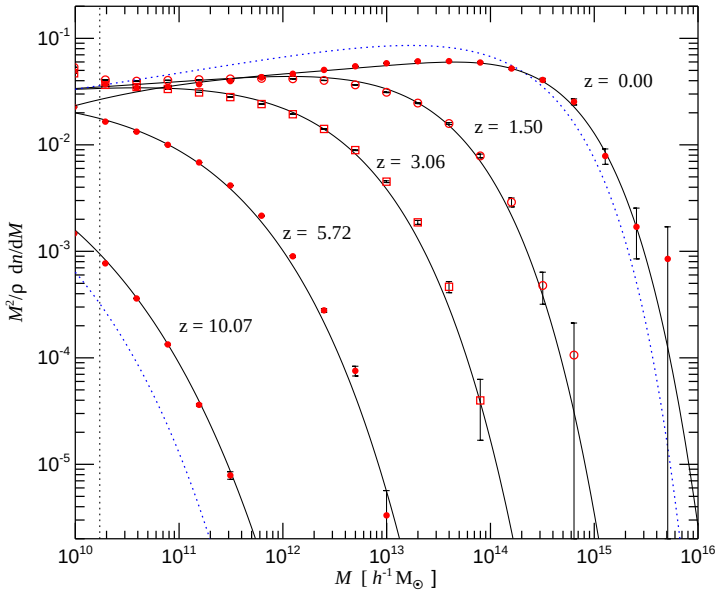


**Figure A.2.** Points with errorbars represent the mass function of dark matter halos identified in a dark matter simulation (Springel et al., 2005) at different redshifts. Solid and dotted curves represent two model mass functions by Press & Schechter (1974) and by Jenkins et al. (2001) respectively.

for the background densities respectively, one can now easily compute the overdensity of the perturbation at the virialization time:

$$\Delta_v = \frac{\rho(t_{vir})}{\rho_0(t_{vir})} = \frac{8\rho(t_{max})}{(1/4)\rho_0(t_{max})} = 32\chi = 18\pi^2 \simeq 178, \tag{A.79}$$

The spherical collapse theory can be extended to other Friedmann models (also with the presence of the cosmological constant), obtaining different values for the overdensity at the virialization (e.g. Eke et al., 1996). In the case of the currently favoured ΛCDM model ($\Omega_M = 0.3$, $\Omega_\Lambda = 0.7$), one obtains $\Delta_v \simeq 100$.

If extrapolated according to linear theory, it can be shown that the critical overdensity at virialization in a EdS model is $\delta_{sc} = 1.686$, with slightly different values for more favoured cosmological models (e.g. Kitayama & Suto, 1997).

Finally, in both observations and simulations of galaxy clusters, it is common practice to define a typical radius $R_\Delta$ by requiring that the mean density inside it corresponds to a given overdensity $\Delta$. All the other quantities (mass $M_\Delta$, temperature $T_\Delta$, entropy $S_\Delta$, etc.) are then computed within such radius. The quantity $\Delta_v$ (computed for the appropriate cosmology) is naturally used to identify the virialized region. Other $\Delta$ values commonly adopted in X–ray observations are 200, 500 and 2500; the first identifies a very large portion of the cluster generally accessible only with low–background long exposures of nearby clusters, the second represents a typical limiting radius for cluster studies, while the third corresponds to the core regions of the cluster.

### A.6.4 The mass function of dark matter halos

Press & Schechter (1974) (PS hereafter) computed the expected mass distribution of

virialized dark matter halos. Their basic assumptions are that the formation process can be described by the spherical collapse model and that the primordial density fluctuations are Gaussian:

$$P(\delta)d\delta = \frac{1}{(2\pi\sigma^2)^{1/2}} \exp\left(-\frac{\delta^2}{2\sigma^2}\right) d\delta. \tag{A.80}$$

In this density field, the expected fraction of points which are surrounded by such a sphere identifies the fraction of fluid elements which are destined to be part of a collapsed halo of mass exceeding the value $M = 4\pi/3(aR)^3\rho_0$, where $\rho_0$ is the mean density:

$$F(R,z) = \int_{\delta_c}^{\infty} P(\delta)d\delta = \frac{1}{\sqrt{2\pi}D(z)\sigma_{R,0}} \exp\left(-\frac{\delta_{sc}^2}{2D^2(z)\sigma_{R,0}^2}\right). \tag{A.81}$$

However, by integrating the above formula one obtains that only one half of the points are part of a lump at any mass. This is due to the fact that the PS derivation neglects the possibility that a region, that is underdense when smoothed on the scale $M_1$, can be overdense on a larger scale $M_2 > M_1$, thus missing a factor 2 in the equations. The predicted mass distribution function is

$$n(M)dM = -2\frac{\rho}{M}\frac{\partial F}{\partial R}\frac{dR}{dM}dM = \frac{\rho}{M}f(\nu)\frac{d\nu}{dM}dM \tag{A.82}$$

with

$$f(\nu) = \frac{1}{\sqrt{2\pi}} \exp(-\nu^2/2) \tag{A.83}$$

The function $f$ depends only on the variable $\nu = \delta_{crit}/\sigma_M$ and is normalised so that $\int f(\nu)d\nu = 1$. The quantity $\delta_{crit}(z)$ is the linear-theory overdensity extrapolated to the present time for a uniform spherical fluctuation collapsing at redshift $z$: $\delta_{crit} = [\delta_{sc}/D(z)]$.

An extension of the PS approach has been proposed by Sheth & Tormen (1999) (ST hereafter), who adopted the *excursion-set* approach of Bond et al. (1991) and introduced the collapse of elliptical rather than spherical perturbations. In this case, the time of the collapse depends not only on the overdensity, but also on the shape of the perturbation. They showed that the virialization occurs earlier for less elliptical clusters and, at a given ellipticity, earlier of less prolate objects. With respect to an approach based on the spherical model, now the less massive objects need a larger overdensity to collapse, while the more massive ones are still well described by the spherical model. With this assumptions, they proposed a new mass distribution for the dark matter halos:

$$f(\nu) = A\left(1 + \frac{1}{(a\nu^2)^q}\right)\left(\frac{2a}{\pi}\right)^{1/2} \exp\left(-\frac{a\nu^2}{2}\right), \tag{A.84}$$

where $a = 0.707$, $q = 0.3$ and $A \simeq 0.322$ for the normalisation. The above equation reduces to the PS expression for $a = 1$ , $A = 1/2$, and $q = 0$.

In addition to theoretical modelling, some empirical fitting formulae for the mass function were proposed on the basis of N–body simulations. For example, Jenkins et al. (2001) (JMF hereafter) analysed a set of simulations having different cosmological parameters and mass resolution and found a unique fitting formula which is able to satisfactory describe all of them. They found convenient to use the quantity $\ln \sigma^{-1}(M,z)$ as the mass variable instead of $M$. The mass function is now described in terms of:

$$f(\sigma,z) = \frac{M}{\rho}n(M,z)\frac{dM}{d\ln\sigma^{-1}} \tag{A.85}$$

where $\sigma^2(M, z)$ is the variance of the linear density field, extrapolated to the redshift $z$ at which aloes are identified, after smoothing with a spherical top-hat filter which encloses mass $M$ in the mean. The use of this new variable "factors out" most of the difference in the mass functions between different epochs, cosmologies and power spectra, and so allows a wider comparison among different simulations.

$$f(M) = 0.315e^{-\left|ln(\sigma^{-1})+0.61\right|^{3.8}}, \tag{A.86}$$

This function is actually very close to the ST one with $a = 0.75$. The main difference between these two formulations is that the ST one predicts more objects at the high mass tail.

Springel et al. (2005) carried out a comparison of the PS and JMF mass functions with a large cosmological simulation which contains only dark matter. Figure A.2 shows a comparison between the mass function found in the simulation and the PS and JMF predictions. Their results show that the JMF function provides a good match with their simulation data, while the PS one underpredicts the high–mass end by up to an order of magnitude. Another comparison by Warren et al. (2006) using another set of simulations leads to similar results.

# Bibliography


Abroe M. E., Balbi A., Borrill J., Bunn E. F., Hanany S., Ferreira P. G., Jaffe A. H., Lee A. T., Olive K. A., Rabii B., Richards P. L., Smoot G. F., Stompor R., Winant C. D., Wu J. H. P., 2002, MNRAS, 334, 11

Aghanim N., Hansen S. H., Lagache G., 2004, ArXiv Astrophysics e-prints

Allen S. W., Schmidt R. W., Ebeling H., Fabian A. C., van Speybroeck L., 2004, MNRAS, 353, 457

Allen S. W., Schmidt R. W., Fabian A. C., 2001, MNRAS, 328, L37

Ameglio S., Borgani S., Diaferio A., Dolag K., 2006, MNRAS, 369, 1459

Ameglio S., Borgani S., Pierpaoli E., Dolag K., 2007, MNRAS, 382, 397

Arnaud M., 2005, in Melchiorri F., Rephaeli Y., eds, Background Microwave Radiation and Intracluster Cosmology X-ray observations of clusters of galaxies. pp 77–+

Arnaud M., Majerowicz S., Lumb D., Neumann D. M., Aghanim N., Blanchard A., Boer M., Burke D. J., Collins C. A., Giard M., Nevalainen J., Nichol R. C., Romer A. K., Sadat R., 2002, A&A, 390, 27

Bagla J. S., 2005, Current Science, 88, 1088

Balogh M. L., Pearce F. R., Bower R. G., Kay S. T., 2001, MNRAS, 326, 1228

Barbosa D., Bartlett J. G., Blanchard A., Oukbir J., 1996, A&A, 314, 13

Barnes J., Hut P., 1986, Nature, 324, 446

Bartlett J. G., 2000, ArXiv Astrophysics e-prints

Bartlett J. G., Melin J.-B., 2006, A&A, 447, 405

Bartlett J. G., Silk J., 1994, ApJ, 423, 12

Benson A. J., Lacey C. G., Baugh C. M., Cole S., Frenk C. S., 2002, MNRAS, 333, 156

Benson B. A., Church S. E., Ade P. A. R., Bock J. J., Ganga K. M., Henson C. N., Thompson K. L., 2004, ApJ, 617, 829

Birkinshaw M., 1979, MNRAS, 187, 847

Birkinshaw M., 1999, Phys. Rep., 310, 97

Birkinshaw M., Gull S. F., Hardebeck H., 1984, Nature, 309, 34

Birkinshaw M., Hughes J. P., 1994, ApJ, 420, 33

Birkinshaw M., Lancaster K., 2005, in Melchiorri F., Rephaeli Y., eds, Background Microwave Radiation and Intracluster Cosmology Observational issues in radiometric and interferometric detection and analysis of the Sunyaev-Zel'dovich effects. pp 127–+

Blain A. W., 1998, MNRAS, 297, 502

Blanton E. L., 2004, in Reiprich T., Kempner J., Soker N., eds, The Riddle of Cooling Flows in Galaxies and Clusters of galaxies The Interaction of Radio Sources and X-Ray-Emitting Gas in Cooling Flows. pp 181–+

Boella G., Butler R. C., Perola G. C., Piro L., Scarsi L., Bleeker J. A. M., 1997, A&AS, 122, 299

Böhringer H., Matsushita K., Churazov E., Ikebe Y., Chen Y., 2002, A&A, 382, 804

Böhringer H., Schuecker P., Guzzo L., Collins C. A., Voges W., Cruddace R. G., Ortiz-Gil A., Chincarini G., De Grandi S., Edge A. C., MacGillivray H. T., Neumann D. M., Schindler S., Shaver P., 2004, A&A, 425, 367

Böhringer H., Schuecker P., Pratt G. W., Arnaud M., Ponman T. J., Croston J. H., Borgani S., Bower R. G., Briel U. G., Collins C. A., Donahue M. e. a., 2007, A&A, 469, 363

Bonamente M., Joy M., LaRoque S., Carlstrom J., Nagai D., Marrone D., 2007, ArXiv e-prints, 708

Bonamente M., Joy M. K., Carlstrom J. E., Reese E. D., LaRoque S. J., 2004, ApJ, 614, 56

Bonamente M., Joy M. K., LaRoque S. J., Carlstrom J. E., Reese E. D., Dawson K. S., 2006, ApJ, 647, 25

Bond J. R., Cole S., Efstathiou G., Kaiser N., 1991, ApJ, 379, 440

Borgani S., 2006, ArXiv Astrophysics e-prints

Borgani S., Dolag K., Murante G., Cheng L.-M., Springel V., Diaferio A., Moscardini L., Tormen G., Tornatore L., Tozzi P., 2006, MNRAS, pp 270–+

Borgani S., Finoguenov A., Kay S. T., Ponman T. J., Springel V., Tozzi P., Voit G. M., 2005, MNRAS, 361, 233

Borgani S., Guzzo L., 2001, Nature, 409, 39

Borgani S., Murante G., Springel V., Diaferio A., Dolag K., Moscardini L., Tormen G., Tornatore L., Tozzi P., 2004, MNRAS, 348, 1078

Borgani S., Rosati P., Tozzi P., Stanford S. A., Eisenhardt P. R., Lidman C., Holden B., Della Ceca R., Norman C., Squires G., 2001, ApJ, 561, 13

Bouchet L., 1995, A&AS, 113, 167

Bregman J. N., 2004, in Reiprich T., Kempner J., Soker N., eds, The Riddle of Cooling Flows in Galaxies and Clusters of galaxies Meeting Summary: Cluster Cooling Flows Become Modest. pp 327–+

Buote D. A., 2000, ApJ, 539, 172

Burenin R. A., Vikhlinin A., Hornstrup A., Ebeling H., Quintana H., Mescheryakov A., 2007, ApJS, 172, 561

Carlstrom J. E., Holder G. P., Reese E. D., 2002, ARAA, 40, 643

Carlstrom J. E., Joy M., Grego L., 1996, ApJL, 456, L75+

Cavaliere A., Danese L., de Zotti G., 1979, A&A, 75, 322

Cavaliere A., Fusco-Femiano R., 1976, A&A, 49, 137

Cavaliere A., Gursky H., Tucker W., 1971, Nature, 231, 437

Cavaliere A., Lapi A., 2006, ApJL, 647, L5

Church S. E., Ganga K. M., Ade P. A. R., Holzapfel W. L., Mauskopf P. D., Wilbanks T. M., Lange A. E., 1997, ApJ, 484, 523

Coles P., Lucchin F., 2002, Cosmology: The Origin and Evolution of Cosmic Structure, Second Edition. Cosmology: The Origin and Evolution of Cosmic Structure, Second Edition, by Peter Coles, Francesco Lucchin, pp. 512. ISBN 0-471-48909-3. Wiley-VCH , July 2002.

Cooray A. R., Grego L., Holzapfel W. L., Joy M., Carlstrom J. E., 1998, AJ, 115, 1388

Croston J. H., Arnaud M., Pointecouteau E., Pratt G. W., 2006, A&A, 459, 1007

Dawson K. S., Holzapfel W. L., Carlstrom J. E., Joy M., LaRoque S. J., Reese E. D., 2001, ApJL, 553, L1

De Filippis E., Sereno M., Bautz M. W., Longo G., 2005, ApJ, 625, 108

De Grandi S., Molendi S., 2002, ApJ, 567, 163

Diaferio A., Borgani S., Moscardini L., Murante G., Dolag K., Springel V., Tormen G., Tornatore L., Tozzi P., 2005, MNRAS, 356, 1477

Dolag K., Jubelgas M., Springel V., Borgani S., Rasia E., 2004, ApJL, 606, L97

Dolag K., Meneghetti M., Moscardini L., Rasia E., Bonaldi A., 2005, ArXiv Astrophysics e-prints

Doré O., Bouchet F. R., Mellier Y., Teyssier R., 2001, A&A, 375, 14

Eke V. R., Cole S., Frenk C. S., 1996, MNRAS, 282, 263

Eke V. R., Navarro J. F., Frenk C. S., 1998, ApJ, 503, 569

Ettori S., 2000, MNRAS, 311, 313

Ettori S., De Grandi S., Molendi S., 2002, A&A, 391, 841

Ettori S., Tozzi P., Rosati P., 2003, A&A, 398, 879

Evrard A. E., Metzler C. A., Navarro J. F., 1996, ApJ, 469, 494

Fabian A. C., 2003, in Avila-Reese V., Firmani C., Frenk C. S., Allen C., eds, Revista Mexicana de Astronomia y Astrofisica Conference Series Vol. 17 of Revista Mexicana de Astronomia y Astrofisica, vol. 27, Cluster cores and cooling flows. pp 303–313

Fabian A. C., Sanders J. S., Ettori S., Taylor G. B., Allen S. W., Crawford C. S., Iwasawa K., Johnstone R. M., 2001, MNRAS, 321, L33

Felten J. E., Gould R. J., Stein W. A., Woolf N. J., 1966, ApJ, 146, 955

Finoguenov A., Guzzo L., Hasinger G., Scoville N. Z., Aussel H., Böhringer H., Brusa M., Capak P., Cappelluti N., Comastri A., Giodini S., Griffiths R. E. e. a., 2007, ApJS, 172, 182

Fischer M. L., Lange A. E., 1993, ApJ, 419, 433

Fowler J. W., ACT Collaboration 2006, in Bulletin of the American Astronomical Society Vol. 38 of Bulletin of the American Astronomical Society, The Atacama Cosmology Telescope. pp 1227–+

Freedman W. L., Madore B. F., Gibson B. K., Ferrarese L., Kelson D. D., Sakai S., Mould J. R., Kennicutt R. C., Ford H. C., Graham J. A., Huchra J. P., Hughes S. M. G., Illingworth G. D., Macri L. M., Stetson P. B., 2001, ApJ, 553, 47

Fukugita M., Hogan C. J., Peebles P. J. E., 1998, ApJ, 503, 518

Gardini A., Rasia E., Mazzotta P., Tormen G., De Grandi S., Moscardini L., 2004, MNRAS, 351, 505

Gehrels N., Chincarini G., Giommi P., Mason K. O., Nousek J. A., Wells A. A., White N. E., Barthelmy S. D., Burrows D. N., Cominsky L. R., Hurley K. C. e. a., 2004, ApJ, 611, 1005

Gelman A., Rubin D., 1992, Stat. Science, 7, 457

Gilks W., Richardson S., Spiegelhalter D., 1996, Markov Chain Monte Carlo in practice. Chapman and Hall

Gingold R. A., Monaghan J. J., 1977, MNRAS, 181, 375

Gladders M. D., Yee H. K. C., 2005, ApJS, 157, 1

Glenn J., Bock J. J., Chattopadhyay G., Edgington S. F., Lange A. E., Zmuidzinas J., Mauskopf P. D., Rownd B., Yuen L., Ade P. A., 1998, in Phillips T. G., ed., Proc. SPIE Vol. 3357, p. 326-334, Advanced Technology MMW, Radio, and Terahertz Telescopes, Thomas G. Phillips; Ed. Vol. 3357 of Presented at the Society of Photo-Optical Instrumentation Engineers (SPIE) Conference, Bolocam: a millimeter-wave bolometric camera. pp 326–334

Grainge K., Jones M. E., Pooley G., Saunders R., Edge A., Grainger W. F., Kneissl R., 2002, MNRAS, 333, 318

Gunn J. E., 1978, in Saas-Fee Advanced Course 8: Observational Cosmology Advanced

Course The Friedmann models and optical observations in cosmology. pp 1–+
Güsten R., Nyman L. Å., Schilke P., Menten K., Cesarsky C., Booth R., 2006, A&A, 454, L13
Guth A. H., Weinberg E. J., 1981, Phys. Rev. D, 23, 876
Haardt F., Madau P., 1996, ApJ, 461, 20
Haiman Z., Allen S., Bahcall N., Bautz M., Boehringer H., Borgani S., Bryan G., Cabrera B., Canizares C., Citterio O., Evrard A., Finoguenov A. e. a., 2005, ArXiv Astrophysics e-prints
Haiman Z., Mohr J. J., Holder G. P., 2001, ApJ, 553, 545
Hallman E. J., O'Shea B. W., Burns J. O., Norman M. L., Harkness R., Wagner R., 2007, ArXiv e-prints, 704
Hastings W., 1970, Biometrika, 57, 97
Henry J. P., Mullis C. R., Voges W., Böhringer H., Briel U. G., Gioia I. M., Huchra J. P., 2006, ApJS, 162, 304
Hernquist L., Katz N., 1989, ApJS, 70, 419
Holder G. P., Mohr J. J., Carlstrom J. E., Evrard A. E., Leitch E. M., 2000, ApJ, 544, 629
Holzapfel W. L., Ade P. A. R., Church S. E., Mauskopf P. D., Rephaeli Y., Wilbanks T. M., Lange A. E., 1997, ApJ, 481, 35
Holzapfel W. L., Arnaud M., Ade P. A. R., Church S. E., Fischer M. L., Mauskopf P. D., Rephaeli Y., Wilbanks T. M., Lange A. E., 1997, ApJ, 480, 449
Hu W., White M., 1997, ApJ, 479, 568
Hubble E., Humason M. L., 1931, ApJ, 74, 43
Hubble E. P., 1926, ApJ, 63, 236
Hughes J. P., Birkinshaw M., 1998, ApJ, 501, 1
Itoh N., Kohyama Y., Nozawa S., 1998, ApJ, 502, 7
Jeltema T. E., Hallman E. J., Burns J. O., Motl P. M., 2007, ArXiv e-prints, 708
Jenkins A., Frenk C., White S., Colberg J., Cole S., Evrard A., Couchman H., Yoshida N., 2001, MNRAS, 321, 372
Jones M., Saunders R., Alexander P., Birkinshaw M., Dilon N., Grainge K., Hancock S., Lasenby A., Lefebvre D., Pooley G., 1993, Nature, 365, 320
Jones M. E., Edge A. C., Grainge K., Grainger W. F., Kneissl R., Pooley G. G., Saunders R., Miyoshi S. J., Tsuruta T., Yamashita K., Tawara Y., Furuzawa A., Harada A., Hatsukade I., 2005, MNRAS, 357, 518
Joy M., LaRoque S., Grego L., Carlstrom J. E., Dawson K., Ebeling H., Holzapfel W. L., Nagai D., Reese E. D., 2001, ApJL, 551, L1
Kaastra J. S., Tamura T., Peterson J. R., Bleeker J. A. M., Ferrigno C., Kahn S. M., Paerels F. B. S., Piffaretti R., Branduardi-Raymont G., Böhringer H., 2004, A&A, 413, 415
Kaneko T., 2006, in Ground-based and Airborne Telescopes. Edited by Stepp, Larry M.. Proceedings of the SPIE, Volume 6267, pp. 62673R (2006). Vol. 6267 of Presented at the Society of Photo-Optical Instrumentation Engineers (SPIE) Conference, Toward the arrival of SZ cluster surveys: the Arcminute Microkelvin Imager Small Array
Katz N., Weinberg D. H., Hernquist L., 1996, ApJS, 105, 19
Katz N., White S. D. M., 1993, ApJ, 412, 455
Kay S. T., Powell L. C., Liddle A. R., Thomas P. A., 2007, ArXiv e-prints, 706
Kay S. T., Thomas P. A., Jenkins A., Pearce F. R., 2004, MNRAS, 355, 1091
Kazantzidis S., Kravtsov A. V., Zentner A. R., Allgood B., Nagai D., Moore B., 2004,

ApJL, 611, L73
Kitayama T., Suto Y., 1997, ApJ, 490, 557
Kneissl R., Jones M. E., Saunders R., Eke V. R., Lasenby A. N., Grainge K., Cotter G., 2001, MNRAS, 328, 783
Knop R. A., Aldering G., Amanullah R., Astier P., Blanc G., Burns M. S., Conley A., Deustua S. E., Doi M., Ellis R., Fabbro S., Folatelli G. e. a., 2003, ApJ, 598, 102
Knox L., Holder G. P., Church S. E., 2004, ApJ, 612, 96
Kolb E. W., Turner M. S., 1990, Frontiers in Physics, 69
Kotov O., Vikhlinin A., 2006, ApJ, 641, 752
Kravtsov A. V., Nagai D., Vikhlinin A. A., 2005, ApJ, 625, 588
Kriss G. A., Cioffi D. F., Canizares C. R., 1983, ApJ, 272, 439
LaRoque S. J., Bonamente M., Carlstrom J. E., Joy M. K., Nagai D., Reese E. D., Dawson K. S., 2006, ApJ, 652, 917
LaRoque S. J., Joy M., Carlstrom J. E., Ebeling H., Bonamente M., Dawson K. S., Edge A., Holzapfel W. L., Miller A. D., Nagai D., Patel S. K., Reese E. D., 2003, ApJ, 583, 559
Lee J., Suto Y., 2004, ApJ, 601, 599
Lewis A., Bridle S., 2002, Phys. Rev. D, 66, 103511
Lin Y.-T., Mohr J. J., Stanford S. A., 2003, ApJ, 591, 749
Loeb A., Refregier A., 1997, ApJL, 476, L59+
Loken C., Norman M. L., Nelson E., Burns J., Bryan G. L., Motl P., 2002, ApJ, 579, 571
Longair M. S., 1998, Modern cosmology-a critical assessment (1992). The Universe Unfolding, pp 275–+
Lucy L. B., 1977, AJ, 82, 1013
MacKay D., 1996, Markov Chain Monte Carlo in practice. Chapman and Hall
Markevitch M., Forman W. R., Sarazin C. L., Vikhlinin A., 1998, ApJ, 503, 77
Markevitch M., Vikhlinin A., 2007, Phys. Rep., 443, 1
Mason B. S., Myers S. T., Readhead A. C. S., 2001, ApJL, 555, L11
Mathiesen B. F., Evrard A. E., 2001, ApJ, 546, 100
Maughan B. J., Jones L. R., Ebeling H., Perlman E., Rosati P., Frye C., Mullis C. R., 2003, ApJ, 587, 589
Mazzotta P., Rasia E., Moscardini L., Tormen G., 2004, MNRAS, 354, 10
McLaughlin D. E., 1999, AJ, 117, 2398
Metropolis N., Rosenbluth A., Rosenbluth M., Teller A., Teller E., 1953, Journal of Chemical Physics, 21, 1087
Mitsuda K., Bautz M., Inoue H., Kelley R. L., Koyama K., Kunieda H., Makishima K., Ogawara Y., Petre R., Takahashi T., Tsunemi H., White N. E., Anabuki N., Angelini L., Arnaud K., Awaki H. e. a., 2007, PASJ, 59, 1
Mohr J. J., Mathiesen B., Evrard A. E., 1999, ApJ, 517, 627
Molendi S., Pizzolato F., 2001, ApJ, 560, 194
Molnar S. M., Birkinshaw M., Mushotzky R. F., 2002, ApJ, 570, 1
Monaghan J. J., 2005, Reports of Progress in Physics, 68, 1703
Morandi A., Ettori S., Moscardini L., 2007, MNRAS, pp 541–+
Muchovej S., Mroczkowski T., Carlstrom J. E., Cartwright J., Greer C., Hennessy R., Loh M., et al., 2007, ApJ, 663, 708
Mullis C. R., Rosati P., Lamer G., Böhringer H., Schwope A., Schuecker P., Fassbender R., 2005, ApJL, 623, L85
Mushotzky R. F., 2004, in Mulchaey J. S., Dressler A., Oemler A., eds, Clusters of Galax-

ies: Probes of Cosmological Structure and Galaxy Evolution Clusters of Galaxies: An X-ray Perspective. pp 123–+
Nagai D., Vikhlinin A., Kravtsov A. V., 2007, ApJ, 655, 98
Navarro J., Frenk C., White S., 1997, ApJ, 490, 493
Neal R. M., , 1993, Probabilistic inference using Markov Chain Monte Carlo methods
Neumann D. M., 2005, A&A, 439, 465
Neumann D. M., Arnaud M., 1999, A&A, 348, 711
Neumann D. M., Arnaud M., 2001, A&A, 373, L33
Nozawa S., Itoh N., Kohyama Y., 1998, ApJ, 508, 17
Padin S., Cartwright J. K., Mason B. S., Pearson T. J., Readhead A. C. S., Shepherd M. C., Sievers J., Udomprasert P. S., Holzapfel W. L., Myers S. T., Carlstrom J. E., Leitch E. M., Joy M., Bronfman L., May J., 2001, ApJL, 549, L1
Padmanabhan T., 2002, Theoretical Astrophysics, Volume III: Galaxies and Cosmology. Theoretical Astrophysics, by T. Padmanabhan, pp. 638. ISBN 0521562422. Cambridge, UK: Cambridge University Press, October 2002.
Patel S. K., Joy M., Carlstrom J. E., Holder G. P., Reese E. D., Gomez P. L., Hughes J. P., Grego L., Holzapfel W. L., 2000, ApJ, 541, 37
Peacock J., Murdin P., 2002, Encyclopedia of Astronomy and Astrophysics
Peebles P. J. E., 1993, Principles of physical cosmology. Princeton University Press
Pérez-Grovas A. S., Schloerb F. P., Hughes D., Yun M., 2006, in Ground-based and Airborne Telescopes. Edited by Stepp, Larry M.. Proceedings of the SPIE, Volume 6267, pp. 626701 (2006). Vol. 6267 of Presented at the Society of Photo-Optical Instrumentation Engineers (SPIE) Conference, The Large Millimeter Telescope
Peterson J. R., Kahn S. M., Paerels F. B. S., Kaastra J. S., Tamura T., Bleeker J. A. M., Ferrigno C., Jernigan J. G., 2003, ApJ, 590, 207
Peterson J. R., Paerels F. B. S., Kaastra J. S., Arnaud M., Reiprich T. H., Fabian A. C., Mushotzky R. F., Jernigan J. G., Sakelliou I., 2001, A&A, 365, L104
Pierpaoli E., Anthoine S., Huffenberger K., Daubechies I., 2005, MNRAS, 359, 261
Pierpaoli E., Borgani S., Scott D., White M., 2003, MNRAS, 342, 163
Piffaretti R., Jetzer P., Kaastra J. S., Tamura T., 2005, A&A, 433, 101
Plionis M., Barrow J. D., Frenk C. S., 1991, MNRAS, 249, 662
Pointecouteau E., Arnaud M., Pratt G. W., 2005, A&A, 435, 1
Pointecouteau E., Hattori M., Neumann D., Komatsu E., Matsuo H., Kuno N., Böhringer H., 2002, A&A, 387, 56
Ponman T. J., Cannon D. B., Navarro J. F., 1999, Nature, 397, 135
Ponman T. J., Sanderson A. J. R., Finoguenov A., 2003, MNRAS, 343, 331
Pratt G. W., Arnaud M., 2002, A&A, 394, 375
Pratt G. W., Arnaud M., 2005, A&A, 429, 791
Pratt G. W., Arnaud M., Pointecouteau E., 2006, A&A, 446, 429
Pratt G. W., Böhringer H., Croston J. H., Arnaud M., Borgani S., Finoguenov A., Temple R. F., 2007, A&A, 461, 71
Predehl P., Hasinger G., Böhringer H., Briel U., Brunner H., Churazov E., Freyberg M., Friedrich P., Kendziorra E., Lutz D., Meidinger N. e. a., 2006, in Space Telescopes and Instrumentation II: Ultraviolet to Gamma Ray. Edited by Turner, Martin J. L.; Hasinger, Günther. Proceedings of the SPIE, Volume 6266, pp. 62660P (2006). Vol. 6266 of Presented at the Society of Photo-Optical Instrumentation Engineers (SPIE) Conference, eROSITA
Press W. H., Schechter P., 1974, ApJ, 187, 425

Press W. H., Teukolsky S. A., Vetterling W. T., Flannery B. P., 1992, Numerical recipes in FORTRAN. The art of scientific computing. Cambridge: University Press, —c1992, 2nd ed.

Puchwein E., Bartelmann M., 2006, A&A, 455, 791

Puchwein E., Bartelmann M., 2007, A&A, 474, 745

Radford S. J. E., Giovanelli R., Sebring T. A., Zmuidzinas J., 2007, ArXiv e-prints, 704

Raftery 2003, Information Theory, Inference, and Learning Algorithms. Cambridge University Press (http://www.inference.phy.cam.ac.uk/mackay/itprnn/book.html

Rapetti D., Allen S. W., 2007, ArXiv e-prints, 710

Rasia E., Ettori S., Moscardini L., Mazzotta P., Borgani S., Dolag K., Tormen G., Cheng L. M., Diaferio A., 2006a, MNRAS, 369, 2013

Rasia E., Ettori S., Moscardini L., Mazzotta P., Borgani S., Dolag K., Tormen G., Cheng L. M., Diaferio A., 2006b, ArXiv Astrophysics e-prints

Rasia E., Mazzotta P., Borgani S., Moscardini L., Dolag K., Tormen G., Diaferio A., Murante G., 2005, ApJL, 618, L1

Rasia E., Tormen G., Moscardini L., 2004, MNRAS, 351, 237

Reblinsky K., 2000, A&A, 364, 377

Reese E. D., Carlstrom J. E., Joy M., Mohr J. J., Grego L., Holzapfel W. L., 2002, ApJ, 581, 53

Rephaeli Y., 1995, ARAA, 33, 541

Riess A. G., Li W., Stetson P. B., Filippenko A. V., Jha S., Kirshner R. P., Challis P. M., Garnavich P. M., Chornock R., 2005, ApJ, 627, 579

Rosati P., Borgani S., Norman C., 2002, ARAA, 40, 539

Rosati P., Tozzi P., Ettori S., Mainieri V., Demarco R., Stanford S. A., Lidman C., Nonino M., Borgani S., Della Ceca R., Eisenhardt P., Holden B. P., Norman C., 2004, AJ, 127, 230

Ruhl J., Ade P. A. R., Carlstrom J. E., Cho H.-M., et al., 2004, in Bradford C. M., Ade P. A. R., Aguirre J. E., Bock J. J., Dragovan M., Duband L., Earle L., Glenn J., Matsuhara H., Naylor B. J., Nguyen H. T., Yun M., Zmuidzinas J., eds, Millimeter and Submillimeter Detectors for Astronomy II.Edited by Jonas Zmuidzinas, Wayne S. Holland and Stafford Withington Proceedings of the SPIE, Volume 5498, pp. 11-29 (2004). Vol. 5498 of Presented at the Society of Photo-Optical Instrumentation Engineers (SPIE) Conference, The South Pole Telescope. pp 11–29

Runyan M. C., Ade P. A. R., Bhatia R. S., Bock J. J., Daub M. D., Goldstein J. H., Haynes C. V., Holzapfel W. L., Kuo C. L., Lange A. E., Leong J. e. a., 2003, ApJS, 149, 265

Rybicki G. B., Lightman A. P., 1986, Radiative Processes in Astrophysics. Radiative Processes in Astrophysics, by George B. Rybicki, Alan P. Lightman, pp. 400. ISBN 0-471-82759-2. Wiley-VCH , June 1986.

Salpeter E. E., 1955, ApJ, 121, 161

Sasaki S., 1996, PASJ, 48, L119

Sazonov S. Y., Sunyaev R. A., 1998, ApJ, 508, 1

Schuecker P., Guzzo L., Collins C. A., Böhringer H., 2002, MNRAS, 335, 807

Sebring T. A., Giovanelli R., Radford S., Zmuidzinas J., 2006, in Ground-based and Airborne Telescopes. Edited by Stepp, Larry M.. Proceedings of the SPIE, Volume 6267, pp. 62672C (2006). Cornell Caltech Atacama Telescope (CCAT): a 25-m aperture telescope above 5000-m altitude

Sereno M., 2007, ArXiv e-prints, 707

Sheth R., Tormen G., 1999, MNRAS, 308, 119
Silk J., White S. D. M., 1978, ApJL, 226, L103
Smail I., Ivison R. J., Blain A. W., 1997, ApJL, 490, L5+
Snowden S. L., Mushotzky R. M., Kuntz K. D., Davis D. S., 2007, ArXiv e-prints, 710
Solovyeva L., Anokhin S., Sauvageot J. L., Teyssier R., Neumann D., 2007, ArXiv e-prints, 709
Spergel D., Verde L., Peiris H., Komatsu E., et al., 2003, ApJ submitted; preprint astro-ph/0302209
Spergel D. N., Bean R., Doré O., Nolta M. R., Bennett C. L., Dunkley J., Hinshaw G., Jarosik N., et al., 2007, ApJS, 170, 377
Spergel D. N., Verde L., Peiris H. V., Komatsu E., Nolta M. R., Bennett C. L., Halpern M., Hinshaw G., Jarosik N., Kogut A., Limon M., Meyer S. S., Page L., Tucker G. S., Weiland J. L., Wollack E., Wright E. L., 2003, ApJS, 148, 175
Springel V., 2005a, MNRAS, 364, 1105
Springel V., 2005b, ArXiv Astrophysics e-prints
Springel V., Hernquist L., 2003, MNRAS, 339, 289
Springel V., White S. D. M., Jenkins A., Frenk C. S., Yoshida N., Gao L., Navarro J., Thacker R., Croton D., Helly J., Peacock J. A., Cole S., Thomas P., Couchman H., Evrard A., Colberg J., Pearce F., 2005, Nature, 435, 629
Springel V., Yoshida N., White S., 2001, New Astronomy, 6, 79
Subrahmanyan R., Kesteven M. J., Ekers R. D., Sinclair M., Silk J., 2000, MNRAS, 315, 808
Sunyaev R. A., Zeldovich Y. B., 1970, Comments on Astrophysics and Space Physics, 2, 66
Sunyaev R. A., Zeldovich Y. B., 1972, Comments on Astrophysics and Space Physics, 4, 173
Tanaka Y., Inoue H., Holt S. S., 1994, PASJ, 46, L37
Tormen G., Bouchet F. R., White S. D. M., 1997, MNRAS, 286, 865
Tornatore L., Borgani S., Dolag K., Matteucci F., 2007, MNRAS, 382, 1050
Tornatore L., Borgani S., Springel V., Matteucci F., Menci N., Murante G., 2003, MNRAS, 342, 1025
Tozzi P., Norman C., 2001, ApJ, 546, 63
Truemper J., 1982, Advances in Space Research, 2, 241
Tsuboi M., Miyazaki A., Kasuga T., Matsuo H., Kuno N., 1998, PASJ, 50, 169
Udomprasert P. S., Mason B. S., Readhead A. C. S., Pearson T. J., 2004, ApJ, 615, 63
Valdarnini R., 2003, MNRAS, 339, 1117
Ventimiglia D. A., Voit G. M., Donahue M., Borgani S., Ameglio S., 2006, in Bulletin of the American Astronomical Society Vol. 38 of Bulletin of the American Astronomical Society, Quantifying Galaxy Cluster Substructure. pp 1000–+
Vikhlinin A., 2006, ApJ, 640, 710
Vikhlinin A., Forman W., Jones C., 1999, ApJ, 525, 47
Vikhlinin A., Kravtsov A., Forman W., Jones C., Markevitch M., Murray S. S., Van Speybroeck L., 2006, ApJ, 640, 691
Vikhlinin A., Markevitch M., Murray S. S., Jones C., Forman W., Van Speybroeck L., 2005, ApJ, 628, 655
Voit G. M., 2005, Reviews of Modern Physics, 77, 207
Voit G. M., Balogh M. L., Bower R. G., Lacey C. G., Bryan G. L., 2003, ApJ, 593, 272
Voit G. M., Bryan G. L., 2001, ApJL, 551, L139

Voit G. M., Bryan G. L., Balogh M. L., Bower R. G., 2002, ApJ, 576, 601
Voit G. M., Ponman T. J., 2003, ApJL, 594, L75
Warren M. S., Abazajian K., Holz D. E., Teodoro L., 2006, ApJ, 646, 881
White M., Hernquist L., Springel V., 2002, ApJ, 579, 16
White S. D. M., Efstathiou G., Frenk C. S., 1993, MNRAS, 262, 1023
Yoshida N., Colberg J., White S. D. M., Evrard A. E., MacFarland T. J., Couchman H. M. P., Jenkins A., Frenk C. S., Pearce F. R., Efstathiou G., Peacock J. A., Thomas P. A., 2001, MNRAS, 325, 803
Yoshida N., Furlanetto S. R., Hernquist L., 2005, ApJL, 618, L91
Zappacosta L., Buote D. A., Gastaldello F., Humphrey P. J., Bullock J., Brighenti F., Mathews W., 2006, ApJ, 650, 777
Zaroubi S., Squires G., de Gasperis G., Evrard A. E., Hoffman Y., Silk J., 2001, ApJ, 561, 600
Zaroubi S., Squires G., Hoffman Y., Silk J., 1998, ApJL, 500, L87+
Zhang T.-J., Wu X.-P., 2000, ApJ, 545, 141
Zhang Y.-Y., Böhringer H., Finoguenov A., Ikebe Y., Matsushita K., Schuecker P., Guzzo L., Collins C. A., 2006, A&A, 456, 55